

STATE OF CALIFORNIA DEPARTMENT OF TRANSPORTATION  
**TECHNICAL REPORT DOCUMENTATION PAGE**  
 TR0003 (REV. 10/98)

1. REPORT NUMBER <b>CA12-2001</b>		2. GOVERNMENT ASSOCIATION NUMBER		3. RECIPIENT'S CATALOG NUMBER	
4. TITLE AND SUBTITLE <b>Seismic Performance of an I-Girder to Inverted-T Bent Cap Connection</b>				5. REPORT DATE <b>September 2011</b>	
				6. PERFORMING ORGANIZATION CODE	
7. AUTHOR(S) Rick Snyder, Justin Vander Werff, Zach Thiemann, Sri Sritharan & Jay Holombo				8. PERFORMING ORGANIZATION REPORT NO.	
9. PERFORMING ORGANIZATION NAME AND ADDRESS Department of Civil, Construction & Environmental Engineering Iowa State University Ames, Iowa 50011				10. WORK UNIT NUMBER	
				11. CONTRACT OR GRANT NUMBER <b>59A0615</b>	
12. SPONSORING AGENCY AND ADDRESS California Department of Transportation Division of Engineering Services, MS-09 1801 30 <sup>th</sup> Street Sacramento CA 95816				13. TYPE OF REPORT AND PERIOD COVERED <b>Final</b>	
				14. SPONSORING AGENCY CODE	
15. SUPPLEMENTAL NOTES					
16. ABSTRACT <p>This report presents the research conducted as part of an investigation for the California Department of Transportation (Caltrans) regarding the seismic response and overall moment capacity of precast I-girder to inverted-T bent cap bridge connections for seismic applications. The current design practice, as outlined by Caltrans' Seismic Design Criteria, assumes that the connection between the precast I-girders and the inverted-T bent cap will degrade in a seismic event and shall therefore be designed as a pinned connection, making the precast girder option for seismic bridges inefficient. A prototype I-girder to inverted-T bent cap bridge and a 50% scale test unit was designed in order to investigate the behavior of the as-built girder-to-cap connection region. Additionally, per the request of Caltrans, an improved girder-to-cap connection detail was developed in order to ensure a fully continuous moment connection between the I-girders and inverted-T bent cap.</p> <p>A finite element grillage model was developed using ABAQUS and SAP2000 and was used to predict the global and local responses of various aspects of the test unit. The test unit was constructed and tested in two phases of quasi-static cyclic testing. The first phase was a horizontal load test phase, which simulated the effects of gravity and seismic loads on the entire test unit. The second phase was a vertical load test phase, which specifically focused on the positive and negative moment capacity of the connections. Both the results of the finite element grillage model and the testing were used to make conclusions regarding the performance of an I-girder to inverted-T bent cap bridges.</p> <p>It was concluded that the current I-girder to inverted-T bent cap bridge connection is capable of acting as a fully continuous connection for both positive and negative moments during both gravity and seismic loading, contrary to the design assumptions stated in Caltrans' Seismic Design Criteria. The improved connection detail demonstrated the ability to ensure a fully continuous moment connection between the I-girders and inverted-T bent cap. Both connection details also exhibited a significant moment resistance beyond what was expected during the vertical load test although the as-built connection eventually failed under positive moments at moderate to large displacements.</p>					
17. KEY WORDS  Pre cast I-girder, inverted-tee bent cap, seismic design			18. DISTRIBUTION STATEMENT No restrictions. This document is available to the public through the National Technical Information Service, Springfield, VA 22161		
19. SECURITY CLASSIFICATION (of this report)  Unclassified		20. NUMBER OF PAGES  306		21. PRICE	

***R. Snyder, J. Vander Werff, Z. Thiemann,  
S. Sritharan, J. Holombo***

**Seismic Performance of an I-Girder to  
Inverted-T Bent Cap Connection**

**Submitted to the  
California Department of Transportation  
Caltrans Project: 05-0160**

**SEPTEMBER 2011**

**Final**

---

***REPORT***

---

**IOWA STATE UNIVERSITY**

OF SCIENCE AND TECHNOLOGY

**Department of Civil, Construction  
and Environmental Engineering**

# **Seismic Performance of an I-Girder to Inverted-T Bent Cap Connection**

by

Rick Snyder  
Former Graduate Research Assistant, Iowa State University

Justin Vander Werff  
Graduate Research Assistant, Iowa State University

Zach Thiemann  
Former Graduate Research Assistant, Iowa State University

Sri Sritharan  
Wilson Engineering Professor, Iowa State University

Jay Holombo  
Senior Bridge Engineer/Project Manager  
T.Y. Lin International (formerly at PBS&J)

---

**Caltrans Project: 05-0160**

---

**A Final Report to the California Department of Transportation**

**Department of Civil, Construction and Environmental Engineering  
Iowa State University  
Ames, IA 50011**

**September 2011**

## **DISCLAIMER**

This document is disseminated in the interest of information exchange. The contents of this report reflect the views of the authors who are responsible for the facts and accuracy of the data presented herein. The contents do not necessarily reflect the official views or policies of the State of California or the Federal Highway Administration. This publication does not constitute a standard, specification or regulation. This report does not constitute an endorsement by the Department of any product described herein.

For individuals with sensory disabilities, this document is available in Braille, large print, audiocassette, or compact disk. To obtain a copy of this document in one of these alternate formats, please contact: Division of Research and Innovation, MS-83, California Department of Transportation, P.O. Box 942873, Sacramento, CA 94273-0001.

## **ABSTRACT**

This report presents the research conducted as part of an investigation for the California Department of Transportation (Caltrans) regarding the seismic response and overall moment capacity of precast I-girder to inverted-T bent cap bridge connections for seismic applications. The current design practice, as outlined by Caltrans' Seismic Design Criteria, assumes that the connection between the precast I-girders and the inverted-T bent cap will degrade in a seismic event and shall therefore be designed as a pinned connection, making the precast girder option for seismic bridges inefficient. A prototype I-girder to inverted-T bent cap bridge and a 50% scale test unit was designed in order to investigate the behavior of the as-built girder-to-cap connection region. Additionally, per the request of Caltrans, an improved girder-to-cap connection detail was developed in order to ensure a fully continuous moment connection between the I-girders and inverted-T bent cap.

A finite element grillage model was developed using ABAQUS and SAP2000 and was used to predict the global and local responses of various aspects of the test unit. The test unit was constructed and tested in two phases of quasi-static cyclic testing. The first phase was a horizontal load test phase, which simulated the effects of gravity and seismic loads on the entire test unit. The second phase was a vertical load test phase, which specifically focused on the positive and negative moment capacity of the connections. Both the results of the finite element grillage model and the testing were used to make conclusions regarding the performance of I-girder to inverted-T bent cap bridges.

It was concluded that the current I-girder to inverted-T bent cap bridge connection is capable of acting as a fully continuous connection for both positive and negative moments during both gravity and seismic loading, contrary to the design assumptions stated in Caltrans' Seismic Design Criteria. The improved connection detail demonstrated the ability to ensure a fully continuous moment connection between the I-girders and inverted-T bent cap. Both connection details also exhibited a significant moment resistance beyond what was expected during the vertical load test although the as-built connection eventually failed under positive moments at moderate to large displacements.

## ACKNOWLEDGMENTS

The research team thanks the following individuals for their support and assistance in the completion of the research presented in this report. Without their help and kindness, much of this research would not have been possible:

- Caltrans for sponsoring this research project and Charlie Sikorsky for serving as the project manager;
- Michael Keever, Jim Ma, Paul Chung and other members of the Caltrans Project Advisory Panel for their advice and assistance;
- Sami Megally of PBS&J for their expertise and guidance in the design and construction of the test unit; and
- Professor José Restrepo and the staff of the Charles Lee Powell Laboratories of the University of California at San Diego (UCSD), including Andrew Gunthardt, Paul Greco, Noah Aldrich, Matt Stone, Christopher Latham, Bob Parks, John Ward, Bob Peters, Dan McAuliffe, Tim McAuliffe, Josh Nickerson, Michael Germeraad, Chris Horiuchi, Habib Charbel, and Taylor Gugino, for all of their hard work, assistance, and expertise in the construction and testing of the test unit. Your hospitality was greatly appreciated.

# TABLE OF CONTENTS

<b>CHAPTER 1. INTRODUCTION</b>	<b>1</b>
1.1 General	1
1.2 Inverted-T Bent Cap Connections	5
1.3 Accelerated Bridge Construction Methods	8
1.4 Research Objective	9
1.5 Report Layout	10
<b>CHAPTER 2. LITERATURE REVIEW</b>	<b>12</b>
2.1 Introduction	12
2.2 Positive Moment Connection	14
2.2.1 Background	14
2.2.2 Causes of Positive Moment at Connections	16
2.2.3 Benefits of Positive Moment Connections	18
2.2.4 Types of Connections	19
2.2.4.1 Bent Bars	20
2.2.4.2 Bent Strands	21
2.2.4.3 Embedded Girder Ends	23
2.2.4.4 Additional Stirrups	23
2.2.4.5 Through Web Reinforcement	23
2.2.4.6 Partial Diaphragm	23
2.2.5 Concerns Regarding Positive Moment Connections	24
2.2.5.1 Fabrication Issues	24
2.2.5.2 Lack of a Well-defined Design Procedure	24
2.2.5.3 Age at which the Connection is Established	25
2.3 Experimental Research	25

<b>2.4</b>	<b>Detailed Modeling Introduction</b>	<b>27</b>
2.4.1	Detailed FEA	28
<b>2.5</b>	<b>Grillage Finite Element Analysis</b>	<b>33</b>
2.5.1	Introduction	33
2.5.2	Background	34
2.5.3	Analysis Limitations	34
2.5.4	Model Construction	35
2.5.5	Nonlinear Behavior	37
2.5.6	Hysteretic Behavior	39
2.5.6.1	Takeda Model	39
2.5.6.2	Pivot Model	40
2.5.7	Torsional Behavior of Concrete	43
2.5.8	Strain Penetration	48
2.5.9	Bond-Slip Behavior of Strands in Concrete	49
<b>CHAPTER 3.</b>	<b>DESIGN OF TEST UNIT</b>	<b>51</b>
<b>3.1</b>	<b>Prototype Structure</b>	<b>51</b>
<b>3.2</b>	<b>Model Concept</b>	<b>52</b>
<b>3.3</b>	<b>Test Unit Plan Details</b>	<b>54</b>
<b>3.4</b>	<b>Improved Connection Detail</b>	<b>62</b>
<b>CHAPTER 4.</b>	<b>ANALYTICAL EVALUATION</b>	<b>63</b>
<b>4.1</b>	<b>Three-dimensional finite element model</b>	<b>63</b>
4.1.1	Introduction	63
4.1.2	Material Model	63
4.1.3	Contact and Constraint Modeling	66
4.1.4	Boundary Conditions	68
4.1.5	Modeling of Components	68
4.1.5.1	Cap Beam	69

4.1.5.2	Cap Beam Diaphragm	69
4.1.5.3	Girders and Slab	70
4.1.5.4	Reinforcing Bars and Prestressing Strands	71
<b>4.2</b>	<b>Grillage model</b>	<b>72</b>
4.2.1	Introduction	72
4.2.2	Element Properties	72
4.2.2.1	Column	74
4.2.2.2	Girders	75
4.2.2.3	Cap Beam	79
4.2.2.4	Diaphragm	80
4.2.2.5	Deck	81
4.2.2.6	Abutments	84
4.2.3	Boundary Conditions	85
4.2.4	Nonlinear Elements	85
4.2.4.1	Column Plastic Hinges	85
4.2.4.2	Cap Torsion	91
4.2.4.3	Girder-to-Cap Connection	94
4.2.4.4	Cap-to-Diaphragm Reinforcement	95
4.2.4.5	Improved Connection	98
4.2.5	Staged Construction	101
4.2.6	Loading Conditions	102
4.2.7	Modifications Made for Phase 2 Model	103
<b>CHAPTER 5.</b>	<b>EXPERIMENTAL WORK</b>	<b>104</b>
<b>5.1</b>	<b>Construction Sequence</b>	<b>104</b>
5.1.1	General Sequence	104
5.1.2	Construction Challenges	110
5.1.2.1	Pouring the Bent Cap	110
5.1.2.2	Installing the Ducts through the Cap Beam	111
5.1.2.3	Inserting the Strands through the Ducts in the Cap Beam	113
5.1.2.4	Partial Pour of the Diaphragm	114
5.1.2.5	Termination of Untensioned Strands	115

<b>5.2</b>	<b>Instrumentation</b>	<b>116</b>
5.2.1	Strain Gauges	116
5.2.1.1	Column-to-Cap beam Connection	116
5.2.1.2	Column	120
5.2.1.3	Footing	122
5.2.1.4	Cap-to-Diaphragm Interface	122
5.2.1.5	Girders	125
5.2.1.6	Girder-to-Diaphragm Connections	128
5.2.1.7	Deck	130
5.2.2	External Instrumentation	131
5.2.2.1	Horizontal Displacement of Cap and Superstructure	131
5.2.2.2	Vertical Displacement of Girders/Superstructure	132
5.2.2.3	Column Curvature and Growth	134
5.2.2.4	Cap Beam Twist and Dilation	135
5.2.2.5	Connection Rotation and Neutral Axis Depth	136
5.2.2.6	Girder Curvature	137
5.2.2.7	Lateral Displacement Measurement Between Girders	137
5.2.2.8	Improved Connection Strand Slip	138
5.2.2.9	Footing Movement	139
<b>5.3</b>	<b>Material Testing</b>	<b>141</b>
<b>5.4</b>	<b>Phase 1 Test</b>	<b>142</b>
5.4.1	Actuator Setup	142
5.4.2	Loading Protocol	143
5.4.2.1	Application of Stage 1 Hold-Down	143
5.4.2.2	Application of Stage 2 Hold-Down	143
5.4.2.3	Horizontal Actuator Protocol	143
5.4.2.4	Vertical Actuator Protocol	144
5.4.3	Hold-Down Forces	148
5.4.3.1	Whiffle Tree	154
<b>5.5</b>	<b>Phase 2 Test</b>	<b>156</b>
5.5.1	Actuator Setup	156

5.5.2	Loading Protocol	156
<b>CHAPTER 6. TEST RESULTS</b>		<b>158</b>
6.1	<b>Phase 1 Test Observations</b>	<b>158</b>
6.2	<b>Phase 1 Test Results</b>	<b>162</b>
6.2.1	Overall Response	162
6.2.2	Column Response	168
6.2.3	Connection Response	174
6.2.4	Deck Reinforcement	184
6.2.5	Girder Load Distribution	185
6.3	<b>Final Observations of Phase 1 Test</b>	<b>190</b>
6.4	<b>Phase 2 Observations</b>	<b>190</b>
6.5	<b>Phase 2 Test Results</b>	<b>200</b>
6.5.1	Overall Vertical Load Response	200
6.5.2	Girder-to-Cap Connection Response	212
6.5.3	Girder Load Distribution	220
<b>CHAPTER 7. SUMMARY AND CONCLUSIONS</b>		<b>225</b>
7.1	<b>Overview</b>	<b>225</b>
7.2	<b>Summary of Test Results</b>	<b>227</b>
7.2.1	Phase 1	227
7.2.2	Phase 2	228
7.3	<b>Conclusions</b>	<b>228</b>
7.3.1	Experimental Study	228
7.3.2	Analytical Study	230
7.4	<b>Design Recommendations</b>	<b>231</b>

<b>7.5</b>	<b>Future Research Directions</b>	<b>232</b>
	<b>REFERENCES</b>	<b>234</b>
	<b>APPENDIX A: Prototype Drawings</b>	<b>239</b>
	<b>APPENDIX B: Prototype Calculations</b>	<b>247</b>
<b>B.1</b>	<b>Prototype Configuration</b>	<b>247</b>
<b>B.2</b>	<b>Material Properties</b>	<b>247</b>
<b>B.3</b>	<b>Column Design</b>	<b>248</b>
<b>B.4</b>	<b>Cap Beam</b>	<b>251</b>
<b>B.4.1</b>	<b>Construction Loads</b>	<b>251</b>
<b>B.4.2</b>	<b>Service Loads</b>	<b>259</b>
<b>B.4.3</b>	<b>Torsional Demand on the Cap Beam</b>	<b>264</b>
<b>B.5</b>	<b>Inverted Tee Ledge Design</b>	<b>266</b>
<b>B.6</b>	<b>Dapped End Beam</b>	<b>280</b>
<b>B.7</b>	<b>Dapped End Reinforcement</b>	<b>282</b>
<b>B.8</b>	<b>Top Deck Reinforcement</b>	<b>285</b>
<b>B.9</b>	<b>Column-Bent Cap Joint Shear</b>	<b>287</b>
	<b>APPENDIX C: Prototype Material Properties</b>	<b>292</b>

# **Chapter 1. Introduction**

## **1.1 General**

The State of California has experienced a significant number of earthquakes over the past few decades, quite a few of which resulted in significant structural damage to both bridges and buildings in the surrounding areas. As a direct result, a considerable amount of time, money, and more importantly, human life were lost by the state of California. The 1994 Northridge earthquake alone resulted in 57 fatalities and property damage estimated to be in excess of \$20 billion dollars in 1994 (PEER, 2005). However, each earthquake exposed design deficiencies and provided the engineering community with another opportunity to gain more information regarding the design of structures in earthquake-prone regions. This was particularly evident after the 1989 Loma Prieta Earthquake.

The Loma Prieta earthquake resulted in significant damage to a number of bridges and highway structures near the San Francisco and Oakland areas, including the San Francisco-Oakland Bay Bridge and the Cypress Street Viaduct. Damage to the Bay Bridge resulted in significant time and economic losses as it had to be closed for a month. The damage to the Cypress Street Viaduct was even more catastrophic as 48 of the 83 bents supporting the roadway collapsed, resulting in 41 human fatalities (Housner & Thiel, 1990). Based on the observations made from the Loma Prieta earthquake, as well as other significant earthquakes that had occurred within the past decades, the Governor of California appointed a Board of Inquiry to investigate the Loma Prieta earthquake in order to address the apparent design and regulation inadequacies with respect to the seismic performance of structures. In 1990, the Governor of California signed Executive Order 86-90, which set a policy stating that, “All state owned and operated structures are to be seismically safe and that important structures are to maintain their function after earthquakes,” (Housner & Thiel, 1990). Additionally, one of the significant findings and recommendations that the Board of Inquiry made was that the California Department of Transportation (Caltrans), “Fund a continuing program of basic and problem-focused research on earthquake engineering issues pertinent to Caltrans responsibilities,” (Housner & Thiel, 1990).

Many of the bridges that are currently in place in California were designed in the 1950's and 1960's. Since little was known about the seismic behavior of structures, the practice at that time was to overdesign structures with the intention that they would remain elastic during an earthquake. However, observations of bridges that were designed to remain elastic and were severely damaged during earthquakes, in addition to experimental research, indicated that the design methods that were employed during that time period were inadequate. It was determined that the earthquake design forces were grossly underestimated, which resulted in an underestimation of deflections and an inability for the structure to develop a stable inelastic response mechanism. Fortunately, the elastic design philosophy was able to somewhat cope with the underestimated forces, as the working stress was often greater than what was assumed in the design. However, the main deficiency with the elastic design philosophy was that there was no plan to accommodate the higher than expected forces, meaning a stable inelastic response hierarchy was not built into the structural system. As a result, the following inadequacies often developed in response to a seismic event: brittle failure mechanisms; incorrect quantities, placement, and termination of reinforcement; unseating of the girders; structural pounding; shear, confinement, anchorage, and lap-splice failure; joint failure; and buckling of longitudinal reinforcement (Priestley, Seible, & Calvi, 1996). Figures 1.1 and 1.2 illustrate a number of the aforementioned inadequacies that were observed during both the 1971 San Fernando and 1989 Loma Prieta earthquakes. Therefore, as a direct result of California's Board of Inquiry, in order to improve the seismic performance and ensure that the structure behaved in a more predictable manner, the capacity design philosophy was adopted (Housner & Thiel, 1990).



Figure 1.1: Example of 1971 San Fernando Earthquake Damage (*Courtesy of UCSD*)



Figure 1.2: Example of 1989 Loma Prieta Earthquake Damage (*Courtesy of UCSD*)

The goal of the capacity design philosophy was to allow the structure to behave in an inelastic manner through flexural yielding, but detail it such that a strength hierarchy was formed so that a stable response mechanism could occur. The locations of inelastic flexural yielding, referred to as plastic hinges, were preselected and detailed in order to achieve a specified level of ductility, without allowing the rest of the structure to experience any of the aforementioned failure mechanisms in the event of an earthquake. Plastic hinges are typically placed within the columns of a bridge structure to prevent any catastrophic damage from occurring in the superstructure, while maintaining the ability of the structure to support its self-weight in addition to carrying any dead or live load. Bridges typically have less redundancy than buildings. Therefore, in order to prevent the entire bridge from failing, it is of crucial importance that the column does not fail. This is typically achieved by designating the sections of the structure that are meant to remain elastic and designing them to be protected under the capacity design philosophy, which is often referred to as capacity protected design. This is accomplished through the use of overstrength factors in order to ensure that the members are designed with enough capacity that they remain elastic even under the highest expected magnitude of force to be experienced by the structure. While it is likely that the bridge will need significant maintenance, and in some cases complete replacement after an earthquake, the potential for catastrophic damage and loss of life is dramatically reduced through the use of the capacity design philosophy.

Following the 1994 Northridge Earthquake, it was shown that the bridge retrofits that were developed under the more modern design philosophy performed very well compared to those that were not retrofitted and were designed prior to the advances made as a result of the Loma Prieta Earthquake (Priestley, Seible, & Uang, 1994). Though the new design procedure and the research that was performed as a result of the Loma Prieta earthquake inspire a greater sense of confidence in structures that are built today, extensive research is still required in order to ensure that the structures that were designed previously, as well as those designed in the future, will behave sufficiently in a seismic event. Additionally, although a significant amount of research was aggressively carried out on the majority of the transportation structures within California immediately after the Loma Prieta earthquake, some structural details have yet to be investigated. More specifically, further research into the connection details between the

superstructure and substructure is required. As the infrastructure in the United States continues to age, the 24,000 bridges throughout the state of California (California Department of Transportation, 2007) will be in need of replacement and/or repair and the seismic performance of both the new and old structures will be pushed to the forefront. Furthermore, the ability to build quality structures at an accelerated and efficient pace, through the use of precast components, will be preferred over the traditional methods of cast-in-place components.

## **1.2 Inverted-T Bent Cap Connections**

One such connection, which requires further investigation, is the inverted-T bent cap-to-girder connection. The detail has been used in a number of bridges, primarily in county bridges or overpasses, throughout the state of California. However, its moment capacity and thus its influence on the behavior of the rest of the bridge during a seismic event are still unknown. Therefore, before Caltrans incorporates this detail in any of their future designs, extensive research into its behavior must be conducted. Additionally, depending on the capacity of the connection, a retrofit or revisions to other aspects of the bridge may need to be made. Currently, no research regarding this topic has been performed and presented to Caltrans for review.

The inverted-T bent cap system can be used for single or multi-column bent configurations and consists of a cap beam, placed on top of the columns, in the shape of an upside-down letter “T”. Precast girders, typically with dapped ends, are then placed with ease in the field on the ledge of the inverted-T, as shown in Figure 1.3. The structure is made continuous for live load by pouring the concrete deck over the length and width of the structure, in addition to pouring a diaphragm around the girders and cap. Hooked reinforcement is typically placed between the cap and diaphragm to establish a connection between the diaphragm and inverted-t bent cap. Additionally, dowel bars are often placed within the girders, which extend into the diaphragm in order to further establish a connection between the embedded ends of the girders and the diaphragm.

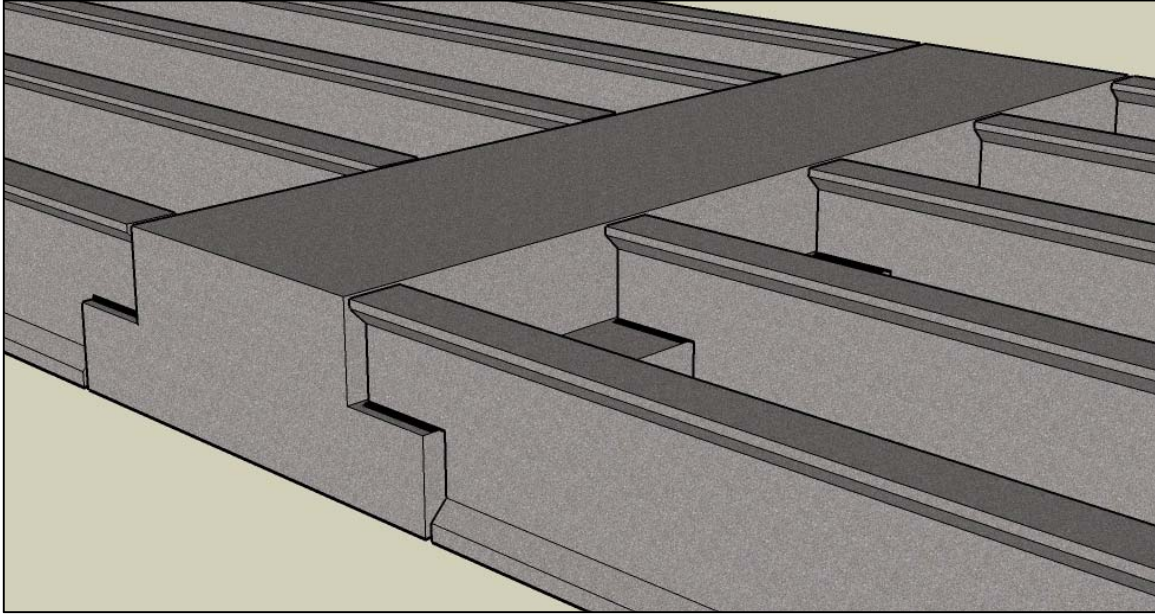


Figure 1.3: Inverted-T Bent Cap

Use of the inverted-T bent cap system has a number of significant advantages, when compared to traditional cast-in-place systems, as well as other precast methods including spliced girders made continuous. First, inverted-T bent caps allow for the use of precast girders, which can be cast in a controlled environment off site and shipped to the site for placement. Not only does this result in a higher quality girder than would be produced in the field, but it also allows for substantial economic savings as it lends itself to accelerated bridge construction practices. Construction time is typically reduced when precast components are employed as they may be cast ahead of schedule. Additionally, once they arrive at the job site, they are typically easier and quicker to place; this reduces the amount of congestion created due to stopping or delaying traffic during construction. Also, environmental benefits may be observed, such as a reduction in noise and air pollution. Second, the use of the inverted-T system decreases the required depth of the superstructure when compared to more traditional types of bent caps; this is especially noticed when using girders with dapped ends. Finally, compared to the method of spliced girders made continuous, the inverted-T system requires less supporting falsework, as it would only be required when casting the inverted-t bent cap. The girders may then be placed directly on the bent cap without any direct support from falsework. This advantage will also result in economic, time, and environmental savings.

Unfortunately, precast components are still not frequently used for bridges in areas of seismic activity, which is mainly due to lack of a definite design methodology and research validation confirming adequate seismic performance of the connections involving the precast members. However, if a design methodology were developed and proven to be reliable, it is very likely that the use of precast construction would become widely accepted in seismic areas. The advantages of this practice would be numerable, as previously discussed, and the use of precast components would contribute significantly to the accelerated bridge construction methods, which has become a significant interest in today's industry due to the significant time and cost savings that it provides. Furthermore, if the connection between the precast I-girders and the inverted-T bent cap were improved and tested successfully, the system could be used in future bridges as a very viable precast system, which would easily lend itself to accelerate bridge construction.

Currently, when designing bridges incorporating the inverted-T bent cap detail, Caltrans design engineers assume that the connection has no positive or negative moment resistance. In other words, the top of the column is assumed to be a pinned connection for any transverse or longitudinal loading conditions. This is done in accordance with California DOT's Seismic Design Criteria, which assumes, based on the previous seismic behavior of precast girders, that the moment connection between the girders and cap beam would likely degrade to a pinned connection (Caltrans, 2006). Therefore, the columns are designed with only one plastic hinge, located at the base of the column. However, it is likely that a significant amount of negative moment resistance would be provided given the reinforcement in the deck over the bent cap. Furthermore, given the reinforcement extending from the cap and into the diaphragm, as well as the dowel bars extending from the girders into the diaphragm, it is possible that the connection could support enough moment to develop a hinge at the top of the column as well. If that were the case, it would be possible to reduce the size of both the columns and the footings, as each hinge would experience a reduced moment demand. As a result, significant cost savings could be achieved. Additionally, the use of two plastic hinges provides additional redundancy to the system, reduces the displacement at the top of the column and therefore the likelihood of unseating of the girders, and allows for the use of a pinned-base if desired. Conversely, if the connection does have a significant moment capacity, then the inverted-T bridges that are

currently in place must be inspected as the connection could potentially pose serious consequences in the event of an earthquake. It is possible that the existing connection would not have been detailed with an adequate shear or moment capacity or an inappropriate amount of anchorage of the reinforcement that is entering column. More importantly, an unstable mechanism of inelastic response could occur at the top of the column, possibly resulting in a failure of the column. Damage to various parts of the structure, including the column and the superstructure, may also be likely if they were not designed under the capacity protection design philosophy, which ensures a suitable strength margin in order to prevent undesirable inelastic action from occurring in areas outside the specified plastic hinge regions. Finally, it has been identified that, given the potential for large rotations between the superstructure and the cap, the potential for damage of the girders and surrounding superstructure exists. This damage could be further compounded by the fact that a relatively small contact area between the girders and inverted-T cap is available to transfer shear forces into the joint, which could potentially further damage the concrete within the joint area. Therefore, it is likely that simply fixing the column to avoid failure would not solve all of the potential problems that could be encountered by the structure. These consequences must be addressed, as a serious possibility for large economic and human losses would exist.

### **1.3 Accelerated Bridge Construction Methods**

Several reasons have already been mentioned pertaining to why precast concrete structures are advantageous when seeking to utilize accelerated bridge construction (ABC) methods. ABC methods continue to be advanced around the country and have already been implemented in many states, including Texas, Washington, New York, and Massachusetts, to name a few (FHWA, 2009). ABC advantages include decreased construction and labor cost since more work is moved from the field to the shop and field time is reduced, increased safety because of the decrease in onsite time and in time required for rerouting traffic, and decreased traffic congestion due to reduced onsite construction activities and workers.

However, the application of ABC methods in seismic regions has been limited thus far. This hesitation has primarily been due to lack of adequate investigation in seismic detailing and performance of ABC connections and a consequent lack of availability in current bridge guidelines and specifications for design guidelines regarding seismic design of precast concrete

bent caps. Limited research in such topics has been completed, including the relatively recent NCHRP Project 12-74 (Tobolski, Matsumoto, & Restrepo, 2006). The work detailed in this report furthers this body of knowledge and provides much-needed investigation into connections that will allow and promote the use of ABC methods in seismic regions.

#### **1.4 Research Objective**

The objective of the following research was to quantify the behavior and moment resistance of the inverted-T bent cap-to-girder connection in order to gain a better understanding of its performance under seismic conditions. Additionally, modifications to the previous inverted-T details were proposed in order to achieve a connection that would provide a substantial resistance to positive moment as well as a more predictable seismic response.

A prototype bridge was developed based on the current Caltrans procedures used for bridges incorporating inverted-T bent caps. Unlike the inverted-T bridges that were designed previously, the prototype bridge was detailed with a plastic hinge in both the top and bottom of the column. This was done based on the initial hypothesis that the connection would be able to develop enough moment to activate the hinge. Also, the decision to use I-girders, over bulb-tee or bathtub girders, was made by Caltrans as the majority of the bridges using inverted-T bent caps that are currently in place within the state of California were built using I-girders.

The test unit was then developed based on a 50% scale of the prototype bridge. As shown in Figure 1.4, it consisted of a single column; an inverted-T bent cap; and a half span of five girders on each side of the bent cap. The current inverted-T connection details were used on one side of the bent cap, while the proposed modifications were employed on the other. This was done in order to make efficient use of the test unit specimen, as it was possible to test both connection types independently based on the side of the bent cap experiencing a positive moment demand. The test unit was constructed, heavily instrumented, and subjected to two phases of testing at the Powell Laboratory of the University of California San Diego (UCSD). The first phase involved cyclic lateral load testing of the bridge model in the longitudinal direction in order to simulate the horizontal earthquake effects on the entire bridge model. The second phase focused more on the behavior of the connection and involved cyclic pushing and pulling of the

superstructure in the vertical direction with respect to the inverted tee cap beam. This was done on both sides of the bent cap simultaneously, in order to test both connection details.

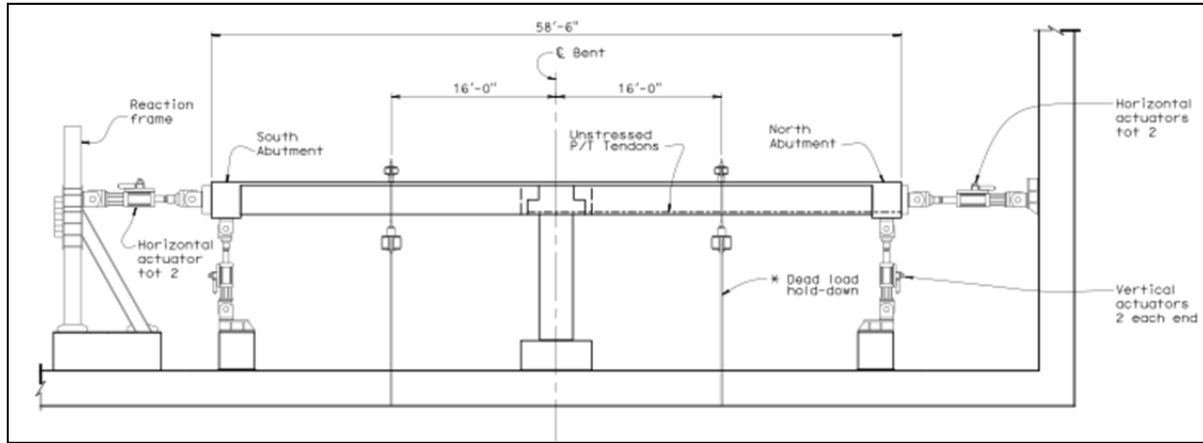


Figure 1.4: Proposed Test Unit Structure

A finite element grillage model of the test unit was produced, using ABAQUS and SAP2000, based on the plan set provided by PBS&J. The grillage model was used in order to predict the results of the physical testing and highlight any areas of the structure that needed special consideration during the testing phases. Additionally, the grillage model was used in connection with the physical testing in order to validate any results and conclusions.

Finally, a set of recommendations and conclusions regarding both the current and future performance of the inverted-T bent cap have been developed and are discussed in detail in the body of the report.

## 1.5 Report Layout

Following the introduction presented in Chapter 1, a literature review regarding previous research of positive moment connections as well as the use of three-dimensional finite element modeling and grillage finite element modeling is provided in Chapter 2. Chapter 3 gives an overview of the design of the test unit. Chapter 4 provides a thorough explanation of the development of both the three-dimensional finite element model and the grillage model, including description, validation, and predictions from each model. Chapter 5 is a discussion of the experimental specimen design, construction, instrumentation, and loading. Chapter 6

provides the results of both phases of experimental testing. Finally, Chapter 7 gives a series of conclusions and recommendations for future work to be presented to Caltrans.

## **Chapter 2. Literature Review**

### **2.1 Introduction**

In order to better understand the seismic performance of an I-Girder to inverted-T bent cap connection, as well as the various finite element models and details required to complete the project, an in-depth literature review was performed. It was found that little research has been performed on precast girder-to-cap connections under seismic loading. The previous research mainly focused on the use of integrally cast cap beams, some with the use of precast girders, both steel and concrete, while no research was discovered relating to the use of inverted-T cap beams or a complete precast system for seismic regions.

It is now widely known that the use of precast components offers a substantial amount of benefits to both contractors and designers. For example, construction time is reduced, less falsework is required, the construction requires less of an impact on the surrounding environment, and the components are constructed in a more controlled environment, which results in a higher quality of craftsmanship. However, it could be argued that the use of spliced girders with an integral cap beam could be a disadvantage in terms of constructability, when compared to an inverted-T cap. If an adequate moment resisting connection can be developed and practically implemented in the field in order to achieve continuity with an inverted-T system, then this type of system may be used more frequently than it is currently. Since the girders would not need to be supported by falsework while constructing the integral cap beam for an inverted-T concept, a smaller environmental impact, less labor intensive construction procedures, and improved cost savings could be achieved with this system compared to those described in the studies presented above.

As these precast systems become more common, the need for experimental studies to predict their behavior during seismic events becomes an increasing priority. Specifically, the connection behavior between the precast girders and cap system is of interest, as it will govern the placement and possibly the formation of the column plastic hinges as well as the generalized behavior. Previous experimental studies, which will be discussed in more detail below, have

indicated that the negative moment resistance provided by these connections can most often be developed by the reinforcement placed within the deck slab. However, more information is still desired regarding the formation of any positive moment resistance within the connection.

The use of lab testing, of any scale, is of common use in engineering research. A search of bridge research proves that a high percentage of the research projects include lab testing, either dedicated exclusively to experimental work or including lab work for validation of analytical predictions. This method can effectively predict the true response of a bridge as long as any scaling has been done properly. The use of lab testing to validate other analytical models has been a common practice in the past. Superstructure to cap beam connection testing by (Almer & Sanders, 2007) has shown that a scaled test unit can be used to validate the analytical work done using more simplified means. This research focused on precast girder to cast-in-place bent cap connections; they were able to investigate the performance of the superstructure to cap beam connection for both positive and negative moment when subjected to simulated seismic actions. They had tested two test units at the time of publishing their work and were designing the next two units to improve upon the response of the first tests. The information gathered from laboratory testing for research is valuable, as long as the setup is correct, and is the best indicator of true response of a system. However, lab testing is not always the most efficient way to gather the response of a system. The cost of a few bridge test units can become very costly when considering the labor, materials, lab space, etc. The ability to secure funding to test multiple designs is challenging, now that other more cost effective means have been found to analytically predict the same response.

The following literature review begins with a brief background on the experimental research that has been conducted on the seismic performance of bridges made continuous for positive moment at the girder-to-cap connection. Information regarding positive moment connection and then the use of finite element analysis techniques to predict and understand the behavior of various aspects of the bridge, such as the rotation, strains and displacements, are presented. Finally, the need, benefits, and means for establishing positive moment connections between girders and bent cap systems, as well as related previous experimental studies, are discussed.

## **2.2 Positive Moment Connection**

### **2.2.1 Background**

The use of precast girders has become a common place in bridge design, as it allows for the construction time to be greatly reduced. However, careful consideration has to be given to the area over the cap beams to ensure that sufficient continuity is provided through the girder-to-cap connection. For negative moment resistance, reinforcing bars are typically placed in the deck over the cap beam to provide the necessary moment resistance (Miller, Castrodale, Mirmiran, & Hastak, 2004). Mechanical splices, provided directly between the girder top flanges and the cap beam, have also been used in order to develop negative moment resistance. Testing of the connection from the superstructure to cap beam has been conducted by Portland Cement Association, and discussed in the NCHRP 519 report (Miller, Castrodale, Mirmiran, & Hastak, 2004), that showed that using the reinforcing in the deck for negative moment was adequate in design. During the aforementioned testing, cracking was observed in the diaphragms and the cause was believed to be from positive moment. The positive moment was caused from time-dependent effects on the girders. Therefore, a recommendation was made that a connection from the bottom of the diaphragm, next to the girder, to the girder should be provided. Multiple positive moment connections, which are discussed later, were then constructed and tested. During the testing, it was observed that the formation of cracks in the slab was the first sign of failure of the positive moment connection. Once the connection failed, the slab acted as a hinge during further loading (Miller, Castrodale, Mirmiran, & Hastak, 2004).

Many states currently use precast, prestressed girders for continuous highway bridges (Freyermuth, 1969). A survey of 150 agencies in Japan, Canada and the United States was performed regarding the use of positive moment connections. One-third of the surveys were returned and about half of the respondents said they had designed less than 200 continuous precast girder bridges while seven-percent responded indicating that they had designed more than 1,000 (Hastak, Mirmiran, Miller, Shah, & Castrodale, 2003). The main application of continuous, precast bridges was on interstates and high volume urban highways. Another observation from the survey was that over 60 percent of the respondents reported that they

considered positive moment continuity for live load and superimposed dead load during their design process. For seismic regions, most of the respondents preferred positive moment continuity to be provided in all multi-span bridges. The connections were used with girders primarily of the AASHTO Type III and IV size. Other girder sizes that have been used were the PCI-BT, Quad-T, NEBT, U-Beams and Texas shapes. Finally, for the design of the cap beam to superstructure connections, half the respondents replied that a standard detail was used regardless of the application while the majority of the remaining responses used the PCA Method developed by Freyermuth, which is briefly discussed below. It was reported that some found the PCA Method to be conservative in design.

One of the first research projects undertaken to provide details for moment connections was performed to develop what is known as the PCA method, which provided details for designing connection between the superstructure and cap beam to resist creep, shrinkage and live load moments at the cap beam (Freyermuth, 1969). Testing was conducted on the connection that was considered most practical, shown in Figure 2.1, and was performed both in a static manner and a fatigue test with a stress range of 20,000 psi. Based on the results, some design recommendations were presented. During the design of the structure, it is recommended that the stress on the bottom face of the girder be limited to 80 percent of the modulus of rupture. A similar recommendation was stated to limit the stress in the connection reinforcing bars to 0.6 times the yield stress. The limit was developed to keep the diaphragm concrete from cracking under positive moments. Also, multiple connections were tested and it was found that most of the bars failed at 670,000 applications of the load. The failure was of the brittle manner at knee of the hooks. As a result, in order to avoid this mode of failure, a recommendation was made that the maximum stress where the bar bends begin should be limited to 50 percent of the fatigue strength (Freyermuth, 1969). Also, it was recommended that, due to the amount of design calculations, standard details should be used for each of the common girder types in all loading scenarios.

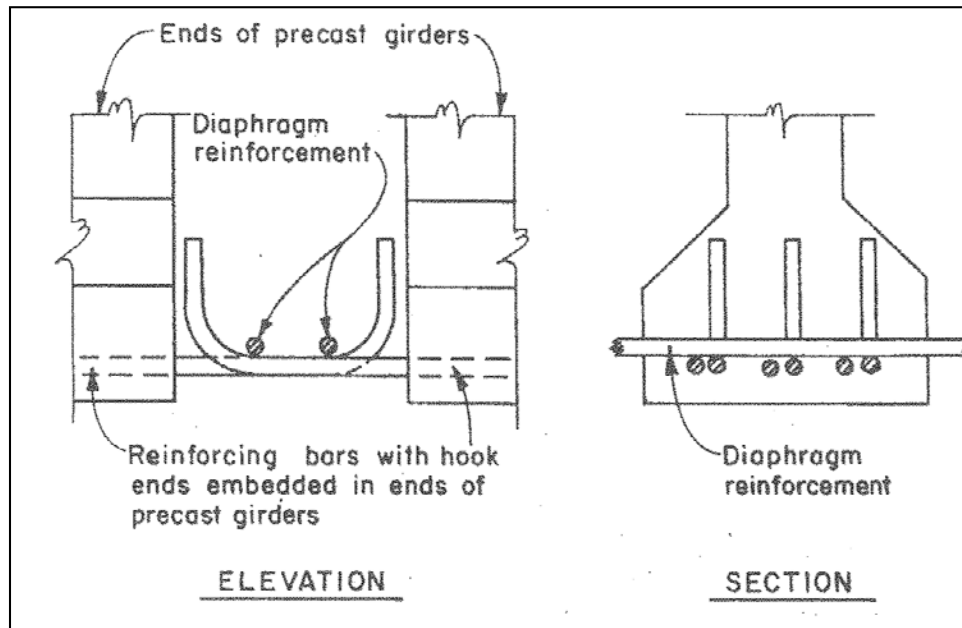


Figure 2.1. Connection Selected for Testing by Freyermuth (1969)

### 2.2.2 Causes of Positive Moment at Connections

The cause of positive moment comes from multiple effects, while each could appear minor, they can have large effects on the behavior of the structure. A few common causes of positive moment are creep, shrinkage and temperature strain in the decks and girders (Miller, Castrodale, Mirmiran, & Hastak, 2004). In the testing performed for the NCRHP 519 Report, creep, shrinkage and temperature strains were assumed to produce a positive moment equivalent to the nominal cracking moment at the beam-diaphragm interface (Miller, Castrodale, Mirmiran, & Hastak, 2004). The combined creep, shrinkage and thermal effects may cause the girder to camber up resulting in end rotations of the girders. When this occurs, a positive moment develops at the diaphragm next to the girder and may be large enough to crack the diaphragms as seen in Figure 2.2 (Hastak, Mirmiran, Miller, Shah, & Castrodale, 2003). However, it was found that the creep effects are partially counteracted by the differential shrinkage between the precast girders and the cast-in-place deck (Freyermuth, 1969).

In some cases the shrinkage did not appear to cause any negative moment. The reactions actually showed that additional positive moment was forming (Miller, Castrodale, Mirmiran, & Hastak, 2004). The thermal effects were found to be significant as it caused a daily moment change of over one-half the cracking moment capacity of the diaphragm (Miller, Castrodale, Mirmiran, & Hastak, 2004). Finally, once the spans are made continuous, the effects in one span will cause positive moment in remote spans leading to additional positive moment demands. In addition to those investigations, seismic excitation of a structure was also found to produce positive moments in the connection regions (Priestley, Seible, & Calvi, 1996). As the superstructure displaces laterally from the seismic excitation, one side of the cap beam will experience positive moment while the other will undergo negative moment.

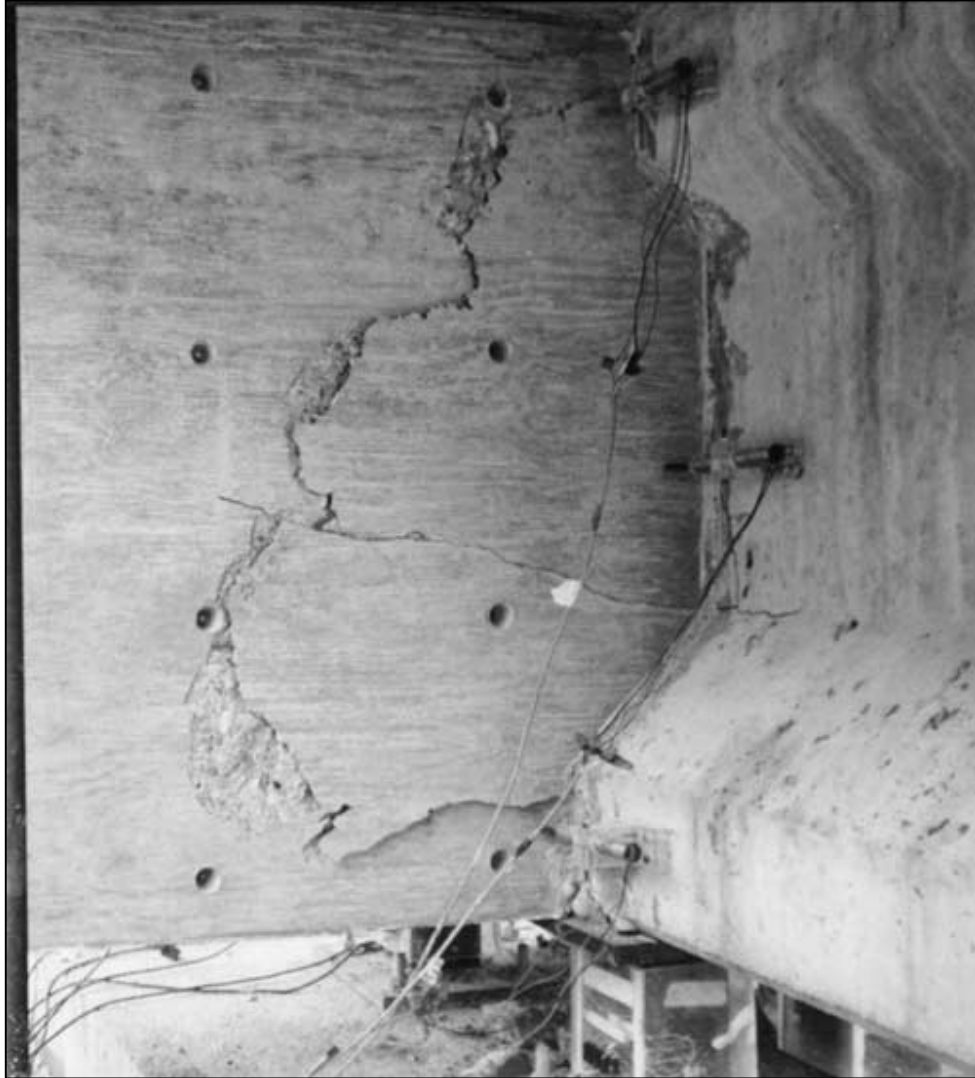


Figure 2.2. Diaphragm Cracking from Positive Moment (Hastak et. al., 2003)

### **2.2.3 Benefits of Positive Moment Connections**

A general goal for many state DOT's is to make bridges continuous-for-live-load using prestressed, precast concrete components. The obvious reasons for this goal are to counteract the aforementioned causes of positive moment in order to prevent cracking of the diaphragm, deck and girders. A structure with a sufficient positive moment connection will exhibit an enhanced seismic resistance (Tadros, Ficence, Einea, & Holdsworth, 1993). In addition, superior structural integrity and lower deflection levels can result when a positive moment connection between the superstructure and cap beam is active. Also, providing positive moment continuity between the girders and cap beam via integral bents, or connecting the girder ends across the depth of the cap beam, allows for the combined depth of the cap beam and girders to be reduced (Sritharan,

Vander Werff, Abendroth, Wassef, & Greimann, 2005). Providing integral connections also eliminates girder bearings, which, in turn, reduce future maintenance costs. In general, the benefits of a continuous bridge are the improved durability, elimination of bridge deck joints and reduced maintenance costs (Hastak, Mirmiran, Miller, Shah, & Castrodale, 2003).

Several additional advantages of a positive moment connection directly benefit the seismic performance of the bridge (Priestley, Seible, & Calvi, 1996). The redundancy in the bridge structure is increased, which allows for additional plastic hinges to be formed. With additional plastic hinges forming, the potential for energy dissipation increases. When the response of the bridge in the longitudinal direction is concerned, the columns will be under double bending when the plastic hinges are formed at the top and bottom of the column. This allows for greater shear resistance of a given section size and reinforcement content of the columns. Additionally, a double bending behavior of multi-column bents is preferred because the stiffness in the longitudinal and transverse direction is equal, which is the optimum condition for seismic design. Also, by allowing a moment transfer at the top of the column, a pin connection can be designed at the column base; this will significantly lower the cost of the substructure. Furthermore, a pinned base is preferred for bridge columns in areas of low soil stiffness and a positive moment connection will allow for that to occur. Finally, under small seismic displacements, the connection is insensitive to the seismic displacement.

#### **2.2.4 Types of Connections**

A number of systems have been developed in order to establish a positive moment connection between the superstructure and cap beam. Most of these systems require a connection mechanism to be developed between the girder and the diaphragm, in order to resist moment at the connection due to the applied loading. The following are examples of systems that have been incorporated into a bridge structure in order to establish the desired positive moment connection: bent bars and untensioned prestressing strands, straight bars, welded bars, reinforcement placed through the web of the girders and into the diaphragms, additional stirrups placed in the diaphragms, mechanical strand connectors, a partial diaphragm to pre-compress the section, and embedding the ends of the girders into the diaphragms at the cap. However, the most commonly used systems for the superstructure to cap beam connection are bent bars and bent strands extending into the diaphragm, and both bars and strands seem to be used equally as

frequently (Hastak, Mirmiran, Miller, Shah, & Castrodale, 2003). Therefore, the advantages, limitations, and applications of these two systems will be of focus in the following text. The research has mainly been performed for non-seismic applications, to resist creep, shrinkage and vehicular live loads; however, some experimental research has been performed and will be discussed in the next section.

#### *2.2.4.1 Bent Bars*

According to (Freyermuth, 1969), the most practical positive restraining moment connection was the hooked bar connection. This type of connection was further tested, under monotonic and cyclic loading, and the results were published in NCHRP 519 (Miller, Castrodale, Mirmiran, & Hastak, 2004). The 90-degree hooks used in the testing were designed using the AASHTO Standard Specifications regarding hooked bars (Miller, Castrodale, Mirmiran, & Hastak, 2004). It should also be noted, according to (Freyermuth, 1969), that the maximum bar size used for this connection, if the bars are bent in the field, should be limited to No. 6 (diameter = 0.75 in.). The full-scale test specimen used in the NCHRP report consisted of two I-girders, which were connected using eight hooked No. 5 bars (diameter = 0.625 in.). The girders were placed 10 in. away from each other and a diaphragm and deck was poured around the girders in order to establish the connection, shown in Figure 2.3. Though some cracking occurred at the connection during the testing, the end reactions and strains within the section demonstrated that continuity was achieved and that the connection detail was effective for the dead and live loading cases (Miller, Castrodale, Mirmiran, & Hastak, 2004). This test focused on the use of bars hooked at a 90-degree angle; however, it was also noted in this report that the use of a 180-degree bend might also be a viable option.

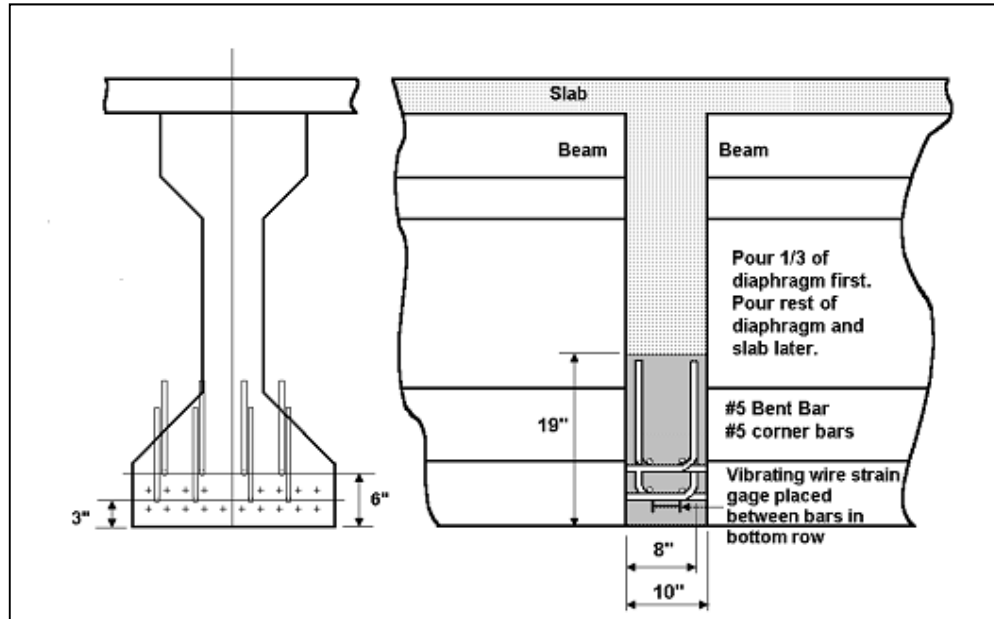


Figure 2.3. NCHRP Bent Bar Specimen (Miller et. al., 2004)

#### 2.2.4.2 Bent Strands

The aforementioned NCHRP report also performed a positive moment connection test, under monotonic and cyclic loading, on a similar full scale test specimen incorporating bent strands as the connection mechanism, as shown in Figure 2.4. Scaled pullout tests were also conducted on specimens using 90 degree bent, straight, and frayed strands. The results of the full-scale test demonstrated that bent strands are able to effectively establish positive moment continuity in the system, even if cracking occurs at the joint. Continuity was only lost when the slab and diaphragm cracked and the connection was near failure. The scaled tests also showed that the bent strands resulted in the optimum anchorage when compared to the straight or frayed strands, which slipped twice as much as the bent strands. Additionally, these tests found that systems involving bent strands and girder ends that were not embedded in a diaphragm, had a tendency for the girders to separate from the face of the diaphragm. However, this separation from the diaphragm did not result in any damage. Finally, the results of the testing did show that, though the specimens did provide continuity, the bent strands also had a tendency to slip under cyclic loading. As a result, it may be concluded the bent strand detail would not be preferred for seismic applications.

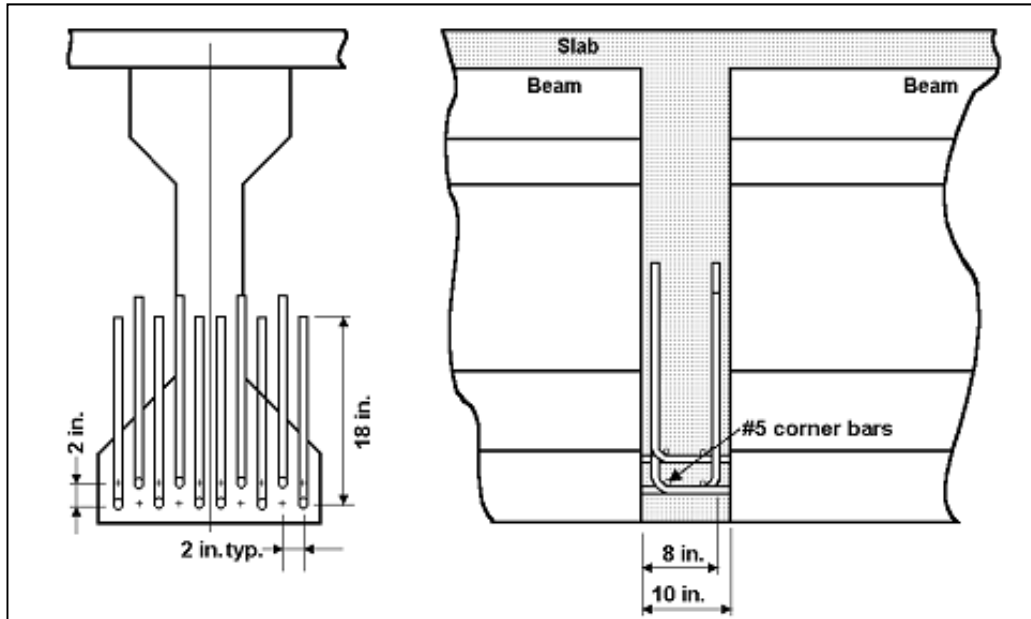


Figure 2.4. NCHRP Bent Strand Specimen (Miller et. al., 2004)

The behavior of untensioned prestressing strands, for use in positive moment connection details, was also investigated by Salmons and McCrate (Salmons & McCrate, 1977). Their findings showed that the helical orientation of the strands tended to unscrew the strand from the surrounding concrete. Additionally, under high stress levels, local crushing at the strand-concrete interface was observed, which contributed to both creep and slipping effects on the strand. However, under cyclic loading, additional creep was not experienced until the load returned to its previous maximum. Similar to the findings presented in the NCHRP report, Salmons and McCrate concluded that bent strands provided a higher strength and stiffness when compared to straight and frayed strand configurations. Salmons and McCrate went further to investigate which characteristic of the section had an influence on the slip behavior experienced by the untensioned strands. First, it was concluded that the relationship between stress within the strand and slip were independent of the embedment length of the strand. Second, varying the concrete between 3750 and 6900 psi did not have a significant effect on the bond characteristics of the strand before slipping occurred. Finally, the diameter of the strand also did not have a significant effect on the stress-slip behavior of the steel strands. Based on these findings, Salmons and McCrate were able to develop and present a series of equations pertaining to the embedment length of the untensioned strands to establish a superstructure to cap beam moment connection.

#### *2.2.4.3 Embedded Girder Ends*

The aforementioned NCHRP report also investigated the effect that embedding the ends of the girders into the diaphragm had on establishing a positive moment connection. In general, it was determined that embedding the ends of the girders 5 in. into the diaphragm reduced the stresses in the connection and allowed for a higher number of cycles to be reached before failure of the positive moment connection. Girders that were connected using bent strands and embedded ends failed at a number of cycles that was three times greater than that required for the same detail without embedded ends as the strains in the embedded details were lower than those in the non-embedded. As a result, it appeared as though embedding the ends of the girders for sections connected with bent strands was beneficial. However, the general effects of the embedded were hard to quantify, specifically for the bent bar details, and as a result, it was recommended that the effects of embedment be ignored in the design process.

#### *2.2.4.4 Additional Stirrups*

A few other connection components were also examined as a part of the NCHRP report, one of which was the placement of additional stirrups within the diaphragm in the joint region. During testing, it was noted that the additional stirrups helped to control diagonal cracking and increase ductility after the main bars fractured. However, in general, the stirrups had little effect on the overall strength of the connection. Finally, the report suggested that the ends of the girders should be embedded in order for the stirrups to provide the additional ductility.

#### *2.2.4.5 Through Web Reinforcement*

Another NCHRP connection component was the use of reinforcement placed through the webs of the girders and into the diaphragm. It was found that, though the web reinforcement improved the performance of the connection, the bars caused cracks to develop in the webs of the girders, which is undesirable.

#### *2.2.4.6 Partial Diaphragm*

The final connection component that was investigated as a part of NCHRP 519 was the use of a partial diaphragm to improve the connection performance. It was initially assumed that the partial diaphragm would place the bottom of the diaphragm in compression, which would reduce the tension in the section caused by the positive moments within the joint and increase the capacity of the connection. However, it was found that though the concept worked, it was not by

the originally assumed mechanism and that it did not provide continuity. Based on the results of the testing, it was implied that more research regarding the use of partial diaphragms should be performed in order to better understand this mechanism.

### **2.2.5 Concerns Regarding Positive Moment Connections**

Though methods for establishing positive moment connections and their respective behaviors have been established, there are still a number of concerns and issues associated with positive moment connections. This primarily includes fabrication issues, the lack of a well-defined design procedure, and the age at which the connection is established.

#### *2.2.5.1 Fabrication Issues*

In general, the additional reinforcement that is required in order to achieve continuity in the connection often results in congestion within the section, which causes difficulties related to construction in the field. However, it was found that, though the diaphragm may be congested, the connection should still have adequate strength. Additionally, the bent connection bars are difficult to construct, labor intensive, and are often asymmetrical, which can lead to uneven stresses and failure in the section (Miller, Castrodale, Mirmiran, & Hastak, 2004). The asymmetry is due to the fact that the bent connection bars must be installed straight and then bent in the field. Also, it is not uncommon for the extended bars or strands to be damaged or fractured during fabrication and transport. In the event of a fractured piece of reinforcement, holes must be drilled into the girder ends in which the new reinforcement is embedded in epoxy. Finally, it has been observed that strands that are detensioned have a tendency to experience a “bird cage” effect, where the wires unravel, which renders the section ineffective; however, it is also noted that this unraveling can be advantageous to improve anchorage.

#### *2.2.5.2 Lack of a Well-defined Design Procedure*

Though NCHRP 519 makes design recommendations based on the results of their extensive testing of positive moment connections, a design method for determining the amount and spacing of reinforcement for the connection has not yet been accepted. As a result, there are often concerns associated with placing too many reinforcing bars in one area without an adequate spacing within the diaphragm. It is typically assumed that cracking will occur at the interface of the beam-to-diaphragm connection region, but the failure will not occur within the diaphragm. However, it is unclear as to whether or not this cracking will affect the continuity of the system.

Furthermore, it has been found that the cracking did not affect the negative moment capacity, but it did reduce the negative cracking moment. Therefore, in order to help ensure an adequate capacity, designers recommend that the positive moment connection at the diaphragm have a capacity no greater than 1.2 times the cracking moment of the section. This limit is imposed in order to prevent the section from being overdesigned, as additional reinforcement in the section will only increase congestion, while providing little impact on the overall behavior of the connection.

#### *2.2.5.3 Age at which the Connection is Established*

Based on the results of the NCHRP testing, it was found that the age of the girders at the time at which continuity was established was the “single most important factor in the behavior” of the section. If the girder is relatively young, creep can produce significant positive moments within the connection. Conversely, if the girders are older, the differential shrinkage that will be experienced between the girder and the deck can produce significant negative moments within the connection. Therefore, it was decided that it would be unnecessary to limit the age of the girder, but rather a minimum advisable limit for the age is advisable in order to limit the formation of large positive moments, which might be generated during aging.

### **2.3 Experimental Research**

One example of previous research regarding the use of precast components in a bridge structure made continuous was a report and research completed at the University of California at San Diego (Holombo, Priestley, & Seible, 1998) regarding the use of precast spliced-girder bridges. In this report, an investigation on the seismic behavior of bridges using precast girder segments, which were spliced together using prestressing strands and made continuous for seismic loading as well as any live load or self-weight, was presented. The benefits of using spliced precast girders over a more conventional, cast-in-place or simply supported precast girder system are that longer spans may be achieved and that the design moment may be reduced, resulting in a reduced superstructure depth, smaller foundation, and ultimately a reduction in cost.

The results of the testing by Holombo et al. showed that spliced precast girders, both the bulb-tee and bathtub, could be used effectively in areas of high seismic activity with a high

degree of performance. Both of the test units used in this research achieved a level of ductility ( $\mu_{\Delta}= 8$  for the bulb-tee unit and  $\mu_{\Delta}= 6$  for the bathtub unit) that was significantly greater than that of the design value ( $\mu_{\Delta}=4$ ), while only minor cracking in the superstructure was observed.

Another example is the experimental research performed in order to develop design guidelines for integrally constructed cap beam to steel girder joint regions (Patty, Seible, & Uang, 2002). Four specimens were tested with combinations of cap reinforcement, either post-tensioning or conventional reinforcement, and girder stiffeners, with or without. The study focused on the torsional behavior of the cap beam with the different concepts, as shown in Figure 2.5.

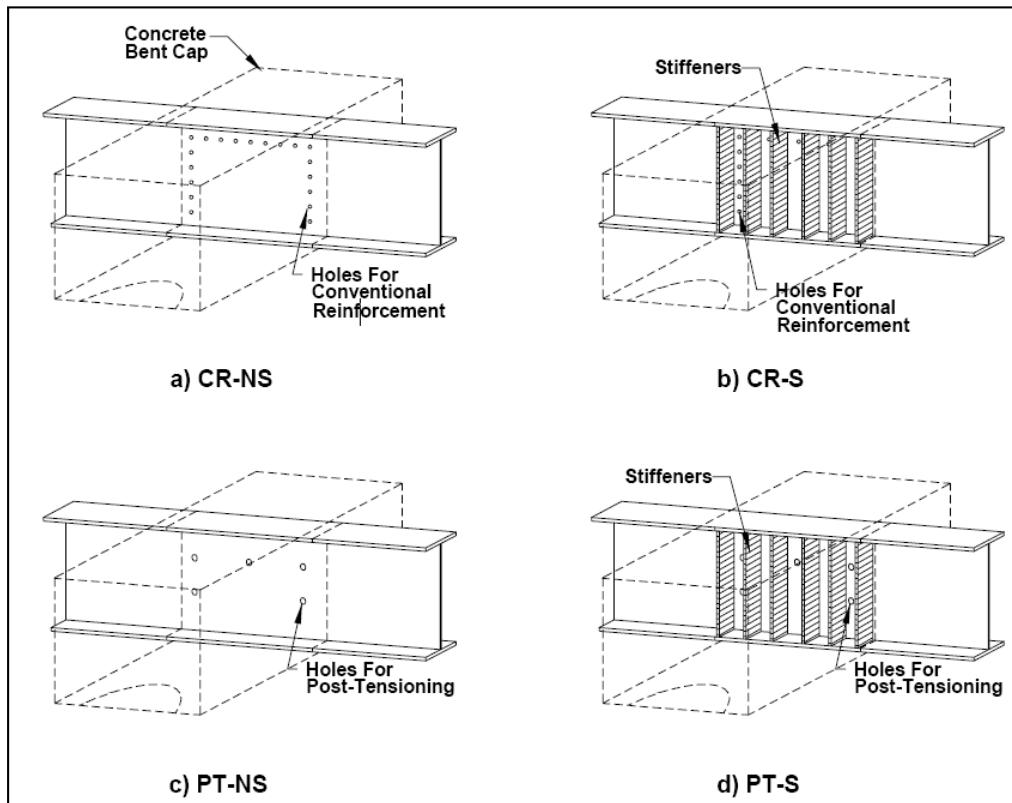


Figure 2.5. Test Concepts for Torsional Behavior of Integral Cap Beam (Patty et. al., 2002)

After testing the four concepts, the results showed that the torsional moment capacity of the component with stiffeners increased by 25%. The strain gauges recorded higher strains on the outer stiffeners than the inner stiffeners, indicating the outer stiffeners are more effective in transferring the flexural moment of the girders to the cap beam, resulting in a torsional moment. The stiffeners also contributed in reduced dilation of the bent cap by approximately 33%

compared to the specimens without stiffeners. Next, the effect of the post-tensioning from the concept testing was discussed. Bent caps with post-tensioning experienced almost zero dilation and significantly less cracking up to maximum moment. Also, the bent caps with post-tensioning instead of conventional reinforcement are easier to construct.

Additional experimental research was conducted at Iowa State University into the behavior of a concrete column, steel cap beam, and steel girders constructed integrally as part of a project sponsored by the National Cooperative Highway Research Program (Sritharan, Vander Werff, Abendroth, Wassef, & Greimann, 2005). The connection between the concrete column and steel box beam pier cap was accomplished by providing concrete anchorage of the column longitudinal reinforcement inside the cap beam. The girder-to-cap connection detail provided moment continuity of the girders through the cap beam by utilizing flange plates above and below the cap beam connected to the girder flanges with full-penetration welds. Shear continuity was provided by including web plates inside the steel box beam. Two units were designed and tested under simulated seismic loading, and it was noted that the superstructure, girder-to-cap-beam connection and the column-to-cap beam connection all remained essentially elastic. Minor spalling in the deck was observed, which was attributed to the incipient punching of column longitudinal bars through the bridge deck. The failure of the test units was measured to occur at a displacement ductility of 4; however, it was noted that modification to the shear connectors that extended from outside of the cap beam into the column would have allowed for greater ductility.

## **2.4 Detailed Modeling Introduction**

The ability to understand the response of a bridge to its prescribed loads is important to formulate the best design. To achieve the best design, testing of materials and structure are performed to understand the response components such as stress-strain behavior, deflections and rotations. To ensure that the forces are transmitted from the superstructure to the column, an effective connection must be designed to pass the forces from one component to the other. Without a sufficient connection, the response of the bridge may change dramatically and have ill-advised effects. To understand the response, research has been undertaken to model the structures in such a manner as to be able to capture the needed information. Many different means of modeling a structure have been used such as lab testing, strut-and-tie analysis and detailed finite element analysis. Each of these analysis techniques has been proven to be an

effective way to model the structural response for a given application. The three analysis techniques listed will be discussed in greater detail below and concerns will be raised regarding their adequacy for joint modeling.

#### **2.4.1 Detailed FEA**

Detailed finite element analysis has become a more common entity of research and design in the recent years (Roylance, 2001). A detailed analysis can be a powerful tool for engineering purposes only if the user has sufficient knowledge in its usage. In the modeling, many different options are available for elements, meshing, material properties, contact controls, etc. and sufficient understanding of each of these topics is needed to properly establish a model. When modeling, an incorrect assumption or incorrect technique can lead to a solution, however, it may be incorrect. Therefore, to have full confidence in any finite element analysis, experimental results or a closed-form solution needs to be presented to validate the results. In the following section, the purpose, advantages and challenges of finite element analysis will be discussed.

The finite element method allows for solutions to complicated problems to be obtained with ease. Many programs are available over a wide cost range for microcomputers and supercomputers. This leaves little reason for analysts to write their own software (Roylance, 2001). The commercial codes generally consist of three modules to build a model: preprocessor, analysis and postprocessor. Preprocessors in the commercially available codes undergo continuous upgrades to make the most user-friendly version. Some of the more sophisticated software can import CAD or other drawing files directly to the program and mesh the geometry, making the process of building the model easier. The analysis module imports the code from the preprocessor and analyzes the model. Another advantage of finite element analysis is the ability during analysis to address many different element types by simply specifying the appropriate element from the library (Roylance, 2001). Finally, the postprocessor compiles the results from the analysis into a user-friendly interface that allows the analyst to visualize the results.

The main advantage of the finite element analysis is the ability to mimic expensive experiments (Prabha, Seetharaman, Arul Jayachandran, & Marimuthu, 2007). In this process, the analyst has to have the knowledge to run the program and accurately model the structure

being considered. Once the analyst has finished the modeling, the program will analyze the structure and provide the results. This method is applicable for a wide range of applications: solid mechanics, dynamics, heat problems, fluids, electrostatic, etc. If modeled correctly, indeterminate structures can be solved along with applications with complex loadings and interactions. Once a model has been verified for accuracy, multiple loadings and restraints can be modified and analyzed with relative ease compared to other analysis techniques, such as the strut-and-tie method.

The finite element method provides many advantages; however, the disadvantages need to be considered to ensure the response is applicable. One possible disadvantage is the processing time, depending on the size of the model, the analysis time can become costly and inefficient when compared to other methods, especially when considering non-linearity. However, a detailed finite element analysis can be used in conjunction with a simplified model to reduce processing time. Main areas of interest on the structure can be modeled in detail and the behavior can be inputted into the simpler model to capture the global response accurately, like the moment-rotation characteristics of a connection for example. Another disadvantage of the finite element method is that the model can return results that are inaccurate if an aspect of the structure wasn't modeled correctly. To overcome this, verification needs to be performed to ensure the results being reported are correct (Biggs, Barton, Gomez, Massarelli, & McKeel, 2000). For accurate prediction of the structural behavior, correct geometric and material properties are vital (Chowdhury & Ray, 1995). The geometry of the key components needs to be accurately inputted to ensure that the correct response is captured. The complexity of the material models is dependent upon the material that is used. Materials with well-defined constitutive properties, such as steel and aluminum, are able to be modeled easily with accurate results in FE programs. However, a material such as concrete does not provide easy analysis. The discrete cracking, different response in compression, and the changing stiffness after crushing and cracking occurs, provides considerable problems in modeling the behavior (Chen, Yamaguchi, Kotsovos, & Pan, 1993). An extensive study was completed to demonstrate a methodology to analyze reinforced-concrete structures to overcome the previous concerns which will be discussed below (Biggs, Barton, Gomez, Massarelli, & McKeel, 2000).

The FE software ABAQUS was selected to perform the analysis of reinforced-concrete bridge decks (Biggs, Barton, Gomez, Massarelli, & McKeel, 2000). A specific objective of the study was to develop a model that could accurately predict global bridge behavior and strains, stresses and displacements in the deck. The FE model included a plasticity-based constitutive model for concrete. The elements used were shell elements to model the slab and beam elements to model the girders. Reinforcing bars were also included and modeled using one-dimensional truss elements. A uniform load was applied with a maximum near the ultimate load of the beam. Deflections and stresses were determined from the FE model and compared to hand calculations that were performed by the approach given in the American Concrete Institute code. The compressive stress in the beam is presented below in Figure 2.6. In Figure 2.7, the stress in the reinforcing bars is presented and Figure 2.8 presents the deflection of the slab across the span. The difference in the stress in the reinforcing bars near the support was attributed to the tension stiffening effects of the concrete model. Overall, the results from this study prove that the response of the concrete slab can be adequately predicted using the concrete models in ABAQUS. To further validate this conclusion, the model was modified to predict the response of a two-way reinforced, simply supported concrete slab that was experimentally tested previously.

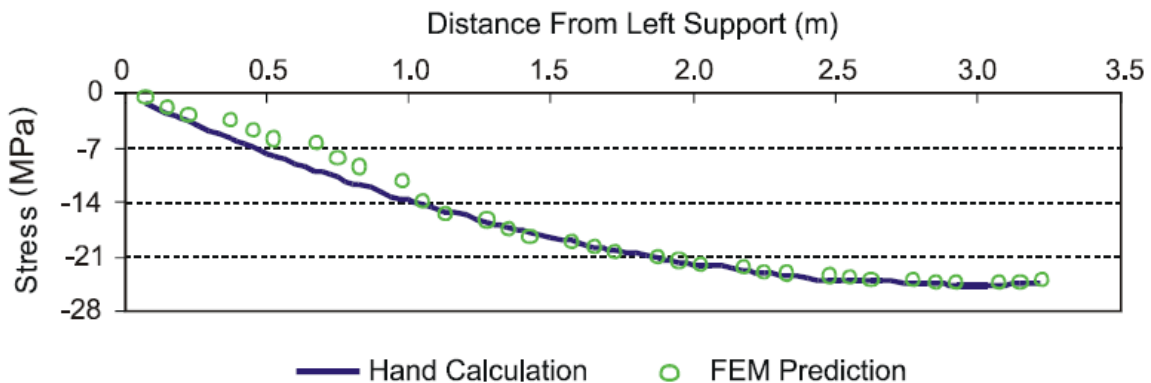


Figure 2.6. Compressive stress in top fiber of the beam (Biggs et. al., 2000)

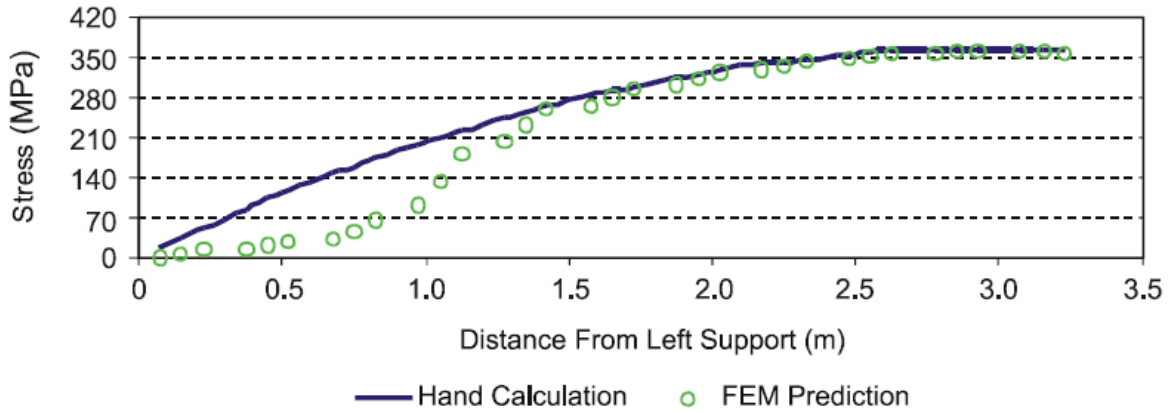


Figure 2.7. Steel Reinforcement Stress Along Beam (Biggs et. al., 2000)

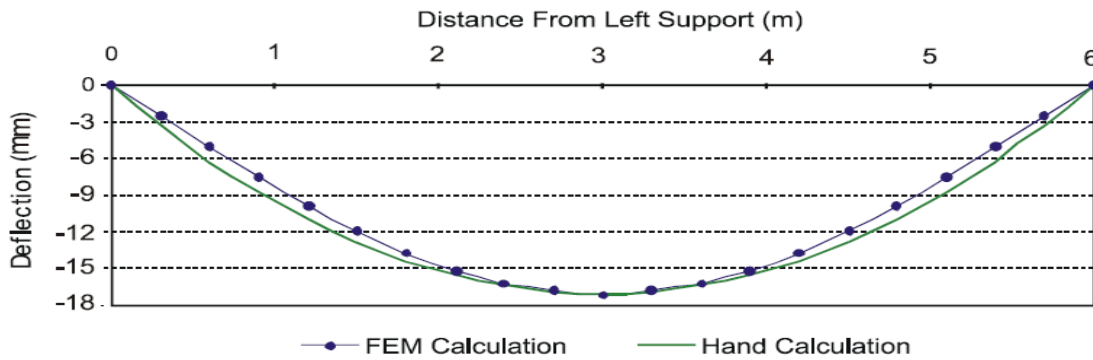


Figure 2.8. Deflection Across Span (Biggs et. al., 2000)

The FE model was able to predict the load-deflection behavior and flexural cracking load similar to the test results. Additional models were developed and the results were also analyzed. The conclusions from the report were that ABAQUS has the ability to model concrete and steel, simulate their interaction, apply loads and accurately calculate results and predict behaviors not generally obtained through experimentation. Also, ABAQUS has the ability to predict deflections, strains and stresses of realistic structures (Biggs, Barton, Gomez, Massarelli, & McKeel, 2000).

Another study using ABAQUS was performed to develop the moment-rotation behavior of semi-rigid steel bolted connections (Prabha, Seetharaman, Arul Jayachandran, & Marimuthu, 2007). The beam-to-column connection was modeled with 8-noded solid elements. The

elements do not have rotational degrees of freedom; however, they are discretized across the thickness to allow for the effect of bending. Additionally, contact modeling was used between the beam and column, bolts and bolt holes and pre-tensioning in the bolts. The moment-rotation results from the FE model and experimental results are presented in Figure 2.9.

With the validated model in ABAQUS, additional lab testing was able to be avoided and additional FE analysis models were run. This allowed for a large time and cost saving since there was a need to test up to 34 combinations of connections.

Additional studies have used ABAQUS for 3D FE modeling. A study was conducted involving a bulb-tee deck bridge, which was modeled by finite element analysis and field testing using a loaded end-dump truck was performed (Ma, Chaudhury, Millam, & Hulse, 2007). After the field testing was finished, the FE model was calibrated and the resulting strain values were similar to the field results.

Although the finite element method does possess disadvantages that may cause inaccurate results, with proper diligence the disadvantages may be overcome. Once the model is validated, future analyses can be completed more cost effectively while providing great detail when compared to lab testing and other analytical models.

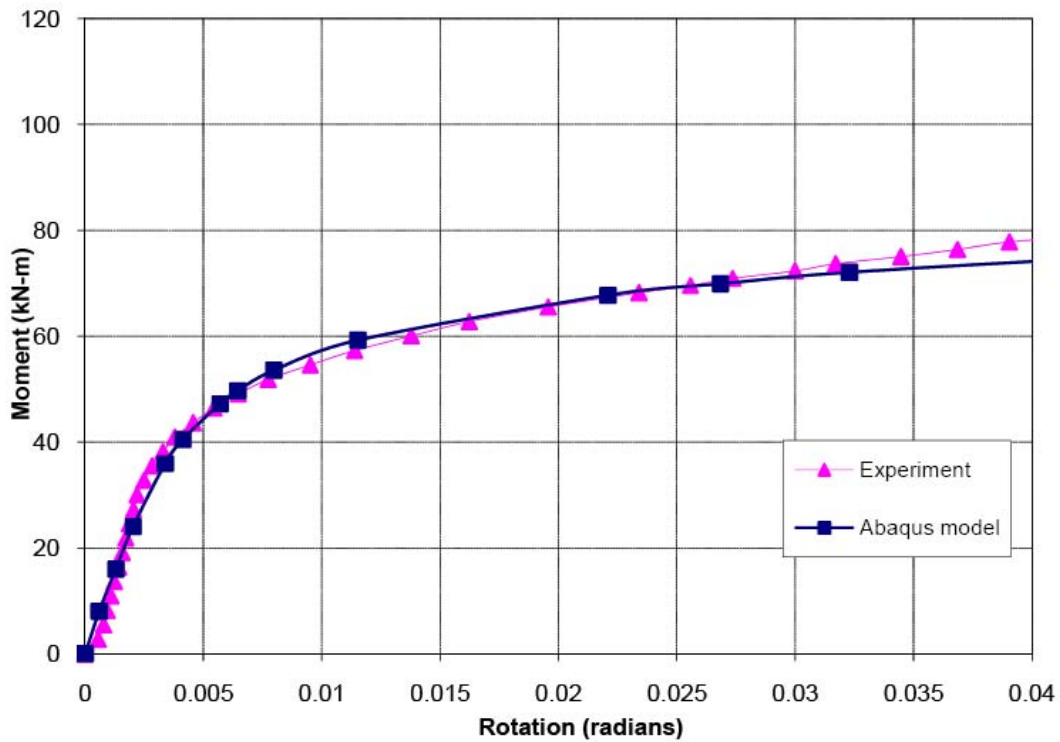


Figure 2.9. Comparison of moment-rotation curves (1 kN-m = 0.737 kip-ft) (Prabha et. al., 2007)

## 2.5 Grillage Finite Element Analysis

### 2.5.1 Introduction

The use of finite element analysis in structural engineering has become commonplace in today's industry. Complex structures, that were once thought to be unapproachable, can now be analyzed to an approximate solution in a cost effective manner involving minimal engineering time. However, engineers are constantly searching for innovative methods to make the use of a finite element analysis more user-friendly, time-efficient, and overall simpler for use on a regular basis. As a result, it is often more convenient for an engineer to employ the use of the simpler finite element model, known as a grillage model, in order to gain a basic understanding of the forces, stresses, strains, and displacements of a structure due to various load cases.

### **2.5.2 Background**

A grillage model consists of a network, or grid, of longitudinal and transverse beam elements, used to model specific aspects of the structure. In a bridge application, the longitudinal members typically represent the girders and a portion of the slab for which they support (Jaeger & Bakht, 1982). The transverse members typically model members that act across the structure, for example: cap beams, diaphragms, and effective portions of the bridge deck. Simplifying the model in this manner, when compared to a more complex finite element model, often reduces the likelihood of introducing errors or uncertainties associated with using unfamiliar elements in the analysis (Kostem & Ragazzo, 1993). Also, simplifying the model often allows the engineer to more easily visualize and organize the model, thus reducing the time spent to produce the model and making it easier to understand and verify its results (Srinivas, Ramanjaneyulu, Sukhesh, Sasmal, & Gopalakrishnan, 2004), (Jaeger & Bakht, 1982). According to the article entitled, “Grillage Analogy for Multigirder Bridges,” (Kostem & Ragazzo, 1993), “The effort required for a grillage model is about 10% of the effort required for a true finite element model.”

Grillage analysis has been used to model a wide variety of structural engineering applications. Though it is most commonly used to model bridge structures, it has also been used to model slabs, buildings, and other structures. Complicated bridge features, a variety of bridge decks, prestressed girders, I-, T-, and bathtub girders, and other unique bridge components have also been accurately modeled using the grillage analogy. As a result of its wide range of flexibility, ease-of-use, and time saving potential, the grillage analysis is a commonly used tool for analysis.

### **2.5.3 Analysis Limitations**

Though the use of a grillage analysis offers a lot of appealing benefits over a complicated finite element analysis, it is not without its own limitations. First, it is important to note that all finite element analyses offer an approximate solution rather than an exact solution. The accuracy of any finite element model depends on the knowledge and assumptions made by the user, the elements used in the model, the enforced boundary conditions, etc. (Kostem & Ragazzo, 1993). Grillage analyses typically result in an equilibrium solution that may often be used as lower bound solution (Gordon & May, 2004). In other words, the results are often used to obtain more

of a general feel for how the structure will behave given specific loading conditions (Jaeger & Bakht, 1982). However, this is not to say that the results could not, or should not, be used for design purposes.

Comparisons to more accurate finite element models, as well as actual test results, have shown that, while certain characteristics of the models agreed very well, other aspects showed a gross disagreement (Kostem & Ragazzo, 1993). For example, it has also been shown that the accuracy of mid-span moment predictions may vary with the length of the girders being modeled (Kostem & Ragazzo, 1993). Short-to-medium span bridges can predict moment values with roughly 10% error, while the accuracy decreases as the span length increases. However, long span bridges do tend to provide an acceptable degree of accuracy when predicting mid-span moments (Kostem & Ragazzo, 1993). The same study also showed that the grillage analysis provides better results when used to model simple span bridges with prestressed concrete girders, than bridges with reinforced concrete decks and steel girders (Kostem & Ragazzo, 1993). These types of errors, often associated with over simplification of the model, have led some researchers to conclude that the use of a grillage analysis should be avoided when a more accurate finite element analysis is feasible (Gordon & May, 2004).

#### **2.5.4 Model Construction**

As stated earlier, a grillage analysis consists of network of longitudinal and transverse beam elements. The structural components that those elements represent depend upon the structure being modeled. A typical bridge grillage model consists of members representing the column, cap, girders, diaphragms, and the bridge deck. In order to accurately capture the behavior of the structure, it is crucial that the properties of these elements be accurately modeled within the analysis software.

Typically the various member properties, cross-sectional area, moment of inertia, etc. should be computed and input into the program using typical mechanics of materials equations. In order to reflect the nonlinear behavior and plastic hinging of the column, it is recommended that plastic hinges, or springs elements, be placed at the top and bottom of the column. More information regarding the modeling of this nonlinear behavior will be presented below.

When modeling a bridge, the girders are a very important component of the grillage analysis. Typically the longitudinal beam elements within the grillage analysis are used to model the girders. In order to accurately model the girders and their contribution to the system, the beam elements are usually located at the centroid of the girder that it represents (Keogh & O'Brien, 1996), (Jaeger & Bakht, 1982). Also, if a deck is present above the girders and composite action between the girders and the deck is considered, a portion of the deck should be included when calculating the various section properties for the member in order to reflect the composite section (Jaeger & Bakht, 1982). The effective flange width of the deck above the girder should be calculated per AASHTO guidelines (Staudt, 2002). Also, a common means to approximate the effective stiffness of the girders after cracking is to reduce the gross stiffness by 75% (Holombo, Priestley, & Seible, 1998).

Since the majority of lateral load is transferred to the column and supports by the diaphragm action of the deck, it is important to accurately model the deck within the grillage analysis (Kostem & Ragazzo, 1993). The majority of the transverse beam elements in the grillage model are used to capture the behavior of the deck. The primary concern when modeling the deck is the spacing of the transverse beam elements. Though some researchers have argued that a coarse mesh is sufficient for design and that the spacing is somewhat arbitrary, if the mesh is too coarse, the deck will not deflect in a smooth manner and could generate inaccurate forces on surrounding members (Hambly, 1990). As a result, it is recommended that the members be spaced at approximately one quarter to one eighth of the effective span as a guideline. It is also convenient to maintain a uniform spacing, when possible, of the transverse members. The section properties of the grillage elements should then be calculated based on the tributary area of the deck for which they represent. Other grillage analyses have also suggested that half the gross section properties of the deck be used to reflect the cracked properties of the deck when bending about its transverse, while zero stiffness should be considered for bending about the axis perpendicular to the surface of the deck (Holombo, Priestley, & Seible, 1998). When diaphragms are present in a structure, it is also important to model them with a transverse beam element. The properties of the diaphragm should be calculated considering the contribution of the deck as an effective flange width acting with the diaphragm (Hambly, 1990).

Finally, once all of the members are placed within the grillage model, it is important to mesh or link them together so that they may act as a unified network. Though there are many options that can be considered when joining elements (rigid end links, springs, etc.), it has been shown that extending the elastic member properties to the centerline of their respective joints typically provides more accurate results when compared to other options, specifically rigid end links (Holombo, Priestley, & Seible, 1998).

Another crucial aspect of the grillage model is accurately capturing the boundary conditions. This becomes a greater concern when only a portion of the actual structure is being modeled; this is likely due to symmetry. Typically, for a symmetric structure, only half of the structure need be modeled as it may be split down a longitudinal centerline. In this case, it is important to accurately capture the effects of the other half by applying boundary conditions along the “line of cut.” In such a case, it is usually recommended that the centerline be restrained against a translation perpendicular to the centerline as well as rotation about the centerline (Holombo, Priestley, & Seible, 1998). These boundary conditions are used, as the structure (a bridge for example) would not likely translate horizontally due to the displacements being applied in the longitudinal direction for a typical push-over analysis. However, if it were not for the applied boundary conditions, the model might have a tendency to do so as it is would be asymmetric. Also, the model should not be allowed to rotate about its longitudinal axis as the presence of its other half would result in zero rotational displacement along the centerline.

### **2.5.5 Nonlinear Behavior**

Nonlinear behavior is a very important aspect that must be captured within a model, especially if the structure is located within a seismic region. Bridges in seismic regions are typically designed to develop plastic hinges in their columns during a seismic event in order to preserve its superstructure and prevent catastrophic damage. Therefore, these nonlinear characteristics should also be present within a grillage model. The modeling of nonlinearity has been accomplished primarily through two methods: event scaling analysis and the use of nonlinear springs or hinges.

An event scaling analysis, also commonly referred to as a collapse mechanism analysis, is a sort of roundabout method of performing a nonlinear analysis. Essentially, the method

requires a linear elastic grillage model and knowledge of the behavior of the structure at each significant nonlinear event, i.e. the formation of a plastic hinge, reinforcement yielding, cracking, etc. A series of linear analyses are performed using the linear elastic grillage model until the forces within the model reach the first specified nonlinear event; at which point, adjustments are made to the model to reflect the occurrence of the nonlinear event, which is typically done by changing the stiffness of specific members surrounding the nonlinear event. Another linear analysis is then performed using the updated member properties and the process is continued until the final nonlinear event, or a failure mechanism, is reached. Though the method can be performed through hand calculations, the structures being analyzed are typically too complicated and require the use of automated software (Priestley, Seible, & Calvi, 1996). However, this analysis technique is somewhat outdated and is significantly more time consuming when compared to more current techniques. As a result, this method is not typically preferred over other nonlinear analysis techniques such as the use of nonlinear springs or hinges.

Briefly, another method is based on the “Linear elastic stiffness matrix approach” (Deng, Ghosn, Znidaric, & Casas, 2001). This method of analysis includes the effects due to nonlinear behavior of the structural members by adjusting the stiffness matrix at the end of each load increment in order to reflect the softening of a given member.

Currently, the standard method used to perform a nonlinear grillage analysis is through the use of nonlinear spring, hinge, or link elements. In order to accurately employ this method, the location of potential plastic hinges must be known (Deng, Ghosn, Znidaric, & Casas, 2001). In the case of a bridge structure located in a seismic region, the current design practice is to design the structure such that plastic hinges will form within the columns. Therefore, the springs should be placed at their respective locations within their respective column. Typically, the behavior of the nonlinear springs is based on a moment-rotation, or moment-curvature, relationship that is input by the user into the analysis software (Deng, Ghosn, Znidaric, & Casas, 2001). As a result, it will often be necessary to perform a moment-curvature analysis on the portions of the structure that will develop the plastic hinges. The moment-curvature relationship can then be converted into a moment-rotation analysis and input into the spring parameters within the analysis software. Once the nonlinear springs are in place, the analysis can be run as a

nonlinear analysis and the structure will undergo normal elastic deformation before undergoing plastic deformation per the moment-rotation properties of the given spring. This method is much more efficient and accurate compared to the former methods, and thus, is often the preferred method for a nonlinear grillage analysis.

### **2.5.6 Hysteretic Behavior**

The nonlinear behavior in a bridge is usually forced into specific plastic hinge locations, which are defined by a nonlinear plastic spring or hinge, as mentioned previously. Seismic loading on a structure occurs in a cyclic manner and, as a result, the nonlinear spring will be forced to load in a given direction, unload, and reload in the opposite direction. However, once the hinge region has reached a given amount of nonlinearity, the effective stiffness of the column will be reduced. Hence, the manner in which the spring unloads and reloads will change with loading and will not simply follow the original curve as it must reflect the energy that is dissipated due to hysteretic damping as plastic behavior is developed. Therefore, it is important to accurately reflect these changes in behavior by incorporating some form of a plastic hinge hysteretic model. Currently, there are two main hysteretic models that are widely used and accepted: The Takeda Model and the Pivot Model.

#### *2.5.6.1 Takeda Model*

Toshikazu Takeda developed the Takeda Model in 1970 with a focus on modeling the hysteretic behavior of reinforced concrete (Takeda, Sozen, & Nielsen, 1970). This model defines an initial “Primary curve” to define the initial loading of the hinge. This primary curve is tri-linear and defined by the load and displacement at first cracking as well as the load and displacement at yield, as depicted by the curve (a) of Figure 2.10. The slope of the final segment of the tri-linear curve is defined by the strain-hardening properties of the reinforcement, as the section has previously cracked and the reinforcement has yielded. The curve then follows a series of case-specific rules for unloading and reloading, which are governed by the amount of load or displacement that has been reached within the hinge. Unfortunately, the rules are a bit too complex and lengthy to list in their entirety; for a more in-depth description refer to (Takeda, Sozen, & Nielsen, 1970). Curves (b) and (c) in Figure 2.10 display an example of how a given hinge might load and unload based on the aforementioned set of rules provided in (Takeda, Sozen, & Nielsen, 1970). As part of the development of the model, Takeda performed dynamic

excitation tests on a reinforced concrete test specimen. The results of these tests were then compared to the results of the calculated dynamic response based on the Takeda Model. A comparison of the results obtained via the testing provided satisfactory agreement and the model has since been widely accepted as a valid hysteresis model. A modified version of the Takeda Model has also been developed, which updates the rules of the original simplified model in order to provide more accurate results. One main difference from the original model is that the initial stiffness of the member is based on the cracked section properties rather than the pre-cracked properties (Dowell, Seible, & Wilson, 1998).

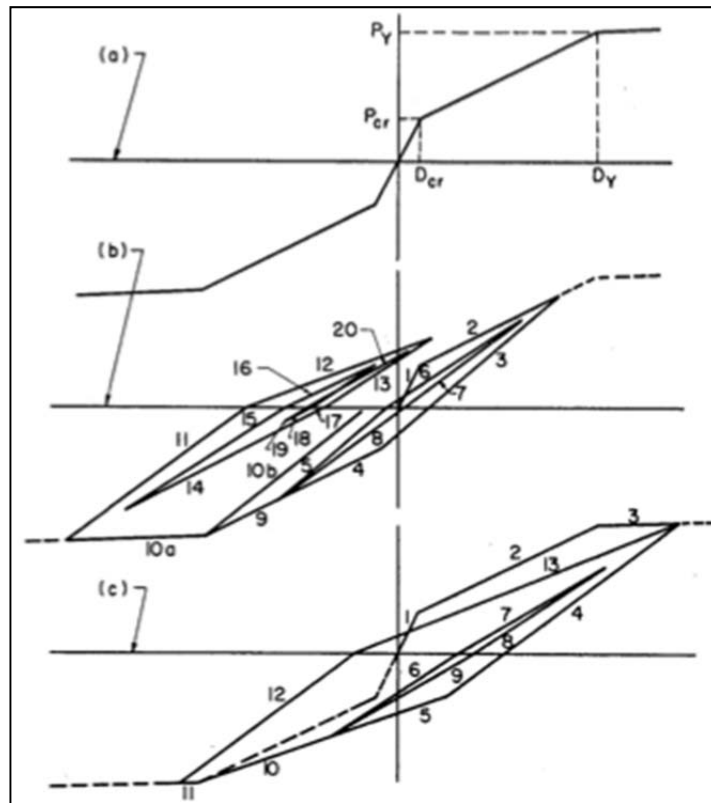


Figure 2.10: Takeda Model (Takeda et. al., 1970)

### 2.5.6.2 Pivot Model

Another commonly used model is the Pivot Model, which was recently developed by Dowell et al. in 1998 (Dowell, Seible, & Wilson, 1998). Similar to the Takeda Model, the Pivot Model was also developed for plastic hinges in reinforced concrete members. The Pivot Model

has the ability to account for cyclic axial loads, asymmetric sections, and strength degradation. However, compared to the Takeda Model, it is much simpler as the response can be predicted by three rules based on the geometry of the member. By observing the force-displacement hysteresis results from reinforced concrete members subjected to cyclic forces, Dowell was able to make the following conclusions (Dowell, Seible, & Wilson, 1998): First, the unloading stiffness decreases as ductility increases. Second, once the load is reversed after a nonlinear event, the hysteresis plot crosses the initial stiffness line before reaching the corresponding idealized force. When unloading to a condition of no load, from any point on the plot, it usually follows a path that points towards a single point along the initial stiffness line. This point is referred to by Dowell as the, “Primary pivot point.” Finally, during loading, it was observed that the plot tended to cross the elastic loading lines shown in Figure 2.11 at the same point, known as the “Pinching pivot point.” All of these observations form the backbone of the Pivot Model. The elastic loading lines mentioned earlier are also used to divide the plot into four quadrants, as shown in Figure 2.12. These quadrants are used to determine which set of rules will apply to the hysteresis plot given the force and displacement condition at which the load or unloading is applied. Unless a reversal in displacement direction occurs, the hysteresis will follow a given strength envelope; one envelope is used prior to yielding of the section and another envelope is used after the section has yielded. Figure 2.13 shows a typical post-yield strength envelope that a section may be expected to follow. In order to incorporate strength degradation under cyclic loading, the pinching pivot points are allowed to move towards the origin and the plot is adjusted to intersect at these new points. Also, after a nonlinear event, the initial stiffness will often soften. As a result, the model allows the elastic loading lines to rotate in order to reflect these changes in stiffness. Comparisons of the Pivot Model to both the Takeda Model and test results from the dynamic loading of a reinforced concrete member led to the conclusion that the Pivot model generally behaved as well as, if not better than, the Takeda Model. However, the Pivot model currently does not account for the strength degradation experienced under cyclic loading to the same amount of displacement, strength degradation in one direction due to a sudden strength loss in the opposite direction, or biaxial bending effects (Dowell, Seible, & Wilson, 1998).

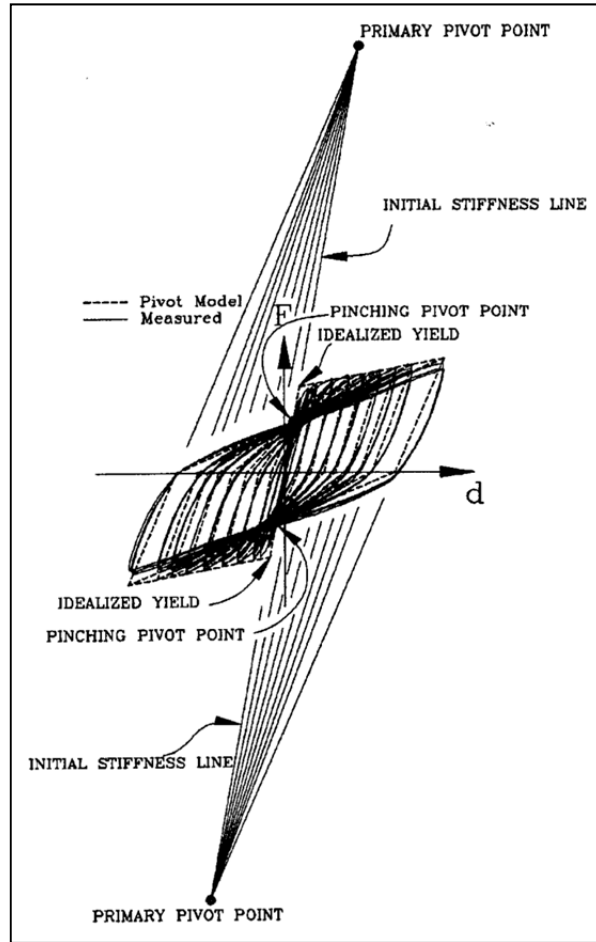


Figure 2.11: Pivot Model Observations (Dowell et. al., 1998)

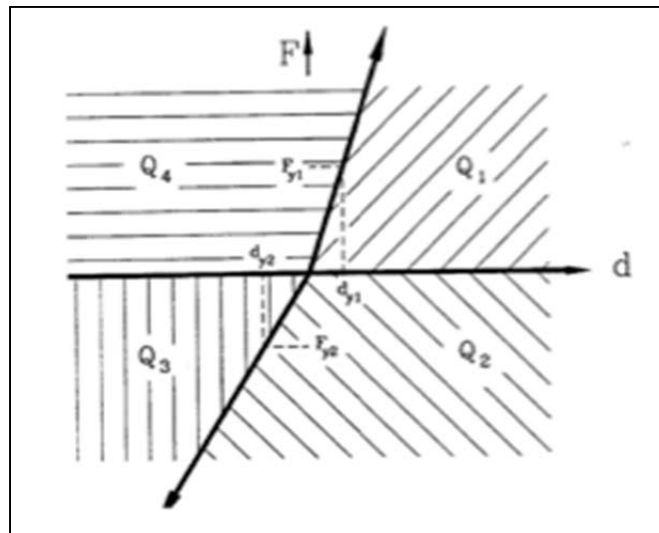


Figure 2.12: Elastic Loading Line Quadrant Division (Dowell et. al., 1998)

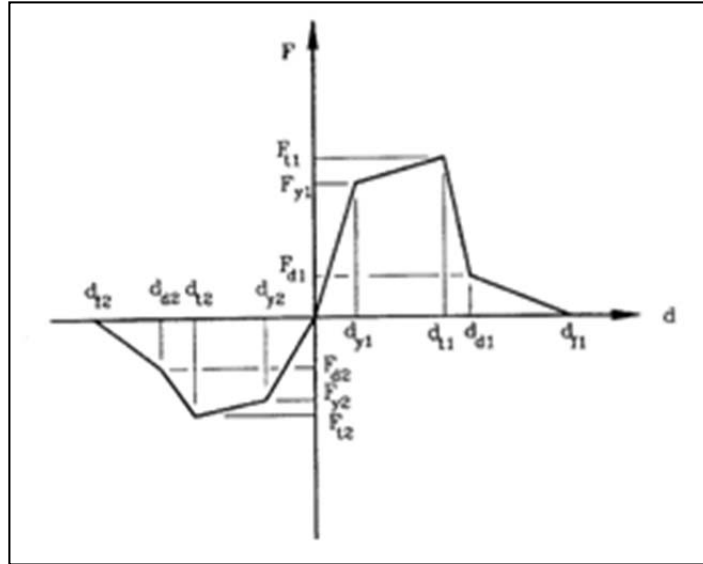


Figure 2.13: Typical Strength Envelope (Dowell et. al., 1998)

### 2.5.7 Torsional Behavior of Concrete

The torsional behavior of reinforced concrete is still a relatively new field of study. As a result, compared to other areas of focus within structural engineering, little information exists and much of the predictions made regarding this topic are based on a series of assumptions. However, in order to develop a more accurate finite element model, or make any sort of prediction, many of these assumptions must be adopted.

It is known, however, that an applied torsion will generate shear stresses along the perimeter of a given cross-section. Therefore, the inner core of the given cross-section is typically neglected in regard to the contribution of torsional resistance. This assumption has also been validated through experimental testing (Rahal K. N., 2000). Instead, a hollow tube analogy, which considers only the outer portion of the section for torsional resistance, is often used when analyzing the torsional behavior of the cross-section, as shown in Figure 2.14 (Collins & Mitchell, 1991), (Rahal K. N., 2000). The following equation, Equation 2.1, which was presented by Rahal and Collins and validated through experimental results, may then be used to predict the cracking torque for a given section. The variables  $A_c$  and  $p_c$  represent the cross-sectional area and the perimeter of the section, respectively.

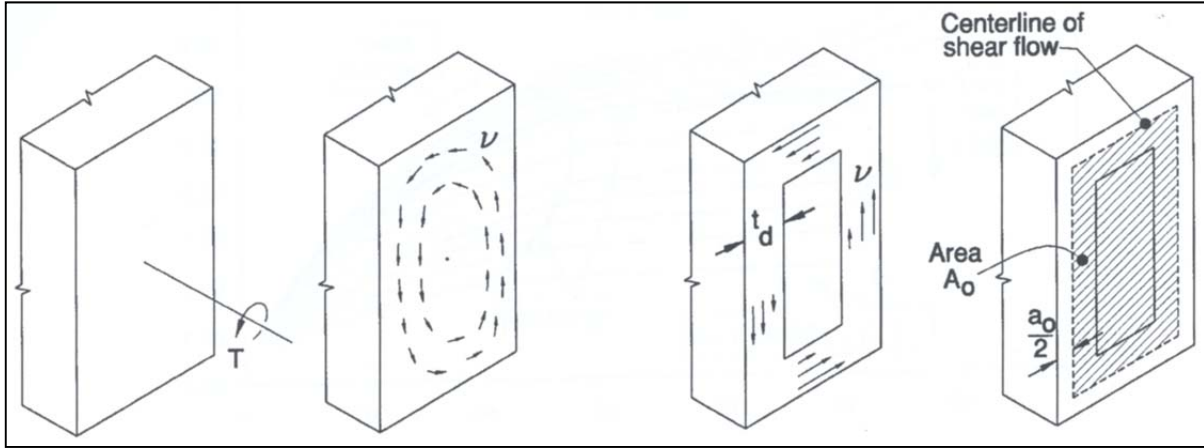


Figure 2.14: Torsion Hollow Tube Analogy (Collins & Mitchell, 1991)

$$T_{cr} = \frac{A_c^2}{p_c} 4\sqrt{f_c'} \sqrt{1 + \frac{f_{pc}}{4\sqrt{f_c'}}} \quad (psi) \quad (2.1)$$

Collins and Mitchell also present an approach to calculating the ultimate torque for a section, post-cracking. After torsional cracking occurs along a section, the torsion is typically resisted by the diagonal compressive stresses in the concrete that wrap around the beam at an angle  $\theta$ , as shown in Figure 2.15. However, due to the applied torsion, the outer surface of the section is no longer planar, resulting in a non-uniform diagonal stress distribution along its surface. Eventually, at a certain depth below the surface, the stresses become tensile rather than diagonal, leaving the remainder of the section ineffective in resisting the applied torsion. Additionally, as the section continues to deform, the cover concrete will spall and fall away from the section. Therefore, a version of the hollow tube analogy may continue to be used when analyzing the section post-cracking, shown in Figure 2.16. As a result, the following equations may be used together in an iterative manner, as outlined by Collins and Mitchell, to converge on the torque and angle of twist at the ultimate limit state for the section (Collins & Mitchell, 1991).

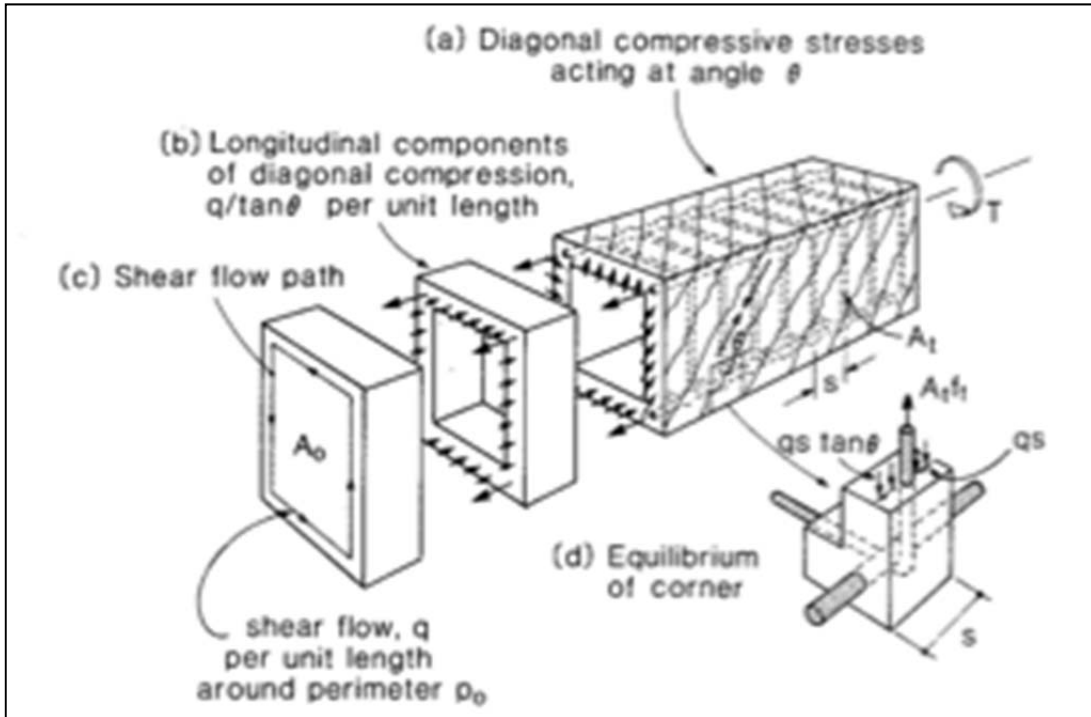


Figure 2.15: Torsional Behavior Post-Cracking (Collins & Mitchell, 1991)

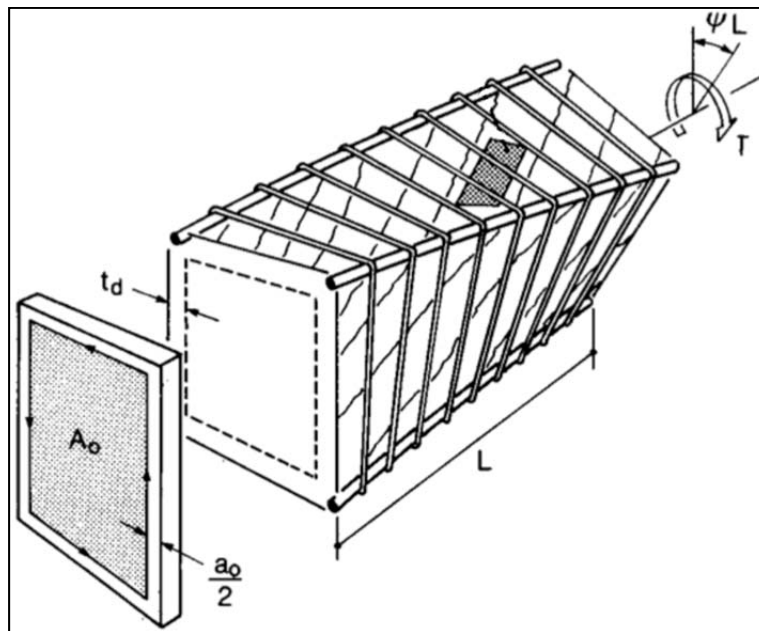


Figure 2.16: Post-Cracking Hollow Tube Analogy (Collins & Mitchell, 1991)

$$T = 2A_o \frac{A_t f_t}{s} \cot \theta \quad (2.2)$$

In the above equation, Equation 2.2,  $A_o$  represents the area surrounded by the shear flow path as shown in Figure 2.16.  $A_t$  and  $f_t$  represent the area and tensile stress in the hoop reinforcement surrounding the section, respectively, while  $s$  represents the spacing of the hoop reinforcement.

$$a_o = \frac{A_{oh}}{p_h} \left[ 1 - \sqrt{1 - \frac{Tp_h}{\alpha_1 f_c' A_{oh}^2} (\tan \theta + \cot \theta)} \right] \quad (2.3)$$

Equation 2.3 is used to solve for the thickness around the section that is used in resisting the applied torsion,  $a_o$ .  $A_{oh}$  represents the area enclosed by the centerline of the hoop reinforcement, while  $p_h$  represents the perimeter of the centerline of the hoop reinforcement. The value for  $\alpha_1$  is typically assumed to be 0.70.

$$N_v = \frac{Tp_o \cot \theta}{2A_o} \quad (2.4)$$

Equation 2.4 is used to calculate the tensile force,  $N_v$ , in the longitudinal reinforcement. The variable  $p_o$  represents the perimeter of the shear flow path.

$$\epsilon_x = \frac{N_v}{A_l E_s} \quad (2.5)$$

Equation 2.5 determines the longitudinal strain in the reinforcement and has been simplified by removing the terms accounting for prestressing.  $A_l$  and  $E_s$  represent the area and modulus of elasticity of the longitudinal steel, respectively.

$$f_2 = \frac{Tp_h}{A_{oh}^2} (\tan \theta + \cot \theta) \quad (2.6)$$

Equation 2.6 is used to quantify the principal compressive stress in the concrete,  $f_2$ , and is used to check whether or not the concrete has experienced any diagonal crushing.

$$\epsilon_1 = \epsilon_x + \frac{\epsilon_x - \epsilon_2}{\tan^2 \theta} \quad (2.7)$$

Equation 2.7 is used to calculate the principal tensile strain in the concrete,  $\epsilon_1$ . The value for  $\epsilon_2$  is typically estimated to be -0.0015.

$$f_{2\max} = \frac{f_c'}{0.8 + 170\epsilon_1} \quad (2.8)$$

Equation 2.8 is used to determine the limiting compressive stress,  $f_{2\max}$ , in the concrete, for which the compressive stress is not allowed to exceed.

$$\varepsilon_t = \varepsilon_1 - \varepsilon_x - 1.5 \times 10^{-3} \quad (2.9)$$

Equation 2.9 is used to calculate the tensile strains in the stirrups to confirm that they are yielding at failure.

$$\gamma_{xy} = 2(\varepsilon_x - \varepsilon_y) \cot \theta \quad (2.10)$$

Equation 2.10 determines the shear strain in the section at failure.

$$\psi = \frac{\gamma_{xy} P_o}{2A_o} \quad (2.11)$$

Equation 2.11 may then be used to predict the angle of twist in the section at failure.

One commonly used method for determining the torsional capacity of a section is the torsion shear-friction model shown below in Figure 2.17. The model assumes a constant shear friction stress over the section and that it is subjected to horizontal and vertical shear forces  $V_V$  and  $V_L$ , torque  $T$ , and a clamping force acting normal to the section  $P$ . The clamping force  $P$  is defined in Equation 2.12, where  $F$  is the prestressing force on the section,  $V_T$  is an axial force acting on the section produced by any transverse shear, and  $A_{st}$  is the total area of the reinforcement in the section. The constant term in the equation, 0.0006, corresponds to the assumed maximum dilation strain in the steel, due to doweling action of the reinforcement, at the point of torsional failure.

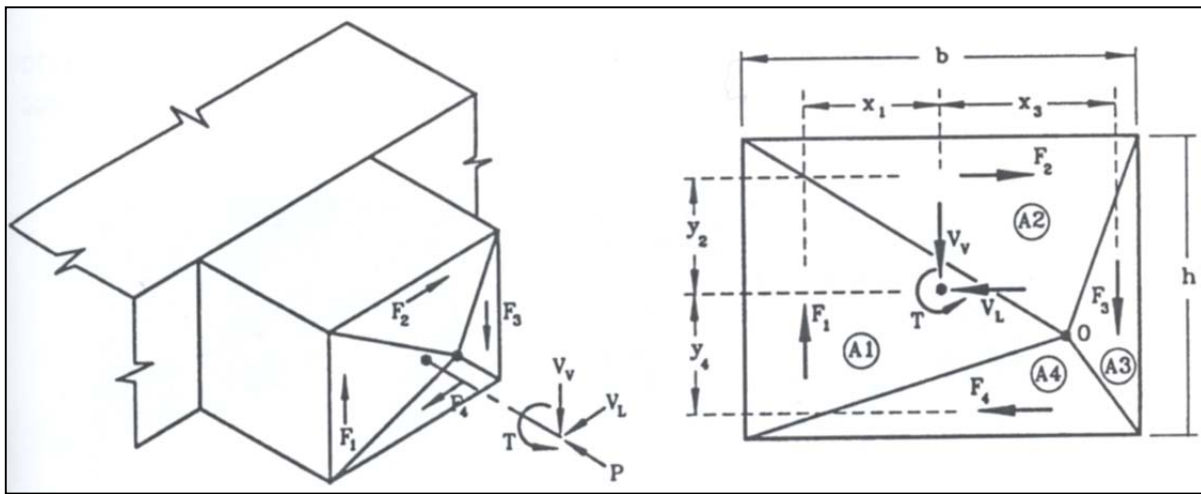


Figure 2.17: Torsion Shear-Friction Model (Priestley et. al., 1996)

$$P = F + V_T + 0.0006E_s A_{st} \quad (2.12)$$

The section may be divided into four unequal quadrants, each of which contributes a shear friction resistance to the applied torque  $T$ . The shear friction of each quadrant is defined by a force,  $F$ , acting parallel to the outer edge of the quadrant, where  $F = \tau A$  and  $\tau = \mu P/A$ ;  $A$  is the cross-sectional area of the section and  $\mu$  is the coefficient of friction over the interface. Therefore, the resisting shear forces to  $V_V$  and  $V_L$  may be defined and used to determine the resulting torsional capacity of the section via the following equations:

$$V_V = F_1 - F_3 \quad (2.13)$$

$$V_L = F_2 - F_4 \quad (2.14)$$

$$T = F_1 x_1 + F_2 y_2 + F_3 x_3 + F_4 y_4 \quad (2.15)$$

The variables  $x_1$ ,  $y_2$ ,  $x_3$ , and  $y_4$ , in Equation 2.15, represent the distance between the shear friction force,  $F$ , which acts through the centroid of its respective quadrant and the centroid of the entire section (Priestley, Seible, & Calvi, 1996).

### 2.5.8 Strain Penetration

It is often critical that the effects of strain penetration be included in a nonlinear analysis of a structure in order to achieve an accurate behavioral prediction. Strain penetration is a slip experienced by the reinforcement, typically at the end of a member, and is caused by the localized crushing of the concrete surrounding the reinforcement as the strain in the concrete increases. The effects due to strain penetration, such as increased displacements and rotations due to slip, are particularly noticeable in the joint regions during seismic-type loading conditions. Therefore, the following equation, Equation 2.16, may be used to calculate the amount of slip experienced at the yield condition,  $s_y$  (Zhao & Sritharan, 2007).

$$s_y (mm) = 2.54 \left( \frac{d_b (mm)}{8437} \frac{f_y (MPa)}{\sqrt{f'_c (MPa)}} (2\alpha + 1) \right)^{1/\alpha} + 0.34 \quad (2.16)$$

The value for  $\alpha$  is taken as 0.4 in the above equation per (Zhao & Sritharan, 2007), while the variable  $d_b$  represents the bar diameter and  $f_y$  is the yield strength of the reinforcement that is experiencing slip;  $f'_c$  is the compressive strength of the surrounding concrete.

### 2.5.9 Bond-Slip Behavior of Strands in Concrete

Bond slip is another critical effect that must be included for an accurate analysis. The effect occurs along the length of reinforcement that is embedded in either concrete or grout and is caused by strain penetration along its length. As the stresses and strains on a given bar increase, the surrounding concrete crushes and allows for the bar to slip relative to the concrete. Eventually, this will penetrate to the end of the specimen, resulting in an entire slip of the bar relative to the concrete, otherwise known as a bond failure of the bar (Raynor, Lehman, & Stanton, 2002). Though experimental tests have been performed on specific bar and strand sizes, not all of the data is immediately applicable to any size and configuration. Also, the tests are typically performed on short specimens, which can be inaccurate when applied to a global response, as the results are more indicative of the localized behavior of an embedded strand. However, the results of the test have been used to develop empirical equations that may be used to predict the behavior of a given diameter strand. Raynor presented the following equation, Equation 2.17, in order to predict the average debonded length of a given prestressing strand diameter, which may be multiplied by the strain in the strand to determine the amount of overall bond-slip experienced by the strand:

$$l_{ua} = \frac{2.1(\sigma_u - \sigma_y)}{(f_g')^{1.5}} d_b \quad (2.17)$$

The values  $\sigma_u$  and  $\sigma_y$  represent the ultimate and yield stress of the strand, respectively, and are expressed in terms of MPa. The value  $f_g'$  represents the compressive strength of the grout surrounding the strand and  $d_b$  represents the strand diameter. Figure 2.18, below, depicts the effects of bond-slip and what is meant by the term debonded length of the strand (Raynor, Lehman, & Stanton, 2002).

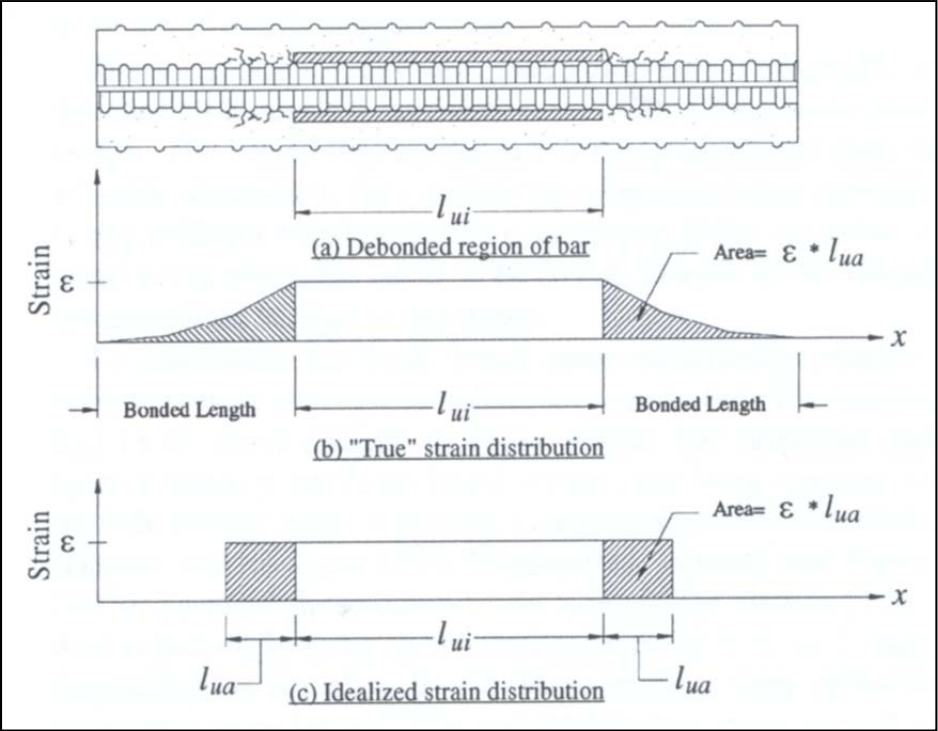


Figure 2.18: Bond-Slip Unbonded Length (Raynor et. al., 2002)

## **Chapter 3. Design of Test Unit**

### **3.1 Prototype Structure**

A prototype bridge was designed and used for this research project. The methods of design used were representative of existing inverted-tee cap beam bridges for Caltrans and followed current seismic design practice. The prototype structure was used for the finite element analysis and also, a portion of it was used to establish a large-scale test specimen for laboratory testing under simulated seismic loads. Before the design was undertaken, aspects of the bridge had to be decided, including bent style, number of girders and style of girders. A single-column was chosen and the section was used efficiently to create the maximum load at the column-to-cap-beam interface. A multi-column bent would require a much wider superstructure to develop the maximum demand at the column-cap interface when using the same size column. This would not be feasible for experimental research due to the lab space and cost limitations. A circular column was chosen since it is the preferred cross-section in seismic regions as the moment capacity of this column section is the same in any given earthquake loading direction. The superstructure was considered to have five girders to allow for the maximum width for this bridge. Four girders were considered, but the maximum demand on the column would have been less since the superstructure width is limited by the maximum girder spacing of 8 ft., as allowed by the AASHTO LRFD Bridge Design Specifications 3<sup>rd</sup> Edition for the live loads of the bridge (AASHTO, 2003). For girders, the California I-girder was chosen, as recommended by Caltrans to closely replicate the existing bridges with inverted-tee bent cap. It was decided that the deepest girder should be chosen to create the greatest demand on the girder-to-cap-beam connection. Successfully showing that the new connection has the capacity to withstand this setup, it would follow that the shallower sections would also have an adequate capacity.

The prototype bridge, presented in Appendix A, was designed in accordance to the AASHTO LRFD Bridge Design Specifications 3<sup>rd</sup> Edition with 2006 Interims and California Amendments (AASHTO) (AASHTO, 2003), as well as the Caltrans Bridge Design Aids (Caltrans, Bridge Design Aids, 1995) for the design of Inverted-T Cap, Caltrans Bridge Design Specifications (BDS) (Caltrans, Bridge Design Specifications, 2003) and Seismic Design Criteria v. 1.4 (SDC) (Caltrans, Seismic Design Criteria, v. 1.4, 2006). Computer software packages

WinRECOL (TRC/Imbsen Software Systems), Xtract (TRC/Imbsen Software Systems) and Conspan (Bentley Systems, Inc., 2008) were used to aid in the design. A design of the column, cap beam, girder dapped end and slab for the prototype was performed and discussed below. The prototype bridge drawings are given in Appendix A, and the prototype bridge calculations are provided in Appendix B.

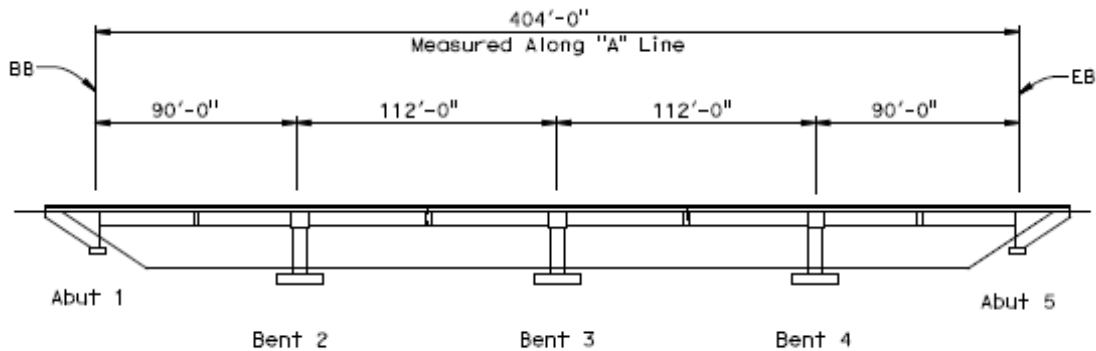


Figure 3.1 Prototype Bridge Elevation View

### 3.2 Model Concept

The test unit was developed based on a 50% dimensional scale of the prototype structure, which represented a typical inverted-T bridge. The specifics regarding the design of both the prototype and the test unit are outlined in Appendix B and in (Thiemann, 2009). Since the behavior of the connection between the girders and the inverted-T cap beam was the main focus of this study, only one column with half of a span on each side was constructed and tested. Therefore, the test unit consisted of a single column with an inverted-T cap beam and a superstructure of five I-girders overlaid with a deck on each side. In order to test both the “as-built connection” as well as the proposed “improved connection” without building two test units, one side of the inverted-T cap beam was constructed using the as-built details while the other was constructed using the improved connection details for the girder-to-cap region. This was possible as the majority of the negative moment contribution was provided through the deck (Hastak, Mirmiran, Miller, Shah, & Castrodale, 2003), which meant that regardless of the type of positive moment connection incorporated, both sides would behave identically when subjected to a negative moment. As a result, based on whether the superstructure of the test unit was pushed or pulled horizontally, it was possible to isolate the effects of the behavior of only one of the

connection types. Given the orientation of the test unit within the lab at UCSD, the South side represented the as-built condition while the North represented the behavior of the improved connection, as shown in Figure 3.2.

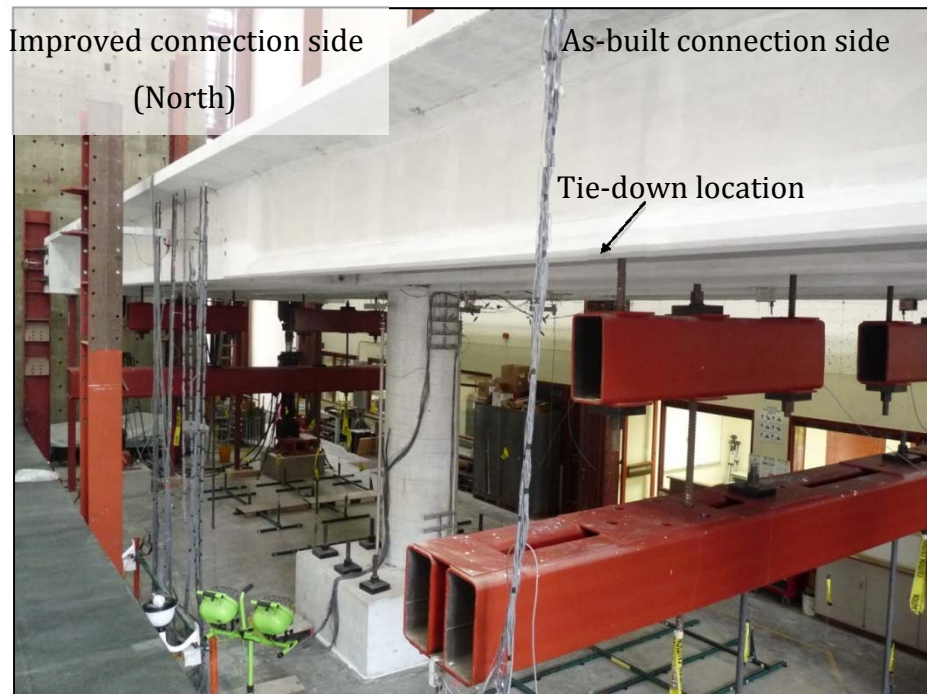


Figure 3.2: Test Unit Orientation

It was decided that two phases of testing would be necessary in order to fully capture the behavior of each connection detail and their influence on the overall behavior of the test unit. The first phase of testing, referred to as Phase 1, was a horizontal cyclic testing of the superstructure. Using two horizontally mounted actuators on each end of the abutment, the superstructure was cyclically pushed and pulled through the following series of increasing system displacement ductility levels,  $\mu_{\Delta}$ , until the specimen reached a maximum displacement ductility of 10. The nature of the test was quasi-static, which meant that the cycles were performed over a very long duration relative to that of a real earthquake. However, cycling the structure at various displacement levels ensured that the test unit was subjected to the same, if not greater, displacement demands than expected from an actual earthquake. The second phase of testing, referred to as Phase 2, isolated the local performance of each connection region. Vertical actuators were used to simultaneously cycle each span of the superstructure up and

down. This allowed the individual local response of each connection detail to be captured at various displacement levels until the ultimate condition was reached.

### **3.3 Test Unit Plan Details**

The prototype bridge and test unit were designed by PBS&J and independently checked by the Iowa State research team. These calculations are discussed in detail in Appendix B of this report and in (Thiemann, 2009). The design drawings developed for the test unit by PBS&J are reproduced in Figures 3.3 to 3.9.

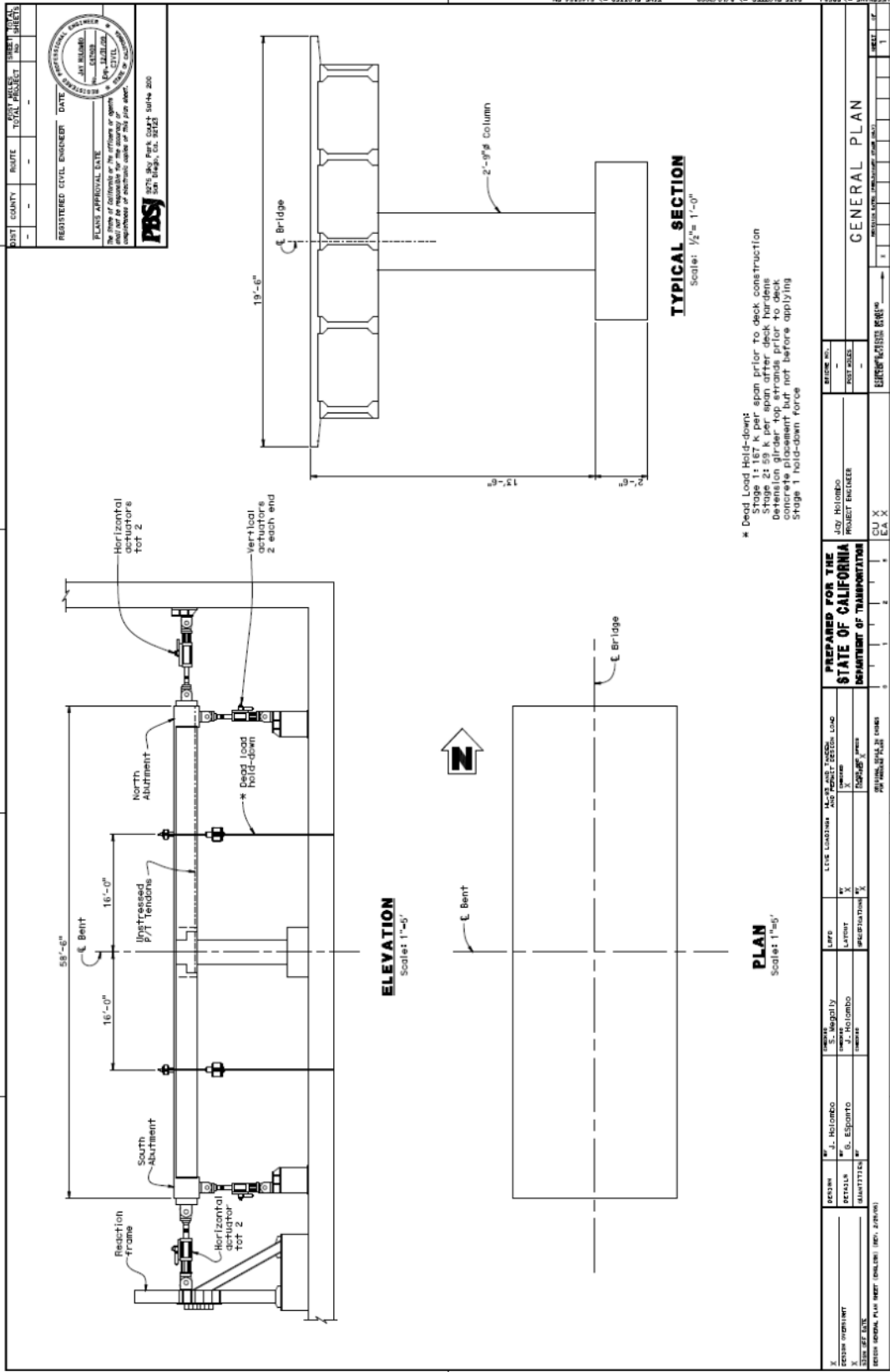
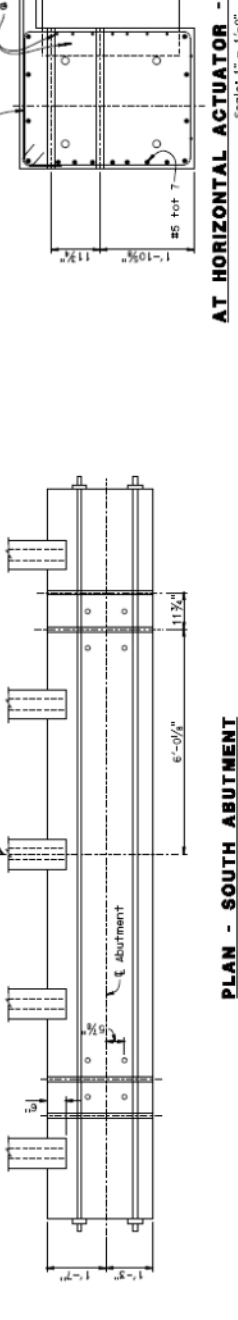
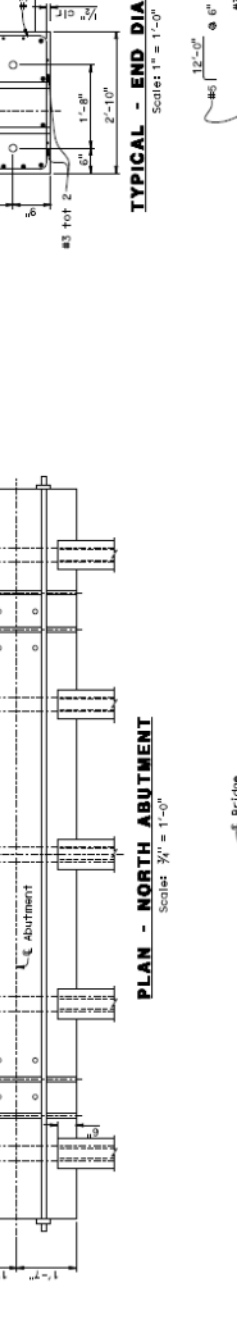
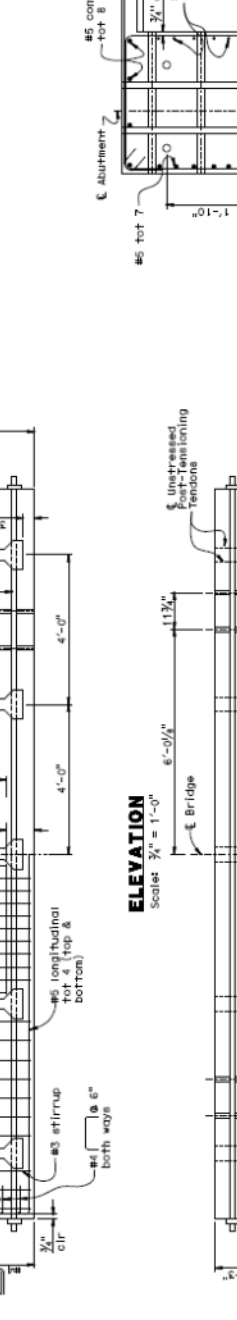
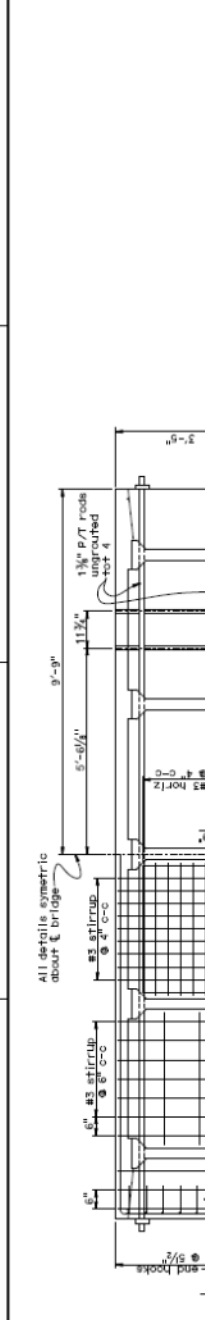


Figure 3.3: General Plan

DIST	COUNTY	ROUTE	POST MILE	TOTAL PROJECT	SHEET NO.	TOTAL SHEETS
-	-	-	-	-	-	-

REGISTERED CIVIL ENGINEER DATE \_\_\_\_\_  
 JAY HILGEMAN  
 CIVIL ENGINEER  
 No. 10000  
 State of California  
 The State of California, by the authority of which this plan is approved, hereby certifies that the undersigned is a duly licensed and qualified civil engineer and is duly qualified to perform the duties and obligations of such position.

**PBS** 3000 100th Ave. Suite 200  
 San Diego, CA 92126-3400



**AT HORIZONTAL ACTUATOR - END DIAPHRAGM**  
 Scale: 1" = 1'-0"

**TYPICAL - END DIAPHRAGM**  
 Scale: 1" = 1'-0"

**AT HORIZONTAL ACTUATOR - END DIAPHRAGM**  
 Scale: 1" = 1'-0"

**PLAN - NORTH ABUTMENT**  
 Scale: 3/4" = 1'-0"

**PLAN - SOUTH ABUTMENT**  
 Scale: 3/4" = 1'-0"

DESIGNER	DATE	PROJECT	NO.
J. Hilgeman	8/10/2008	Structural	1

PREPARED FOR THE  
**STATE OF CALIFORNIA**  
 DEPARTMENT OF TRANSPORTATION

DESIGNED BY: J. Hilgeman  
 CHECKED BY: S. Espinoza  
 DATE: 8/10/08

PROJECT ENGINEER  
 JAY HILGEMAN  
 CIVIL ENGINEER

FILE: \\s:\Structural\Invent\Hilgeman\Project\1-2008\1-2008.dwg

DATE PLOTTED	TIME PLOTTED	SCALE
8/10/2008	8:54:15 PM	1" = 1'-0"

Figure 3.4: Abutment Details



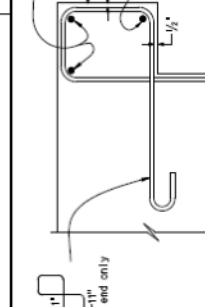
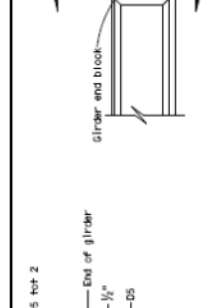
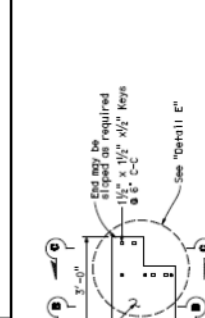




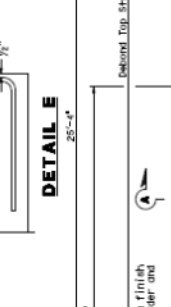
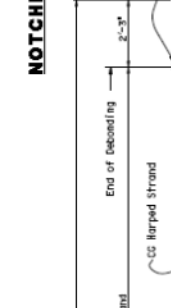
CITY	COUNTY	ROUTE	COST	TOTAL	SHEET	TOTAL

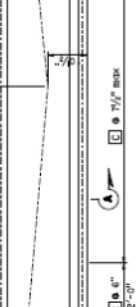
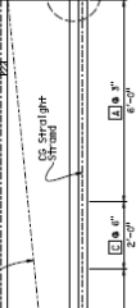
REGISTERED CIVIL ENGINEER	DATE	RESERVED
PLATE APPROVAL DATE		
THE SEAL OF A REGISTERED CIVIL ENGINEER OR ARCHITECT IS THE PROPERTY OF THE STATE OF CALIFORNIA AND IS NOT TO BE REPRODUCED OR USED IN ANY MANNER WITHOUT THE WRITTEN PERMISSION OF THE BOARD OF PROFESSIONAL ENGINEERS AND ARCHITECTS.		



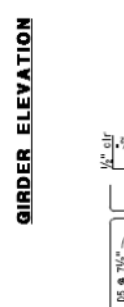
**PRESTRESSING NOTES**  
 Concrete strength:  $f'_{ci} = 5.5 \text{ ksi}$  at time of initial stressing,  
 $f'_{cs} = 7.0 \text{ ksi}$  at 28 days, min.  
 $F_{peak} = 282 \text{ kips}$  (total jacking force)



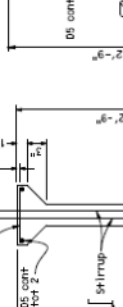
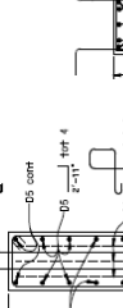
**PRESTRESSING NOTES**  
 Concrete strength:  $f'_{ci} = 5.5 \text{ ksi}$  at time of initial stressing,  
 $f'_{cs} = 7.0 \text{ ksi}$  at 28 days, min.  
 $F_{peak} = 282 \text{ kips}$  (total jacking force)



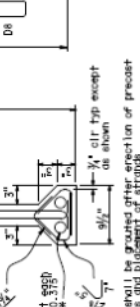
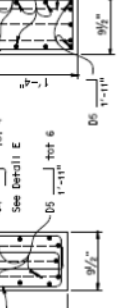
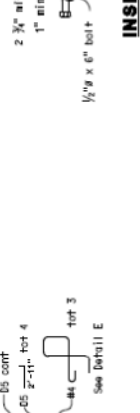
**PRESTRESSING NOTES**  
 Concrete strength:  $f'_{ci} = 5.5 \text{ ksi}$  at time of initial stressing,  
 $f'_{cs} = 7.0 \text{ ksi}$  at 28 days, min.  
 $F_{peak} = 282 \text{ kips}$  (total jacking force)



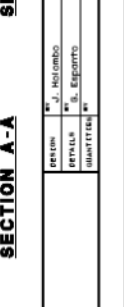
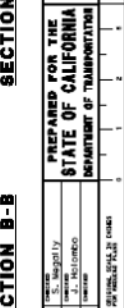
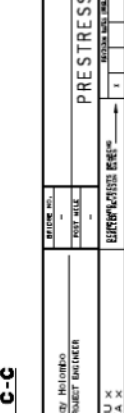
**PRESTRESSING NOTES**  
 Concrete strength:  $f'_{ci} = 5.5 \text{ ksi}$  at time of initial stressing,  
 $f'_{cs} = 7.0 \text{ ksi}$  at 28 days, min.  
 $F_{peak} = 282 \text{ kips}$  (total jacking force)



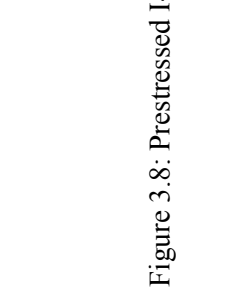
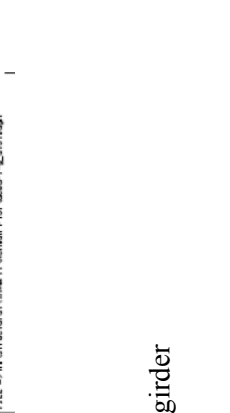
**PRESTRESSING NOTES**  
 Concrete strength:  $f'_{ci} = 5.5 \text{ ksi}$  at time of initial stressing,  
 $f'_{cs} = 7.0 \text{ ksi}$  at 28 days, min.  
 $F_{peak} = 282 \text{ kips}$  (total jacking force)



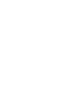
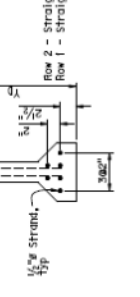
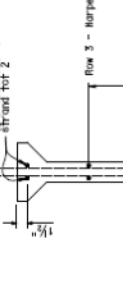
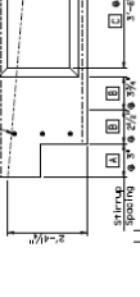
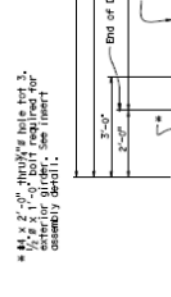
**PRESTRESSING NOTES**  
 Concrete strength:  $f'_{ci} = 5.5 \text{ ksi}$  at time of initial stressing,  
 $f'_{cs} = 7.0 \text{ ksi}$  at 28 days, min.  
 $F_{peak} = 282 \text{ kips}$  (total jacking force)



**PRESTRESSING NOTES**  
 Concrete strength:  $f'_{ci} = 5.5 \text{ ksi}$  at time of initial stressing,  
 $f'_{cs} = 7.0 \text{ ksi}$  at 28 days, min.  
 $F_{peak} = 282 \text{ kips}$  (total jacking force)



**PRESTRESSING NOTES**  
 Concrete strength:  $f'_{ci} = 5.5 \text{ ksi}$  at time of initial stressing,  
 $f'_{cs} = 7.0 \text{ ksi}$  at 28 days, min.  
 $F_{peak} = 282 \text{ kips}$  (total jacking force)





### **3.4 Improved Connection Detail**

After considering several alternative connection details that could be used to establish a fully positive moment resisting connection, it was decided that placing untensioned, bonded prestressing strands through the connection was the preferred alternative. As shown in Section B-B of Figure 3.6, four 1-3/8 in. diameter strands were placed along the length of each girder and were continued through the cap beam. The strands were then grouted in place, however they remained untensioned. This method was selected because it was relatively simple and economical to install. Additionally, since prestressing strands can develop much higher stress levels at relatively low strains, compared to Grade 60 steel, it was determined that the addition of the untensioned strands would provide enough additional tension force resistance to make the connection behave with the desired positive moment resistance. Furthermore, a finite element analysis of the connection demonstrated that adding the untensioned strands should develop a more than adequate moment capacity in order to develop a plastic hinge at the top of the column in the test unit as shown in Section 4.1 and (Thiemann, 2009).

When used in the prototype structure, these strands would run continuously along the length of each girder and through the cap from one end of the structure to the other. This, however, was not the case for the test unit. As stated previously, the test unit was detailed such that both the as-built connection and the newly proposed connection could be tested using the same test unit. In order to make that possible, the untensioned strands were terminated at the edge of the corbel on the as-built connection side; that way the untensioned strands would not alter the performance of the as-built connection.

## **Chapter 4. Analytical Evaluation**

### **4.1 Three-dimensional finite element model**

#### **4.1.1 Introduction**

This section describes the details of the finite element model developed for the prototype structure and the test unit, which included the cap beam, diaphragms, girders, slab and reinforcing bars. ABAQUS v6.8 (Dassault Systemes Simulia Corporation, 2008), a commercial finite element package, was used for the analysis. Two element types were primarily used in the development of the model: C3D8R and T3D2. The C3D8R element is the continuum three dimensional 8-noded solid element, commonly known as the “brick” element. Each of these nodes has three degrees of freedom, allowing translation in the x-, y- and z-direction. The elements do not have rotational degrees of freedom; however, this limitation can be overcome. One approach is to use the incompatible mode of the element which internally adds deformation modes that allow the element to overcome parasitic shear effects, creating a better bending behavior. Another alternative to overcome the bending problem is to discretize sufficiently over the thickness of the object to consider the effect of bending. For the model, the concept of discretizing sufficiently through the thickness of the object was used. The other element used extensively was the T3D2, which is a three dimension 2-node truss element. This element only resists forces in the axial direction, which is similar to the action of a reinforcing bar.

#### **4.1.2 Material Model**

The concrete material model was of great importance during the model development process. In ABAQUS, there are three different models that can be used for defining concrete material behavior: brittle cracking, smeared cracking and damaged plasticity. Each model has been developed for distinct purposes with many differences between them. The brittle cracking model assumes that the concrete compressive response remains linearly elastic while the tension is the cause of failure (Dassault Systemes Simulia Corporation, 2008), which is controlled by a specified tensile strength value that is user defined. The smeared cracking model was developed for use during loading in a monotonic manner with a low confining stress. This allows the concrete to experience either compressive crushing or tensile cracking. Large cracks are not

tracked in the specimen modeled. However, once the stress exceeds the cracking strength, the material stiffness is reduced to account for the softening behavior. A drawback of this model is the mesh size; a fine mesh will lead to narrow crack bands (Hillerborg, Modeer, & Petersson, 1976). Also, after compressive crushing occurred in an element, the unloading stiffness is softened when compared to the original stiffness. This is not captured by the model as the post-cracking stiffness is assumed to be constant in the model regardless of the magnitude of inelastic strain. In comparison, the tensile stiffness is reduced after cracking, but as unloading occurs, the stiffness always allows for the tensile response to exhibit no residual displacement. The stress-strain responses in compression and tension are provided in Figure 4.1 for the smeared cracking model.



a) Tensile response

b) Compressive response

Figure 4.1. Stress-strain behavior of the smeared cracking model in ABAQUS

The third model is the damaged plasticity model and is the most complex of the three models. This model is suitable for modeling a concrete member subjected to either monotonic or cyclic loading, with low confining pressures. This material model is a compilation of many attempts to create an effective model to capture the true behavior of concrete (Lee & Fenves, 1998). Originally, concrete models were developed to capture the effects of crushing and cracking with one damage variable for all the damage states (Lubliner, Oliver, Oller, & Onate, 1989). This was ineffective as the responses in each damage state are significantly different. The damaged plasticity model incorporates two damage variables, one for compression and one for tension, to model the stiffness degradation during the inelastic action of concrete. Using damage variables for each response, the concrete stiffness can accurately be modeled during

inelastic action in each state, if calibrated properly. The damage variables also allow for the stiffness to continuously undergo degradation depending on the extent of inelastic action that occurs in the member. The unconfined concrete properties are defined by providing the stresses at various elastic and inelastic strains. For the elastic portion of the concrete curve, an elastic option is defined with a Young's Modulus and a Poisson's Ratio. Once the concrete strain exceeds the elastic strain limit, the damage variables are activated and any response at higher stress incorporates the effects. The general response of the concrete is presented in Figure 4.2. The model also has the ability to incorporate the confining effects of reinforcing steel; validation of this capacity will be presented in Chapter 5. For modeling of the inverted-tee bridge, the damaged plastic model was chosen. Additional inputs such as dilation angle, eccentricity, uniaxial to biaxial stress ratio, stress variant and viscosity parameter are required to completely define the damage plasticity model of concrete. The suggested default values from ABAQUS were used and listed in Table C.1 in Appendix C. The material properties used in the model are given in Table C.2 in Appendix C.

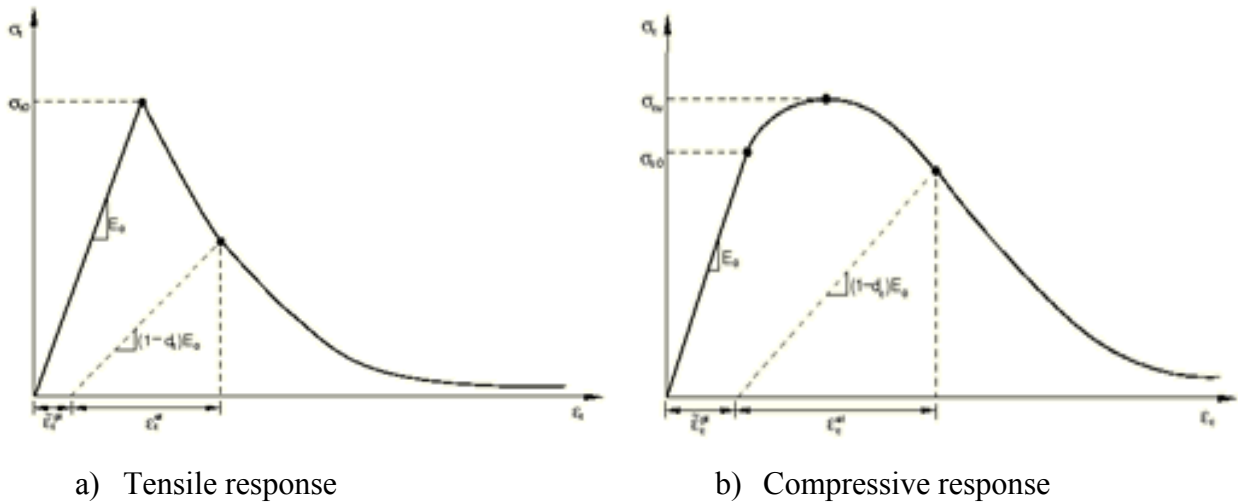


Figure 4.2. Concrete stress-strain behavior according to the Damaged Plasticity Model in ABAQUS

For the steel elements, a general elastic-plastic model was used. Both the prestressing steel and mild reinforcing steel were modeled accordingly. Similar to concrete, the elastic portion of the response was defined by providing values for Young's Modulus and Poisson's Ratio. However, for the post-yielding response, a separate plastic model was used. For the analysis, five points were defined to capture the strain hardening effect of the mild reinforcement steel. Once the material experienced a plastic strain, the original stiffness was used for unloading,

causing a residual strain at zero stress. For the prestressing, three points were defined to replicate the actual behavior including yielding and fracture. The values used for the concrete model are given in Table C.2 in Appendix C.

#### **4.1.3 Contact and Constraint Modeling**

Representing the contact between the different components in the model was an important aspect to accurately capture the moment-rotation characteristics of the cap-beam-and-girder interface model. Because the bridge under consideration had precast girders set in place, followed by embedment of reinforcing bars, multiple contact assignments and embedding commands were needed. Contact assignments were applied at the cap beam-to-diaphragm interfaces, diaphragm-to-girder interfaces, and cap beam-to-slab interfaces. Additional interactions were used for embedding the reinforcement. For the contact assignments, the surface-to-surface option was chosen with the contact properties including a friction tangential behavior and a “hard” contact normal behavior. The concrete-to-concrete friction coefficient was taken as 0.6 as specified by the ACI 318-05 code (ACI Committee 318, 2005) for concrete poured against existing components where the edges would be smooth. The value for the friction coefficient was chosen since the pieces were not expected to slide much since the pieces were held in place with reinforcing bars but to actually open and close gaps. The “hard” contact normal behavior was not expected to resist any pressure when a gap was opened, but as soon as the gap would be closed, the compressive stress would be transmitted from one surface to the other, which is illustrated in Figure 4.3. The contact between the cap beam and slab was modeled with a tie command. By using the tie command, the nodes on the edge of the deck were tied to the nodes on the edge of the cap beam intersecting the deck. In doing this, the nodes on the deck were eliminated and the nodes of the cap beam were used in replacement. Therefore, the deflections at each point on the overlapping faces of the cap beam and deck were the same. This approach was used because the reinforcement between the deck and slab were considered to be effective in not allowing the deck to slip with respect to the reinforcing bars and subsequently separate, as that was not within the scope of the project. For the all the reinforcement modeled in the analysis the embedding command was used in ABAQUS to model the interaction. The embedding ties the nodes of the embedded element to the nodes of the master element that it is embedded within. By using this method, a perfect bond is assumed between the reinforcement and surrounding concrete.

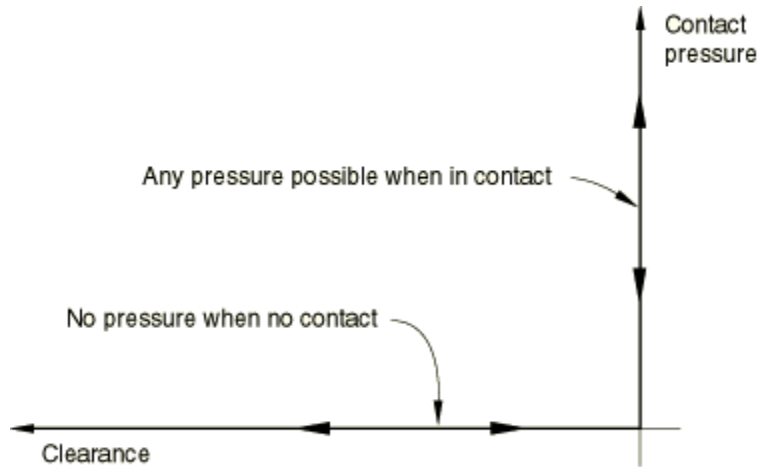


Figure 4.3. "Hard" contact behavior assumed in ABAQUS

In the new connection modeling, the unstressed strands were initially coupled to the girder, diaphragm and deck beam using the coupling command. This command is intended to use the coupled displacements of the master node, the girder, as the displacement for the slave node, the prestressing strand. At the girder ends, the strand was pinned to the girder end and was not able to displace relative to the girder. However, along the girder and at the connection interface the longitudinal direction degree-of-freedom was released to allow the strand to slip since it was initially considered to be unbonded. Another coupling command was used at the cap face where a rotational boundary condition was applied. The coupling command was needed due to the lack of rotational degrees-of-freedom within the elements of the cap beam. A reference point was used as the master node and then the cap cross-section and the portion of the deck directly above the stem of the cap were all constrained as slave nodes, seen in Figure 4.4.

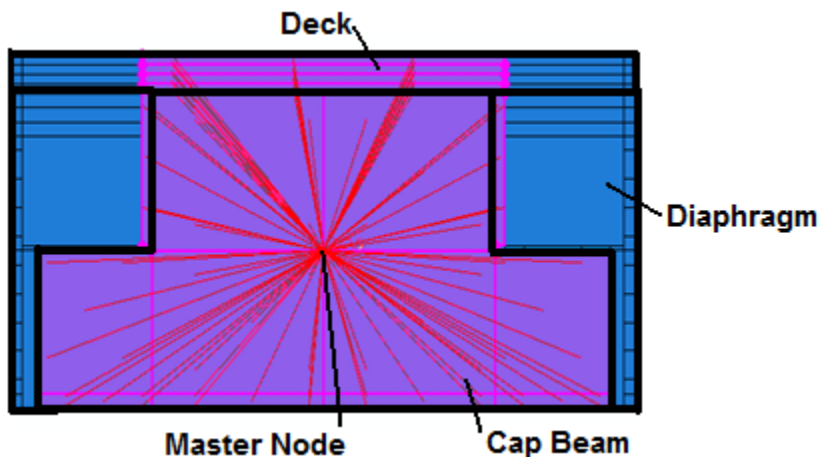


Figure 4.4. Cap Beam pivot constraint achieved through the use of the coupling command

#### **4.1.4 Boundary Conditions**

The proper boundary conditions were of significant importance to ensure that the modeling was completed as accurately as possible to the true behavior. Here, a general discussion of the boundary conditions will be presented.

For the analysis, the cap beam was pinned through the center of area of the cap beam and allowed to pivot. The girder ends were restrained with a z-symmetry boundary condition. This boundary condition allows for displacement in the transverse and longitudinal direction of the bridge but restrained movement of the girder ends in the vertical direction. The boundary condition was applied at the same height as the boundary condition on the cap beam. Also, only the girder ends were restrained, not the length of the end diaphragm.

Additionally, for the single girder model, the edges of the slab in the longitudinal direction were restrained with a z-axis symmetry condition, allowing the edges to deflect vertically and longitudinally but restraining the movement in the transverse direction. This condition was chosen since the slab has been sliced for a single-girder model. For a full bridge, the slab will not be able to freely move in the transverse direction for the middle and intermediate girders and this constraint will properly model this aspect.

Also, for the multiple girder models, the middle girder had to be restrained along the longitudinal cross-section for symmetry purposes. To do this, a z-axis symmetry condition was applied. The behavior of the boundary condition has been discussed above.

Additional boundary conditions were analyzed, but were not common to the model for every analysis and the effects will be discussed in the following chapter.

#### **4.1.5 Modeling of Components**

The modeling of different components will be discussed below and additional details will be included. The dimensions and material descriptions are provided on the structure details in Appendix A.

#### 4.1.5.1 Cap Beam

The cap beam was modeled according to the structural drawings. On the cap beam, the bearing pads were included monolithically to the ledges. However, the area of the bearing pads was modeled with a material property corresponding to the bearing materials. The rest of the cap beam was modeled with the damage plasticity model with a concrete strength of 4.5 ksi, which is the expected material strength of the concrete in the field. Figure 4.5 shows the cap beam model that was created using solid elements that were used for the modeling of the cap beam. The same element type was used for the bearing pads.

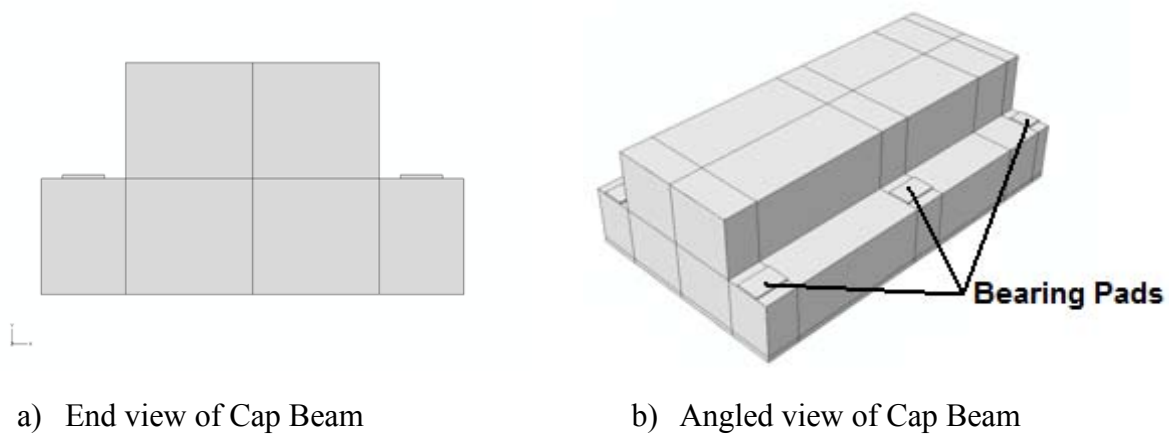


Figure 4.5. Views of modeled Cap Beam

#### 4.1.5.2 Cap Beam Diaphragm

The diaphragm is cast around the cap beam after the girders are placed, which was modeled as one piece for each side of the cap beam. A solid L-shaped piece was made using solid elements and the areas where the bearing pads and girders would be located had to be cut out of the solid piece, as seen in Figure 4.6.

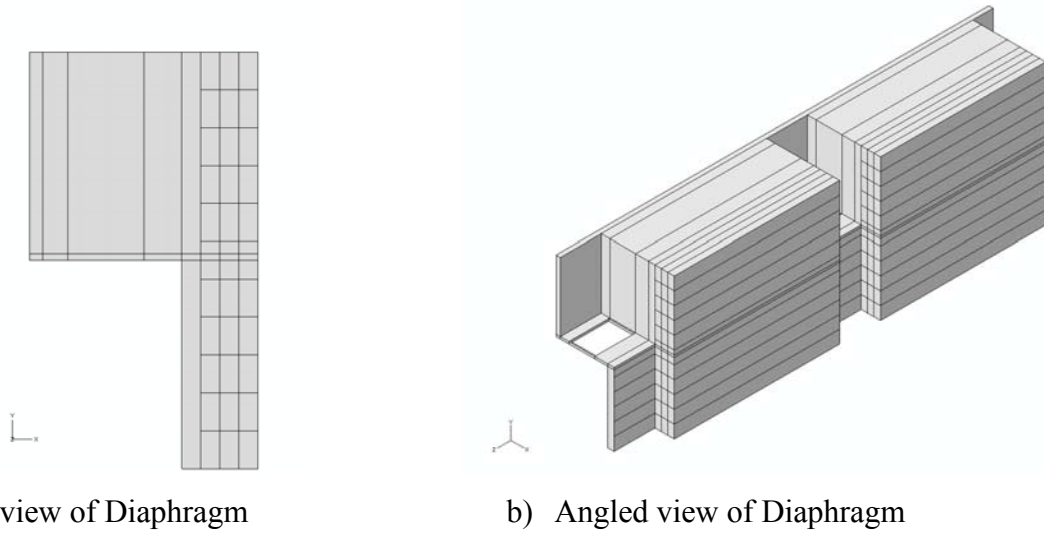
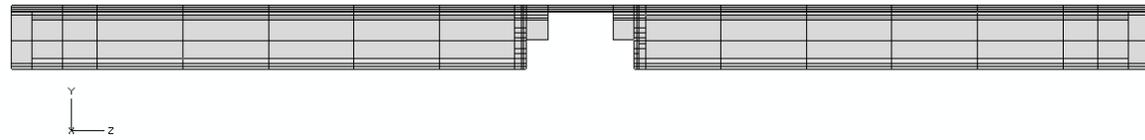


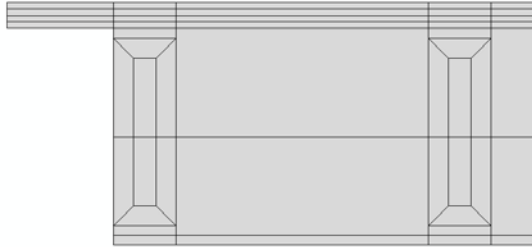
Figure 4.6. Views of modeled Diaphragm

#### 4.1.5.3 Girders and Slab

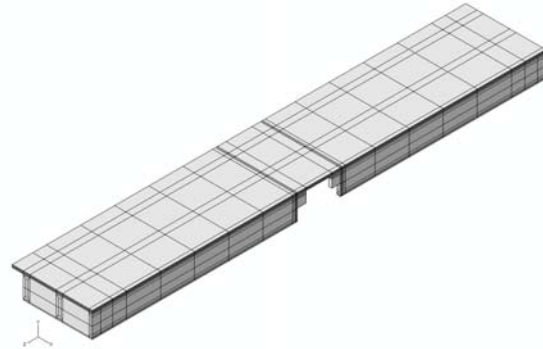
The precast girders and the in-situ slab were modeled monolithically since the interaction between the two members was not anticipated as the exposed vertical girder reinforcement was embedded into the deck. A solid, rectangular block was modeled, to be formed into the girders and deck, extending the length corresponding to the mid-span to mid-span distance. Next the outlines of the girder and slab were drawn and the remaining volume was removed from the block. Then the cap beam cross section was removed from the girders. Finally, the volume was partitioned to allow section to be meshed using solid elements. The model of the girder and slab can be seen in Figure 4.7. Similar to the cap beam and bearing pads, the slab and the girders were modeled with their respective material properties. Concrete in both of the members was modeled using the damaged plasticity model with an unconfined concrete strength of 7 ksi for girders and 4.5 ksi for the slab.



a) Side view of girders and deck



b) End view of girders and deck



c) Angled view of girders and deck

Figure 4.7. Views of the modeled girders and slab of model

#### 4.1.5.4 Reinforcing Bars and Prestressing Strands

In the test unit and prototype structure there are multiple sizes and lengths of reinforcing bars, but the modeling technique for each is the same. For the reinforcing bars, a wire part was used to draw the length of the bar. The mesh was then applied and the elements were manually switched from beam elements to truss elements. To accurately model the bar sizes, the truss section was used and the bar area size was defined along with the appropriate material property. The section was then applied to the part and the reinforcing bar was modeled. The differences in the bars were the length of the wire element and the area defined in the section module. For the prestressing strands, the truss elements were also used when the strands were embedded. The same method, as for the reinforcing bars, was followed to define the cross-section being used. The unstressed strands used in the connection were also modeled similarly; the only difference was that the wire was partitioned with breaks in the wire at each point where a coupling was being defined to allow for the prestressing strand to deform similarly to the girder.

The reinforcing bars placed transversely through the girders and cast into the diaphragms were modeled using spring elements in ABAQUS. The springs were used due to time constraints when performing an analysis with three-dimensional solid elements representing the reinforcing bars, as it caused excessive analysis times. Twenty springs were defined on each face of the girders to replace the three reinforcing bars connecting the girders to diaphragms. For the capacity of the springs, the shear capacity of the reinforcing bars was calculated and considered to not slip or allow any displacement until the capacity was reached. Once the capacity was reached, the capacity from the reinforcing bars was kept constant because the model would not converge if the value was decreased.

## **4.2 Grillage model**

### **4.2.1 Introduction**

In order to obtain a better understanding of the generalized behavior of the test unit, a grillage finite element model was developed using SAP2000. Compared to other forms of finite element modeling, a grillage model is typically viewed as being simpler to construct and, as a result, its output is generally simpler to interpret and its use in design offices is relatively frequent. However, in order to produce meaningful results, it is crucial that all elements within the model are defined as accurately as possible, in regard to both their material and behavioral properties and boundary conditions. For example, since the test unit was symmetrical about its longitudinal axis, it was determined that only half the structure needed to be modeled. However, in order to obtain accurate results, special consideration was applied to the boundary conditions along the axis of symmetry, as detailed below. Furthermore, one limitation of a grillage model is that nonlinear behavior cannot be easily included in the analysis, unless the behavior is defined and added to the model via specific nonlinear link elements at any location expected to potentially undergo a nonlinear response. Therefore, some assumptions regarding aspects of the localized behavior of the structure must be made prior to performing the analysis. Greater details regarding all of these concerns will be presented and discussed in the following sections.

### **4.2.2 Element Properties**

A grillage model is a network of frame elements, which are placed at the center of gravity of the various components of the bridge for which they represent, as shown in Figure 4.8. Therefore, the definition of the properties of each frame element was of crucial importance when

developing the model and ensuring its validity. Hence, the development of each set of frame elements and any special considerations given to the development of these elements are discussed below.

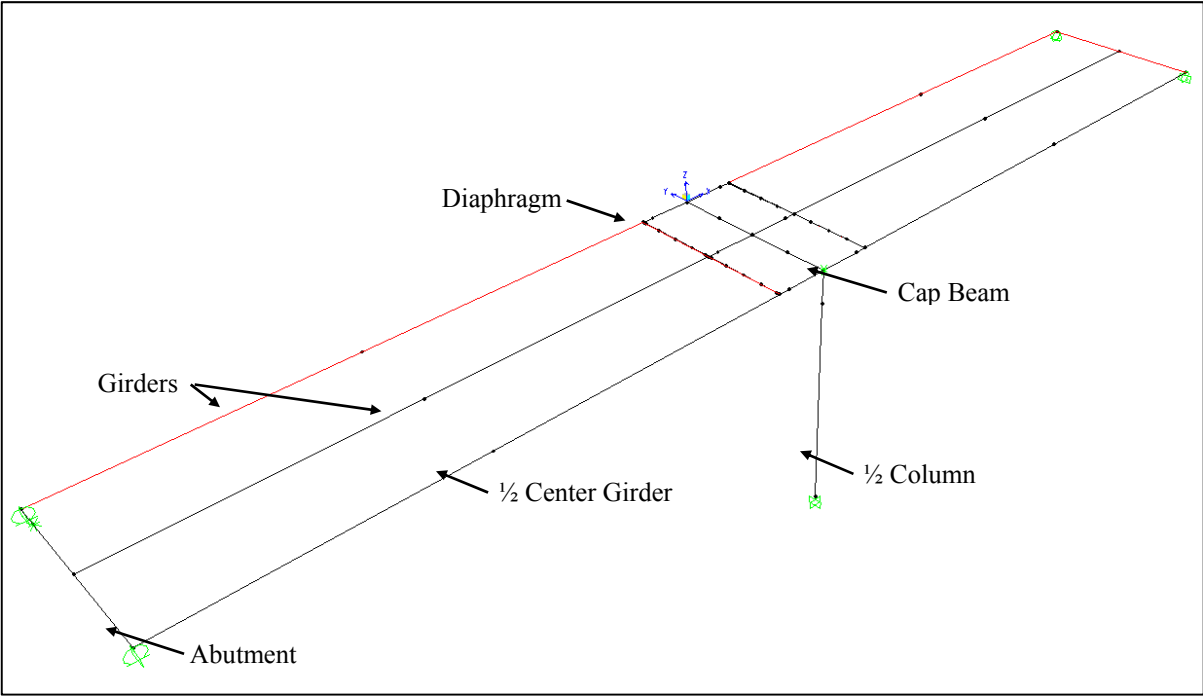


Figure 4.8: Test Unit Grillage Model

Additionally, the method of connecting each frame element to any surrounding frame elements was an important consideration. Previous experimental research involving grillage models have investigated the use of rigidly connecting the elements, using offsets, and connecting the elements directly via their respective elastic properties (Holombo, Priestley, & Seible, 1998). Based on the recommendations, it was decided that connecting the elements directly, based on their effective elastic properties, would lead to a satisfactory result. Therefore, unless otherwise noted, the frame elements were connected in that manner.

Since each member had a specific concrete strength, an isotropic concrete material model was defined using an unconfined Manders stress-strain curve within SAP for each element. The values for  $f'_c$ , modulus of elasticity, and Poisson's ratio were all required in order to define the concrete model within SAP. Since the value for  $f'_c$  was known, Equation 4.1 was used to

calculate the modulus of elasticity,  $E_c$  (Priestley, Seible, & Calvi, 1996). Poisson's ratio was conservatively assumed to be 0.2 (Wight & MacGregor, 2008).

$$E_c = 57000\sqrt{f'_c \text{ (psi)}} \quad (4.1)$$

Finally, some of the elements required property modifiers to be manually input into SAP. The modifiers were necessary when an element met the following circumstances: scaling was required to reduce the member from the prototype level to the test unit level, the element was modeled as a composite section and needed material transformation, minor cracking of the member was expected, or only a portion of a section was modeled due to symmetry. As noted, these properties were determined prior to the analysis and were input via the appropriate element scale factors within SAP.

#### 4.2.2.1 Column

The column was relatively simple to model. The cross-sectional properties of the test unit were directly input into SAP and were scaled by an appropriate 50% scaling factor in order to take into account that only half of the column was modeled due to symmetry. However, based on the moment curvature analysis that was performed on the column, an effective value was determined for the flexural moment of inertia, using Equation 5.2. As a result, an effective scale factor was derived to convert the gross moment of inertia to the effective value and was manually input into SAP. These scale factors may be found below in Table 4.1.

$$I_{eff} = \frac{M_y'}{\phi_y' E} \quad (4.2)$$

Table 4.1: Column Element Properties Used in the Grillage Model

<b>Column Element Properties</b>	
Diameter (in)	33
<i>Material Properties</i>	
$f_c'$ (ksi)	5.042
E (ksi)	4047
<i>Sap Property Modifiers</i>	
Cross-section (Axial) Area	0.5
Shear Area in 2 Direction (Vertical Local Axis)	0.5
Shear Area in 3 Direction (Transverse Local Axis)	0.5
Torsional Constant	0.5
Moment of Inertia about 2 Axis (Vertical Local Axis)	0.1895
Moment of Inertia about 3 Axis (Transverse Local Axis)	0.1895
Mass	0.5
Weight	0.5

The height of the column was 10 ft.-4 in., however it needed to extend to the centerline of the inverted-T cap beam. Therefore, an additional frame element, that was 19 in. in length, was added to the top of the column and connected to the centerline of the cap beam. However, an end offset was applied over its entire length so that its mass and stiffness would not be counted twice within the overlap of the cap beam.

#### 4.2.2.2 Girders

Since SAP has built-in definitions for standard Caltrans girder shapes, only limited information needed to be input for the girder frame elements as well. The 1676 mm I-girder shape was selected and its cross-sectional dimensions were all scaled from the prototype dimension level and manually altered in SAP to match the test unit dimension level. Since the girders were modeled as a composite section, which included the haunch directly above the top flange of the girder, it was necessary to further modify the section properties in order to account for the transformed composite section. As mentioned previously, this was accomplished by altering the scale factors within SAP. The thickness of the haunch was also included in the alteration of the overall height dimension of the girder. This was required in order to achieve the

proper neutral axis height for the composite behavior between the girder and deck element, which is discussed later.

Additionally, based on similar experimental research that was conducted in the past, it was assumed that the superstructure would likely experience some degree of cracking (Holombo, Priestley, & Seible, 1998). As a result, the stiffness of the girders was reduced in order to take into account the weakening in stiffness that would likely be expected due to the cracking. An effective-cracked girder stiffness was determined based on a moment curvature analysis, which was performed for the composite girder and deck section. Two effective stiffness values were obtained based on whether the section was subjected to a positive or negative moment. The appropriate stiffness factor, given the corresponding loading direction, was then input into the model, as indicated in Tables 4.2 and 4.3. It should be noted that this sequence had to be performed separately for both the North and South superstructure spans, as the reinforcement details were different, due to the presence of the untensioned strands used in the improved connection, which ran along the length of the girders on the North side of the bent cap. Furthermore, positive bending was defined as the case in which the bottom flange of the girder was in tension. Through a simplified model of a single cantilevered girder, it was discovered that the same forces would be achieved regardless of whether a gross effective stiffness or a series of decreasing stiffness values were applied along the length of the beam. Therefore, the gross reduction in effective stiffness was applied over the entire length of the girder.

Table 4.2: Grillage Model Girder Properties

<b>Girder Properties</b>	
<i>Material Properties</i>	
$f_c$ (ksi)	8.94
E (ksi)	5389
<i>SAP Property Modifiers</i>	
Cross-section Area	0.980
Shear Area in 2 Direction (Vertical Local Axis)	0.980
Shear Area in 3 Direction (Transverse Local Axis)	0.980
Torsional Constant	1
Moment of Inertia about Axis 2 (Vertical Local Axis)	0.958
Moment of Inertia about Axis 3 (Transverse Local Axis) [Gross]	0.953
Moment of Inertia about Axis 3 (Transverse Local Axis) [+ Moment North Girder]	0.285
Moment of Inertia about Axis 3 (Transverse Local Axis) [- Moment North Girder]	0.643
Moment of Inertia about Axis 3 (Transverse Local Axis) [+ Moment South Girder]	0.25
Moment of Inertia about Axis 3 (Transverse Local Axis) [- Moment South Girder]	0.636
Mass*	1.003
Weight**	1.003
* Between the cap and diaphragm, a modifier of 0.0001 was used in order to prevent the mass from being accounted for twice within the cap region	
** Between the cap and diaphragm, a modifier of 0 was used in order to prevent the weight from being accounted for twice within the cap region	

Table 4.3: Grillage Model Center Girder Properties

<b>Center Girder Properties</b>	
<i>Material Properties</i>	
$f'_c$ (ksi)	8.94
E (ksi)	5389
<i>SAP Property Modifiers</i>	
Cross-section Area	0.490
Shear Area in 2 Direction (Vertical Local Axis)	0.490
Shear Area in 3 Direction (Transverse Local Axis)	0.490
Torsional Constant	0.5
Moment of Inertia about Axis 2 (Vertical Local Axis)	0.479
Moment of Inertia about Axis 3 (Transverse Local Axis) [Gross]	0.477
Moment of Inertia about Axis 3 (Transverse Local Axis) [+ Bending North Girder]	0.1425
Moment of Inertia about Axis 3 (Transverse Local Axis) [- Bending North Girder]	0.322
Moment of Inertia about Axis 3 (Transverse Local Axis) [+ Bending South Girder]	0.125
Moment of Inertia about Axis 3 (Transverse Local Axis) [- Bending South Girder]	0.318
Mass*	0.501
Weight**	0.501
* Between the cap and diaphragm, a modifier of 0.0001 was used in order to prevent the weight from being accounted for twice within the cap region	
** Between the cap and diaphragm, a modifier of 0 was used in order to prevent the weight from being accounted for twice within the cap region	

Since the girders extended from the centerline of the cap to the centerline of the abutment, end offsets were applied to both ends in order to prevent the overlapping stiffness and mass from being accounted for twice within the analysis. Additionally, since half the structure

was modeled about its centerline, only half of the center girder was modeled, as reflected by its SAP property modifiers being defined as half of what was used for the other girders.

#### 4.2.2.3 Cap Beam

The cap beam was modeled as a composite rectangular section that included the inverted-T as well as the deck and portions of the diaphragms within the cross-sectional span of the inverted-T, as shown in Figure 4.9. Therefore, it was necessary to transform the section, so that all sections had the same effective  $f'_c$  as the bent cap, which was 5.27 ksi, when calculating the effective cross-sectional properties. Additionally, since the girders extended to the centerline of the cap, and the cap was modeled as a solid rectangular section, it was necessary to apply end offsets to the ends of the girders in order to prevent their stiffness from being included twice within the model.

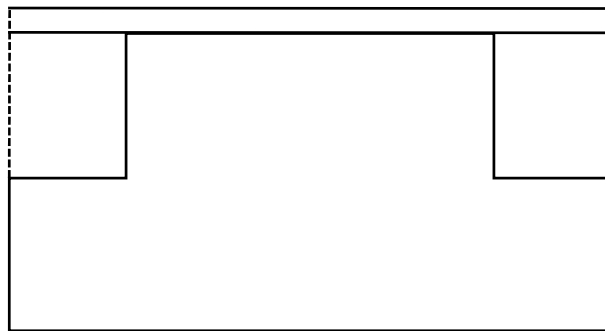


Figure 4.9: Cap Beam Composite Cross Section

It was determined that the cap beam would likely experience some torsional cracking during testing, which will be discussed in the nonlinear element section of the following text. As a result, it was necessary to include nonlinear link elements along the length of the cap beam in order to capture the axial rotations associated with the torsional cracking. However, in order to prevent the elastic rotation of the cap from artificially increasing the rotation that was specified within the nonlinear link elements that were placed along the length of the cap beam, a modifier was input into SAP to make the cap torsionally rigid, as shown in Table 4.4

Table 4.4: Grillage Model Cap Beam Properties

<b>Cap Element Properties</b>	
Depth (in.)	38
Width (in.)	60
<i>Material Properties</i>	
$f'_c$ (ksi)	5.27
$E_c$ (ksi)	4138
<i>SAP Property Modifiers</i>	
Cross-section Area	1
Shear Area in 2 Direction (Vertical Local Axis)	1
Shear Area in 3 Direction (Transverse Local Axis)	1
Torsional Constant	1.0E+10
Moment of Inertia about Axis 2 (Vertical Local Axis)	1.002
Moment of Inertia about Axis 3 (Transverse Local Axis)	0.994
Mass	1
Weight	1

#### 4.2.2.4 Diaphragm

Even though the cap beam and diaphragms would normally be treated and modeled as a monolithic section, it was necessary to create separate elements for the vertical portion of the diaphragm in order to provide a transverse member at the location of the cap-to-diaphragm reinforcement; the transverse member was used to accommodate the nonlinear link elements that were used to model the slip behavior of the hooked reinforcement between the cap and the diaphragm. However, since two elements were required and each were used to model the diaphragm, it was necessary to reduce the properties of each element by 50%, in order to prevent the effects of the diaphragm from being doubled within the model. Furthermore, since a partial pour of the diaphragm was completed prior to the final pour of the deck and diaphragm, it was necessary to transform the section properties to a uniform concrete strength. The two elements were each modeled with a rectangular cross-section, which represented only the vertical portion of the diaphragm located beyond the corbel of the inverted-T cap beam, as well as the portion of the deck directly above this section of the diaphragm. Each element was placed as close to one

another as possible within the model and the two were connected by the nonlinear link elements representing the diaphragm reinforcement, to be discussed later. Finally, since any elastic effects of their behavior were captured within the nonlinear link elements representing both the diaphragm reinforcement and the girder-to-diaphragm connection, it was necessary to make each diaphragm element torsionally rigid. The properties used for each diaphragm element are listed below, in Table 4.5.

Table 4.5: Grillage Model Cap Diaphragm Element Properties

<b>Cap Diaphragm Properties</b>	
Depth (in.)	38
Width (in.)	6
<i>Material Properties</i>	
$f'_c$ (ksi)	5.36
$E_c$ (ksi)	4208
<i>SAP Property Modifiers</i>	
Cross-section Area	0.488
Shear Area in 2 Direction (Vertical Local Axis)	0.488
Shear Area in 3 Direction (Transverse Local Axis)	0.488
Torsional Constant	1.0E+10
Moment of Inertia about Axis 2 (Vertical Local Axis)	0.488
Moment of Inertia about Axis 3 (Transverse Local Axis)	0.489
Mass	0.5
Weight	0.5

#### 4.2.2.5 Deck

Initially, the deck was modeled using a series of transverse frame elements. The deck was divided into sections and each element represented its respective section. In this configuration, the girders were also modeled as a composite section, based on an effective width as specified in AASHTO.

However, based on the results of the analyses of the superstructure that were performed in ABAQUS (see Section 4.1) it was determined that the aforementioned method did not

adequately include the membrane or strut action of the deck. Therefore, the slab was modeled using an area element, as shown in Figure 4.10, and the girders were modeled as a non-composite section as described above. The area deck element improved the results, as it was able to more accurately incorporate the membrane and diaphragm action of the deck. Additionally, it was simpler to model, and relied on fewer assumptions, than the initial method. Using the area deck also provided better output data as it made it possible to obtain and visualize stress and strain data within the deck.

As mentioned when discussing the properties used to model the girders (see Section 4.2.2.2), the stiffness of the superstructure was reduced in order to reflect expected cracking. Based on the moment curvature analysis of the composite girder and deck section, it was determined that the deck would crack completely at the condition for which the effective stiffness of the superstructure was calculated, during the case of negative bending. Therefore, the axial stiffness and dominant membrane stiffness were both removed from the area element, as noted in Table 4.6. The deck remained effective for the case of positive bending, and thus, the aforementioned factors were not removed for that case.

Table 4.6: Grillage Model Deck Area Element Properties

<b>Deck Area Properties</b>	
Membrane Thickness (in.)	3.75
Bending Thickness (in.)	3.75
<i>Material Properties</i>	
$f'_c$ (ksi)	5.28
$E_c$ (ksi)	3605
<i>SAP Property Modifiers</i>	
Membrane f11 (Stiffness about Longitudinal Local Axis) [- Bending]	0
Bending m22 (Stiffness about Longitudinal Local Axis) [- Bending]	0

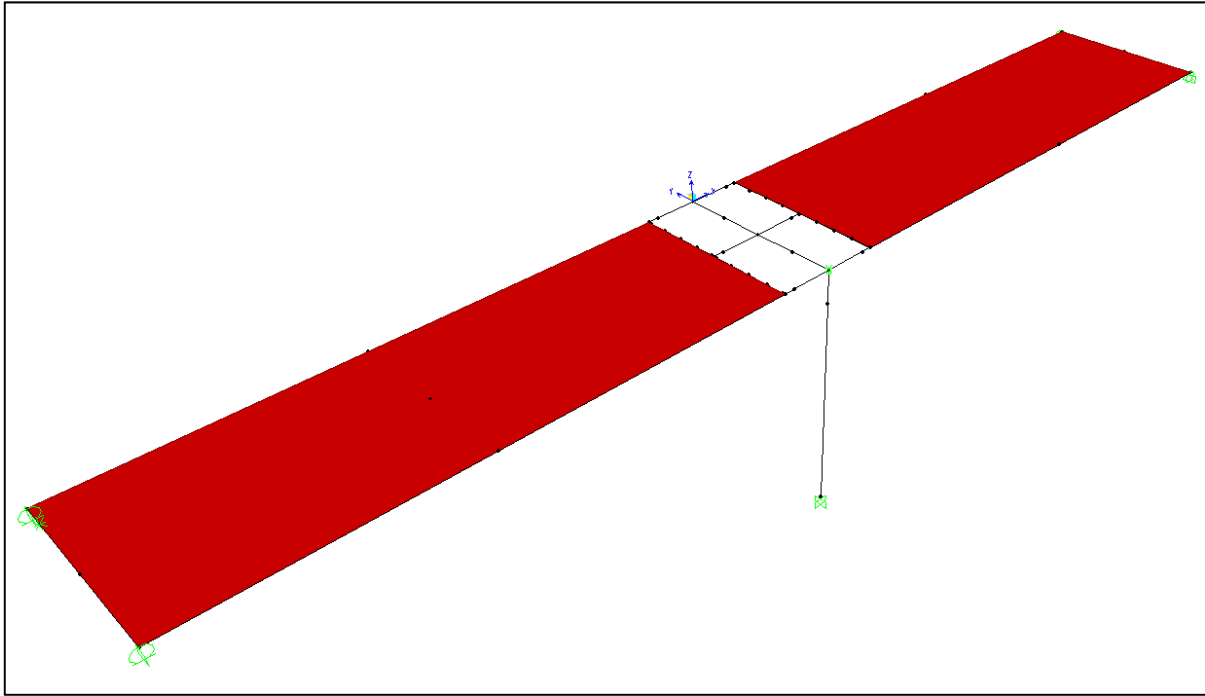


Figure 4.10: Grillage Model after Adding the Area Deck Elements

The properties in Table 4.6 were input into SAP when defining the area deck element. A thick shell element was specified for the area element as it included the desired membrane and bending action and had a tendency to be more accurate, and was thus recommended over the other types of area elements within SAP (Computers and Structures, Inc., 2008). Since the definition of all nonlinear link elements within the cap beam and the connection region included the stiffness contribution from the deck, in order to prevent the stiffness of the deck element from being accounted twice within the analysis, the deck was not allowed to span over the nonlinear link elements. Therefore, two area elements were used to model the deck. One element was used on each side of the cap that extended from the centerline of the abutment to the centerline of the section of diaphragm that was furthest from the cap. In order to still ensure an adequate diaphragm action of the deck within the cap beam region, where the discontinuity of the area element occurred, the cap beam was modeled as a composite cap beam consisting of the dapped ends of the girders, deck, and bent cap. The overhang portion of the deck was also not included in the modeling of the deck. Instead, the dead load of the overhang was calculated and equally distributed between each girder. A representative dead load was then applied to each girder in order to account for the dead load effects of the overhang portion of the deck. The

grillage model was constructed in that manner as it more accurately represented what was done during the design of the test unit structure and would thus provide a means to validate the model. Furthermore, it was assumed that the overhang had little effect on any slab action or the overall behavior of the structure.

Finally, though the deck elements were placed at the centerline of the girder elements, they had to be offset in order to capture the composite action between the girders and the deck. Therefore, the nodes at each corner of the deck elements were offset from the center of the deck by a distance of 19 in., which corresponded to the distance required to make the bottom side of the deck come into contact with the top of the haunch above the girder element, as shown in Figure 4.11.

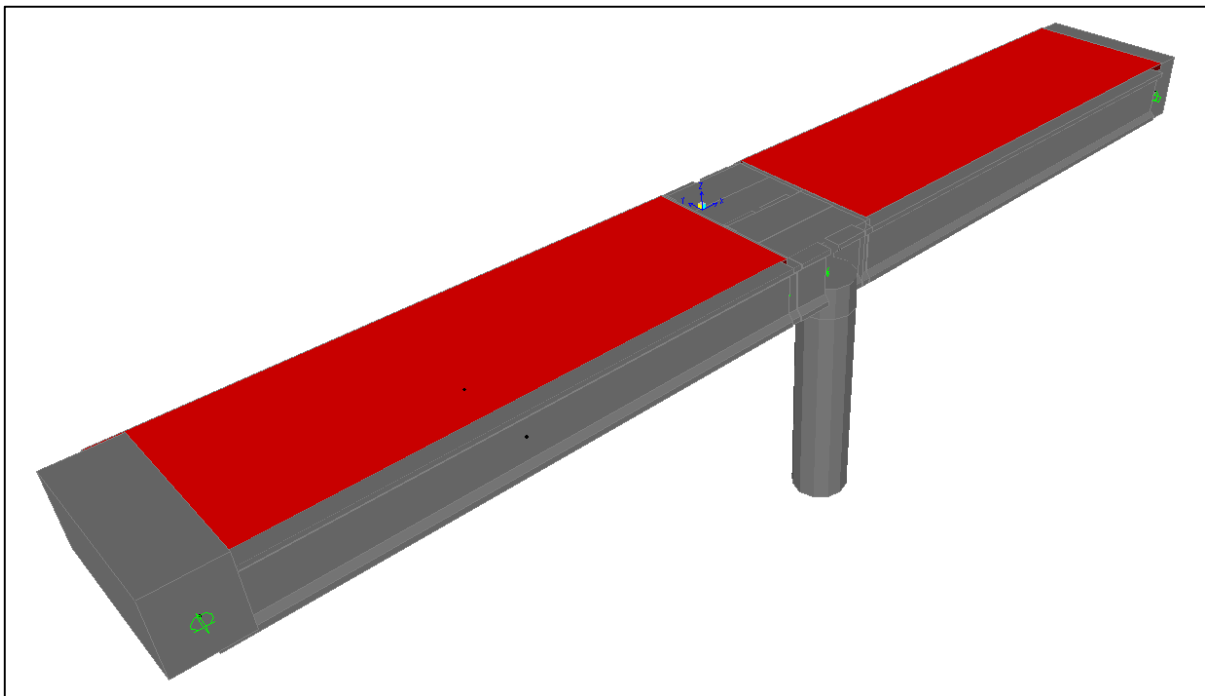


Figure 4.11: Extruded Grillage Model Deck Offset

#### 4.2.2.6 *Abutments*

The abutments were modeled as a simple rectangular cross-section on each end of the span, which included the abutment as well as the composite portion of the deck. As mentioned,

end offsets were used on the portion of the girder within the abutment in order to prevent its mass and stiffness from being accounted twice within the abutment region.

Table 4.7: Grillage Model Abutment Element Properties

<b>Abutment Properties</b>	
Depth (in.)	41
Width (in.)	34
<i>Material Properties</i>	
$f'_c$ (ksi) North End	5.49
$E_c$ (ksi) North End	4223
$f'_c$ (ksi) South End	5.59
$E_c$ (ksi) South End	4262

### 4.2.3 Boundary Conditions

All of the degrees of freedom at the base of the column were restrained as it was designed and performed during testing as a fixed base. The ends of the girders at the abutment were placed on rollers as the superstructure was allowed to translate only in the longitudinal direction. Finally, since only half of the structure was modeled about the longitudinal axis, it was necessary to restrain any transverse displacement as well as any rotation about both the longitudinal, X, and vertical, Z, axes of the superstructure.

### 4.2.4 Nonlinear Elements

The frame elements used in SAP2000, which represented the components of the test unit discussed in Section 4.2, were designed to experience only elastic deformation. Therefore, in order to perform a nonlinear analysis for a structure that was modeled with frame elements, the locations of nonlinearity needed to be determined prior to the analysis and modeled through the placement of user-defined nonlinear link elements. The following nonlinear link elements were defined and placed within the grillage model.

#### 4.2.4.1 Column Plastic Hinges

Since the column was designed to form a plastic hinge at both the top and bottom of the column, it was necessary to include a nonlinear link element, which represented the hinges, at the top and bottom of the column, as shown in Figure 5.12. A moment-curvature analysis of both

the top and bottom of the column was performed using a program developed at Iowa State University, known as VSAT (Levings, 2009). The data from the moment-curvature analysis was then converted to a moment-rotation response using Equation 5.3, which accounts for rotation due to both strain penetration and plastic deformation within the hinge. It should be noted that the rotation due to elastic deformation was taken into account via the elastic frame element used to model the column. The term  $L'_{sp}$  represents the length that the elastic effects of strain penetration extend into either the cap or the footing, depending on the location of the hinge being analyzed. The term  $L_p$  represents the plastic hinge length and includes the length of the plastic effects of strain penetration as well as the length representing the plastic region of the column, as the maximum curvature over this region was assumed to be constant. The terms  $\Phi_e$  and  $\Phi_p$  represent the elastic and plastic curvature components, respectively. The terms  $f_y$ ,  $d_b$ , and  $L$  represent the yield stress of the longitudinal reinforcement, the bar diameter of the longitudinal reinforcement, and the total length of the column, respectively.

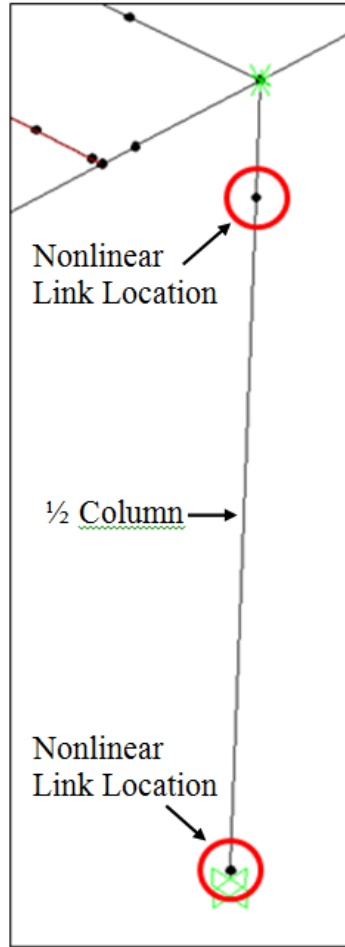


Figure 4.12: Grillage Model Column Nonlinear Link Locations

Therefore, per Priestley, Seible, & Calvi (1996), the total rotation within the column plastic hinge region,  $\theta$ , was defined as:

$$\theta = L'_{sp} \phi_e + L_p \phi_p \quad (4.3)$$

$$L'_{sp} = \frac{2}{3}(0.15)f_y d_b \quad (4.4)$$

$$L_p = 0.08L + 0.15f_y d_b \leq 0.3f_y d_b \quad (4.5)$$

The moment-rotation response input was then directly input into the properties for the nonlinear link element and placed at the top and bottom of the column. The moment-rotation properties that were input into SAP for the nonlinear link elements representing the plastic

hinges are shown below in Figures 4.13 and 4.14. It is important to note that the moment values obtained from the moment-curvature analysis were halved before being input into SAP, as only half of the column was modeled due to symmetry. Also, the responses for both the top and bottom plastic hinges were essentially the same, with the bottom hinge being a little stiffer due to a slightly higher axial load from the self-weight of the column.

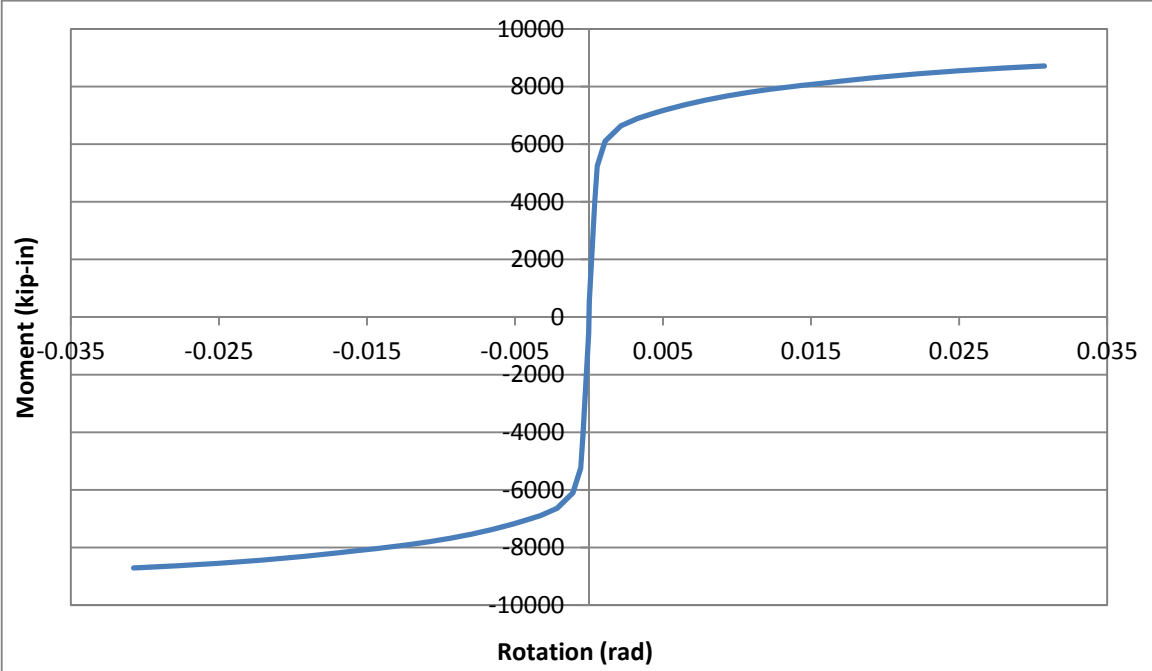


Figure 4.13: Predicted Top of Column Plastic Hinge Moment vs. Rotation Monotonic Response

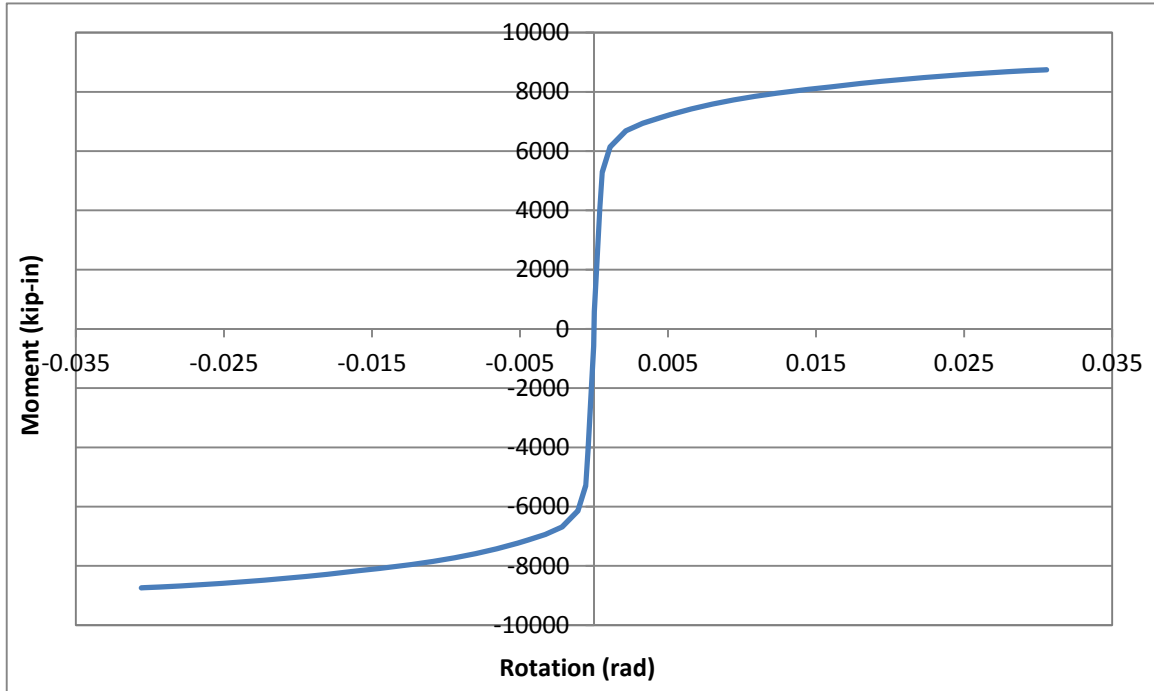
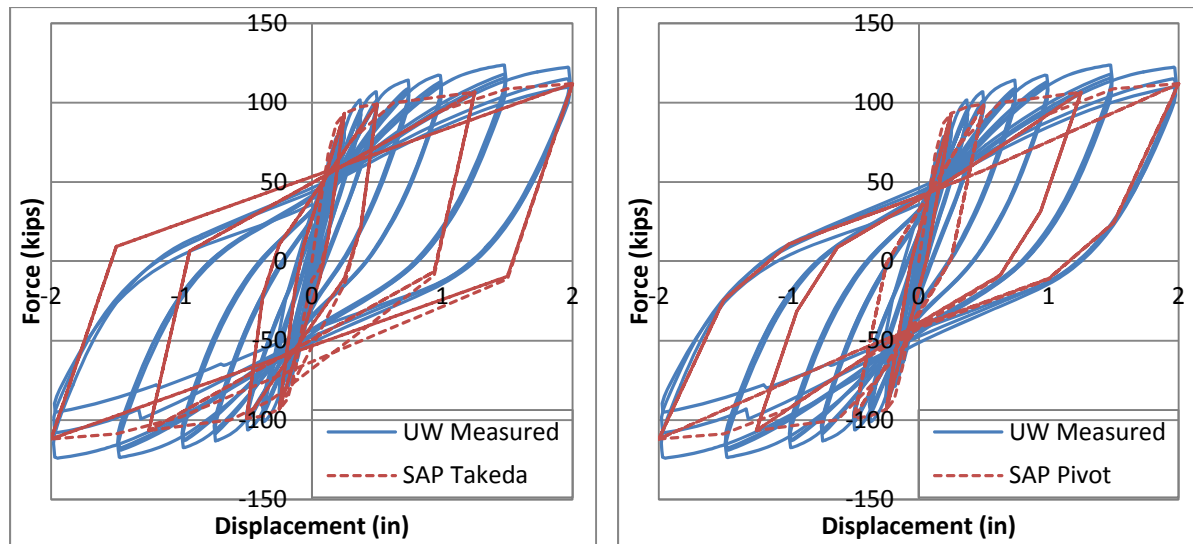


Figure 4.14: Predicted Bottom of Column Plastic Hinge Moment vs. Rotation Monotonic Response

Hysteretic rules were also defined for the nonlinear link element within SAP2000, which provided three possible built-in hysteretic models: Kinematic, Takeda, and Pivot. Since the Takeda and Pivot models are the most widely used for reinforced concrete columns, they were selected as the two primary models of consideration. In order to decide between the Takeda and Pivot models, a comparative analysis was performed based on the results of various column tests provided by the University of Washington column database (University of Washington, 2004). Based on the results of said comparison, specifically column Vu NH3, it was shown that the Pivot model was able to most accurately model the overall hysteretic behavior of the comparison column, as shown in Figure 4.15. Furthermore, the Takeda model defined within SAP2000 did not allow the user to modify its rules, whereas the user was able to define more rules when using the Pivot model, providing a more specific set of rules applicable to the column being analyzed. Therefore, the Pivot model was selected to define the hysteretic behavior of the column nonlinear link elements.



(a) Takeda Hysteresis

(b) Pivot Hysteresis

Figure 4.15: Force-Displacement Hysteresis Comparison

In order to define the Pivot model for both the top and bottom nonlinear link elements, the values for  $\alpha_1$ ,  $\alpha_2$ ,  $\beta_1$ ,  $\beta_2$ , and  $\eta$  had to be defined and input into the SAP2000 hysteretic model. The values  $\alpha_1$  and  $\alpha_2$  were used to define the location of the pivot point used to determine the unloading stiffness when removing the load from a positive and negative moment value, respectively. For the sake of comparison, it was arbitrarily assumed that these values would be approximately the same. The values  $\beta_1$  and  $\beta_2$  were used to define the pinching points that the moment-rotation response would pass through when reversing the moment toward the positive and negative direction, respectively. Again, it was arbitrarily assumed that these values would be approximately equal. It is important to note however, that when defining the moment-rotation response within SAP2000, both the first positive and negative moment-rotation values should correspond to the yield condition. This was done because SAP2000 defines the pinching points at a moment value corresponding to  $\beta F_y$ , in which the program assumed that the first point entered after the origin was used to define yield. The value  $\eta$  was used to define the amount of elastic, or initial, strength degradation experienced after any plastic deformation (Computers and Structures, Inc., 2008), (Dowell, Seible, & Wilson, 1998). The values for  $\alpha$  and  $\beta$  were defined using the charts shown in Figure 4.16 (a) and (b) respectively, which were based on the longitudinal reinforcement ratio and the axial load ratio experienced by the given column

(Dowell, Seible, & Wilson, 1998). The longitudinal reinforcement ratio,  $\rho_l$ , and the axial load ratio, ALR, were calculated using Equation 4.6 and 4.7, respectively, where  $A_{sl}$  represents the area of longitudinal steel,  $A_g$  represents the gross area of the column, and  $f'_c$  represents the concrete compressive strength. The value for  $\eta$  was taken as 8 in order to reflect an arbitrarily assumed amount of elastic strength degradation, to be used solely as a basis for comparison.

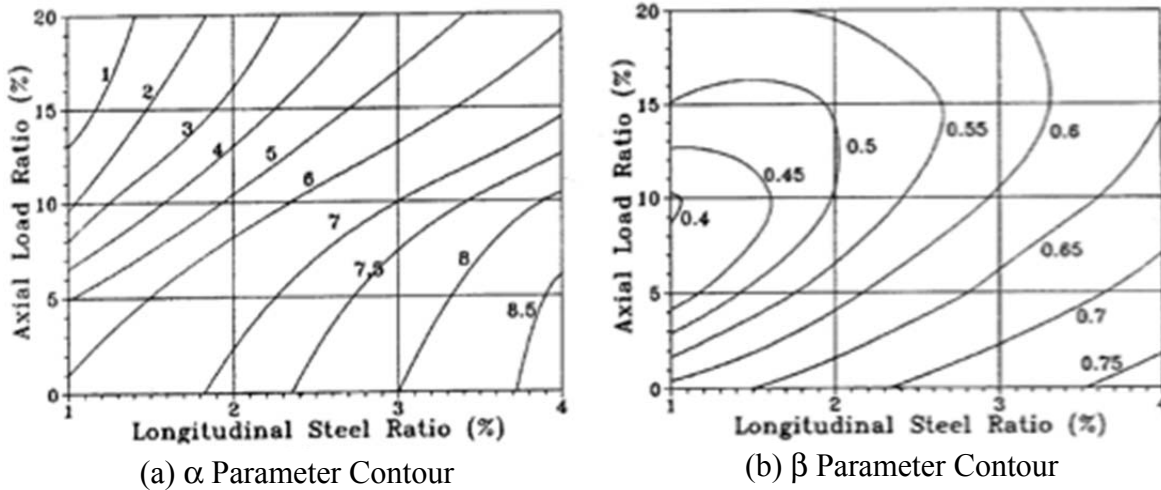


Figure 4.16: Pivot Hysteresis Parameters (Dowell et. al., 1998)

$$\rho_l = \frac{A_{sl}}{A_g} \quad (4.6)$$

$$ALR = \frac{P}{f'_c A_g} \quad (4.7)$$

#### 4.2.4.2 Cap Torsion

Though relatively little is still known regarding the prediction of the torsional behavior of reinforced concrete, it was important to at least consider the effects of torsion on the cap beam in the analysis. The overall capacity of the cap beam was initially checked using a friction model (Priestley, Seible, & Calvi, 1996) in order to ensure that no additional reinforcement or prestressing needed to be added to the cap beam. This was accomplished using Equations 2.12-2.15 and by assuming that the cap beam acted as a composite section with the deck and diaphragm and that a less conservative yield stress was required for friction to develop after any

dowel action. The friction model indicated that the cap beam would have a torsional capacity that was greater than the demand as indicated by PBS&J in their design calculations.

Once it was determined that the cap beam had an adequate capacity, it was then necessary to predict whether any cracking would develop during the testing. Since the majority of a section's resistance to torsion lies along its exterior surface, a hollow tube analogy may be adopted in order to calculate the cracking torque,  $T_{cr}$ , for the given section (Rahal K. N., 2000). Again, assuming that the cap beam acted as a composite section with the surrounding deck and diaphragm, Equation 2.1 was used to calculate the cracking torque of the section. Accordingly, a cracking torque,  $T_{cr}$ , equal to 559 k-ft was predicted. Based on both a preliminary SAP2000 analysis and the ABAQUS analysis (Thiemann, 2009), it was observed that the torsion within the cap beam would likely exceed the calculated  $T_{cr}$  value. Therefore, it was necessary to develop a nonlinear link element to more accurately model the behavior of the inverted-T cap beam.

As previously stated, there is relatively little information regarding the torsion behavior of reinforced concrete members. As a result, it was decided that a bi-linear response curve, based on parameters for which there is a substantial amount of behavioral information, would be adequate in predicting a generalized behavior. An iterative procedure, as outlined in Chapter 2 and based on Equations 2.2-2.11, was used to calculate the angle of twist given the cracking torque, as well as the angle of twist and torque expected at the ultimate condition (Collins & Mitchell, 1991). The amount of rotation was calculated by multiplying the angle of twist by the length of the cap beam between nonlinear link elements,  $L$ , as shown in Equation 4.8. Given the expected torsional behavior at the cracking and ultimate limit states, the following bi-linear torque-twist response curve was developed, as shown in Figure 4.17.

$$\theta = \psi L \quad (5.8)$$

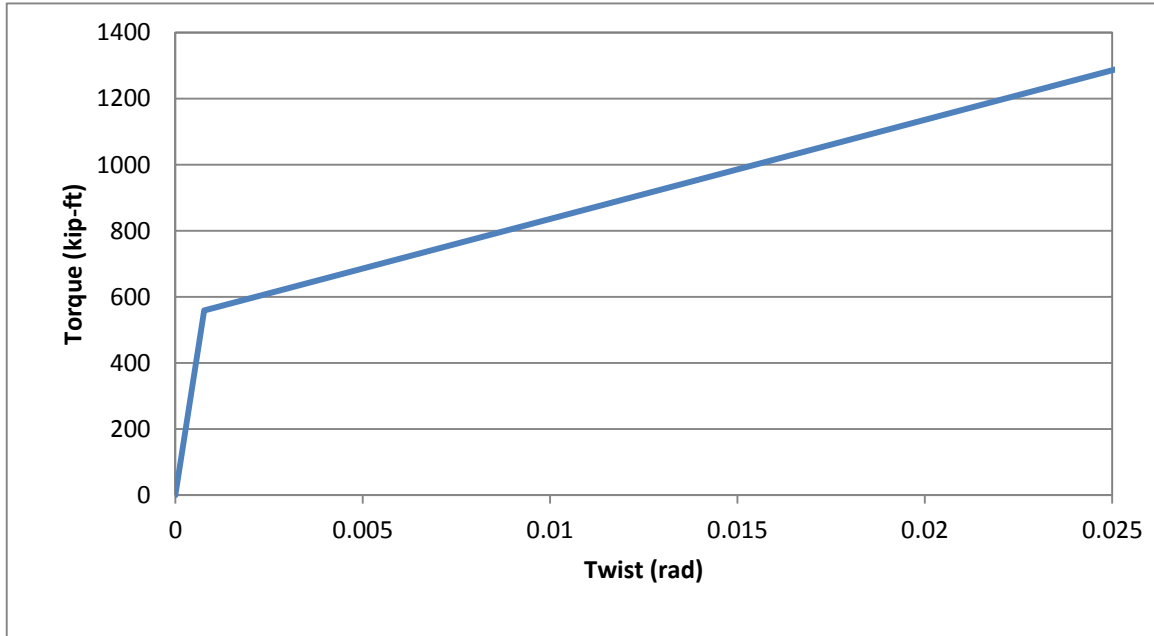


Figure 4.17: Predicted Inverted-T Cap Beam Torque-Twist Response

One nonlinear link element was placed at the midpoint along the cap beam between each girder, as shown in Figure 4.18. It is also important to note that the elastic torsional stiffness of the cap beam was made rigid in order to prevent the elastic portion of the response from being accounted twice within the analysis, thereby resulting in an increased amount of twist for a given torque.

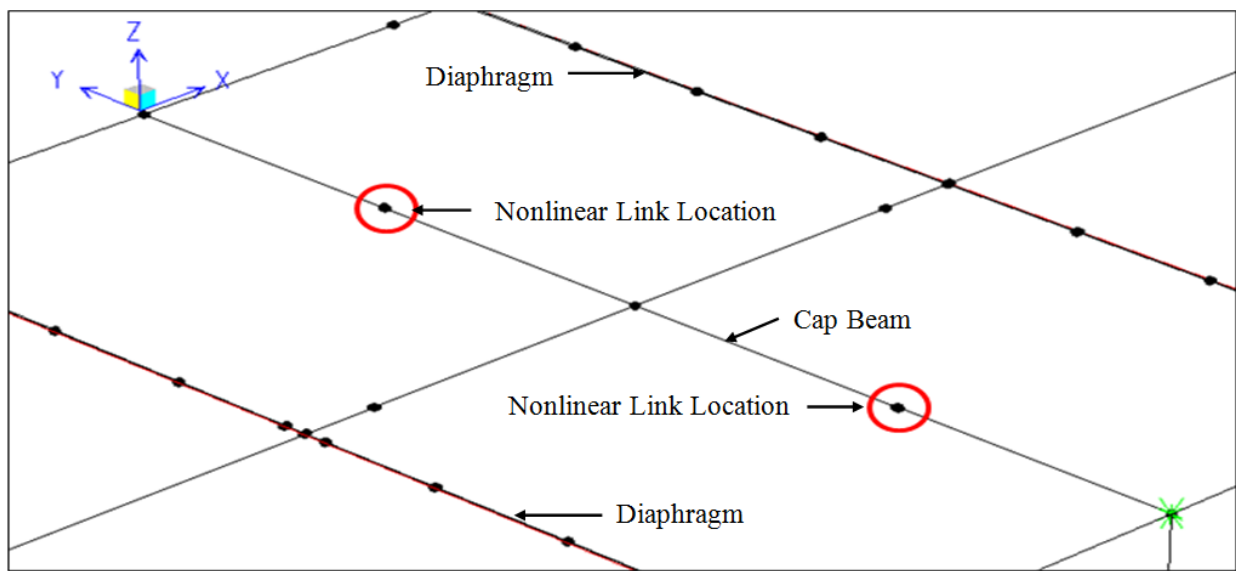


Figure 4.18: Grillage Model Cap Torsion Nonlinear Link Element Locations

#### 4.2.4.3 *Girder-to-Cap Connection*

The girder-to-cap connection was one of the most important areas of the model as it was the focus of the research. The procedure that was used in the development of the nonlinear link element that was used for the connection was presented in “3-D finite element analysis of the girder-to-cap beam connection of an inverted-T cap beam designed for seismic loadings” (Thiemann, 2009). This procedure was used, in combination with the results from the ABAQUS finite element analysis of the connection, to develop a moment vs. rotation response for each girder within the connection region, as shown in Figure 4.19. The response took into account the shear-friction interaction between the girder and diaphragm, the dowel action between the girder and the diaphragm, and the resistance of the hooked reinforcement that extended from the cap into the diaphragm, as shown in Figure 3.6. The properties that were derived based on the aforementioned procedure were input into SAP and a link was placed at the location of the connection along each girder element and was connected to the closest diaphragm element, as shown in Figure 4.20. It is important to note that the defined moment values were halved when defining the links that were used on both the exterior and center girders. This was done because these locations only had half the amount of dowels between the girder and diaphragm as well as half the number of hooks between the cap and diaphragm. It should further be noted that this was only true for the center girder as half of it was modeled due to symmetry; had the entire structure been modeled, the moment values for the center girder would not have been halved. For more information regarding the development of the nonlinear girder-to-cap connection properties, refer to Thiemann (2009).

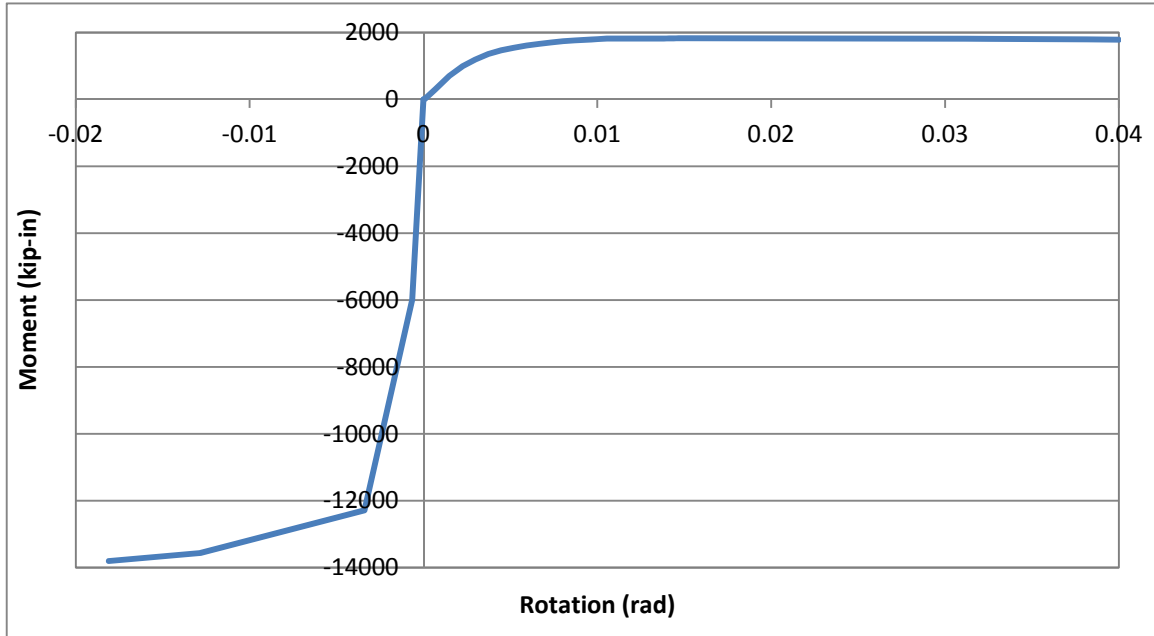


Figure 4.19: Girder-to-Cap Connection Intermediate Girder Moment-Rotation Response

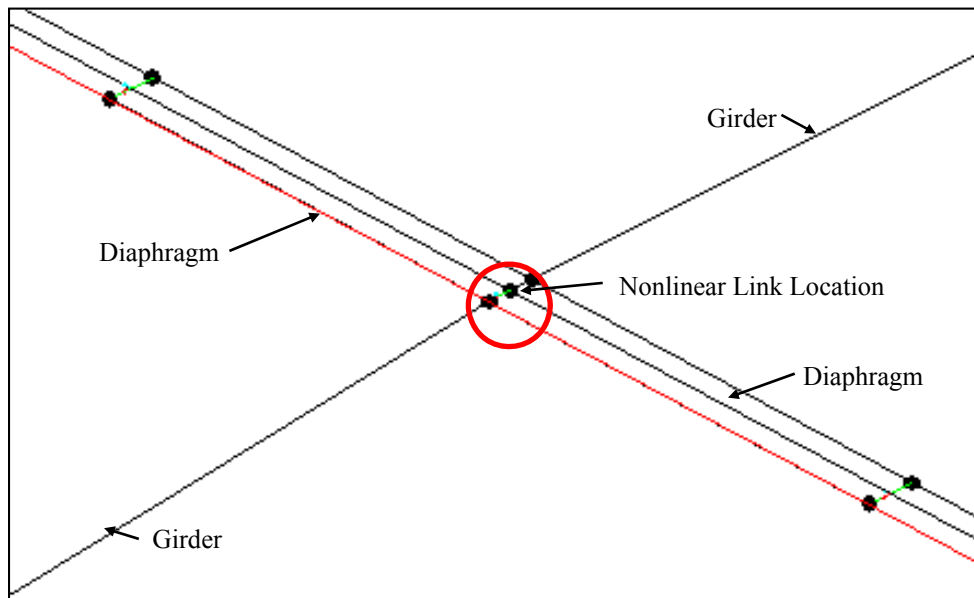


Figure 4.20: Grillage Model Girder-to-Cap Nonlinear Link Location

#### 4.2.4.4 Cap-to-Diaphragm Reinforcement

Though the contribution of the hooked reinforcement between the cap and diaphragm was taken into account in the girder-to-cap connection nonlinear link element, the strain-penetration and resulting slip behavior had to be considered in order to achieve a more accurate response. Therefore, a bi-linear moment vs. rotation response curve was developed using

Equation 2.16 for the stress-slip behavior of reinforcement embedded in concrete at yield using recommendations from Zhao and Sritharan (2007).

The amount of slip experienced at the ultimate limit state was assumed to be approximately equal to 35 times the value of the slip at yield (Zhao & Sritharan, 2007). It is important to note that the calculated slip values were doubled, as the reinforcement would be expected to slip on both sides of the cap-to-diaphragm interface, through both the diaphragm and the cap beam due to anchorage on either side of the diaphragm-to-cap interface. Once the slip values were obtained, the angle of rotation was calculated using simple trigonometry and by assuming that any cracking in the connection would occur in a linear manner to an estimated neutral axis depth,  $y_{N.A.}$ , that was obtained from the ABAQUS finite element analysis (see Section 4.1) as shown in Equation 5.9. Since this nonlinear link element was in series with the nonlinear link element representing the girder-to-cap connection, it was necessary to define the corresponding moment values in the cap-to-diaphragm link based on the moment experienced in the girder-to-cap link so as not to over- or under-estimate the amount of additional rotation experienced in the connection due to slip. In other words, the moment at the yield condition was defined based on the overall moment observed within connection, per the ABAQUS finite element analysis in Section 4.1. It was assumed that the steel reinforcement within the connection would all yield at approximately the same time. Therefore, the idealized yield moment was defined as the moment at which the majority of the reinforcement within the connection had yielded, as shown in Figure 4.21. Since the ABAQUS finite element analysis was not continued to a true representation of the ultimate condition within the connection, an increase of 30% over the yield moment was used to approximate the ultimate moment within the connection. Since no slip should be expected when the connection experienced a negative moment, it was necessary to define the negative response as a rigid behavior. This allowed all of the negative moment from the girder-to-cap link to be transferred across the connection without influencing its rotation. Figure 4.22 depicts the bi-linear curve that was input into SAP2000.

$$\theta = \tan^{-1}\left(\frac{slip}{y_{N.A.}}\right) \quad (4.9)$$

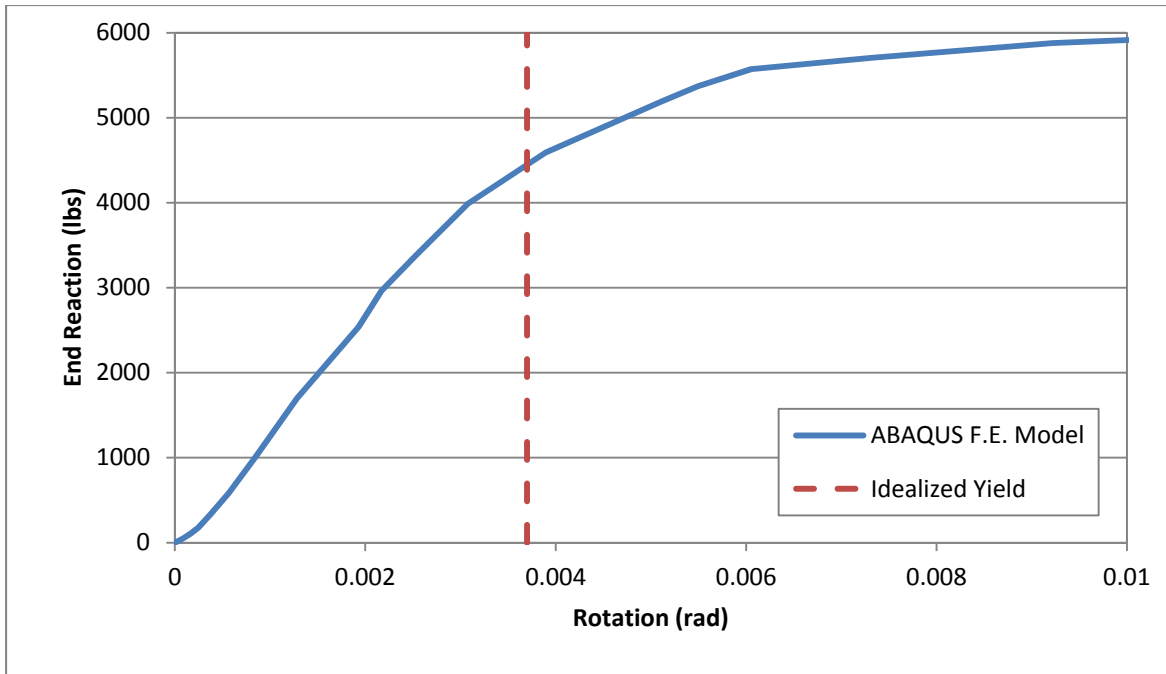


Figure 4.21: Idealized Yield Moment Derivation

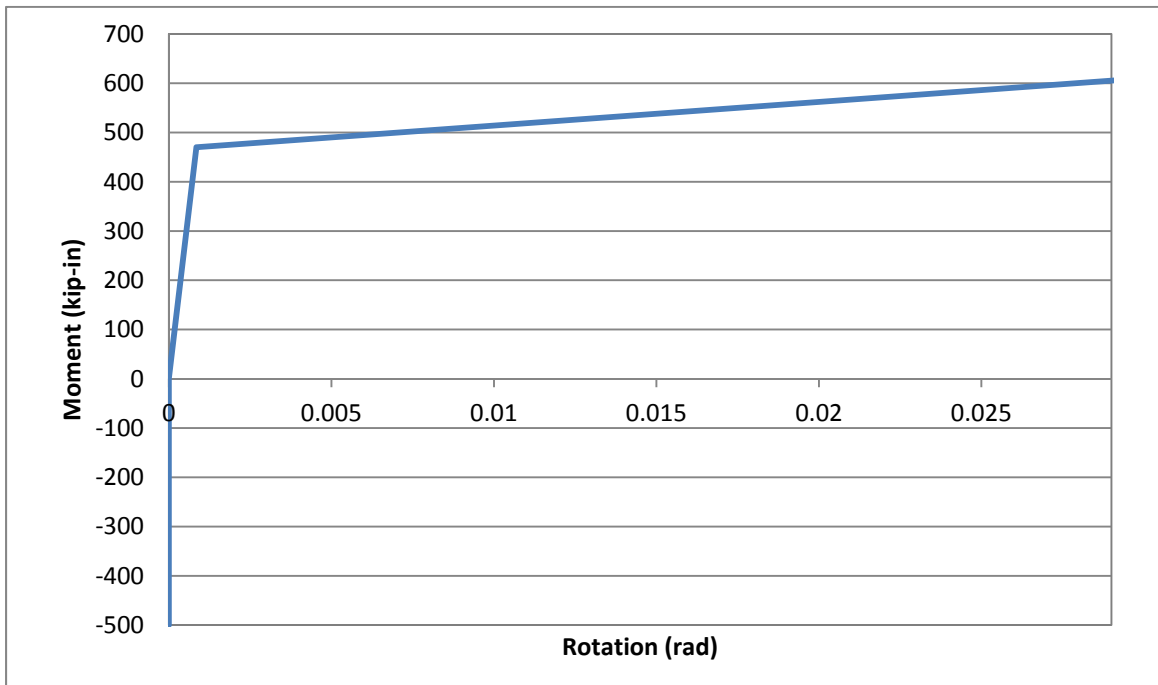


Figure 4.22: Moment vs. Rotation Slip Response of the Cap-to-Diaphragm Reinforcement

The effect that the slip had on the cap-to-diaphragm reinforcement was to increase the amount of rotation experienced at a given moment value. Therefore, as stated earlier, in order to

increase the rotation experienced in the model, without affecting the moment capacity of the connection region, the slip link elements were placed in series with the aforementioned girder-to-cap link element, as shown in Figure 4.23.

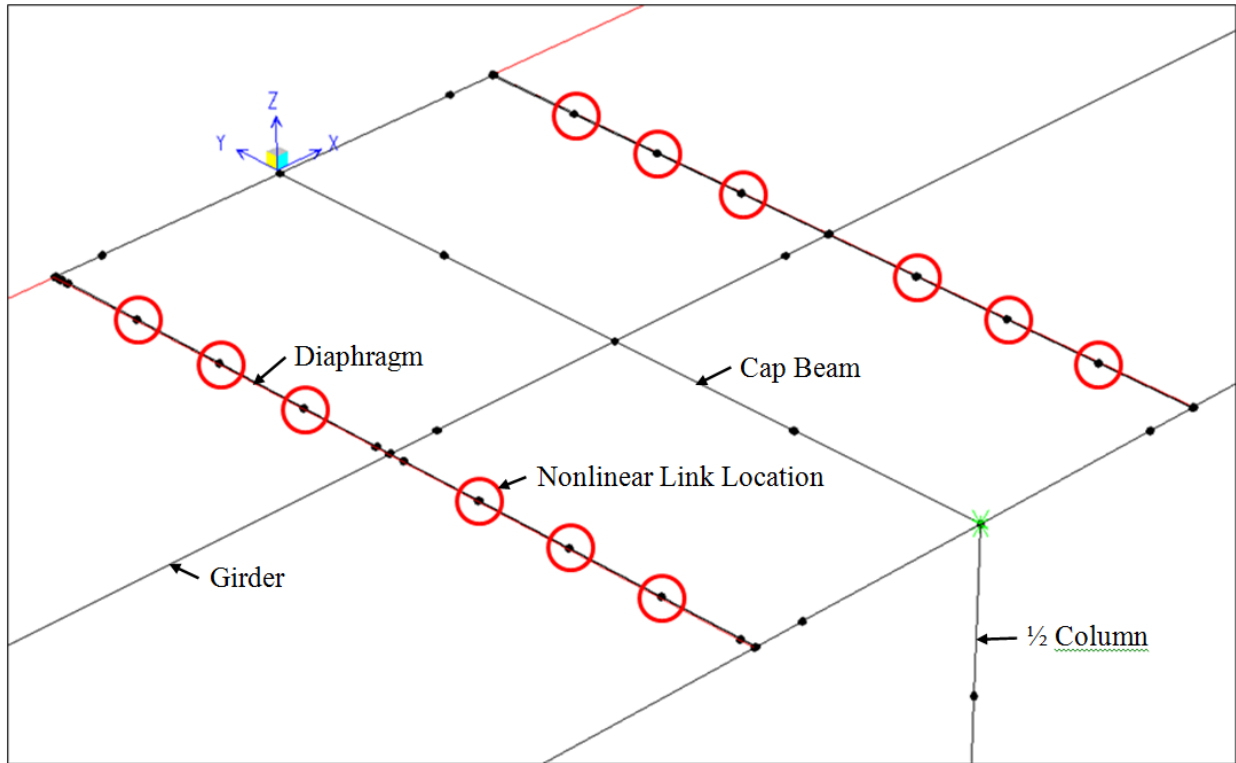


Figure 4.23: Locations of Grillage Model Nonlinear Link Elements Used to Model Cap-to-Diaphragm Reinforcement

#### 4.2.4.5 Improved Connection

The proposed improvement to the positive moment connection, which consisted of unstressed strands grouted in place between the girders and inverted-T cap beam, also had to be included as a source of nonlinearity within the model. The behavior of this connection was developed using a similar procedure to that of the slip experienced by the cap-to-diaphragm reinforcement as outlined in Section 4.4.4. The moment values at the yield and ultimate stress in the unstressed strands were calculated based on the equivalent stress block procedure, using a neutral axis depth that was assumed to be constant and was obtained from the ABAQUS finite element analysis. However, since reinforcement embedded in concrete has different bond characteristics than prestressing strands embedded in a duct filled with grout, an alternate

procedure was developed in order to derive the expected slip behavior within the proposed connection. Additionally, little experimental data was available regarding the bond-slip behavior of standard sized strands embedded in grout over a length greater than the required embedment or development length. This lack of data meant the results of the available experimental data were deemed too unreliable to be used to define a globalized response, as they predicted more of a localized behavior for the strand, rather than the cumulative behavior over the entire length of the strand. Therefore, a procedure for determining the bond-slip behavior of reinforcement grouted in ducts was adopted in order to achieve an estimation of the bond-slip behavior of a strand grouted in a duct. Equation 2.17 provided an approximation of the debonded length over which the slip would occur (Raynor, Lehman, & Stanton, 2002). This equation was based on the assumption that a constant bond stress acted along the length of the reinforcement and was derived via a parametric study.

In order to develop a response profile for the bond-slip behavior of the strand, the value for the debonded length was assumed to be constant for all strain values. To calculate the slip experienced at a given level of moment within the connection, the strain experienced by the strand at the given amount of moment was multiplied by the debonded length. As before, the slip was then used to calculate the angle of rotation experienced by the connection using Equation 4.9. Figure 4.24, shows the moment vs. rotation response that was assumed for the improved connection detail and input into SAP2000.

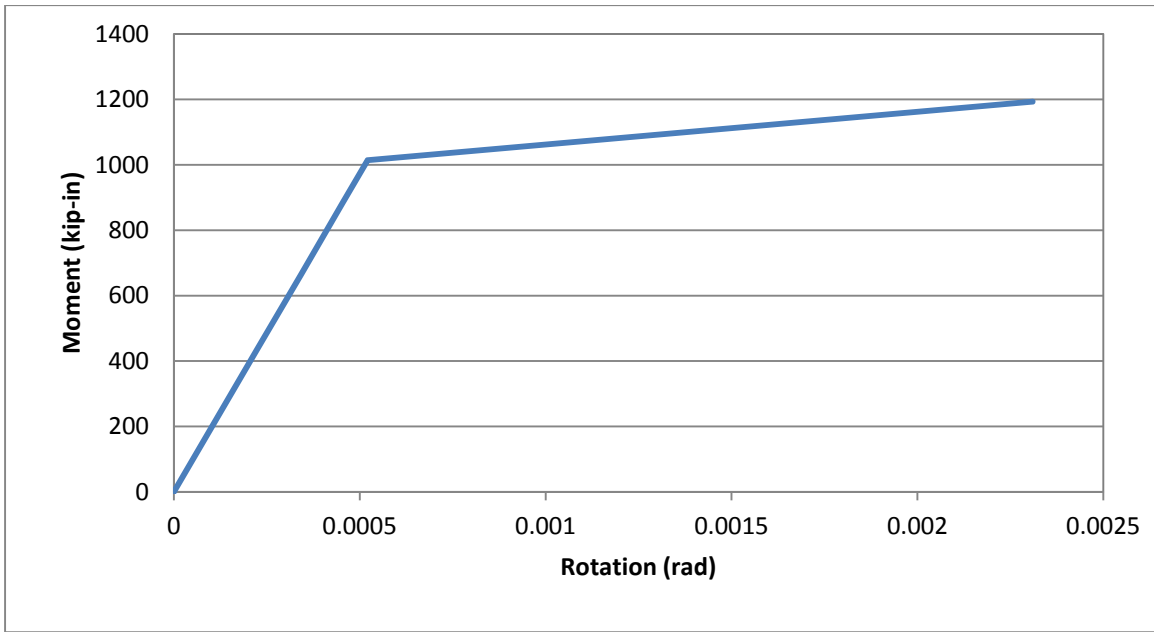


Figure 4.24: Improved Connection Predicted Moment vs. Rotation Response

The nonlinear link element that represented the improved connection detail was placed in parallel with both the girder-to-cap connection and cap-to-diaphragm nonlinear link elements, as shown in Figure 4.25. This was done so that the improved connection could influence both the moment and rotation behavior of both the girder-to-cap and cap-to-diaphragm nonlinear link elements simultaneously. However, since the improved connection had no influence when the connection was subjected to a negative moment, it was necessary to define the negative rotation response of the nonlinear link element as a pinned behavior.

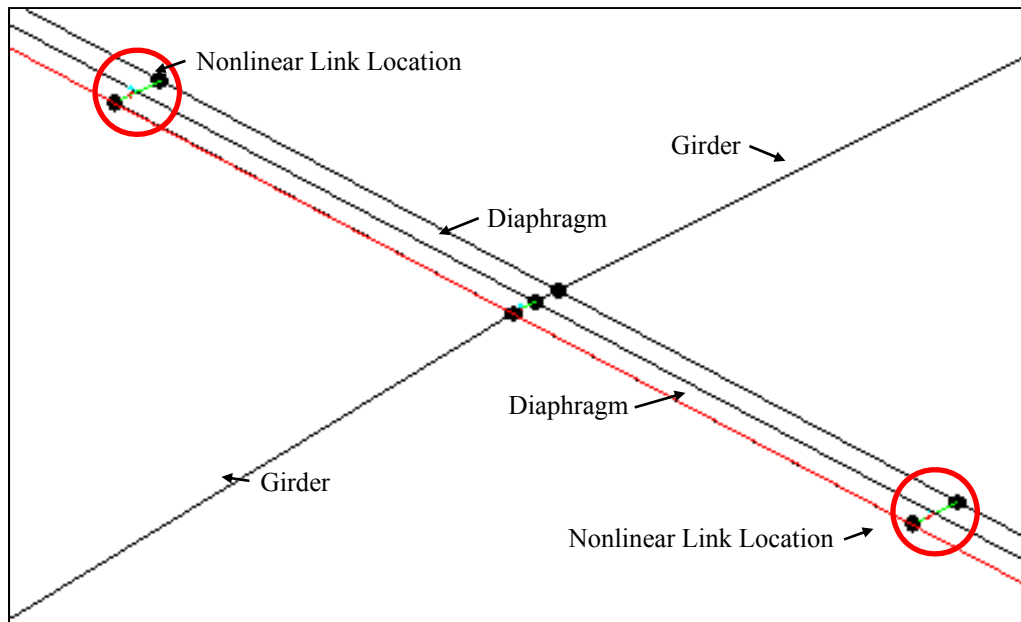


Figure 4.25: Grillage Model Improved Connection Nonlinear Link Location

#### 4.2.5 Staged Construction

Since the test unit was built and loaded in phases, it was necessary to reflect those phases in the model in order to achieve the correct force conditions along the length of the girders as well as at the critical interface between the girders, diaphragm, and bent cap. Fortunately, this was accomplished in SAP2000 through the use of a “Staged Construction” feature that allowed the user to construct and load the model in stages within a given analysis. Through the use of this feature, the model was assembled in two stages. The first stage was the placement of the girders on the cap beam and abutment. During this stage, the girders were simply supported and the stage one hold-down force was applied to the girders. This was accomplished by connecting the girders and deck to the diaphragm element using a link element that behaved as a pinned connection, as shown in Figure 4.26. The second stage changed the boundary conditions on the girders from simply supported to continuous, in order to reflect the fact that the girders, deck, and diaphragm were all acting as a continuous superstructure at this stage. This was achieved by removing the simply supported link element and adding the various nonlinear connection link elements, as their effects were only realized after all of the concrete had cured. Once those boundary conditions were changed, an additional hold-down force was applied, which represented the barriers and other loads that were placed on the prototype structure, but not the test unit. Additionally, a distributed load was applied along the length of each girder that

represented the stay-in-place formwork and the thickened overhang portion of the deck. It was assumed that both of the aforementioned loads were evenly distributed between girders.

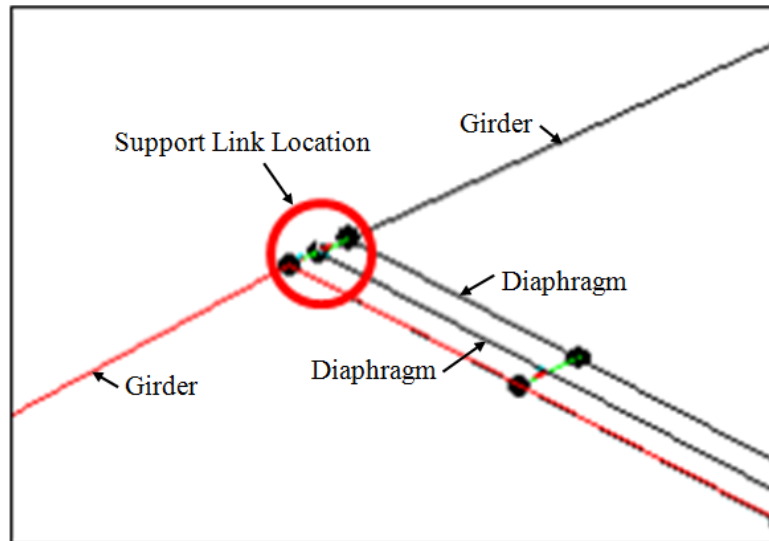


Figure 4.26: Grillage Model Temporary Support Condition Link Element Locations

#### 4.2.6 Loading Conditions

Aside from including the dead load within each analysis, hold-down forces were also applied during each phase of the stage construction in the same manner as they were in the lab. Each of the hold-down forces were applied at nodes that were placed 16ft away from the centerline of the cap beam, as shown in Figure 4.27. More information regarding the hold-down forces is presented in Section 5.1.3. As mentioned previously, an additional distributed load of 0.00416 k/in was placed along each girder in order to reflect stay-in-place formwork and the thickened portion of the deck. It should be noted that this value was halved for the center girder as only half of it was modeled.

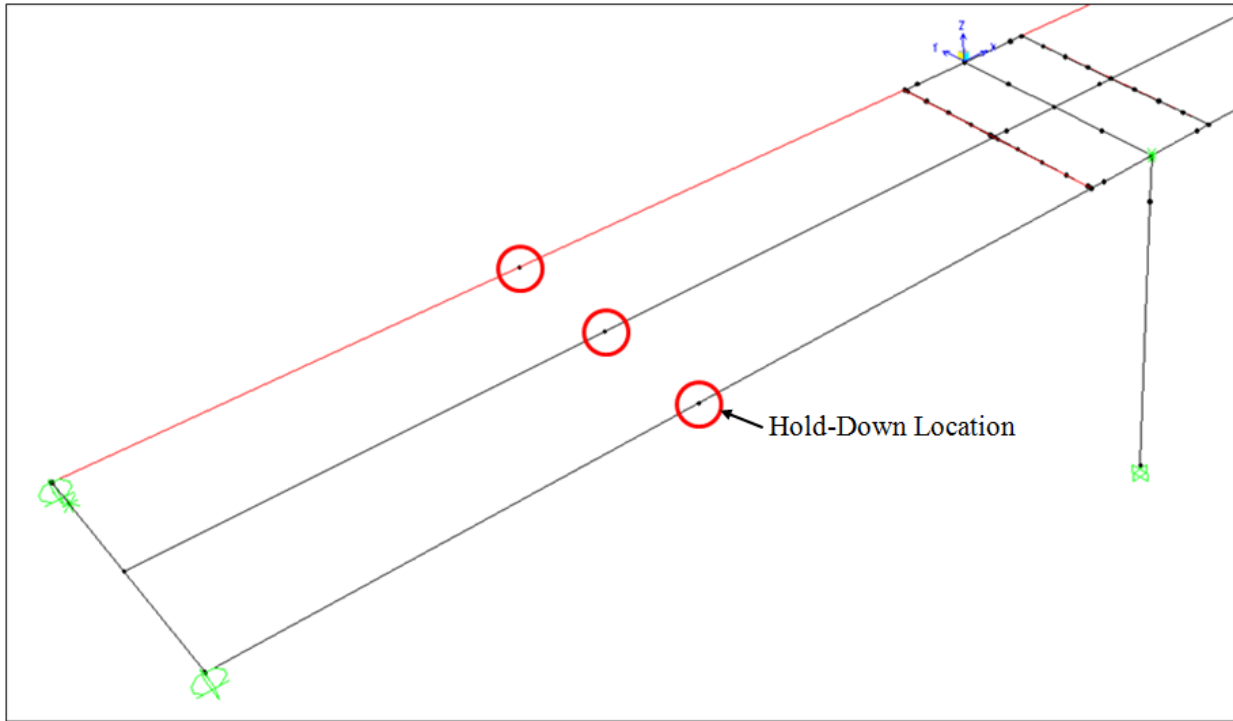


Figure 4.27: Grillage Model Hold-Down Node Locations

#### 4.2.7 Modifications Made for Phase 2 Model

The same model, described above, was used to make predictions for the second phase of the testing; however, a few minor adjustments were made to the model in order to reflect the changes in boundary conditions and loading that were experienced during Phase 2. First, the loading aspect of the staged construction portion of the analysis was altered. The stage 2 hold-down force was not applied, while the stage 1 hold-down force was removed once the superstructure was made continuous. Second, the superstructure support conditions were altered so that the structure was supported on rollers at the former hold-down location, instead of at the abutment, as it was for the beginning of the analysis. Finally, the vertical displacements were applied at the former location of the hold-down, in order to remain consistent with the actual test setup. The Phase 2 model also did not include any of the degradation that was experienced during Phase 1 of testing; however, cracking of the girders, deck, and column was included using the same respective effective stiffness values that were used for Phase 1.

## Chapter 5. Experimental Work

### 5.1 Construction Sequence

#### 5.1.1 General Sequence

In order to make the test unit as close to a real world inverted-T bridge as possible, typical construction practices and techniques that are used in the field were employed in the construction of the test unit in the laboratory at UCSD. The basic construction sequence is shown in Figure 5.1.

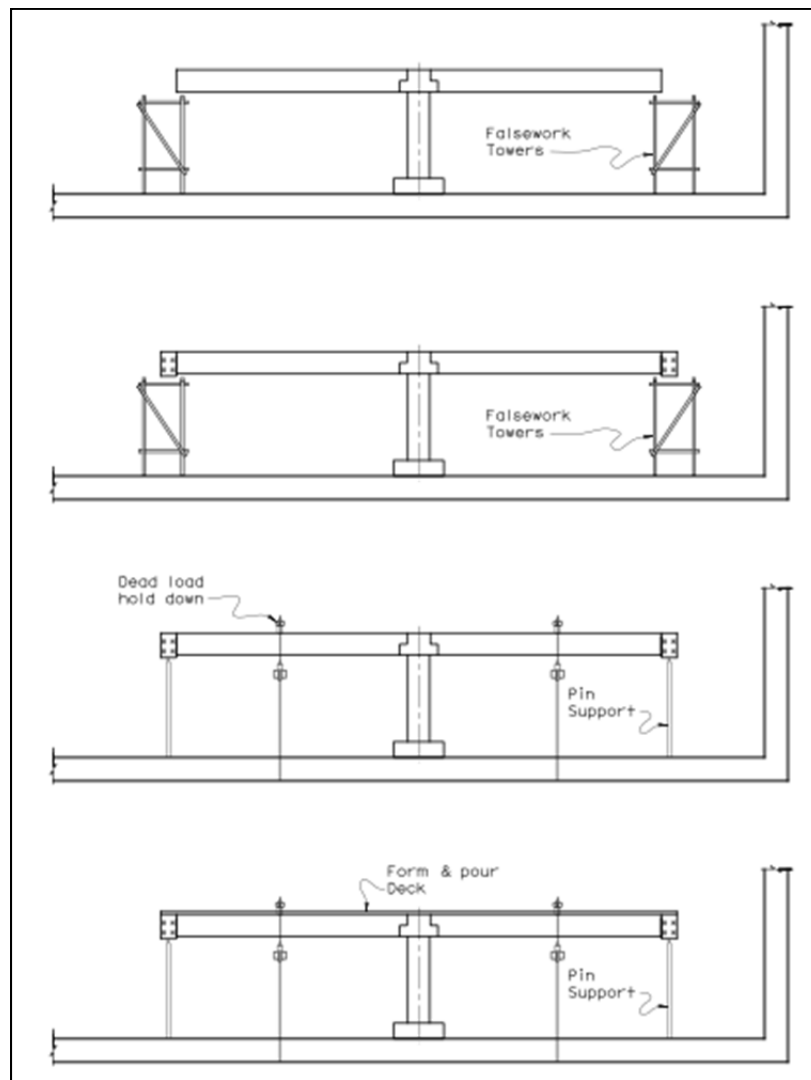


Figure 5.1: Schematic of Construction Sequence Used for Building the Test Unit

However, the availability of space within the laboratory and the concerns associated with the stability of the test unit during certain phases of the construction also dictated portions of the construction sequence as noted. The construction of the test unit proceeded as follows:

1. The footing was first constructed within an available portion of the lab space. The column cage and formwork was then constructed on top of the footing (Figure 5.2).

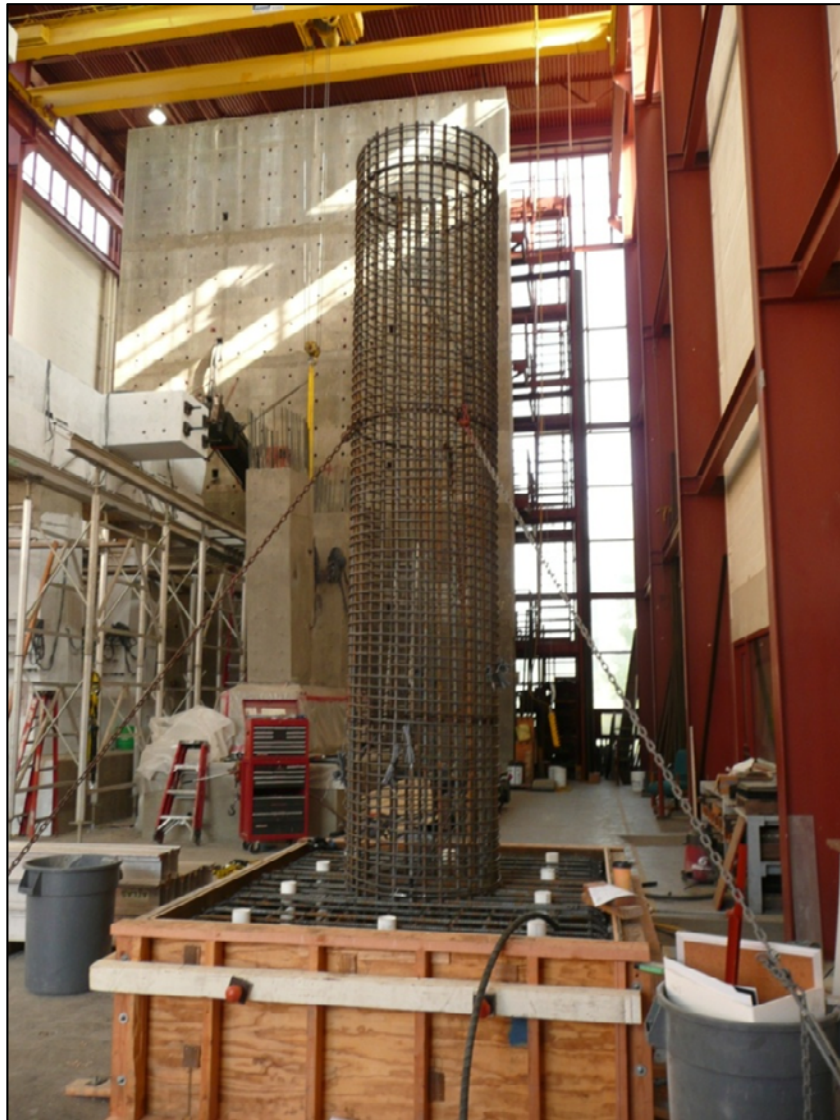


Figure 5.2: Completed Column and Footing Cage

2. As space within the lab opened, the footing and column cage were moved and placed in the space designated for testing (Figure 5.3). Hydrostone was then poured underneath the footing to ensure an even bearing surface. Once this was complete, the concrete was poured for the column. The pour for the column was terminated at the height of the base of the inverted-T cap beam.



Figure 5.3: Repositioning the Column and Footing

3. Temporary shoring was erected around the column to support the construction of the inverted-T bent cap. The bent cap was constructed and poured so that it

would be even with the top flanges of the girders, rather than pouring it to its full height (Figure 5.4).



Figure 5.4: Completed Bent Cap Construction on Top of Column

4. Temporary shoring was also installed on both the North and South ends of the bridge to support the girders as well as to aid the construction of the abutments. However, this set of shoring was installed at a height that was 3 in. lower than that which was used for the cap beam in order to compensate for the increased depth of the abutment that was specified in the plans to adequately embed the girder ends.
5. The girders were lifted into their respective places on both the North and South sides of the bent cap, with the South side being placed first due to the unavailability of space on the North side of the laboratory at that point in time (Figure 5.5).



Figure 5.5: Installation of Southern Girders

6. The abutment cage was then constructed on the ground, lifted into place, and the concrete was partially poured to a height corresponding to the underside of the deck (Figure 5.6). The South side was again constructed first and was followed by the North side.



Figure 5.6: Casting of the North Abutment

7. Prior to removing the falsework under the abutment and placing it on the pinned support system, a partial pour of the diaphragm was completed, adjacent to the cap on both sides, in order to provide added stability to the system. Only the 6 in. wide portion next to the corbel of the inverted-T cap was poured, up to the full height of the corbel.
8. Four support columns were placed beneath each abutment. Half-rounds were welded to the top of each column, which were used to create a pinned condition at the abutments (Figure 5.7). The falsework under both the abutments and the column was removed and the loads at the abutments were subsequently transferred to the support columns.



Figure 5.7: Temporary Support System Used Under Each Abutment

9. The Stage 1 hold-down force of 167 kips was then applied to each span and the ducts within the girders, containing the untensioned strands, were grouted.
10. The deck, along with the remaining portion of the diaphragm, abutment, and the haunch above each girder, was then cast in one large pour.

11. Once the deck hardened, two horizontal and two vertical actuators were mounted to each abutment, as shown in Figure 3.4, and the Stage 2 hold-down force of 59 kips was applied to each span. The specimen was then ready to begin testing.

### **5.1.2 Construction Challenges**

The following are challenges that were encountered during the construction of the test unit and are presented in order to aid with future construction of this bridge type in the field.

#### *5.1.2.1 Pouring the Bent Cap*

Forming and pouring the inverted-T bent cap proved to be somewhat challenging due to the geometry of the bent cap. Prior to pouring the bent cap, the concern was raised that the pressure head of the concrete at the top of the inverted-T would likely be enough to force the concrete in the corbel portion of the bent cap to overflow its formwork. Therefore, in order to remedy this concern, the bent cap was poured in lifts, which necessitated the use of a construction joint. The first lift was poured to the top of the corbel portion and was allowed to set for around 20 minutes. The remainder of the bent cap was then poured in the second lift (Figure 5.8). Though some of the concrete in the corbel still rose slightly above the formwork, pouring the bent cap in lifts seemed to solve the overflow problem. An alternate solution that could be used for bridges of this type in future would be the use of a precast bent cap, instead of cast-in-place. The use of a precast bent cap would also significantly reduce the amount of construction time for the project and result in cost savings.



Figure 5.8: Casting of the Bent Cap

#### 5.1.2.2 *Installing the Ducts through the Cap Beam*

Installing the ducts for the untensioned prestressing strand that was placed through the cap and the Northern girders proved to be a fairly significant challenge. First, since the strand did not extend straight through the cap beam and into the Southern girders, the ducts had to be bent as they passed through the cap so that they would terminate at the edge of the corbel and straddle each girder. Therefore, it was decided that the standard corrugated duct used for prestressing applications would be too stiff to accommodate such bends. As a result, a flexible, corrugated, low-grade steel electrical conduit was used instead. This alternative proved to be very effective as it was easily routed within the cap beam (Figure 5.9). It should be noted, however, that this problem is somewhat specific to the test unit and would likely not be encountered in the prototype structure, as the ducts would continue straight into the Southern

girders, thereby eliminating the need to bend them. However, the rebar in the bent cap should be spaced such that it allows for the accommodation of the duct.



Figure 5.9: Routing of Bent Cap Ducts

Second, it was decided that it would be prudent to make the duct in the cap beam larger than the ducts that were inside the girders. This was done in order to increase the tolerance in the alignment of each section of duct, making it easier to place the ducts in the cap in line with the ducts in the girders to accommodate and grout the strand. Therefore, a 1-½ in. electrical conduit was selected, while 1 in.-diameter sheathing was used in the girders.

Third, the bent cap was highly congested with reinforcement, especially in the vicinity of the column, which made it difficult to place ducts large enough to accommodate the strands (Figure 5.10). This was also true given the fact that a slightly larger diameter conduit was selected within the cap beam. This challenge was solved by routing the ducts around the column instead of passing through it. This problem is not expected if four girders are used instead of five, as a girder would not have had to pass directly through the center of the column.



Figure 5.10: Placement of Ducts in the Bent Cap around the Column

### 5.1.2.3 *Inserting the Strands through the Ducts in the Cap Beam*

Running the strands through the ducts also proved to be difficult, given the bends in the ducts, as there was little clearance within the duct for both strands. Furthermore, grout tubes were mounted on each duct and ran through to the top of the cap to ensure proper grouting. However, in order to mount the grout tubes, a conduit in the shape of a box was placed at the center of the cap beam with a series of connectors that were used to splice on the main duct sections as well as the grout tube. This was a significant obstacle when placing the strands as they had a tendency to get caught in the corners of the conduit, making it difficult to force the strand out and to the other end of the cap beam. This problem would likely not be encountered in the prototype structure as the ducts would not be bent, nor would they likely enter a similar box section. However, in order to remedy the situation, a series of increasingly larger diameter and stiffer objects were fished back and forth across the cap beam. Once a stiff enough wire was pulled through the cap beam, it was attached to one of the strands and was used to pull it through. The first strand was then used to pull the second strand through the cap beam. The

strands were then fed down the length of the girder (Figure 5.11). Though the process was rather time consuming, it proved to be the most effective.



Figure 5.11: Pushing the Strands through the Girder

#### 5.1.2.4 *Partial Pour of the Diaphragm*

Safety concerns were raised regarding the stability of the superstructure while transferring the abutments from the falsework to the pinned support system. Initially, the girders were independent of one another at the cap end as they were supported on the corbel of the inverted-T cap beam. This was done to replicate the simply supported condition that the girders would experience as they were placed in the prototype bridge during construction. However, concerns were raised that the girders might fall out of place during the transfer of the abutment support conditions. Therefore, in order to improve the lateral and rotation stability, and hence safety, of the superstructure, it was decided that a partial pour of the diaphragm would be completed. Only the portion of the diaphragm next to the corbel was poured to the full height of the corbel within each bay between girders, as it would provide lateral stability for the girders while still allowing them to remain in a simply supported condition at the bent cap, as required to produce a realistic moment profile along the length of the girder. This would not have been possible had the entire diaphragm been poured. However, this did introduce a construction joint in the diaphragm along the top of the corbel of the bent cap, as shown in Figure 5.12.



Figure 5.12: Partial Diaphragm Pour between Girders

#### 5.1.2.5 Termination of Untensioned Strands

Unfortunately, due to a miscommunication in the lab as well as the field decision to make a partial pour of the diaphragm, the untensioned strands were not terminated at the face of the inverted-T bent cap on the as-built connection side, as specified. Instead, the strands were extended and grouted all the way to the outside face of the diaphragm. Since the presence of the strands within the effective as-built connection region could have falsely improved the performance of the connection, it was necessary to render the strands ineffective within the as-built connection. Therefore, the grout within the duct on the as-built side of the bent cap was drilled out over the length of the diaphragm, in order to debond the strands, as shown in Figure 5.13. Additionally, as much of the duct was removed as possible, which was somewhat feasible as the electrical conduit that was used could be easily unraveled and fractured over the first couple of inches. It was assumed that any remaining duct would be easily fractured or unraveled as the girder pulled away from the cap.

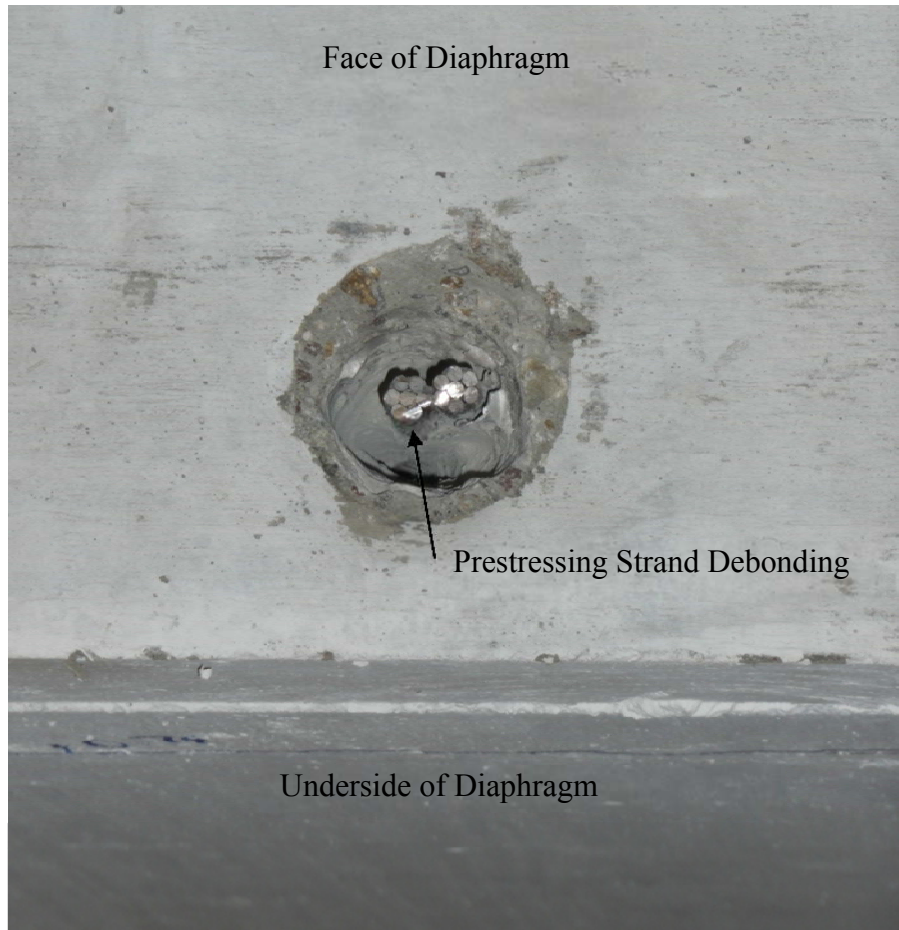


Figure 5.13: Untensioned Strand Debonding

## 5.2 Instrumentation

Given the magnitude of the test specimen, a significant number of both internal strain gauges and external devices were used to capture the response of the structure in its critical regions. A total of 282 strain gauges were used internally, while a combination of 51 string potentiometers, 67 linear potentiometers, and 11 rotation devices were used externally. The following presents the instrumentation plan that was used for both the internal and external instrumentation.

### 5.2.1 Strain Gauges

#### 5.2.1.1 Column-to-Cap beam Connection

Two spirals within the column-to-cap beam connection were instrumented with four strain gauges each, in the configuration shown in Figures 5.14 and 5.15. Note that a red “X” in

the figures indicated the strain gauges. The instrumented spirals were located near the middle of the connection, at approximately 7 and 10 spirals from the point of anchorage at the bottom of the column respectively, and a full un-instrumented spiral was placed in between them, as the spacing was rather tight, as shown in Figure 5.16.

The longitudinal reinforcement within the joint was instrumented with a higher number of gauges placed on the extreme tension and compression bars. Some of the reinforcement in the configuration was only instrumented with two strain gauges, while the extreme tension and compression bars were instrumented with four gauges along their length as shown in Figure 5.17. Starting at the column-to-joint interface, the configuration was evenly spaced along the longitudinal reinforcement at approximately 9.5 in. on center. The sections receiving only two gauges followed the same spacing, but were discontinued along the remainder of the length as shown in Figure 5.18.

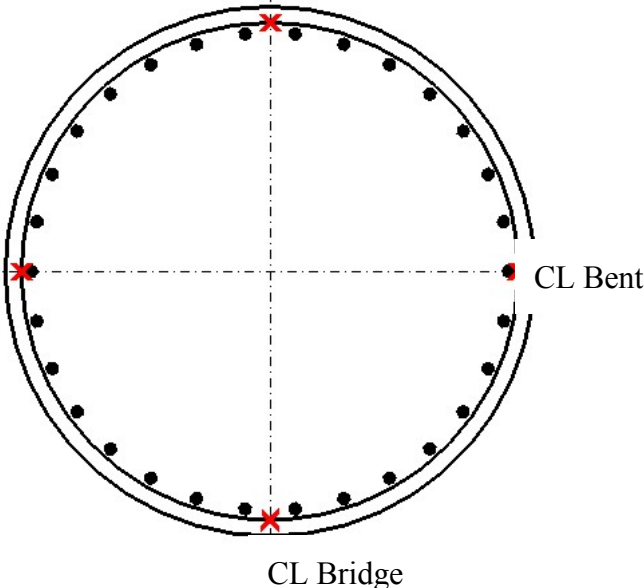


Figure 5.14: Column-to-Cap Beam Spiral Strain Gauge Location within Cap Joint Region

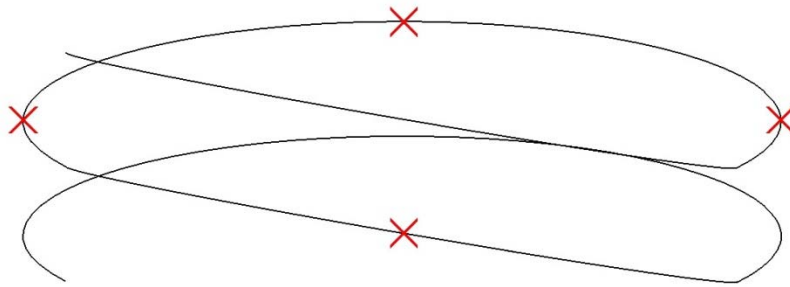


Figure 5.15: Column-to-Cap Beam Typical Spiral Instrumentation Profile

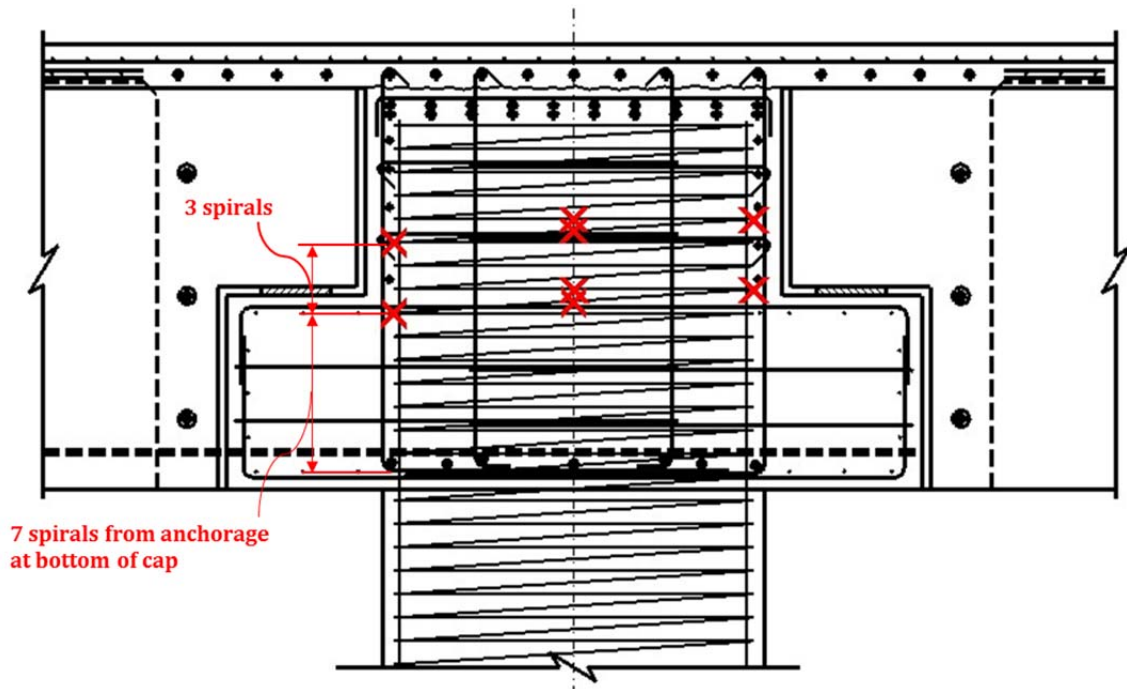


Figure 5.16: Column-to-Cap Beam Spiral Instrumentation within the Joint

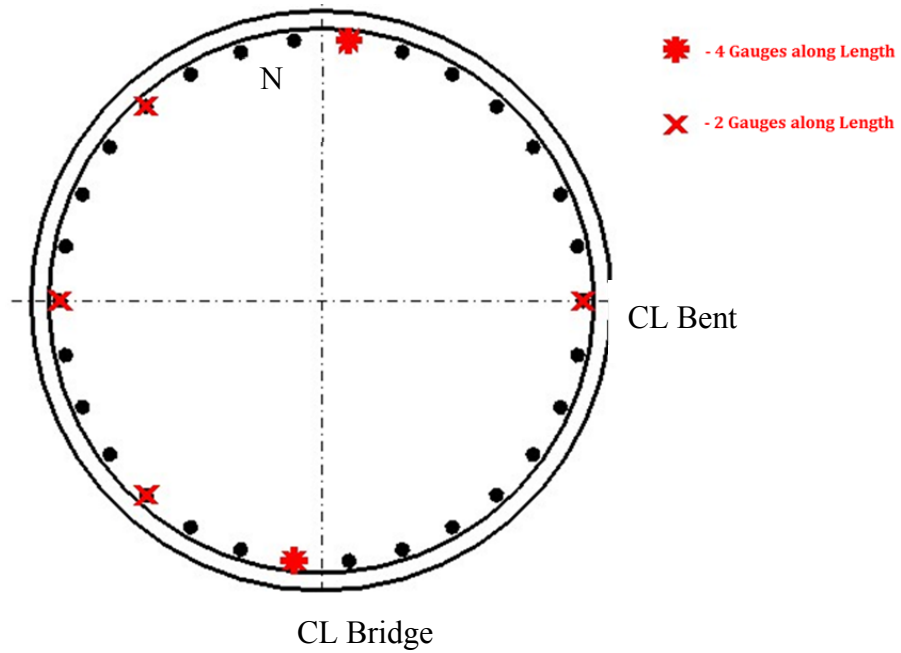


Figure 5.17: Location of Gauged Longitudinal Column Reinforcement

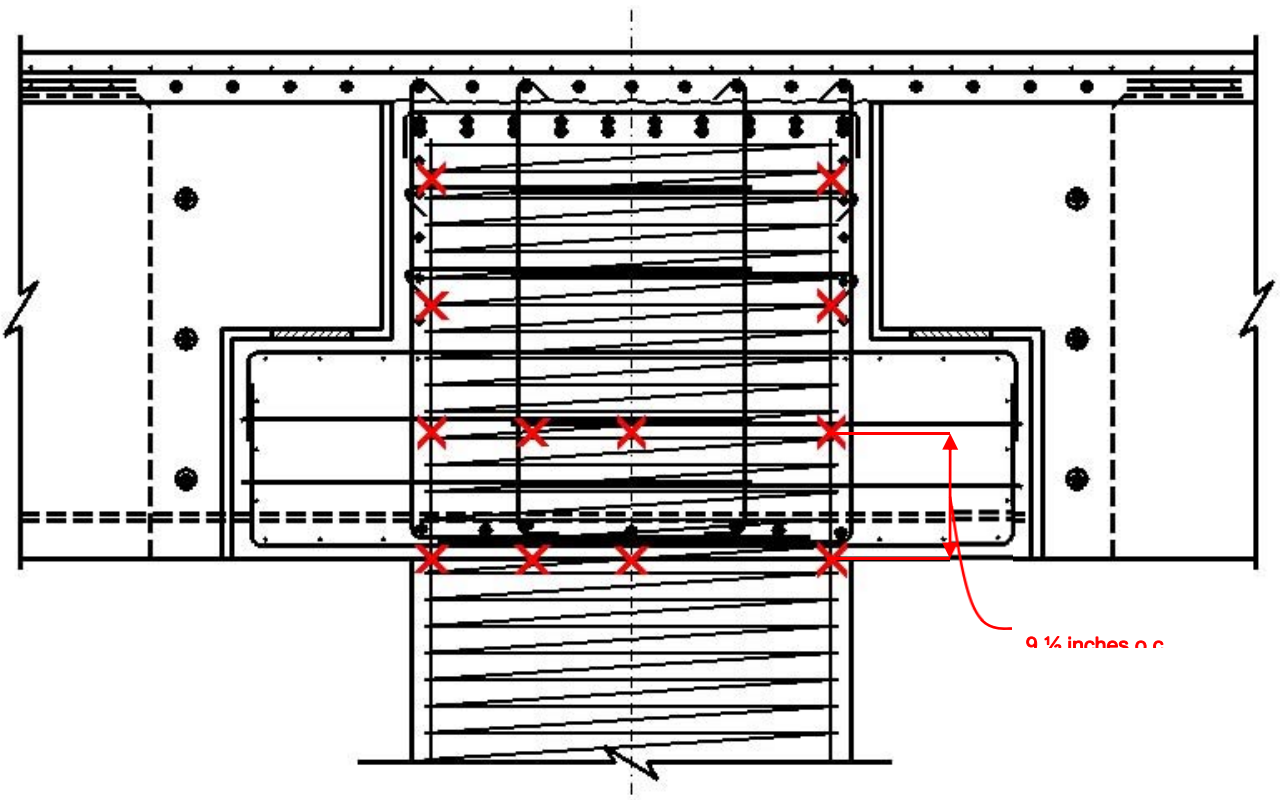


Figure 5.18: Profile of Gauged Longitudinal Column Reinforcement within the Joint

### 5.2.1.2 Column

The performance of the column was not of critical concern; as a result a significantly smaller number of gauges were used within the column. Gauges were placed on the spirals in the configuration as shown in Figure 5.19 in order to capture the behavior of the confinement within the column. One spiral was instrumented within the hinge at both the top and bottom of the column as shown in Figure 5.20.

The longitudinal bars at the base of the column were also minimally gauged. Each bar received only one gauge at approximately 1 in. from the top of the footing, as shown in Figure 5.21.

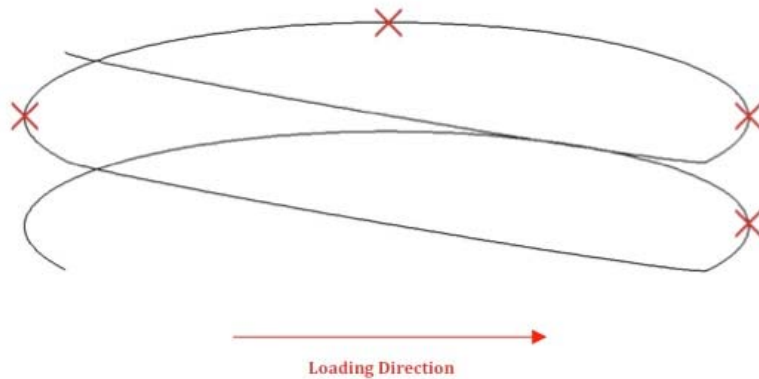


Figure 5.19: Typical Column Spiral Gauge Location

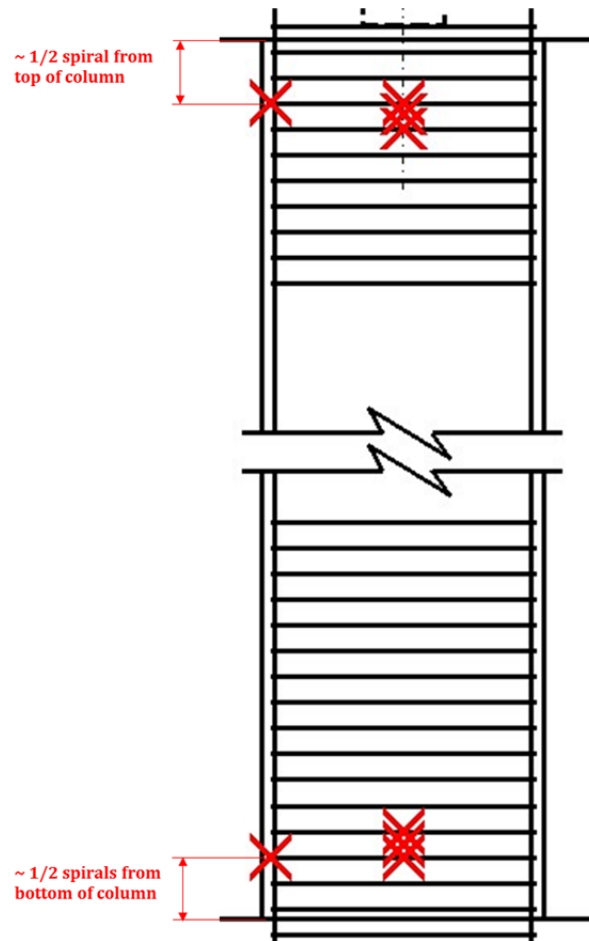


Figure 5.20: Spiral Gauge Location in the Column

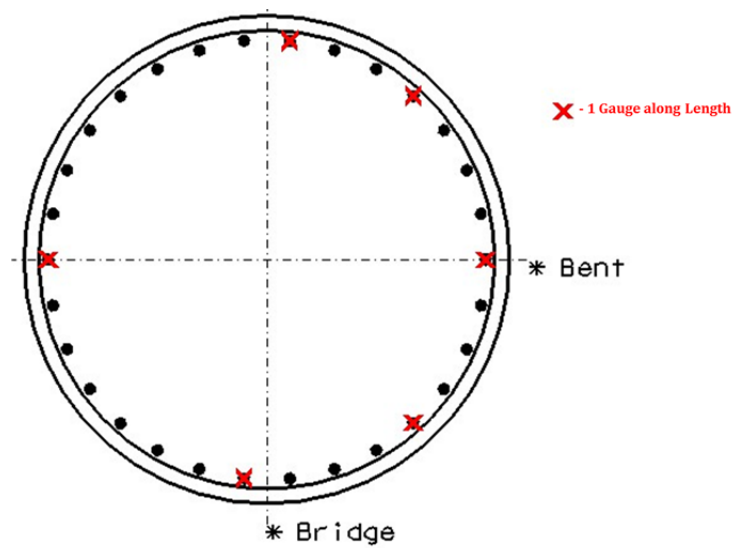


Figure 5.21: Bottom of Column Longitudinal Reinforcement Gauges

### 5.2.1.3 Footing

Since the footing in the test unit did not accurately represent true field conditions, it was not instrumented with any strain gauges.

### 5.2.1.4 Cap-to-Diaphragm Interface

The hooked reinforcement, which spanned the interface between girders, was instrumented in order to monitor the performance of the cap-to-diaphragm connection. Figures 6.22 and 6.23 depict the gauge layout for this section of the test unit. On one side of the column, each bar received one strain gauge, placed at the interface. The bar located closest to the column was instrumented with two additional strain gauges located approximately 5 in. from the interface on each side, as shown, in order to capture the slip behavior of the bar. On the opposite side of the column, only the bars in the center of each set of three were gauged. Each of these bars received one strain gauge, placed at the interface. Also, one gauge was placed at the mid-point of the hooked diaphragm reinforcement. However, rather than instrument each stirrup in the set of three between girders, the center stirrup in each set was excluded. All of the stirrups along the length of the cap were instrumented in this manner in order to further capture the performance of the joint, as shown in Figure 5.23.

Additionally, the stirrups between the girders in this region, shown in Figures 5.24, 5.25, 5.26, and 5.27, were each instrumented with one gauge at the mid-point of each vertical leg. This configuration was applied to a larger number of the stirrup sets on West side of the column than the East side.

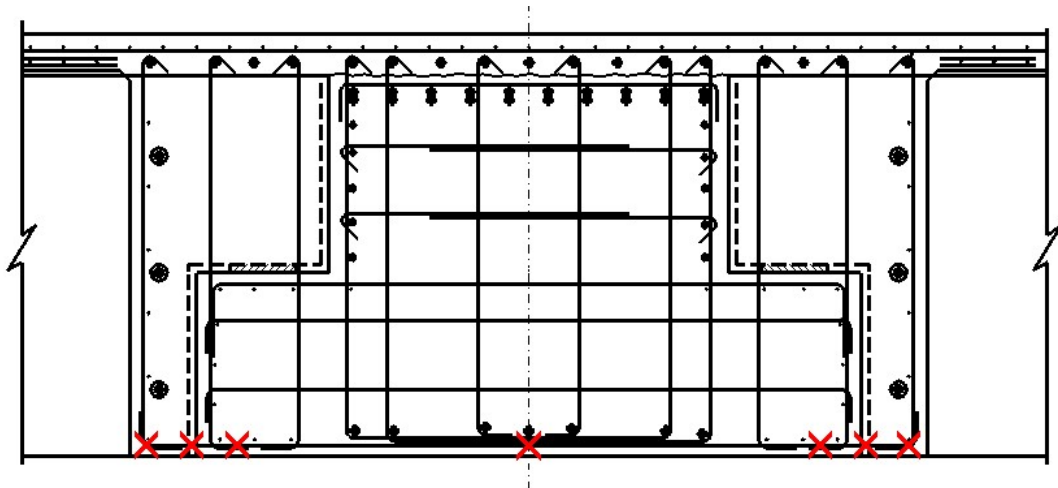


Figure 5.22: Cap-to-Diaphragm Hooked Reinforcement Strain Gauge Layout

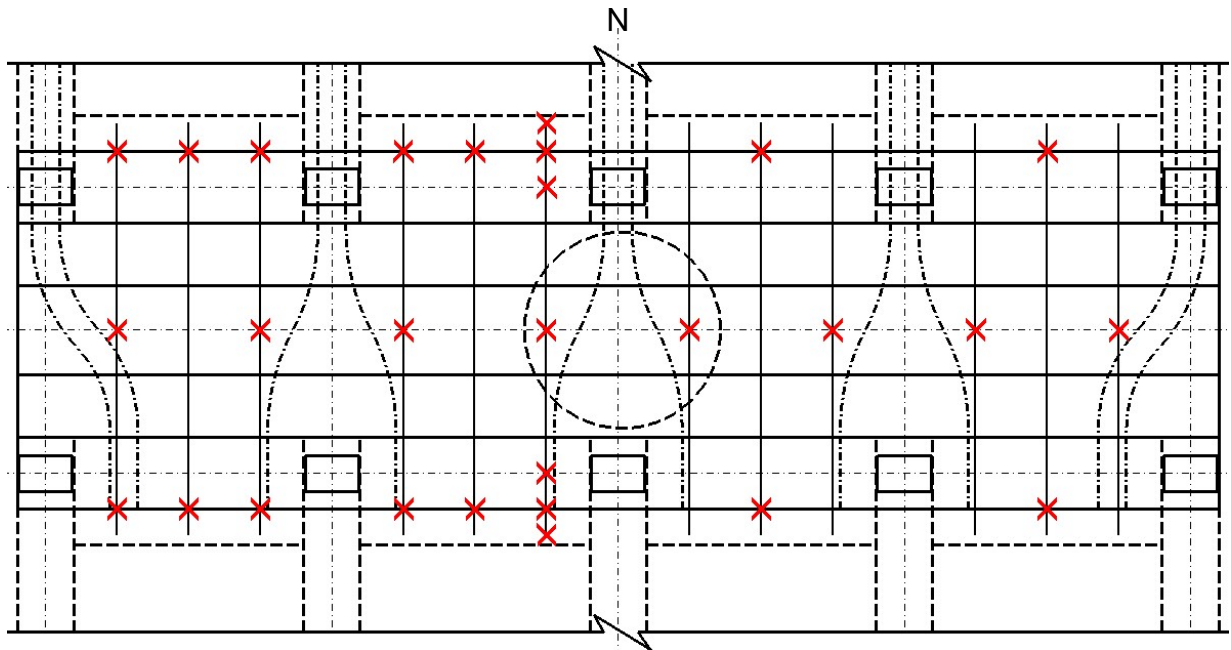


Figure 5.23: Cap-to-Diaphragm Hooked Reinforcement Strain Gauge Layout

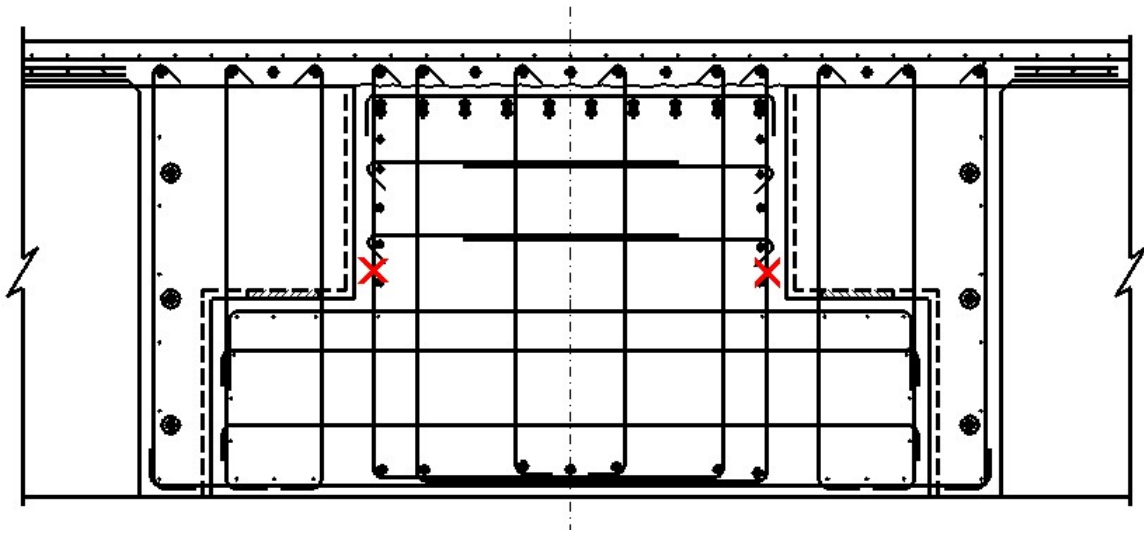


Figure 5.24: Cap Beam Inner Stirrup Strain Gauge Locations

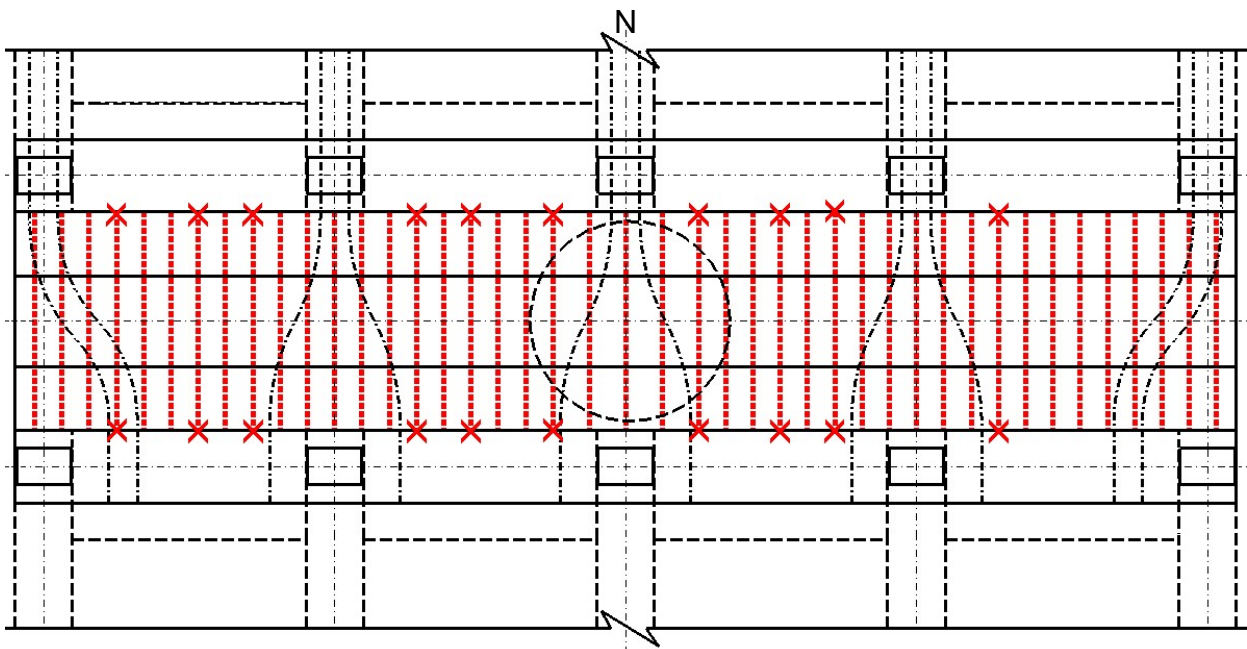


Figure 5.25: Cap Beam Inner Stirrup Strain Gauge Layout

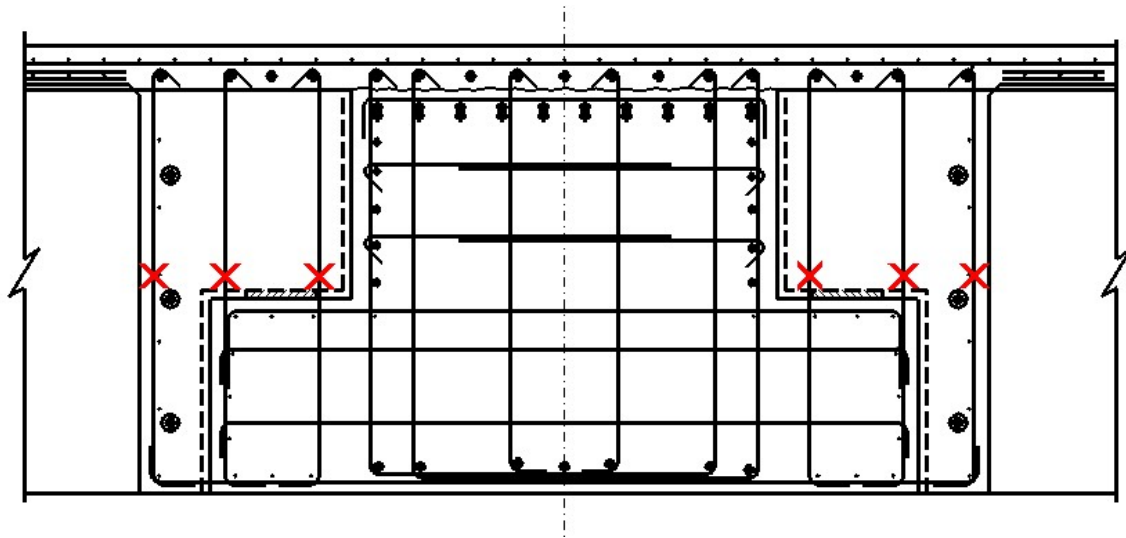


Figure 5.26: Cap Beam Outer Stirrup Strain Gauge Locations

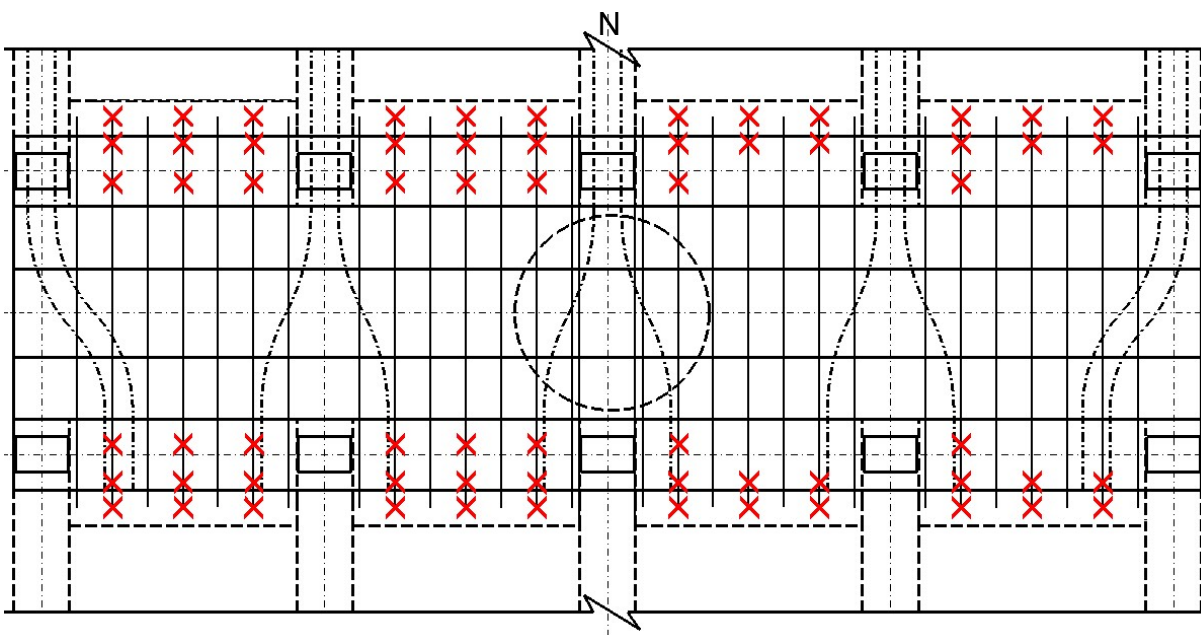


Figure 5.27: Cap Beam Outer Stirrup Strain Gauge Layout

### 5.2.1.5 Girders

The girders were minimally instrumented with strain gauges. The center girders, along with one intermediate and one exterior girder on the as-built side were instrumented.

The stirrups within the girders were instrumented in order to capture the shear demand in the girders. Both vertical legs were instrumented at their mid-point as shown in Figure 5.28. The last stirrup in the blocked-out region at the dapped end of the girder, and the first three beyond this portion, were instrumented as shown in Figure 5.29. One of the stirrups within the dapped end detail of the aforementioned girders was also instrumented as shown in Figure 5.30.

The prestressed strands on one of the center, intermediate, and exterior girders on the as-built side were also instrumented. Each harped strand was instrumented with one gauge at a distance of the transfer length (taken as 40 in.) from the dapped end, as shown in Figure 5.29. The horizontal strand at the bottom of the section, and closest to the center, as shown in Figure 5.28, was also instrumented with two strain gauges: one at the mid-span of the strand and one at a distance of the transfer length (again taken as 40 in.) from the dapped end. Additionally, the horizontal strand at the outside of the bottom layer, as shown in Figure 5.28, was instrumented with one strain gauge at the mid-span of the strand.

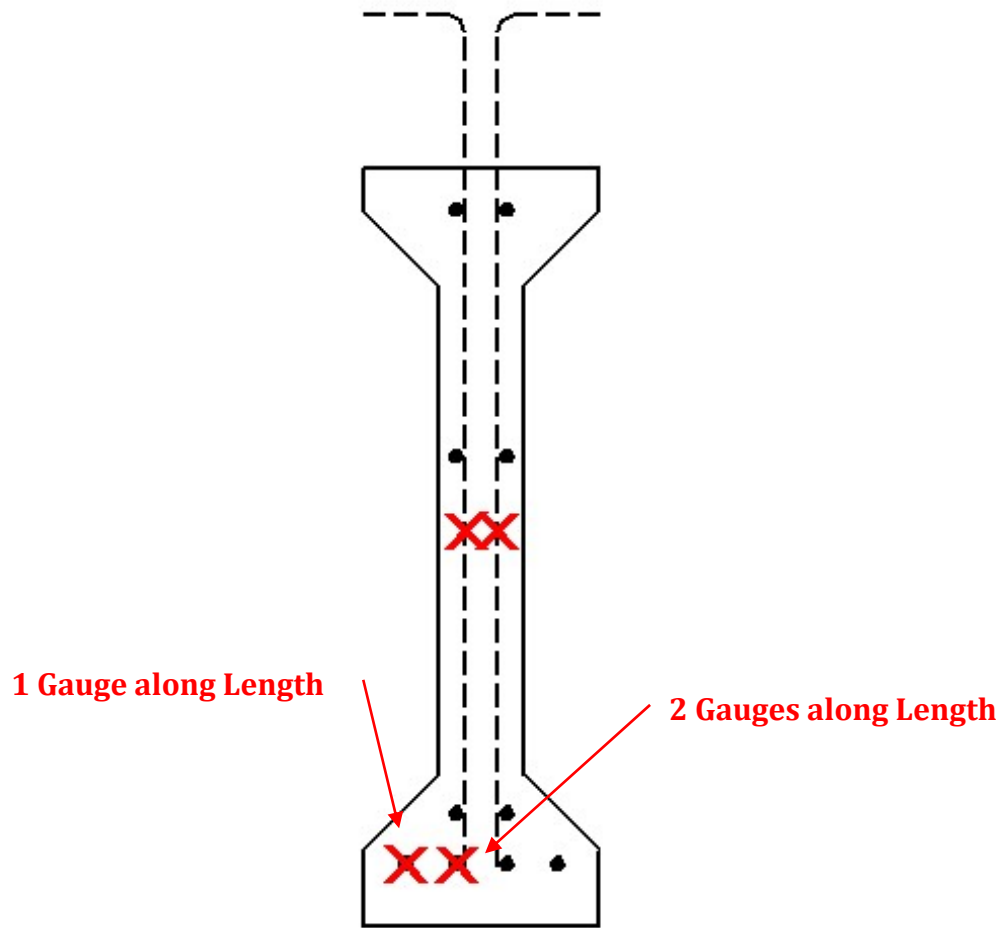


Figure 5.28: Girder Cross-Section Strain Gauge Locations

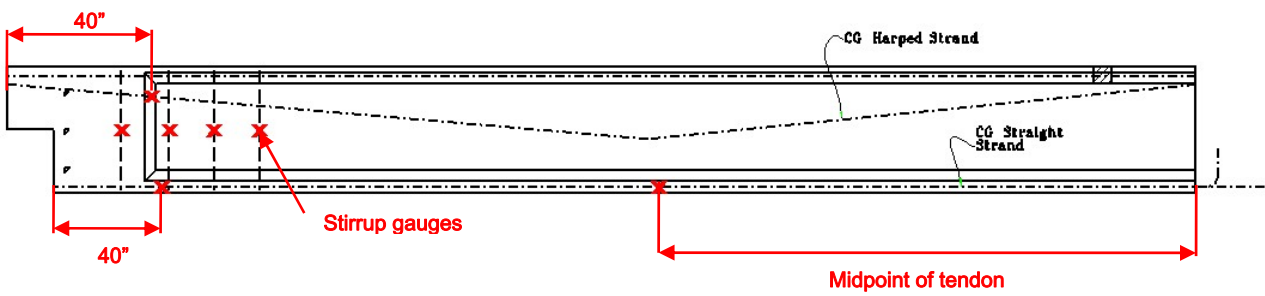


Figure 5.29: Girder Strain Gauge Layout

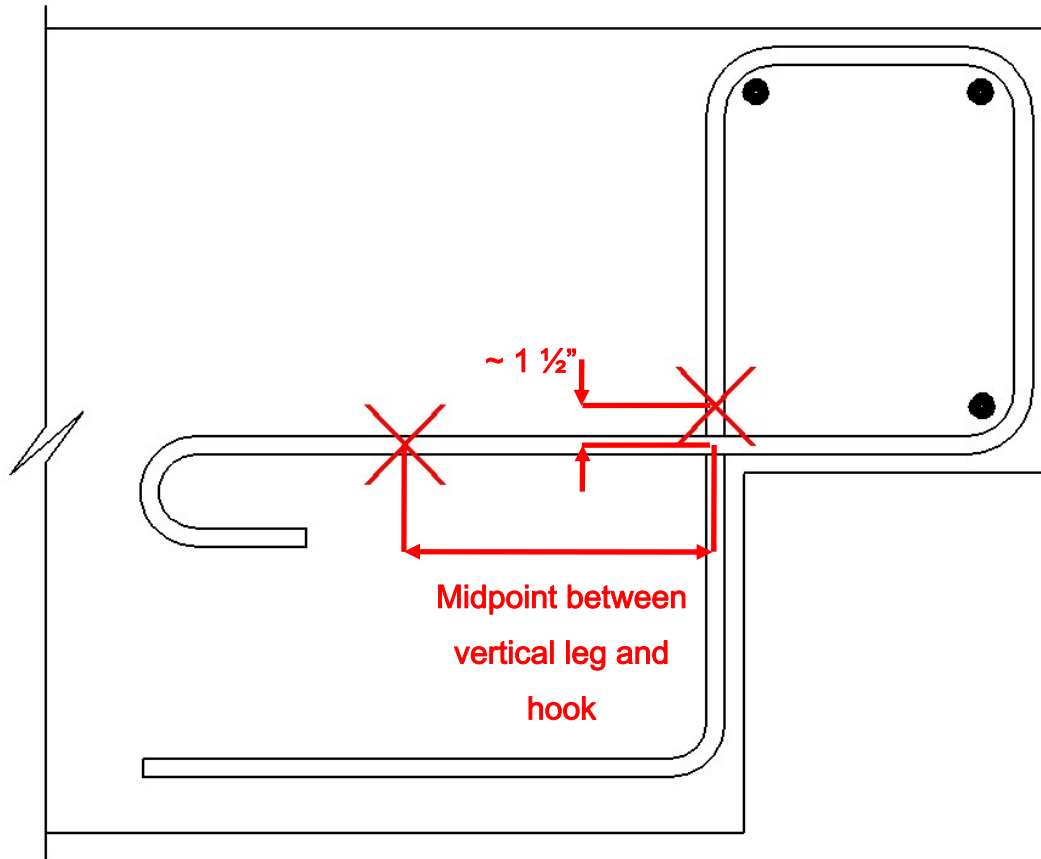


Figure 5.30: Girder Dapped End Detail Strain Gauge Locations

#### 5.2.1.6 Girder-to-Diaphragm Connections

The girder-to-diaphragm connections were one of the most critical regions of the test unit. Therefore, these connections were heavily instrumented.

The dowel bars connecting the girders to the diaphragm, on both the as-built and retrofit side, were instrumented as shown in Figure 5.31. It was decided that the bottom dowel on each girder would be the critical bar as it would be the first to see the effect of a positive moment. Therefore, these bars received additional strain gauges as shown in Figure 5.31. The gauge on the bottom dowel that is placed away from the face of the girder was located at the mid-point of the dowel on which it was placed. It should also be noted that Figure 5.31 was always taken to be looking in the North direction when applying instrumentation to both the as-built and improved connection sides of the cap beam.

Strain gauges were also placed on the unstressed strands within the improved connection detail. As shown in Figure 5.32, one strand per girder, on the improved connection side, was instrumented with four gauges each. One gauge was placed at the interface between the bottom of the cap and the girder. An additional gauge was placed along the strand within the girder, approximately 10 in. from the gauge at the interface. One more gauge was placed on the portion of strand within the cap beam, spaced at approximately 10 in. from the previous gauge.

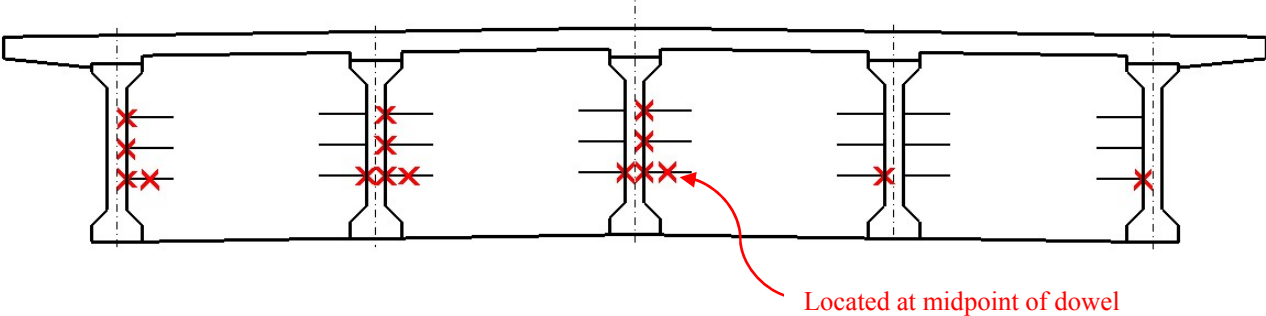


Figure 5.31: Girder-to-Diaphragm Dowel Strain Gauge Locations

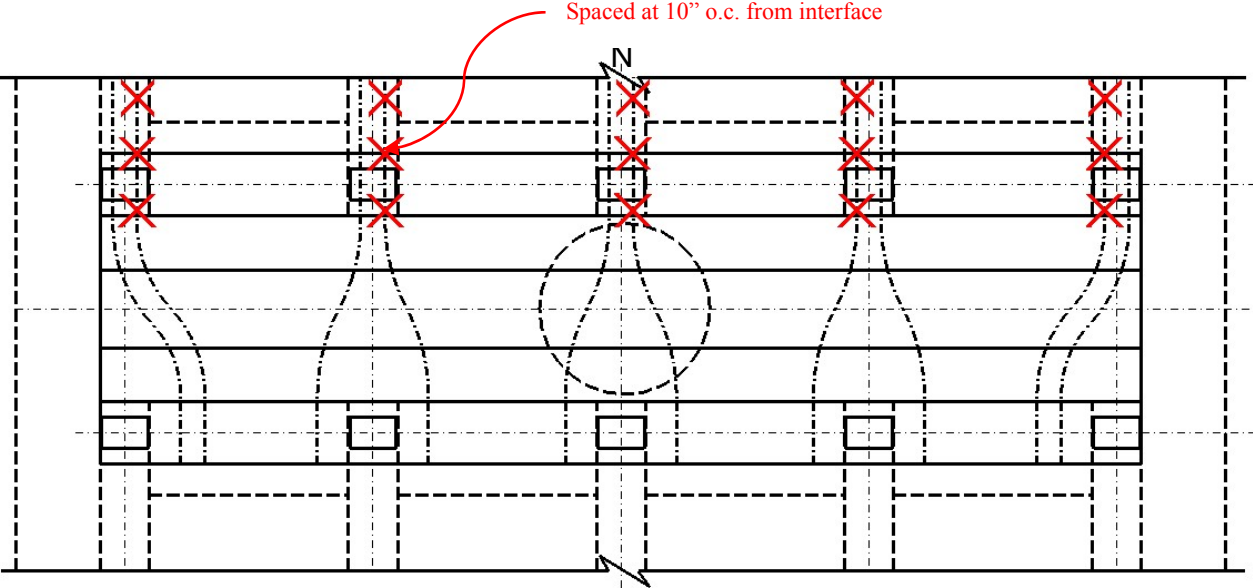


Figure 5.32: Improved Connection Strand Strain Gauge Locations

### 5.2.1.7 Deck

The deck reinforcement was mounted with strain gauges as shown in Figures 5.33 and 5.34, with gauges located both above the girders and at the mid-point between girders. The first set of gauges was placed on the longitudinal reinforcement directly above the gap between the girder and the top portion of the cap. The second set was placed on the longitudinal reinforcement directly above the end of the diaphragm. Both of these sets, as shown in Figure 5.33, were used to monitor the contribution of the deck in the moment resistance of the connection. The final set was placed at a distance of 1.5 ft from the second set of gauges, on each side of the column, as shown in Figure 5.34. These gauges were used to capture the general behavior of the deck away from the connection.

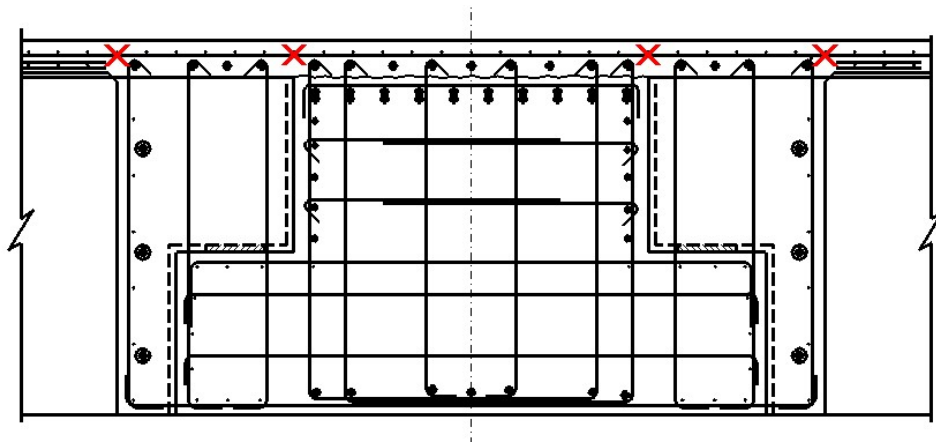


Figure 5.33: Deck Reinforcement Strain Gauge Locations

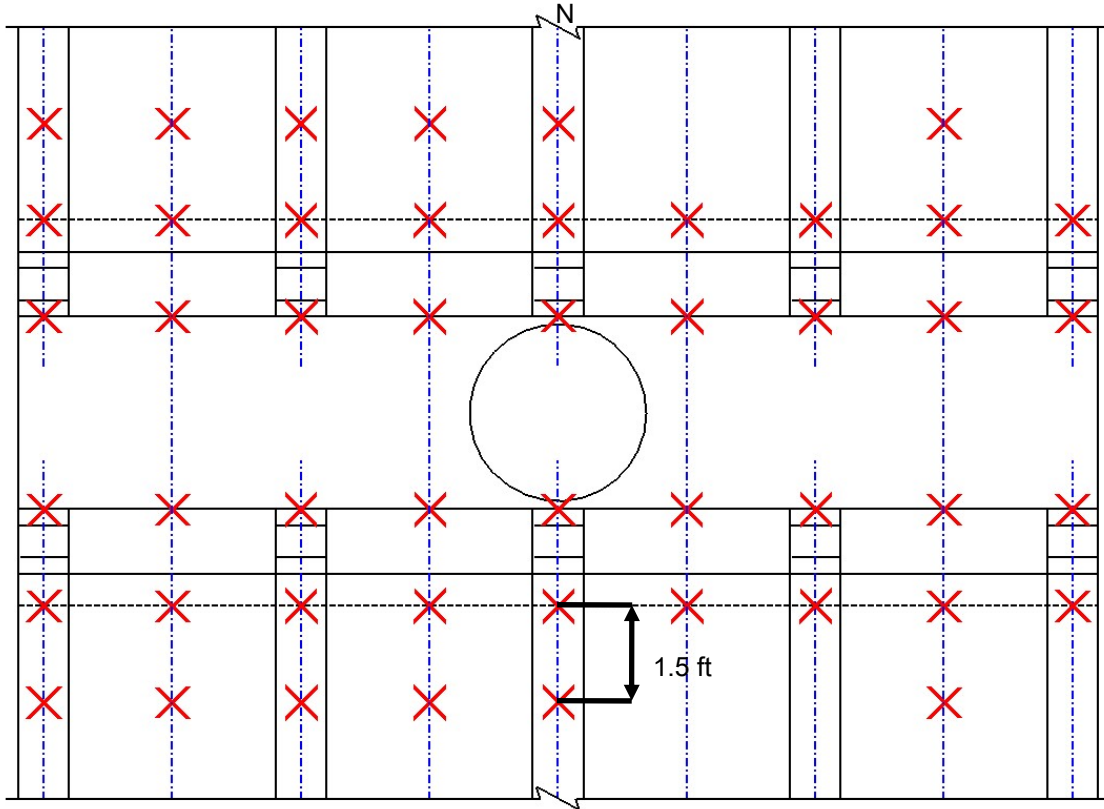


Figure 5.34: Deck Reinforcement Strain Gauge Layout

## 5.2.2 External Instrumentation

### 5.2.2.1 Horizontal Displacement of Cap and Superstructure

Each end of the bridge deck was mounted with a string potentiometer along its centerline in order to validate the displacement readings provided by the horizontal actuators as shown in Figure 5.35. On the reaction frame side of the test unit, an extra string potentiometer was added to the side of the deck in order to obtain an additional displacement and deck rotation reading. Additionally, each end of the cap beam was instrumented with string potentiometers in order to provide both the horizontal displacement of the cap in the longitudinal direction of the bridge and to indicate any twisting of the superstructure as shown in Figure 5.36.

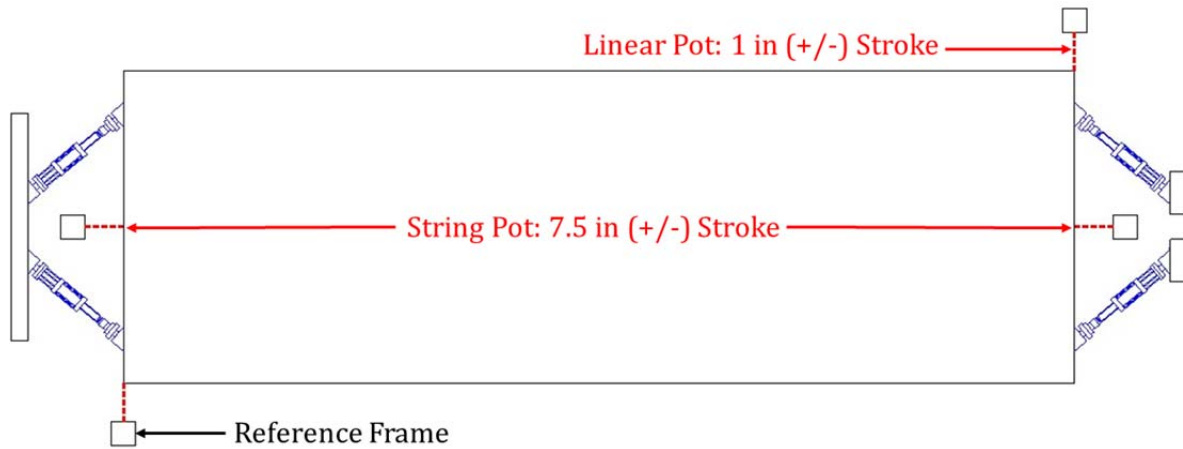


Figure 5.35: Location of Deck Displacement Devices

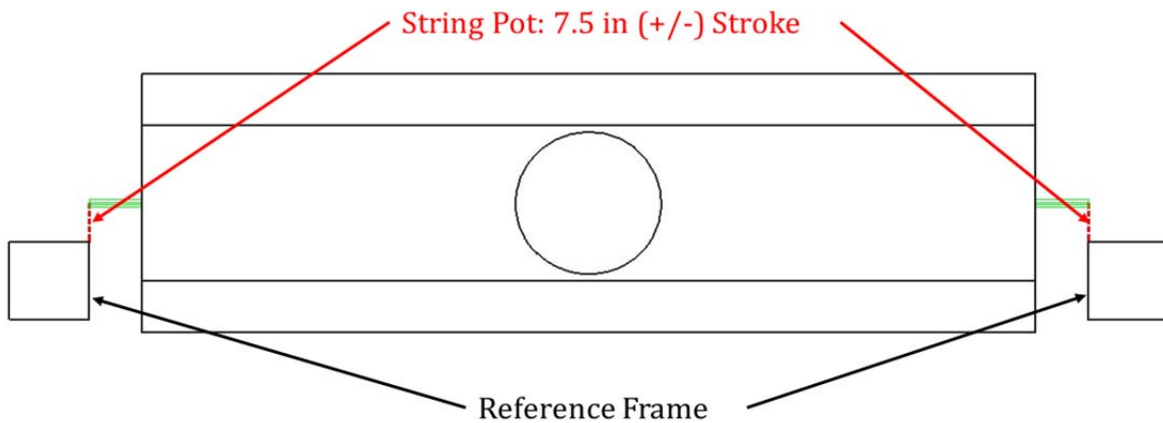


Figure 5.36: Plan View of Horizontal Cap Beam Displacement Devices

### 5.2.2.2 Vertical Displacement of Girders/Superstructure

#### 5.2.2.2.1 Phase 1

It was important to obtain a relative vertical displacement profile for the superstructure and girders in order to investigate the force path along the deck and the moment distribution between the girders. Therefore, string potentiometers were mounted between the bottom side of the flanges of the designated girders and the strong floor, as shown in Figure 5.37. Only half of the bridge was instrumented as shown in Figure 5.38. A string potentiometer was placed next to each actuator, located between the floor and the abutment, in order to verify the displacement readings provided by the actuator.

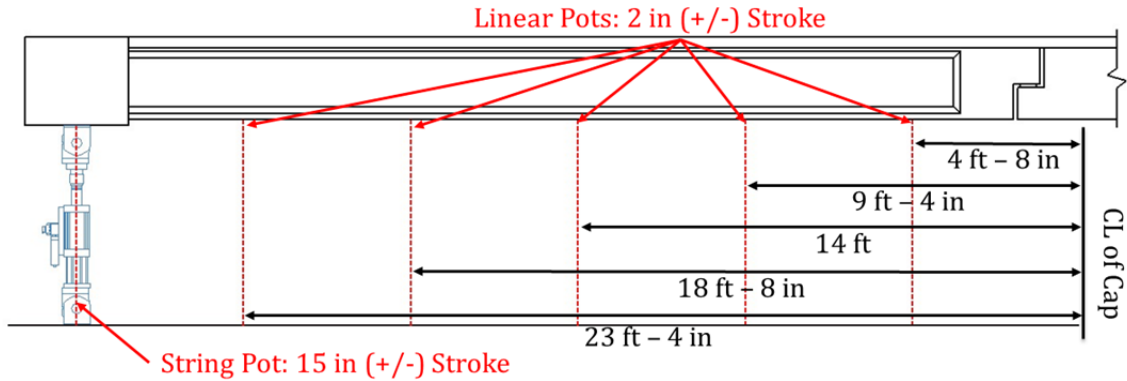


Figure 5.37: Phase 1 Vertical Girder Displacement Device Locations

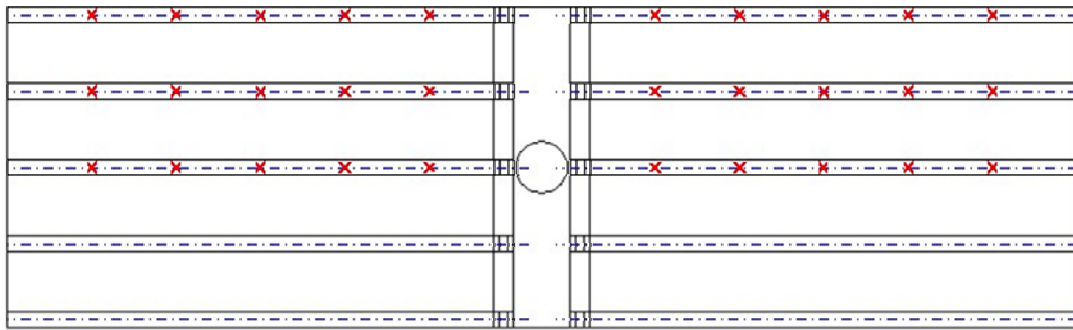


Figure 5.38: Locations of Vertical Displacement Devices along the Girder Length During Phase 1 of Testing

#### 5.2.2.2.2 Phase 2

The vertical displacements of the girders were also measured during Phase 2 of the testing. However, since the expected displacements were larger than those for Phase 1, a combination of string and linear potentiometers with a larger stroke, as shown in Figure 5.39, replaced many of the potentiometers that were specified for Phase 1. It should be noted that, in order to reduce the setup time, the locations of the potentiometers were the same and one set of potentiometers was removed. Additionally, the same girders that were instrumented for Phase 1 were instrumented for Phase 2.

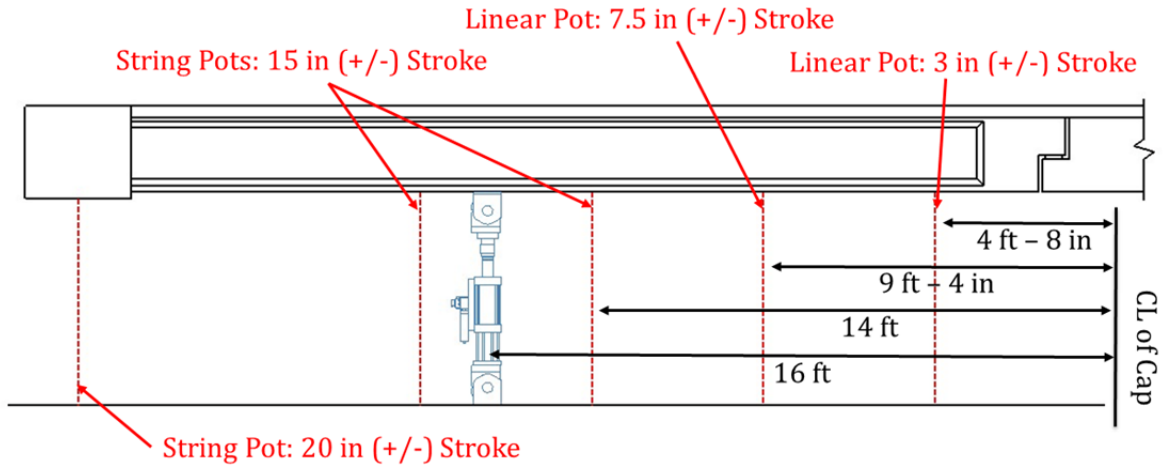


Figure 5.39: Phase 2 Vertical Girder Displacement Device Locations

### 5.2.2.3 Column Curvature and Growth

The curvature of the column, mostly within the plastic hinge regions, was recorded by placing a series of four linear potentiometers, spaced at 6 in. on center, along the extreme tension and compression fibers of the column, as shown in Figure 5.40. An additional linear potentiometer was mounted along the length of the column on both its East and West sides in order to measure any longitudinal column growth.

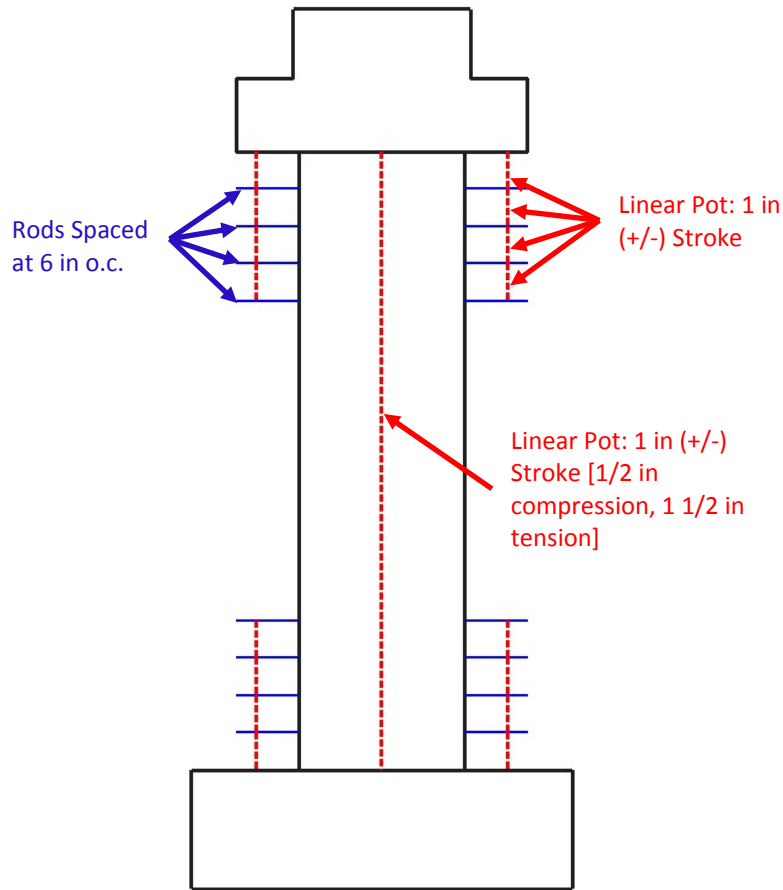


Figure 5.40: Column Curvature and Growth Device Locations

#### 5.2.2.4 Cap Beam Twist and Dilation

The angle of rotation due to torque acting along the length of the column, between girders, was measured via rotation devices placed at the midpoint between girders and along the centerline at the bottom of the cap beam, as shown in Figures 5.41 and 5.42. The sensitivity of these devices needed to be high, as the expected rotations are relatively small. Linear potentiometers were also placed between the rods, to which the rotation devices were mounted, in order to measure the dilation of the cap along its longitudinal axis. Since the column interfered with the linear potentiometers running along the length of the cap beam, the rods and linear potentiometers in the vicinity of the column were placed on the top of the cap beam as shown in Figure 5.41. Only half of the cap beam was instrumented in this manner, again due to symmetry. Additionally, a rotation device was mounted to the rod directly above the column in order to measure the rotation of the cap beam. Finally, a rotation device was placed on each end of the cap beam in order to further measure any twist.

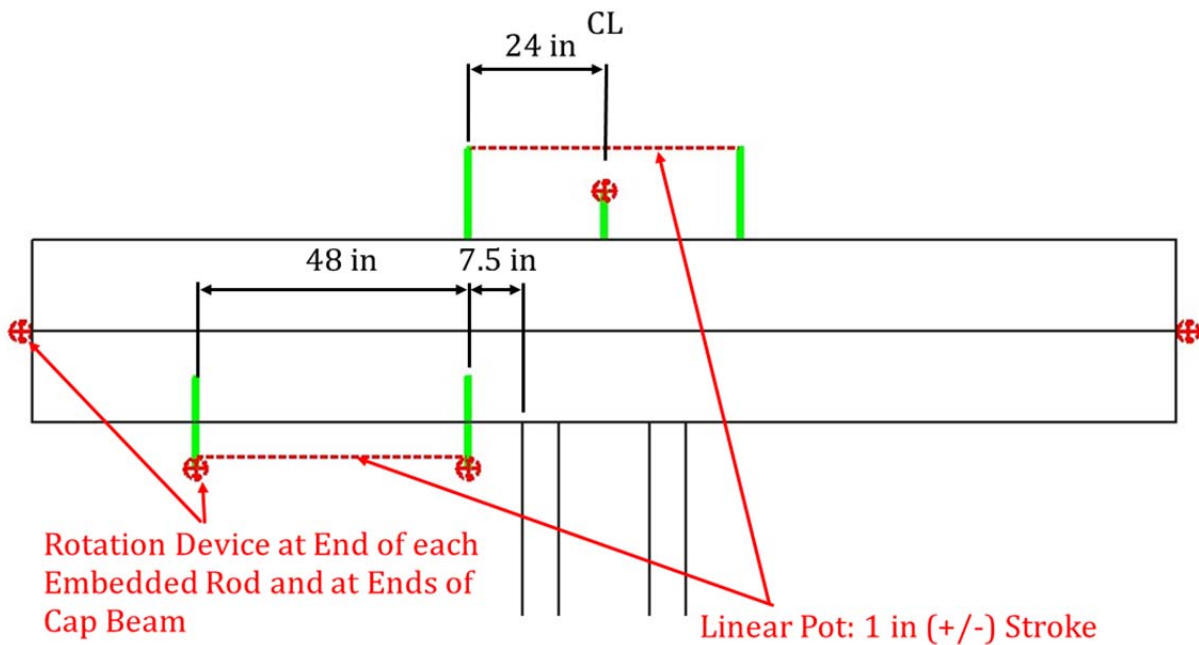


Figure 5.41: Profile View of Cap Beam Twist and Dilation Instrumentation Scheme

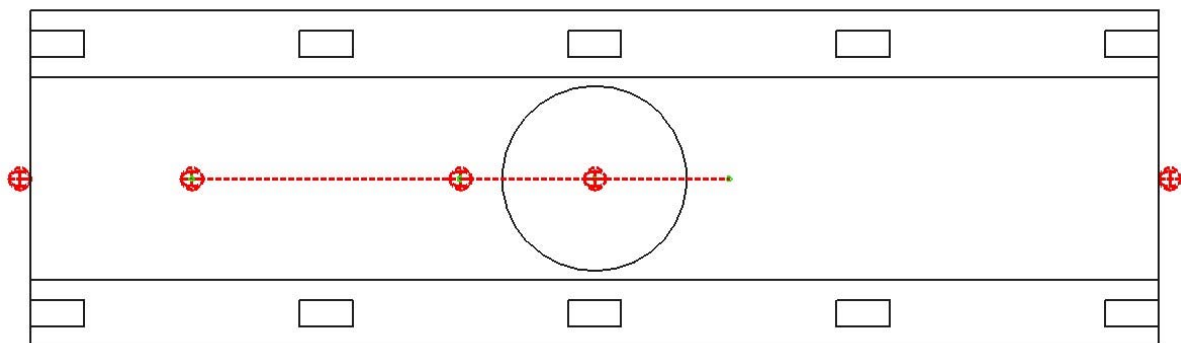


Figure 5.42: Plan View of Cap Beam Twist and Dilation Instrumentation Scheme

#### 5.2.2.5 Connection Rotation and Neutral Axis Depth

Similar to the strain gauge plan, the instrumentation within the connection region was critical. A linear potentiometer was mounted on the underside of the superstructure spanning the connection between the girder and the cap, as shown in Figure 5.43. A rotation device was also mounted on the rod that was embedded in the girder and used in mounting the aforementioned linear potentiometer. Together, the linear potentiometer and the rotation device were used to

determine the neutral axis and rotation of the connection at each girder. One center, intermediate, and exterior girder on each side of the cap was instrumented in this manner.

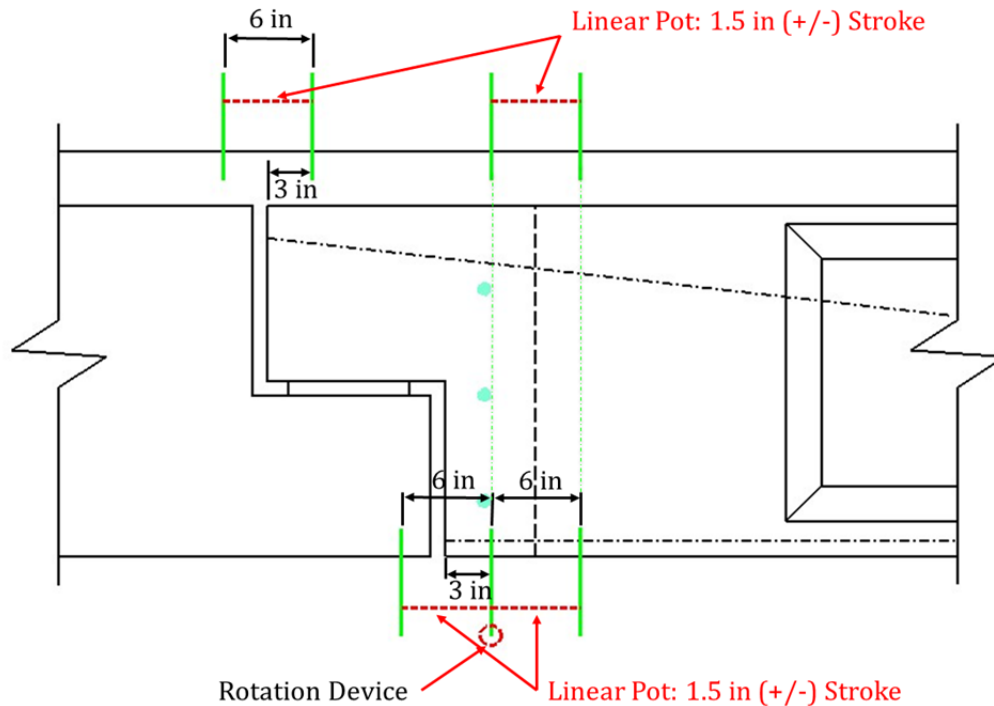


Figure 5.43: Girder-to-Cap Beam Connection Instrumentation Scheme

#### 5.2.2.6 Girder Curvature

The linear potentiometers at the bottom of the girders, as detailed in the previous section, were also used to determine the curvature of the girders near the connection region. An additional linear potentiometer was placed along the bottom of the girder away from the connection. A second linear potentiometer was placed at the top of the girder, directly above the additional pod that was added to the bottom. A third linear potentiometer was placed above the girder and spanned the interface between the girder and cap beam. These details are shown in Figure 5.43. One center, intermediate, and exterior girder on each side of the cap received this instrumentation.

#### 5.2.2.7 Lateral Displacement Measurement Between Girders

Since some lateral displacement between the girders was observed during the preliminary finite element analysis of the superstructure, string potentiometers were placed between girders

at a distance of 16 ft from the center of the cap beam, as shown in Figure 5.44. Both the center and one of the interior girders as well as one of the interior and exterior girders received this configuration. The lateral displacement between girders was only measured on the as-built side of the connection.

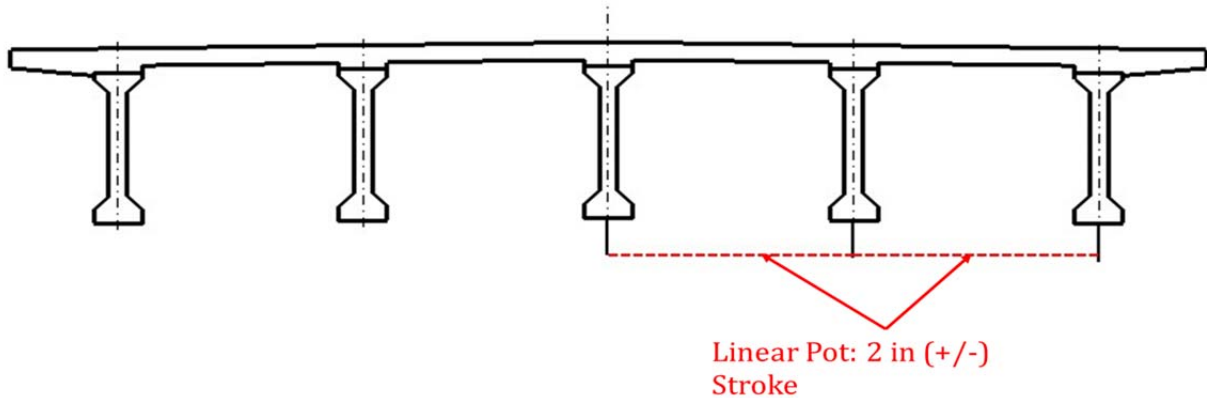


Figure 5.44: Lateral Displacement between Girders Device Locations

#### 5.2.2.8 Improved Connection Strand Slip

As noted previously, the untensioned strands that were used in the improved connection detail were incorrectly terminated at the face of the diaphragm on the as-built connection side of the bent cap. However, this did have one benefit, in that it allowed any slip of the strands to be measured. One strand directly East of the center girder and one strand directly East of the West intermediate girder were therefore mounted with a linear potentiometer in order to measure any strand slip. The potentiometers were mounted to the strand via a circular clamp around the strand, which then measured any displacement relative to the face of the diaphragm, as shown in Figure 5.45.

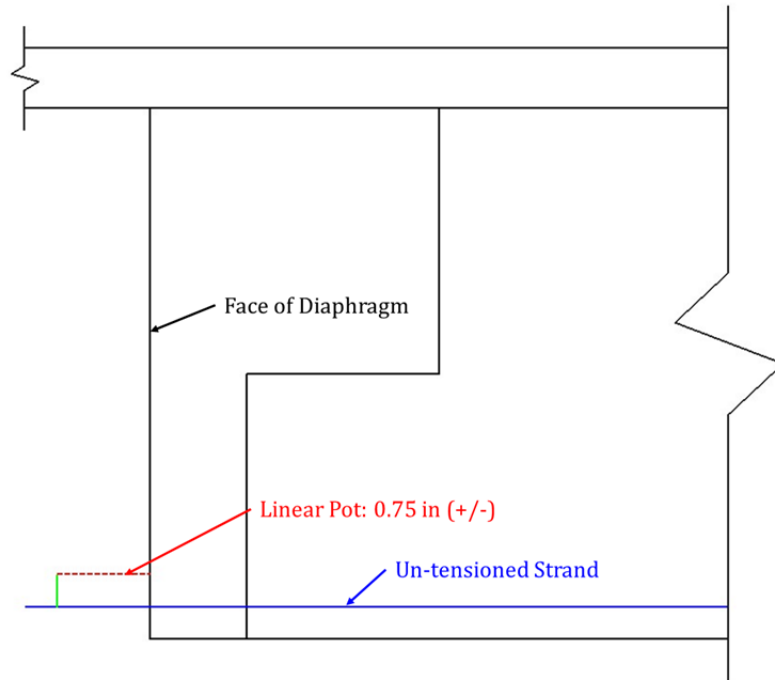


Figure 5.45: Strand Slip Device Location

#### 5.2.2.9 Footing Movement

In order to ensure that the footing did not experience any displacement during the testing, one linear potentiometer was placed between the footing and the floor in the push direction. An additional linear potentiometer was placed perpendicular to the loading direction on each side of the footing. These linear potentiometers were placed diagonally from each other in order to detect any torsion in the footing as well, as shown in Figure 5.46.

The uplift of the footing was also monitored by placing a linear potentiometer on the North and South side of the footing, which was mounted to the floor as a point of reference, as shown in Figure 5.47.

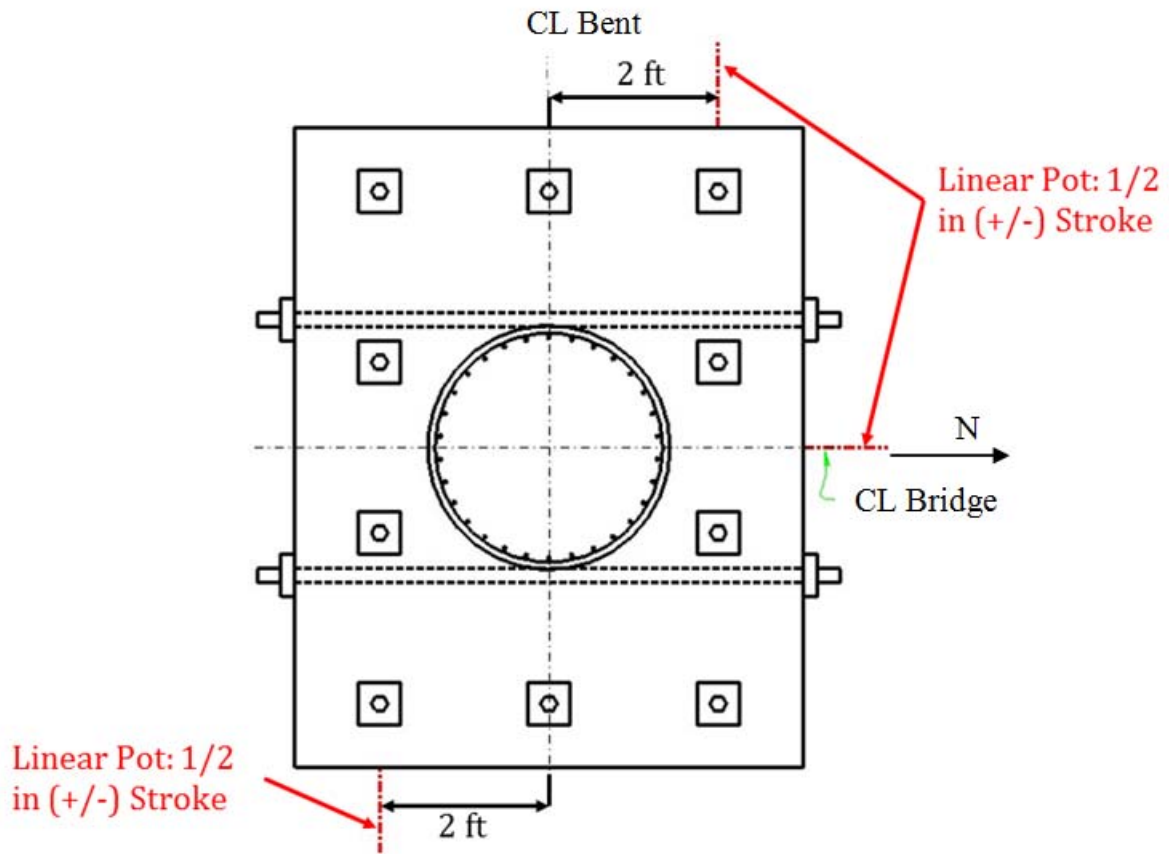


Figure 5.46: Footing Displacement Device Locations

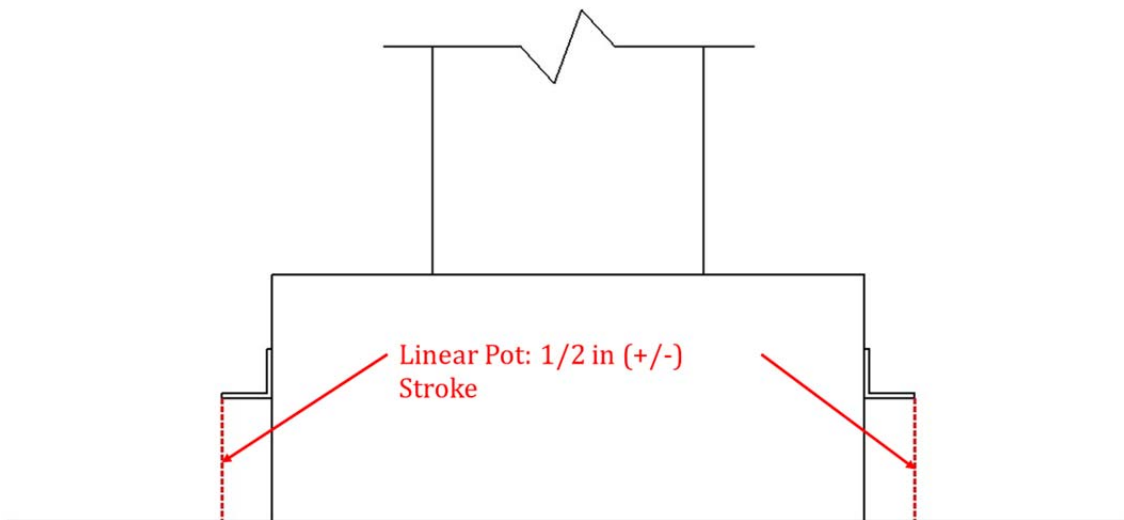


Figure 5.47: Footing Uplift Device Locations

### 5.3 Material Testing

During each concrete pour, unconfined test cylinders were cast in order to establish the compressive strength of the concrete. The compressive strength was determined for each pour at the age of 7, 14, 21, and 28 days, as well as on the day of testing. The average strength of three cylinders was taken as the compressive strength in each case and is represented in Table 5.1.

Table 5.1: Measured Unconfined Concrete Strengths

Member	$f'_c$ (ksi)					
	7 Day	14 Day	21 Day	28 Day	Day of Testing (Phase 1)	Day of Testing (Phase 2)
Footing	3.94	4.36	4.73	4.89	6.70	6.68
Column	3.91	4.36	4.80	5.04	6.81	7.07
Bent Cap	4.27	4.78	5.06	5.27	7.60	7.39
Girders (Average)	6.00	7.36	8.08	8.94	11.36	11.13
North Abutment	-	-	5.31	5.49	7.75	7.89
South Abutment	-	-	5.48	5.59	8.03	7.98
Partial Diaphragm	4.27	4.67	5.28	5.45	6.86	7.31
Deck, Haunch, and Remainder of Diaphragm	4.06	4.79	4.88	5.28	5.67	5.91

Three samples for each batch and bar size of the steel reinforcement were also collected and tested, under a uniaxial tension, in order to obtain the stress-strain response and thus the average yield and ultimate strength and strain parameters for each bar size. Due to the fact the samples for the spirals within the column were previously bent in the shape of a spiral, and had therefore already experienced yielding, they did not have a well-defined yield point or plateau. As a result, the yield stress was approximated at strain of 0.5% in accordance with ASTM A370 specifications (Collins & Mitchell, 1991). The obtained yield stress was then divided by the modulus of Elasticity,  $E_s$ , in order to obtain a theoretical yield strain. The results of the reinforcement testing are summarized in Table 5.2. It should be noted that  $\sigma_y$  and  $\sigma_u$  represent yield and ultimate stress, or strength, and  $\epsilon_y$  and  $\epsilon_u$  represent yield and ultimate strain, respectively. Additionally, a welded wire mesh was used for the girder #3 stirrup reinforcement, which explains the different yield and ultimate stress-strain behavior.

Table 5.2: Reinforcement Material Properties

Specimen		$f_y$ (ksi)	$\epsilon_y$ (in./in.)	$f_u$ (ksi)	$\epsilon_u$ (in./in.)
Abutment	#3	64.7	0.00232	104.5	0.109
	#4	64.7	0.00230	91.9	0.125
	#5	64.2	0.00255	92.2	0.119
	#6	61.7	0.00239	89.5	0.123
Bent Cap	#3	64.6	0.00206	104.5	0.113
	#4	65.4	0.00236	92.5	0.128
	#6	62.6	0.00221	92.2	0.122
Column	#3	59.7	0.00206	97.0	0.121
	#6	62.3	0.00238	92.4	0.115
Deck	#3	62.4	0.00216	101.2	0.111
	#4	61.3	0.00208	89.1	0.127
	#5	63.6	0.00232	91.0	0.130
Footing	#4	64.1	0.00198	91.4	0.124
Girders	#3	71.4	0.00246	76.7	0.0161
	#4	71.3	0.00246	94.4	0.0963

## 5.4 Phase 1 Test

Phase 1 of the testing involved a quasi-static, cyclic test of the 50% scale test specimen. The goal of the testing was to quantify the overall structural behavior of the unit when subjected to seismic loading conditions. Both the as-built and improved girder-to-cap connections were tested simultaneously during this phase.

### 5.4.1 Actuator Setup

The actuator setup for the Phase 1 test consisted of a total of eight actuators. Two horizontal and two vertical actuators were placed at each abutment. The horizontal actuators were placed in a “V” configuration in order to provide more stability against rotation of the superstructure about its vertical axis, when testing the effects of seismic loading by displacing the superstructure horizontally, as shown in Figure 5.48. The vertical actuators provided structural stability, imposed the correct gravity load effects in the test unit, and ensured that the abutment maintained a constant height relative to the top of the column. Maintaining a constant height relative to the top of the column was important in order to prevent the growth of the column, as the plastic hinges developed, from introducing extraneous loads into the system.



Figure 5.48: Horizontal Actuator Configuration used during Phase 1 Testing at Each End of the Test Unit

## 5.4.2 Loading Protocol

### 5.4.2.1 Application of Stage 1 Hold-Down

In order to prevent possible cracking of the column, the following loading protocol was followed when applying the Stage 1 hold-down force: 30% of the total load was applied to the north span; 70% of the total load was applied to the south span; 100% of the total load was then applied to the north span; and finally, 100% of the total load was applied to the south span.

### 5.4.2.2 Application of Stage 2 Hold-Down

Though cracking of the column was not as great of a concern during the application of the Stage 2 hold-down force, as the increase in moment was less than that which was needed to cause flexural cracking within the column, the following load protocol was followed simply out of precaution: 50% of the total load was applied to the north span; 100% of the total load was applied to the south span; and 100% of the total load was finally applied to the north span.

### 5.4.2.3 Horizontal Actuator Protocol

As mentioned previously, the test unit was cycled through a number of progressively increasing displacement targets during the Phase 1 test. Initially, the test unit was subjected to low-level elastic displacements, during which the specimen was cycled through a force of positive and negative  $0.25F'_y$ ,  $0.5F'_y$ , and  $0.75F'_y$ , where  $F'_y$  corresponded to the condition at which the reinforcement within the plastic hinge region of the column was expected to yield first.

Following the aforementioned preliminary cycles, the test unit was cycled through the following levels of displacement ductility,  $\mu_{\Delta}$ , within the column plastic hinges:  $\pm 1$ ,  $\pm 1.5$ ,  $\pm 2$ ,  $\pm 3$ ,  $\pm 4$ , and  $\pm 6$ . In order to more accurately capture the cyclic behavior of the structure, including any possible strength degradation, each level of displacement ductility was subjected to three cycles. Since the maximum expected displacement ductility was approximately 5.4, the actual condition of the specimen at a displacement ductility level of 6 was not well known. It is likely that the plastic hinges within the column could achieve a ductility level higher than what was predicted, given the various assumptions that were made for material properties, especially the confined concrete behavior, which were used in obtaining the expected maximum ductility. Therefore, provided that the column was not near the point of failure at a ductility level of 6, an additional three cycles at a ductility level of 7.5 was planned. Table 5.3 provides the expected displacements and the corresponding lateral force resistance, as obtained from the SAP2000 grillage model, at each force and ductility level during testing.

Table 5.3: Preliminary Horizontal Testing Protocol Established for Phase 1 Testing

Cycle Level	Expected	
	$\Delta_{\text{absolute}}$ (in)	Absolute Actuator Force (kips)
$0.25 F'_y$	0.14	40
$0.5 F'_y$	0.30	80
$0.75 F'_y$	0.46	120
$\mu_{\Delta} = \pm 1$	0.94	198
$\mu_{\Delta} = \pm 1.5$	1.41	225
$\mu_{\Delta} = \pm 2$	1.89	235
$\mu_{\Delta} = \pm 3$	2.83	247
$\mu_{\Delta} = \pm 4$	3.77	257
$\mu_{\Delta} = \pm 6$	5.66	270
$\mu_{\Delta} = \pm 7.5$	7.07	278

#### 5.4.2.4 Vertical Actuator Protocol

In order to ensure that the vertical actuators maintained stability in the system, without introducing any extraneous loads into the column, it was important to program the vertical actuators to accommodate any growth within the column. Therefore, at various horizontal

displacement levels, the column growth was approximated per the procedure outlined in Holombo, Priestley, & Seible (1998).

The column was divided into three sections as shown in Figure 5.49, consisting of two inelastic sections, defined by the respective plastic hinge lengths at the top and bottom of the column, and the elastic portion of the column, located between the plastic hinges. Within the plastic hinge regions, the curvature was assumed to be constant, while it varied linearly over the elastic region of the column. The corresponding axial strains within each section were obtained by using the curvature,  $\phi$ , to calculate the strain at the centerline of the column,  $\epsilon_{cl}$ , per Equation 5.1, where  $D$  and  $y_{N.A.}$  correspond to the column diameter and neutral axis depth of the column cross-section, respectively.

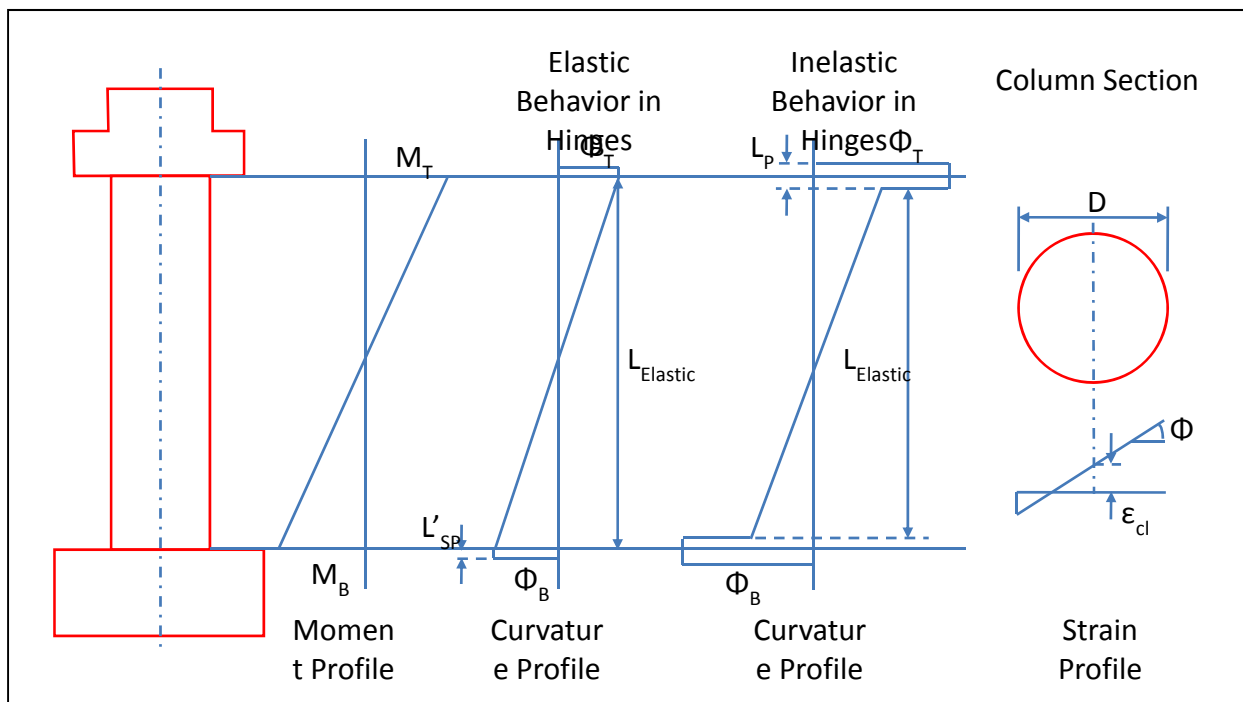


Figure 5.49: Estimating Column Growth in the Vertical Direction

$$\epsilon_{cl} = \phi \left( \frac{D}{2} - y_{N.A.} \right) \quad (5.1)$$

The curvature and neutral axis depths were obtained via the moment curvature analysis of the column section within each plastic hinge region. However, for the elastic portion of the column, an average curvature was calculated via Equation 5.2, where  $I_{cr}$  represents the cracked moment of inertia of the column at first yield and an average absolute moment along the length of the column,  $M_{ave}$ , was computed per Equation 5.3. As stated, both the moment and curvature were assumed to vary linearly along the elastic portion of the column; therefore, an average moment and curvature were used to calculate the growth of the elastic portion of the column, which simplified the integration of growth over the region. The values  $M_T$  and  $M_B$  in Equation 5.3 represent the moments in the top and bottom column hinges, respectively, and were obtained via the SAP2000 grillage analysis at the corresponding level of horizontal displacement. Additionally, the value for the neutral axis depth over the elastic portion of the column was approximated as a value of  $D/4$ .

$$\phi_{ave} = \frac{M_{ave}}{EI_{cr}} \quad (5.2)$$

$$M_{ave} = \frac{M_T^2 + M_B^2}{2(M_T + M_B)} \quad (5.3)$$

Once the strain at the centerline of the column was obtained for each section, it was multiplied by the length of the respective section,  $L_T$ ,  $L_B$ , and  $L_{Elastic}$ , in order to obtain the column growth for the section, per Equation 5.4. The values for  $L_T$  and  $L_B$  were calculated per Equation 4.5. The sum of the growth over each section was then taken as the overall growth of the column.

$$\Delta_{Growth} = \epsilon_{cl}L \quad (5.4)$$

It should be noted, however, that Equation 5.4 is only valid in the inelastic regions after the hinges have experienced inelastic behavior, as the equation for the plastic hinge length accounted for both elastic and plastic strain penetration into the column-to-cap and column-to-footing joint regions. Therefore, for displacement levels less than the expected first yield condition, the value of  $L'_{sp}$  was used for the length of each hinge, as it only accounted for the elastic penetration effects into the joint region, per Equation 4.4.

Since the superstructure flexibility varied between the as-built and improved connection sides, it was appropriate to calculate a horizontal displacement vs. column growth curve for each displacement direction, pushing to the south to engage the as-built positive moment connection or pulling to the north to engage the improved positive moment connection detail. The resulting horizontal displacement vs. column growth curves are shown below in Figure 5.50. It should be noted that when one positive moment connection was tested in a given loading direction, the other side's negative moment connection was also tested. For example, both the positive moment connection on the as-built side and the negative moment connection on the improved side were tested simultaneously when the superstructure was pushed to the South.

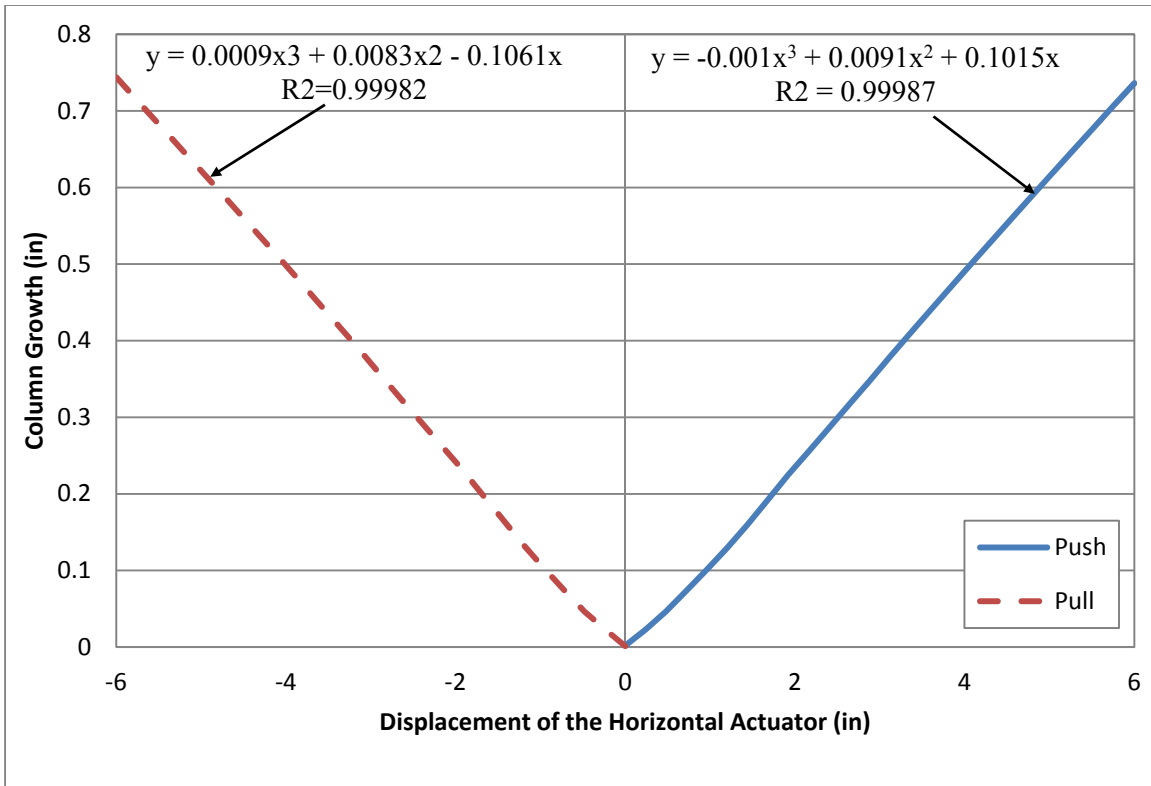


Figure 5.50: Horizontal Actuator Displacement vs. Column Growth

The aforementioned growth curves were used to program the vertical actuators using the best fit equations included in Figure 5.50, in conjunction with active feedback from the external instrumentation, in order to maintain vertical stability within the system.

### 5.4.3 Hold-Down Forces

In order to accurately subject the test unit to the same type of loading that would be experienced by the prototype, it was necessary to apply a vertical hold-down force on each side of the bent cap. The discrepancy between the forces experienced in the test unit and prototype was due to the fact that the test unit consisted of a half span on each side of the cap and that the dimensional scaling applied to the test unit did not result in correctly scaled gravity load effects. Additionally, loads that were applied to the prototype bridge, such as the future wearing surface and barriers, were not modeled in the test unit. Therefore, without compensating for these dissimilarities, the forces and behavior experienced by the test unit would not adequately compare to the prototype structure, as seen in Figures 5.51 and 5.52. It is important to note that the moment and shear profiles shown in these figures have been scaled to the test unit and were based on a preliminary structural analysis of the center girder. The dashed lines represent the location at which girder bears on the bearing pad under its dapped end and on the corbel of the inverted-T cap beam.

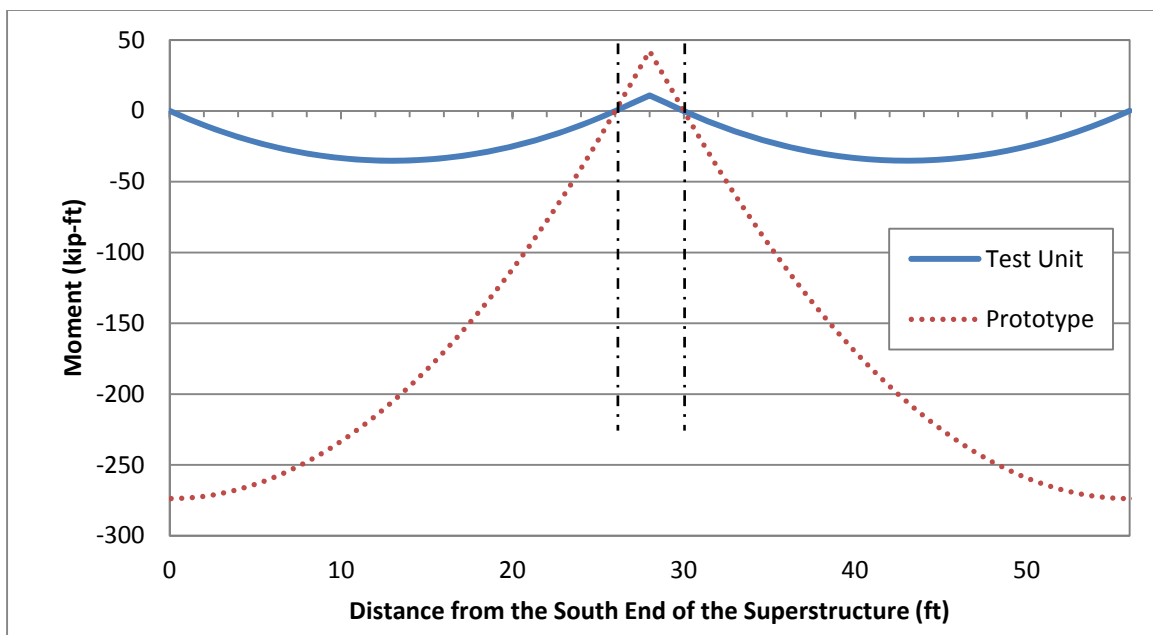


Figure 5.51: Stage 1 Prototype-to-Test Unit Moment Profile Comparison along the Length of the Superstructure without Scaling Compensation

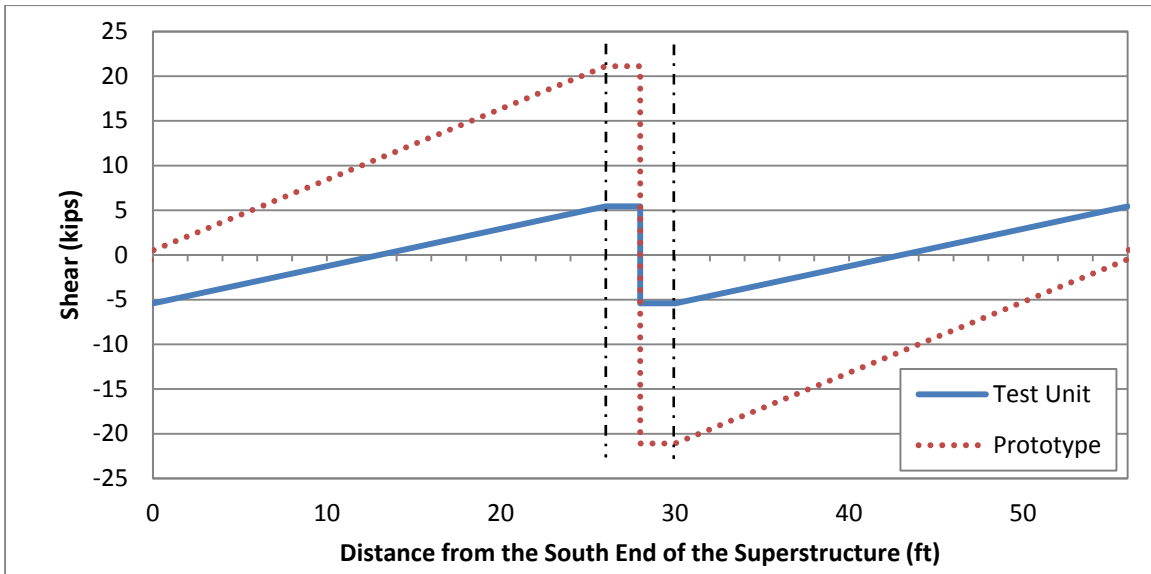


Figure 5.52: Stage 1 Prototype-to-Test Unit Shear Profile Comparison along the Length of the Superstructure without Scaling Compensation

As a result, a whiffle tree arrangement was placed on each side of the column at a distance of 16 feet from the center of the column along the span in order to apply and distribute a hold-down force across the width of the deck and into each girder, as seen in Figure 3.1. This distance was selected based primarily on the anchor-hole layout on the floor of the lab at UCSD as well as the fact that it provided good agreement between the shear and moment profiles within the connection region when the hold-down force was applied. A more detailed description of the whiffle tree is provided in the proceeding section.

A structural analysis of the superstructure indicated that, in order to provide shear and moment agreement within the connection, a hold-down force of 33.4 kips per girder (167 kips total on each span) had to be applied during the construction condition in which the girders were simply supported, which was referred to as “Stage 1.” As shown below, this hold-down force was used to correct the self-weight of the girders. The adjusted moment and shear profiles for Stage 1, after the application of the hold-down force, are presented in Figures 5.53 and 5.54.

Once the superstructure was made continuous, known as “Stage 2,” through the hardening of the deck, an additional hold-down force of 11.8 kips per girder (59 kips total on each span) was applied in order to provide a final agreement between the shear and moments

experienced between the Test Unit and Prototype structures. This hold-down force was also critical in achieving moment agreement within the connection region, which was of primary concern. It should also be noted that the Stage 2 hold-down force represented the additional loads due to the weight of the barriers and other objects that would be experienced by the prototype structure, but were not present on the test unit. Figures 5.55 and 5.56 show the comparison of the moment and shear diagrams after the Stage 2 hold-down. The final adjusted moment and shear diagrams, with the inclusion of the expected seismic inertia forces, which compensate for scaling and the absence of loads observed in the prototype structure are presented below in Figures 5.57 and 5.58.

It is important to note that the goal of the hold-down force was not to achieve complete shear and moment agreement over the entire span. Instead, the intent was only to provide agreement within the area surrounding regions of focus, which for the purposes of the testing were the girder-to-cap connection regions. Furthermore, it may be noted that some of the profiles for the test unit after applying the hold-down forces were greater than those for the prototype. These profiles were deemed acceptable, as the subsequent response of the test unit would be a conservative representation of what would otherwise be expected. Therefore, the results and conclusions could be applied to a full-scale prototype structure with a high degree of confidence.

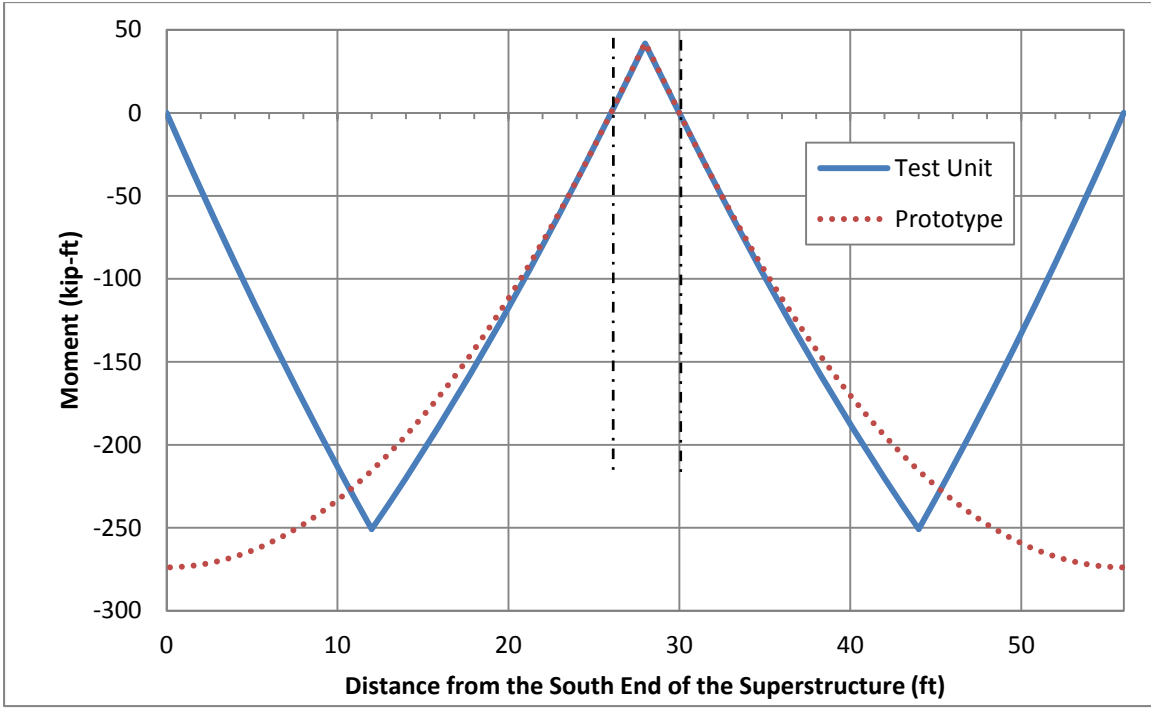


Figure 5.53: Stage 1 Prototype-to-Test Unit Moment Profile Comparison along the Length of the Superstructure after Applying Stage 1 Hold-Down Force

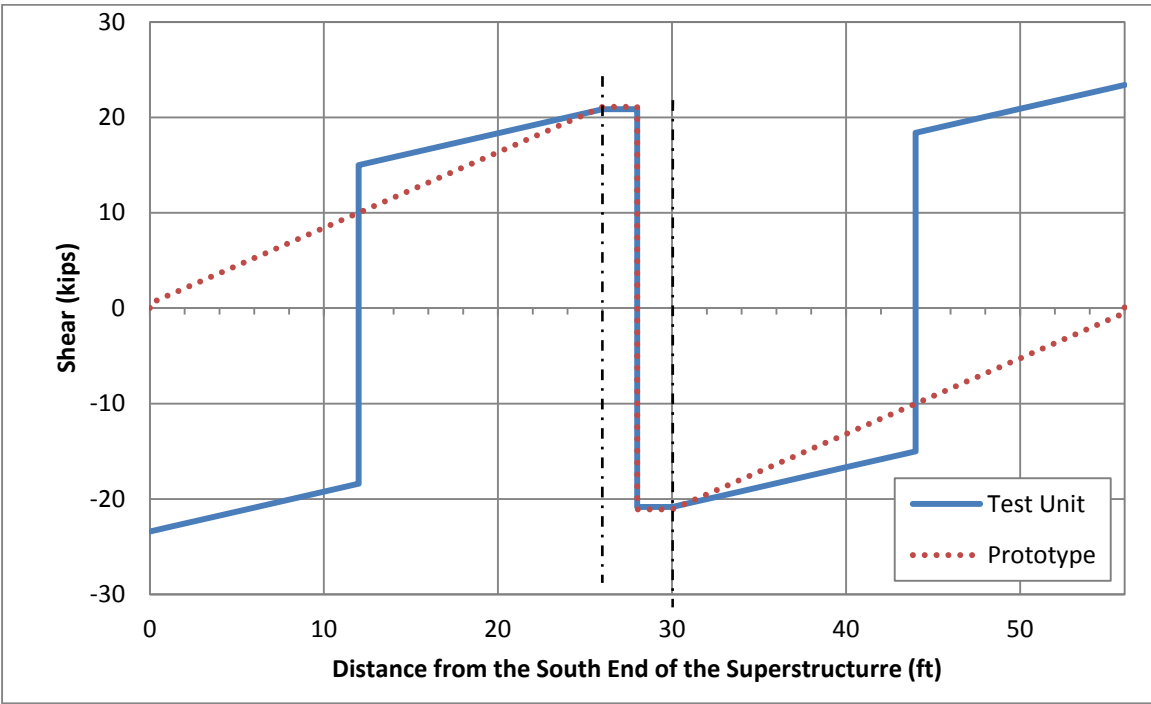


Figure 5.54: Stage 1 Prototype-to-Test Unit Shear Profile Comparison along the Length of the Superstructure after Applying Stage 1 Hold-Down Force

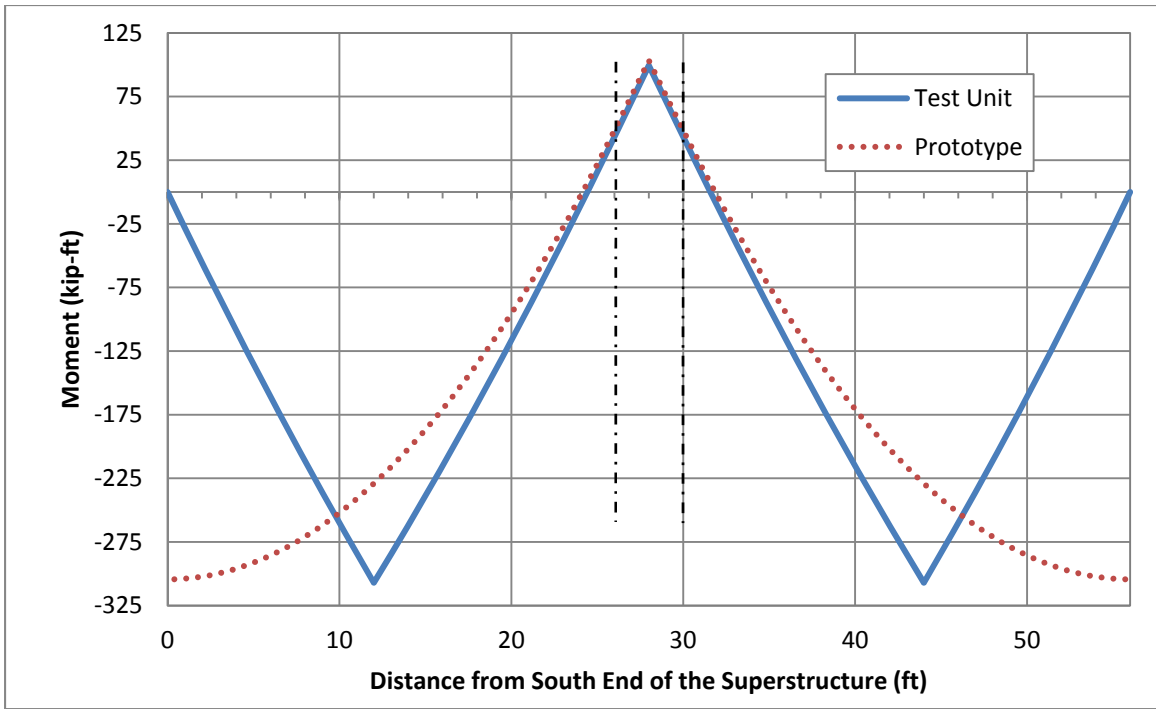


Figure 5.55: Stage 2 Prototype-to-Test Unit Moment Profile Comparison along the Length of the Superstructure after Applying Additional Stage 2 Hold-Down Force

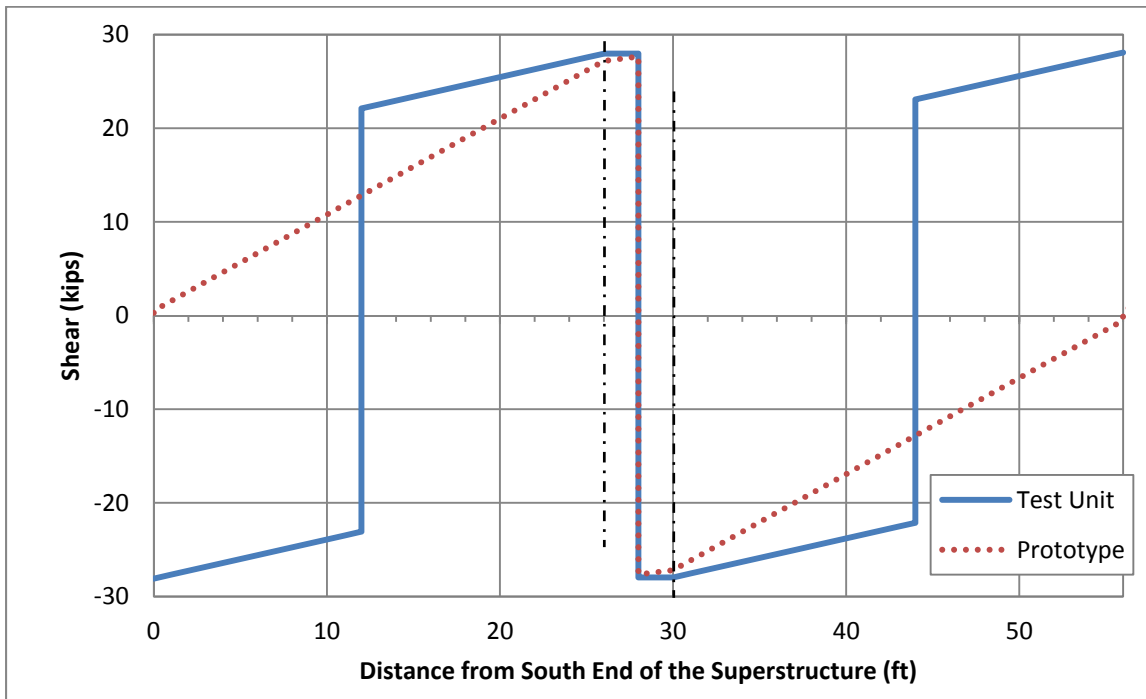


Figure 5.56: Stage 2 Prototype-to-Test Unit Shear Profile Comparison along the Length of the Superstructure after Applying Additional Stage 2 Hold-Down Force

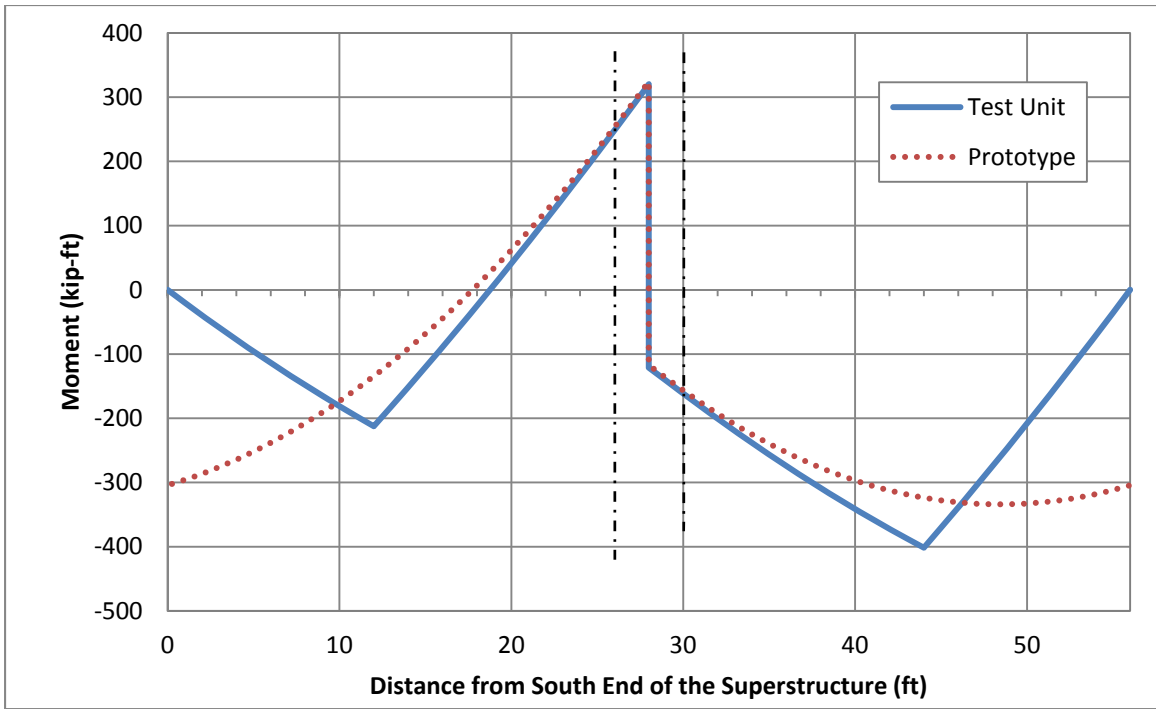


Figure 5.57: Final Prototype-to-Test Unit Moment Profile Comparison along the Length of the Superstructure after Applying Hold-Down Forces and Seismic Effects

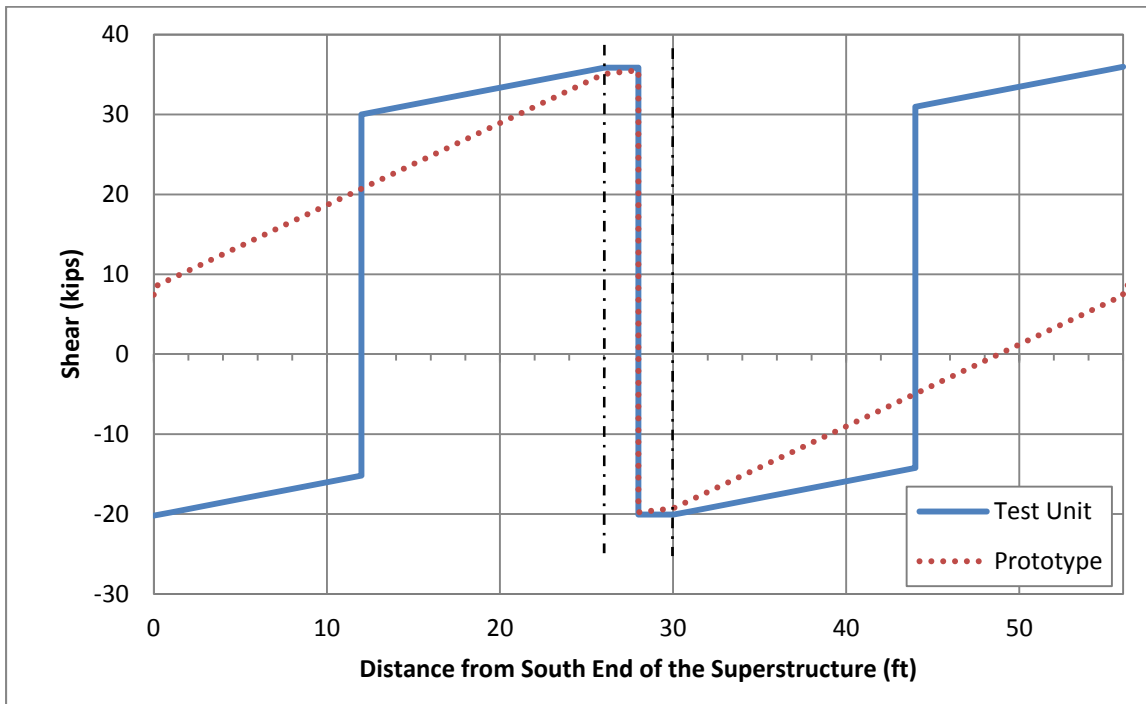


Figure 5.58. Final Prototype-to-Test Unit Shear Profile Comparison along the Length of the Superstructure after Applying Hold-Down Forces and Seismic Effects

### 5.4.3.1 Whiffle Tree

The purpose of the whiffle tree was to evenly distribute two applied jacking forces to each of the five girders in a given span of the test unit to simulate the gravity load effects of the prototype structure as accurately as possible. The whiffle tree was designed as a series of built-up HSS sections, which were placed next to each other and connected via welded plates in order to accommodate the series of rods that connected each beam, as shown in Figure 5.59. A structural analysis was performed in order to determine the location of the rods within the tree arrangement required to achieve an equal load in all five of the girders in a given span. A jacking force was applied to each of the rods that passed through the floor in order to achieve the appropriate hold-down force as mentioned above; that force was then distributed to the bridge superstructure through the whiffle tree.

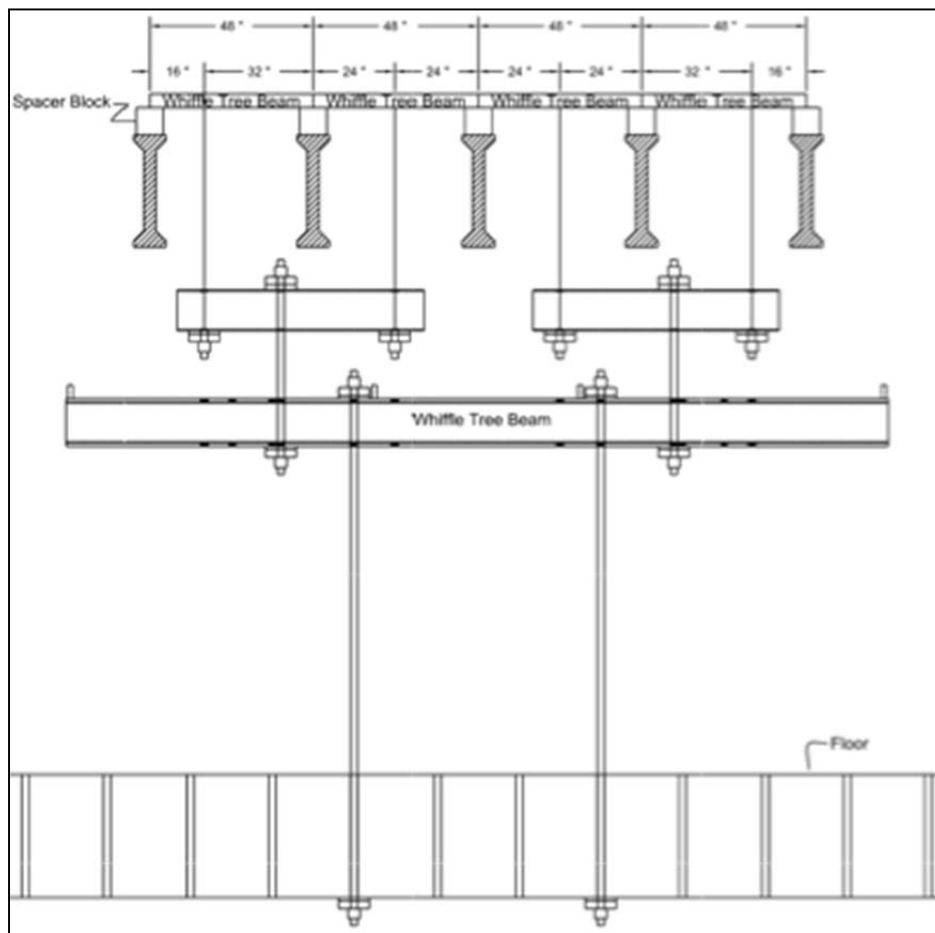


Figure 5.59: Whiffle Tree Arrangement used to Impose Additional Vertical Loads to the Test Unit during Phase 1 Testing

Holes were placed in the deck in order to accommodate the rods that passed through the superstructure and tied into the beams that were placed on the topside of the girders. Spacer blocks were also included in order to provide a bearing surface for the aforementioned beams and to elevate them above the height of the deck, as shown in Figure 5.60. The spacer blocks were constructed by placing a small 8-inch tall HSS section on top of each girder, centered at a distance of 16 feet from the centerline of the cap beam. The steel beam sections were placed on spacers, approximately  $\frac{1}{4}$  in. thick, and were filled with hydrostone. Each spacer block was leveled and shimmed such that they were all at the same elevation on each girder. This configuration provided an even bearing surface both at the interface between the steel HSS section and the girder as well as on the topside of the HSS section and the whiffle tree top beam. Additionally, the stirrups protruding out of the top of the girders, that were located within the HSS spacer section, were left straight and were surrounded by hydrostone in order to provide an additional bond between the spacer block and the girder. It should be noted that the large beam at the bottom of the whiffle tree was also designed so that it could be placed directly beneath the girders and used to mount the vertical actuators, while tying the superstructure together during Phase 2 of the testing.

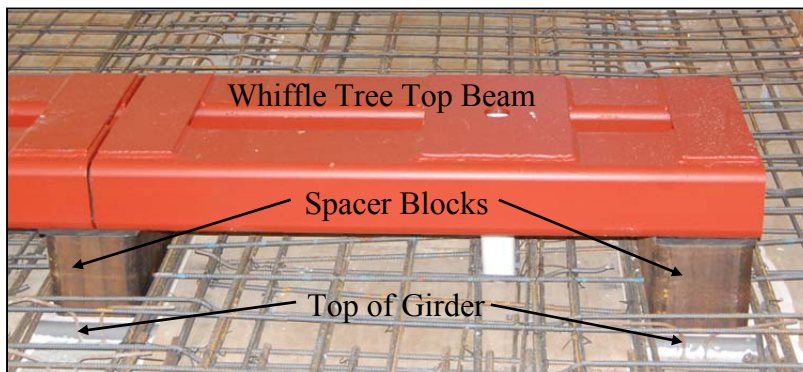


Figure 5.60: Details of Whiffle Tree Spacer Blocks and Top Beams

## **5.5 Phase 2 Test**

As stated previously, Phase 2 of the testing involved a cyclic vertical push and pull test of each span simultaneously. This phase of the testing focused primarily on the localized behavior of each connection to assess its capacity.

### **5.5.1 Actuator Setup**

Once Phase 1 of the testing was completed, the horizontal actuators on the South end of the superstructure were removed, while the horizontal actuators on the North end remained in place in case there was a need for additional stability within the system. The hold-down forces and whiffle tree were removed from the specimen and both sets of vertical actuators at the ends of the specimen were moved in to the location that the whiffle tree previously occupied. As mentioned earlier, the main beam of the whiffle tree was designed such that it could accommodate the mounting of the vertical actuators.

### **5.5.2 Loading Protocol**

Both the removal of the hold-down forces and the change in boundary conditions, between Phase 1 and 2 due to the placement of the actuators, caused residual moments to develop within the connections, resulting in an unrealistic moment value within the connections. Therefore, in order to correct for the aforementioned effects, the total load in both the North and South sets of actuators was increased slightly to approximately 90 kips of upward force before the start of testing. This was done based on analytical results, which indicated that 90 kips of vertical load was required in each span in order to achieve the same moment that was at the girder-to-cap interface at the end of construction, with all of the hold-down forces applied, which was defined as the unstressed state for the test unit.

Once the required actuator load was applied to each span, the superstructure was displaced through the following displacement levels, listed in the order in which they were performed: -0.25 in., -0.5 in., -0.75 in., -1 in., -1.5 in., +0.25 in., +0.5 in., +0.75 in. (the negative sign refers to a vertical downward deflections while the positive sign corresponds to a vertical upward deflection). This was done in order to capture the initial stiffness and elastic behavior of the system, so that an appropriate displacement increment and magnitude could be selected for the cyclic displacement levels. Following the initial low-level displacement increments, both

superstructure spans were then cycled simultaneously through the following positive and negative displacement cycles: +1/-2 in., +1.5/-3 in., +2/-4 in., and +3/-6 inches. Each of the aforementioned cycles consisted of three cycles to the given positive and negative displacements, with the exception of the final cycle. Since significant degradation of the as-built connection was observed at the final displacement level, only one half-cycle was used at +3 in. while two half-cycles were performed at -6 in. It should be noted that the positive and negative displacement magnitudes were not the same, as both connection details had a higher capacity for negative moments than for positive moments.

## Chapter 6. Test Results

### 6.1 Phase 1 Test Observations

During the lateral load testing, the extreme longitudinal bars in the column began yielding at an average lateral displacement of 0.46 inches, which was established based on the measured strains in the extreme column longitudinal reinforcement in the push and pull direction of loading during testing at  $\pm 1.0F'_y$ . By combining this information with the theoretical first yield and idealized yield lateral force resistance, the idealized yield displacement for the test unit was defined as 0.7 inches. Consequently, the displacement at each ductility level was obtained as a factor of 0.7 inches. Table 6.1 outlines the updated loading protocol during Phase 1 testing.

Table 6.1: Updated Horizontal Test Protocol for Phase 1 Testing

Cycle Target	$\Delta$ (in)	Average Absolute Measured Actuator Force (kips)	Number of Cycles
$\pm 0.07 F'_y$	$\pm 0.05$	40	1
$\pm 0.17 F'_y$	$\pm 0.12$	80	1
$\pm 0.36 F'_y$	$\pm 0.25$	120	1
$\pm 0.6 F'_y$	$\pm 0.42$	160	1
$\mu_{\Delta} = \pm 1$	$\pm 0.7$	210	3
$\mu_{\Delta} = \pm 1.5$	$\pm 1.05$	224	3
$\mu_{\Delta} = \pm 2$	$\pm 1.4$	233	3
$\mu_{\Delta} = \pm 3$	$\pm 2.1$	247	3
$\mu_{\Delta} = \pm 4$	$\pm 2.8$	247	3
$\mu_{\Delta} = \pm 6$	$\pm 4.2$	253	3
$\mu_{\Delta} = \pm 8$	$\pm 5.6$	245	2
$\mu_{\Delta} = \pm 10$	$\pm 7.0$	221	1

Under positive moments, cracking between the diaphragm and cap interface did not develop on the underside of the superstructure until a displacement ductility of 1.5 was reached. These cracks were observed in each bay between two girders on the positive moment side and were primarily concentrated near the girders. However, none of the cracks extended along the

entire length of the cap. Additionally, cracking was observed at the interface between the bottom flange of each of the girders and the underside of the bent cap under positive moments. On the as-built connection side of the bent cap, the aforementioned girder to cap interface cracks had a width of 0.4 mm at the center girder. Similar cracks were noticed on the improved connection side, when subjected to a positive moment, at a ductility level of 1.5; however, the crack width was only about 0.2 mm at the center girder. At this ductility level, vertical flexural cracking was also noticed along the interface between the web of the girders and the diaphragm on both the improved and as-built connection sides, when each connection was subjected to a positive moment, and extended roughly half way up to the underside of the deck. Finally, significant cracking was observed on the topside of the deck, primarily outside the edge of the diaphragm on the negative moment side of the bent cap. A significant number of the flexural cracks in the deck, which had developed during earlier cycles due to negative moment, had also connected and spread across the entire length of the deck, indicating the engagement of all five girders in resisting the column moment on each side of the bent cap.

At a ductility level of 2, the previously mentioned flexural cracks between the bottom flange of the center girder and the bent cap on the as-built connection side had widened to 0.5 mm, while the same gap on the new connection side remained at 0.2 mm. The vertical cracks between the webs of the girders and the diaphragm on both sides of the connection extended almost all the way to the underside of the deck. Cracking on top of the deck continued to develop further away from the bent cap and extended across the entire width of the deck. The first signs of crushing and spalling of the concrete at the top and bottom of the column were also noticed.

Between ductility 3 and 8, the majority of the significant changes to the test unit occurred within the column and the deck near the column. A few new cracks developed in the column; however, the primary observation was that the old cracks began to extend and increase in width. The cover concrete at both the top and bottom column ends also began to crush and spall within the plastic hinge regions as the cycles progressed. Incipient buckling to one of the exposed longitudinal column reinforcement bars was observed in the bottom plastic hinge at a ductility level of 8, on the South side of the column. The number of cracks in the deck increased in an

evenly distributed manner and spread across the entire width of the superstructure, the majority of which were located between the diaphragm and vertical tie-down locations on each side of the bent cap. No significant changes were observed in either the as-built or the improved connection regions on the underside of the superstructure. Instead, the cracks remained essentially unchanged in regard to both their extension and width.

By the time the test unit had reached a displacement ductility of 10, or a horizontal displacement of 7 inches, it was apparent that the column had reached its ultimate capacity. A significant amount of concrete had crushed and spalled off of the column within the top and bottom plastic hinge regions, as shown in Figure 6.1. Several spirals and longitudinal bars were visible and concrete within the column core had crushed. The majority of the longitudinal column bars within the hinge regions had also begun to buckle across the spirals. However, no significant further cracking was observed within the connection region between the girders and the cap or diaphragm, as shown in Figure 6.2. Furthermore, no joint cracking between the column and inverted-T bent cap was observed during the entire test. More flexural cracks along the top of the deck had developed between the diaphragm and hold-down locations, while only a few cracks were observed within the cap region. Some of the cracking in the deck, near the stem on the inverted-T also extended all the way through the deck.



Figure 6.1: A Close-Up View of the Column Performance at +7.0 in. of Lateral Displacement ( $\mu_{\Delta}=+10$ )

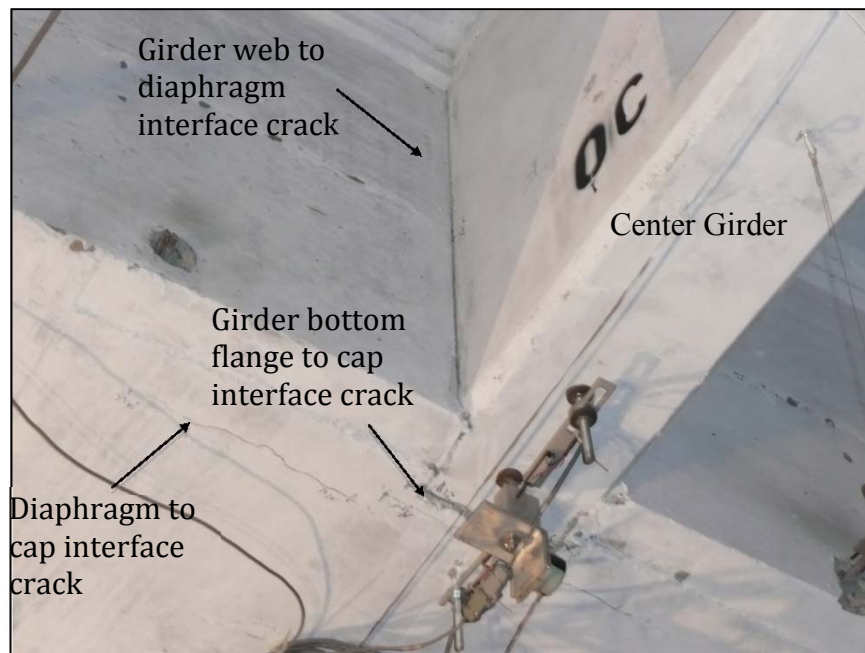


Figure 6.2: Condition of As-Built Center Girder-to-Cap Connection at  $\mu_{\Delta}=+8$

## 6.2 Phase 1 Test Results

### 6.2.1 Overall Response

The structure achieved a displacement ductility of 10, corresponding to 7 inches of total horizontal displacement in each loading direction, before buckling of several column longitudinal reinforcement bars was observed, as well as the beginning of a confinement failure, as shown in Figure 6.3. Both the improved and as-built connections between the precast I-girders and cap beam behaved as a fixed connection and did not show signs of significant damage or degradation throughout the course of the testing. No joint cracking was observed between the top of the column and the underside of the bent cap at any point during the test. Fairly extensive flexural cracking was observed across the width of the deck, indicating that the diaphragm action of the deck had engaged all of the girders, as shown in Figure 6.4.



Figure 6.3: Buckling in the Top Column Hinge on the North Side at  $\mu_{\Delta}=10$

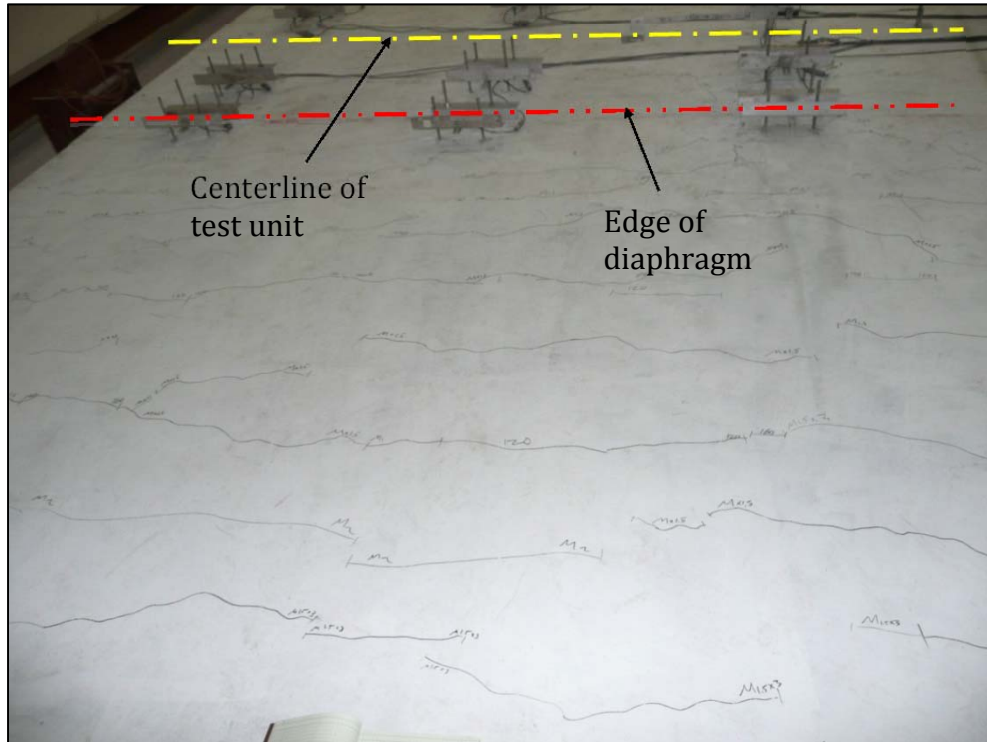


Figure 6.4: Distribution of Flexural Cracking on the Top Side of the Deck at  $\mu_{\Delta}=+10$

A comparison of critical data collected during the test to the predictions based on the SAP2000 grillage model showed generally good results. The horizontal force vs. lateral displacement of the superstructure is shown in Figure 6.5, which shows slight disagreement at small displacements as the grillage model used a cracked effective stiffness for both the column and superstructure sections, rather than the actual gross values for the elastic region of the test. However, the results began to converge at higher levels of displacement as more of the structure began to soften due to the development of cracks and yielding of longitudinal reinforcement. The plot of horizontal displacement vs. positive as-built connection rotation is shown in Figure 6.6. A satisfactory correlation between the recorded predicted stiffness for the connection is seen, but the connection of the test unit exhibited a relatively small rotation compared to what was predicted. This discrepancy could easily have been caused by the increased strength in the concrete at the time of testing, which was further examined during Phase 2. Note that the measured data reported were calculated based on the difference between the measured cap rotation and the measured girder rotation and were determined only at the peak points; thus, the irregularity for the low loads and small rotations early in the test is not unexpected.

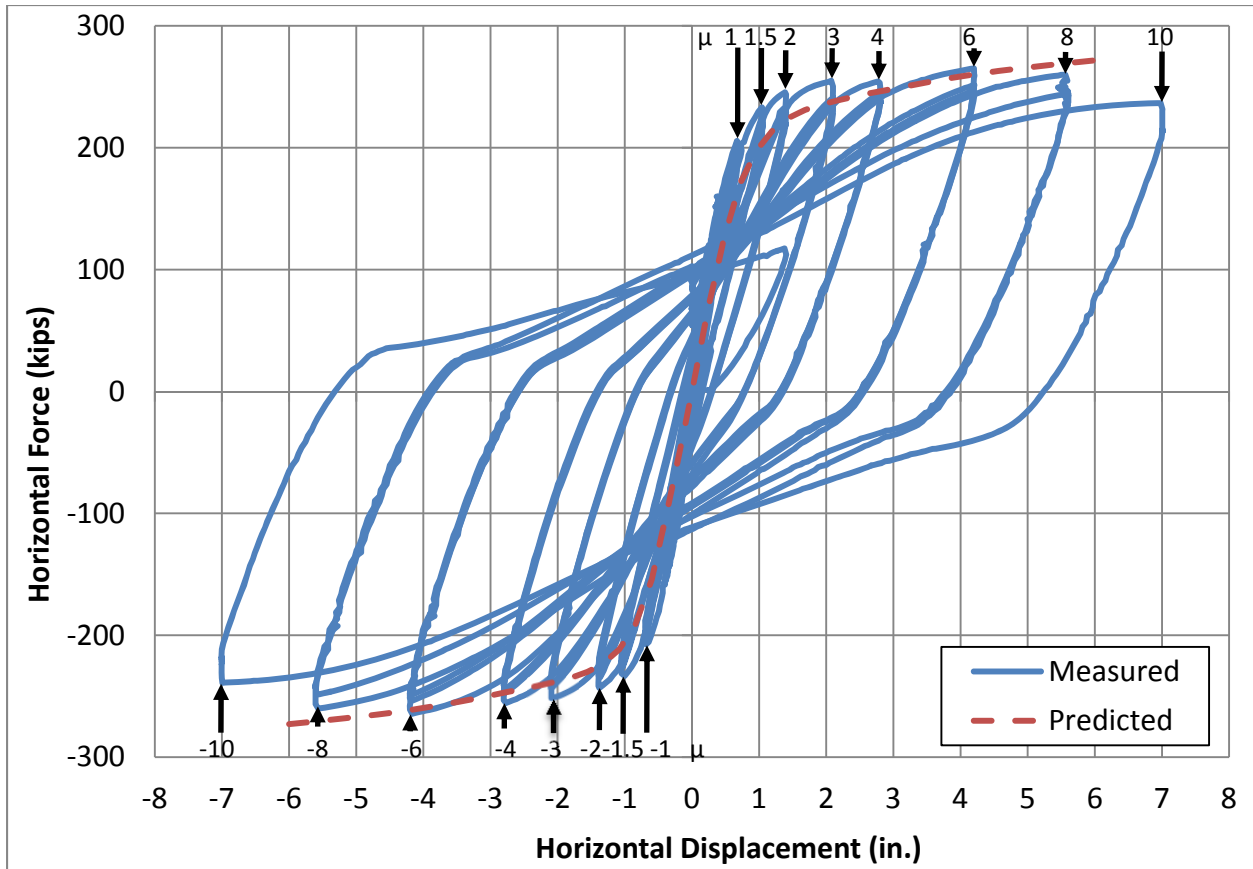


Figure 6.5: Force vs. Displacement Response of Test Unit during Phase 1 Testing

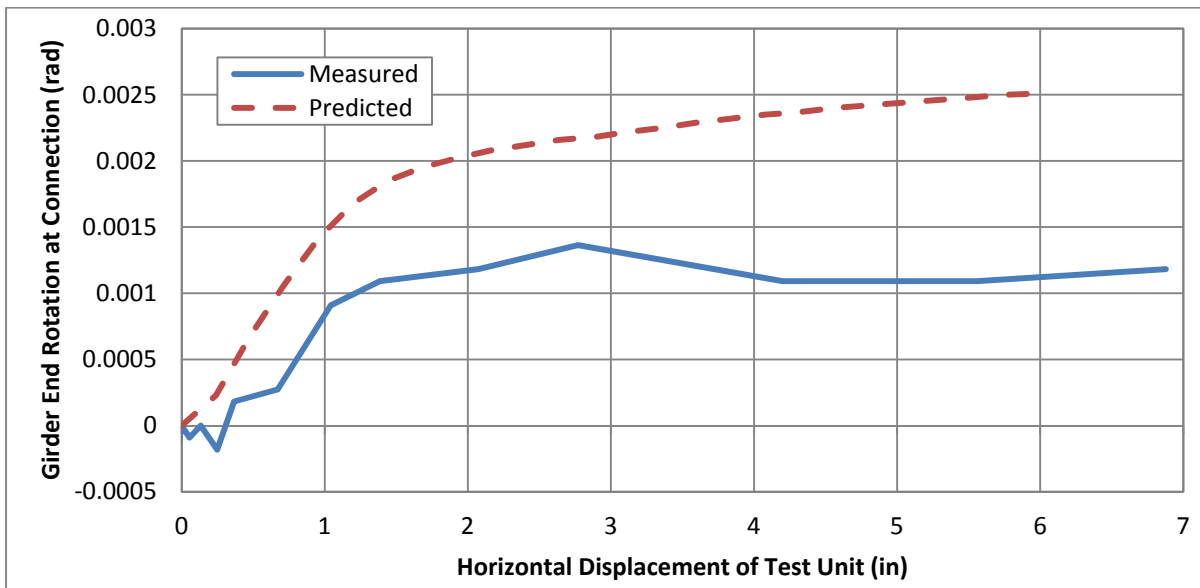


Figure 6.6: Center Girder End Rotation within Girder-to-Cap Connection vs. Horizontal Displacement during Phase 1 Testing

Another localized component for investigation of the overall response was the overall stiffness of the superstructure. Since an effective stiffness value was used for the composite superstructure section, as outlined in Chapter 4, it was understood that the initial stiffness would not match and that the stiffness would not provide a high degree of precision over the course of the entire test, as the test unit experienced varying degrees of stiffness degradation. Therefore, in order to investigate this localized response, the vertical displacement at each potentiometer location was plotted along the length of the structure, for the center girder, at a displacement ductility level of 3 and 8. As expected, the measured and predicted stiffnesses do not agree perfectly at each ductility level. It may be observed that the effective superstructure stiffness used in the grillage model overestimated the mid-span displacements at ductility 3 and somewhat underestimated the same displacements at ductility 8. However, over the entire length of the superstructure, the difference in stiffness is still considered satisfactory, as the displacements were very small relative to the overall girder length. It should be noted that a distance of zero, along the superstructure, was defined as the location of the cap and that the as-built connection detail was located on the negative side of the horizontal axis in Figures 6.6, 6.7, 6.8, and 6.9. Note that, similarly to Figure 6.6, the measured data reported for these figures is plotted only for the peak load conditions, hence the slightly irregular shape of the curves.

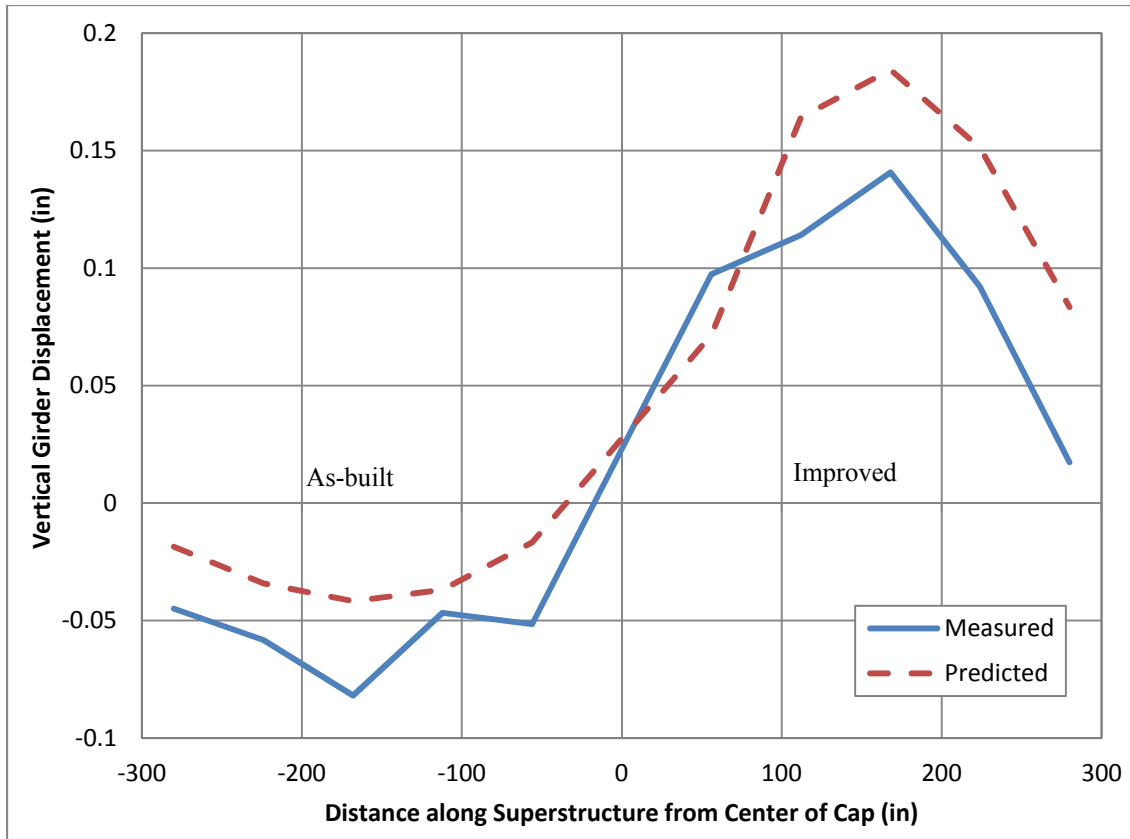


Figure 6.7: Center Girder Vertical Displacements at  $\mu_{\Delta} = +3$

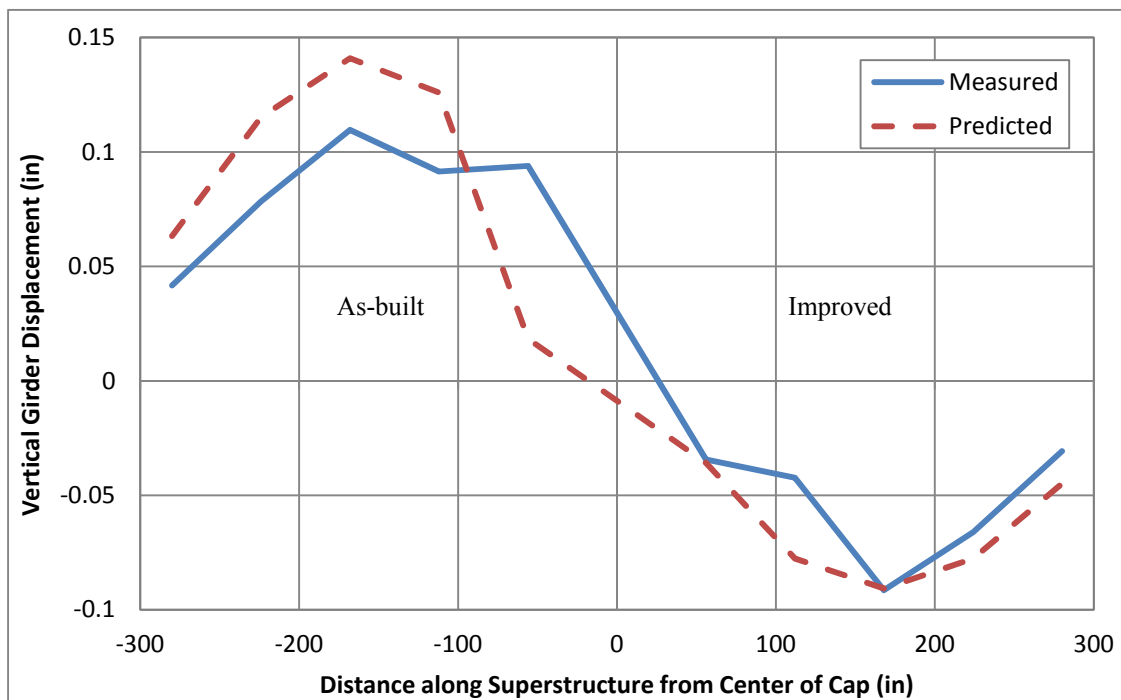


Figure 6.8: Center Girder Vertical Displacements at  $\mu_{\Delta} = -3$

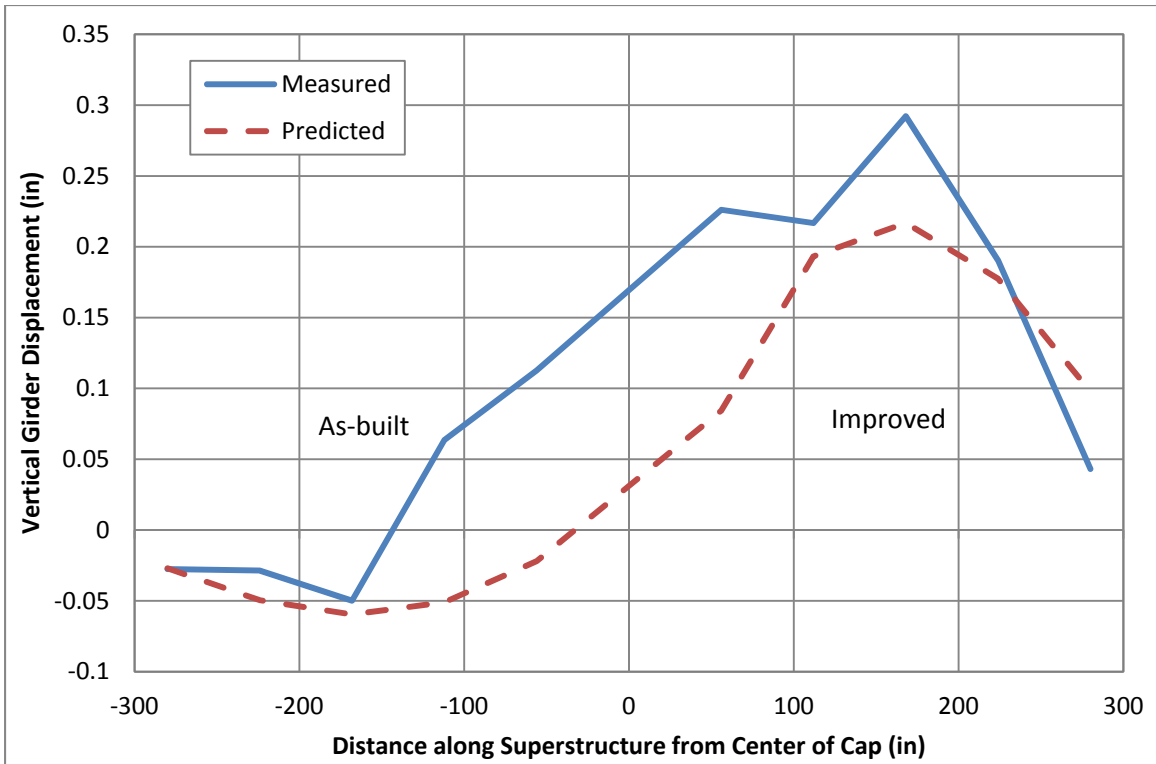


Figure 6.9: Center Girder Vertical Displacements at  $\mu_{\Delta} = +8$

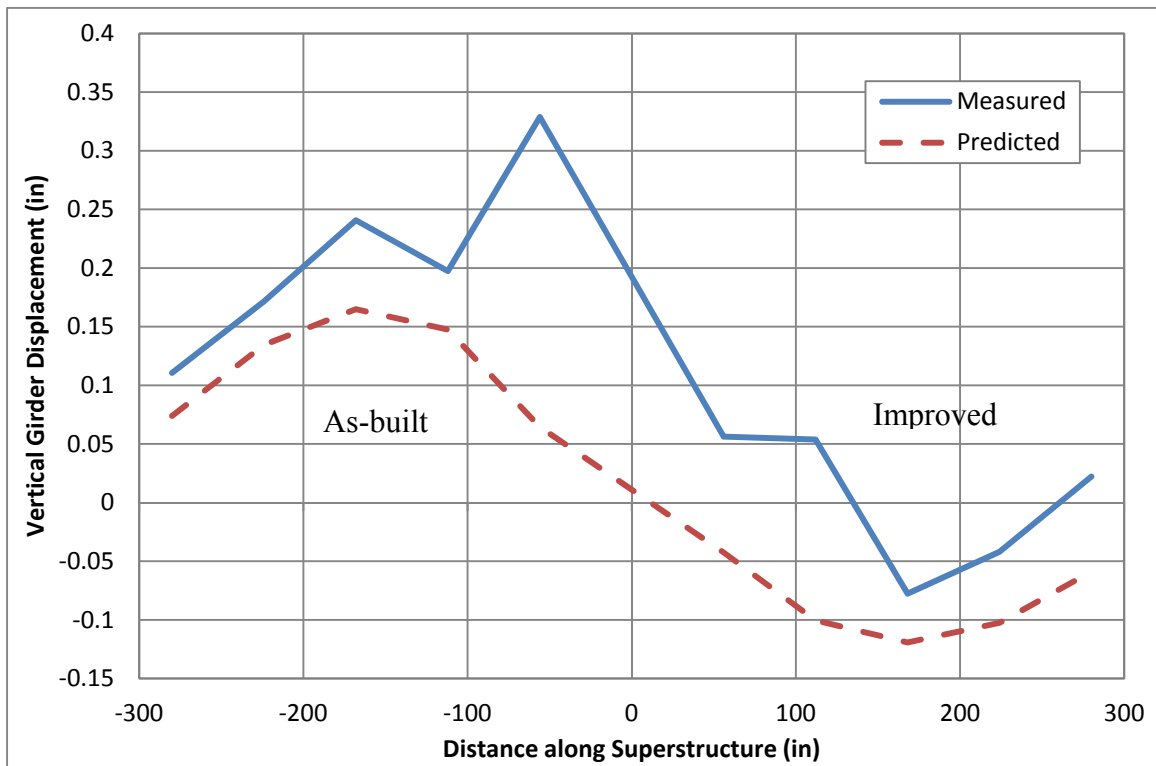


Figure 6.10: Center Girder Vertical Displacements at  $\mu_{\Delta} = -8$

### **6.2.2 Column Response**

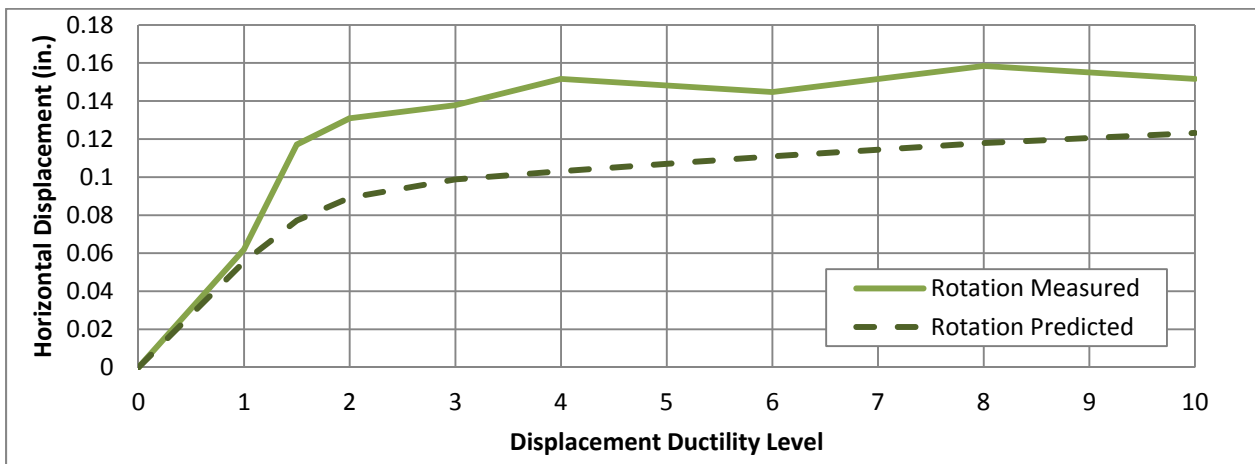
In order to better understand the effectiveness of the grillage model in predicting the behavior of the test unit, as well as any discrepancies between the measured and predicted responses, the response of various localized components were inspected. Since the majority of the overall force vs. displacement response of the structure was largely dependent on the behavior of the column, it was used as a starting point in investigating the localized behavior of the structure. The response of the column was broken into two main components: the primary displacement of the column and the effect that the flexibility of the superstructure had on the rotation at the top of the column, which would in turn influence the overall lateral displacement observed at the top of the column. Investigating the behavior of each of the aforementioned components was crucial in identifying any discrepancies between the predicted and measured local behaviors, which could have influenced the global response. As shown in Figure 6.11, an outstanding agreement was observed between the predicted and measured response for each of the displacement components of interest, as well as the overall, combined response of the column. This indicates that the column was modeled very well and that the effects of any discrepancies observed within the system might have been cancelled out once their effects reached the column. Since the horizontal displacement component that was used in the global force vs. displacement plot was recorded at the location of the actuator, it is likely that the observed discrepancies were due to an inaccurate estimation of either the superstructure or connection stiffnesses. As a result, the displacements due to both stiffnesses were investigated further.



(a) Total displacement



(b) Column displacement

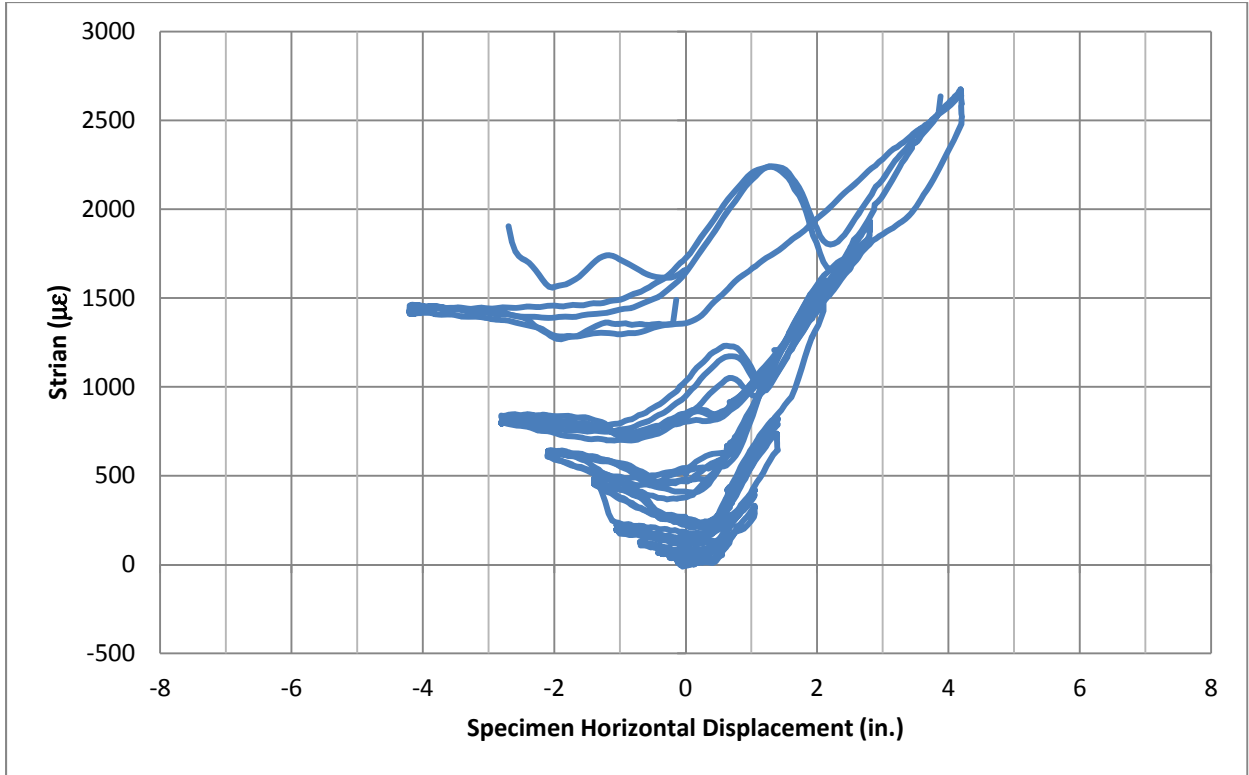


(c) Displacement due to plastic hinge rotation

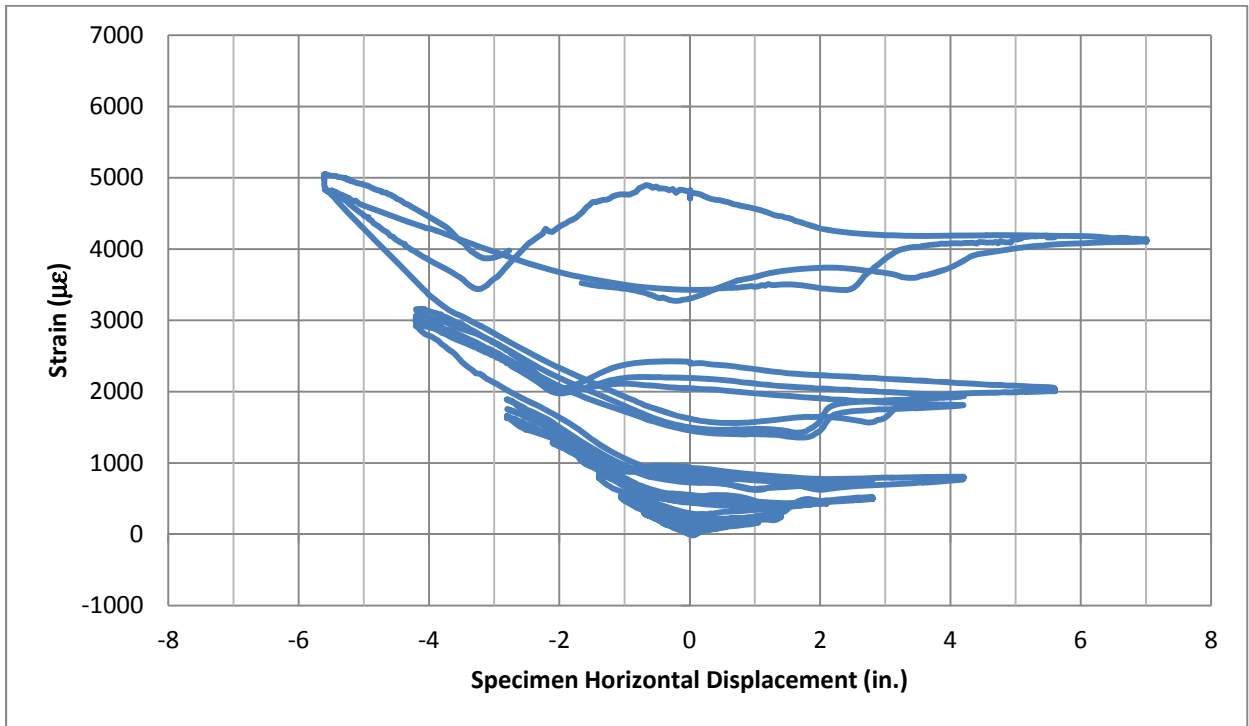
Figure 6.11: Comparison of Column Horizontal Displacement Components

Another localized component for investigation of the column response was the plastic hinge region of the column. Figure 6.12 shows the strains on the spiral reinforcement in the hinge region from both the north and the south sides, about one-half spiral from the column-to-cap interface. Measurable strains on both sides of the spiral were recorded already at early load steps, and fractional strains with magnitudes between 0.02 and 0.05 were recorded for larger specimen displacements. This strain behavior indicates the engagement of the spiral reinforcement and confirms that confinement was established and maintained during the test.

Additional data of interest in the plastic hinge region are the strains from the column longitudinal reinforcement. Figure 6.13 and Figure 6.14 provide strain profiles from the extreme bars on the north and south sides for the peak loads in both the push and pull directions. The profile shapes from both the north and south bars indicate adequate anchorage of the longitudinal reinforcement and successful development of the load in the reinforcement, with the recorded strains varying from maximum values at the column-to-cap connection interface to smaller values into the joint.

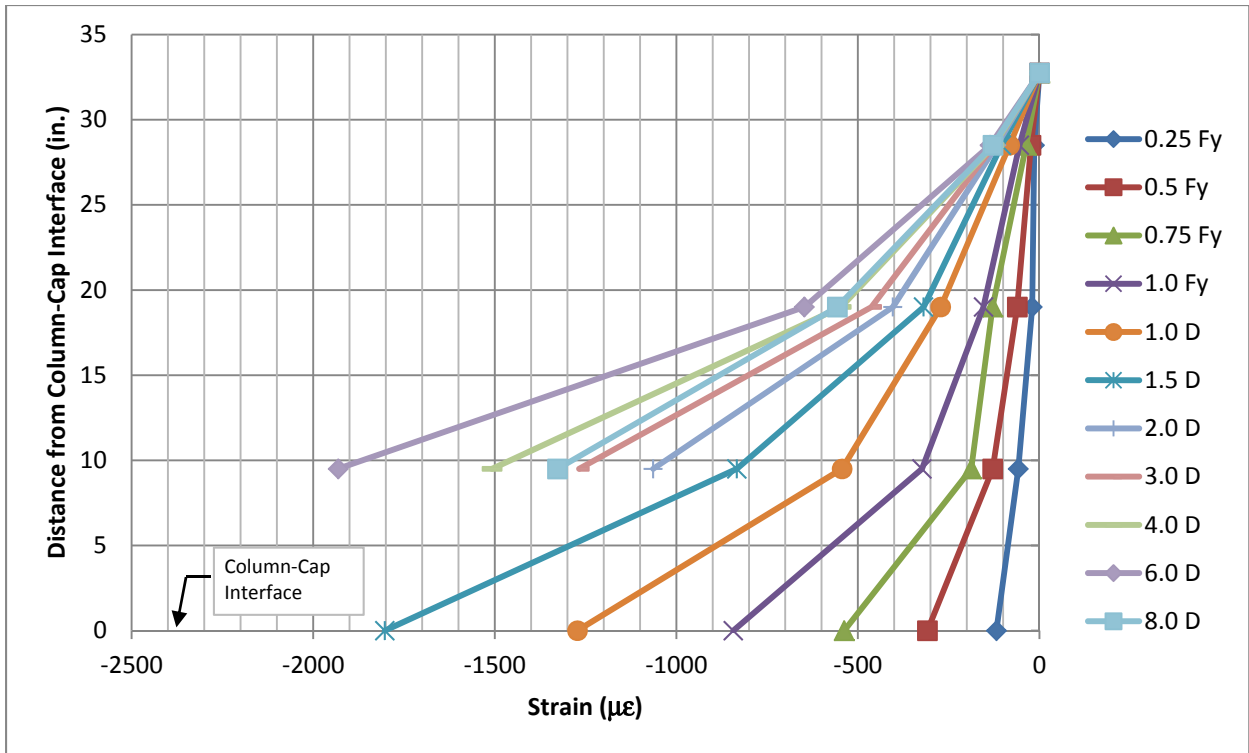


(a) Improved side

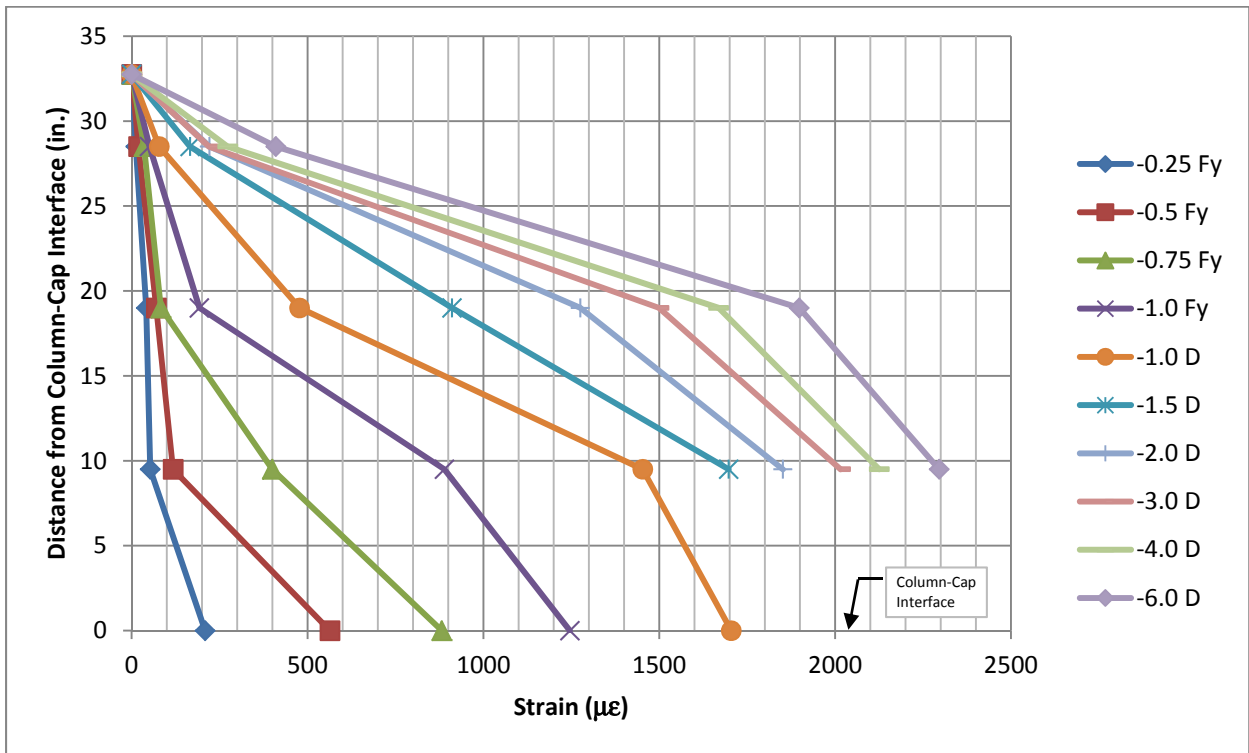


(b) As-built side

Figure 6.12: Column Spiral Reinforcement Strain indicating Confinement Effectiveness

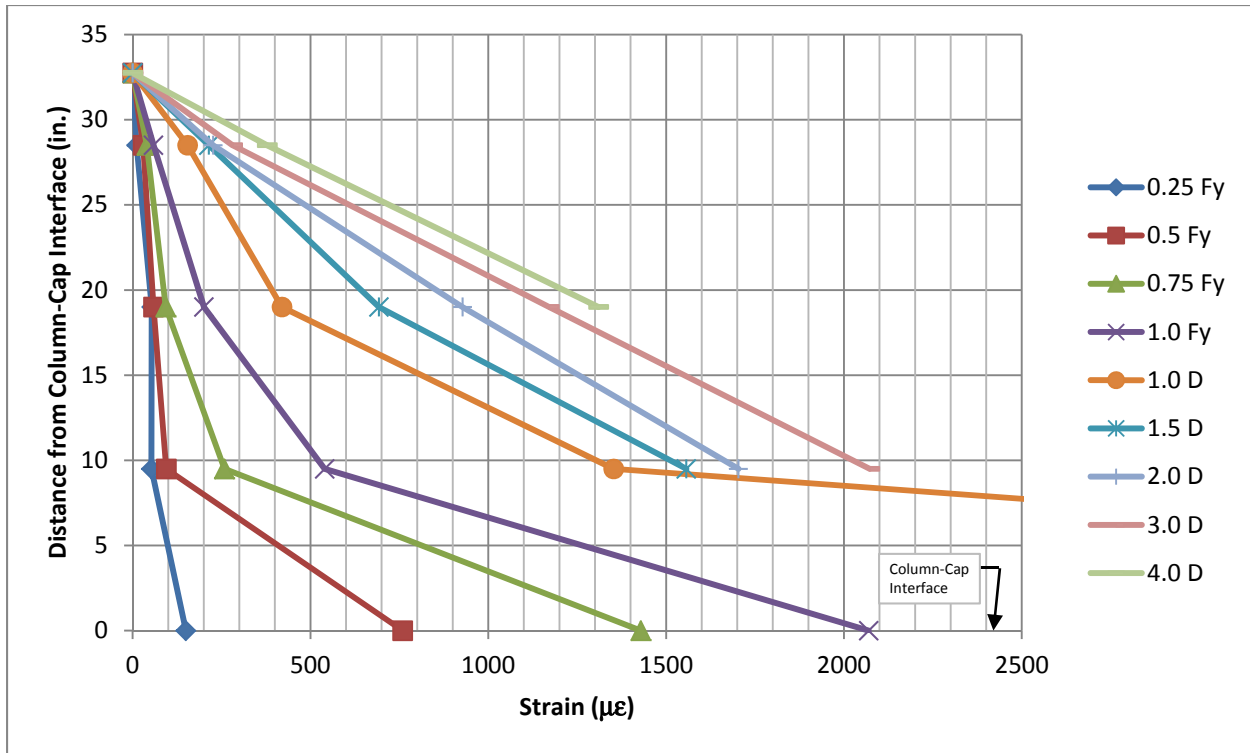


(a) Push direction loading (tension on improved connection side)

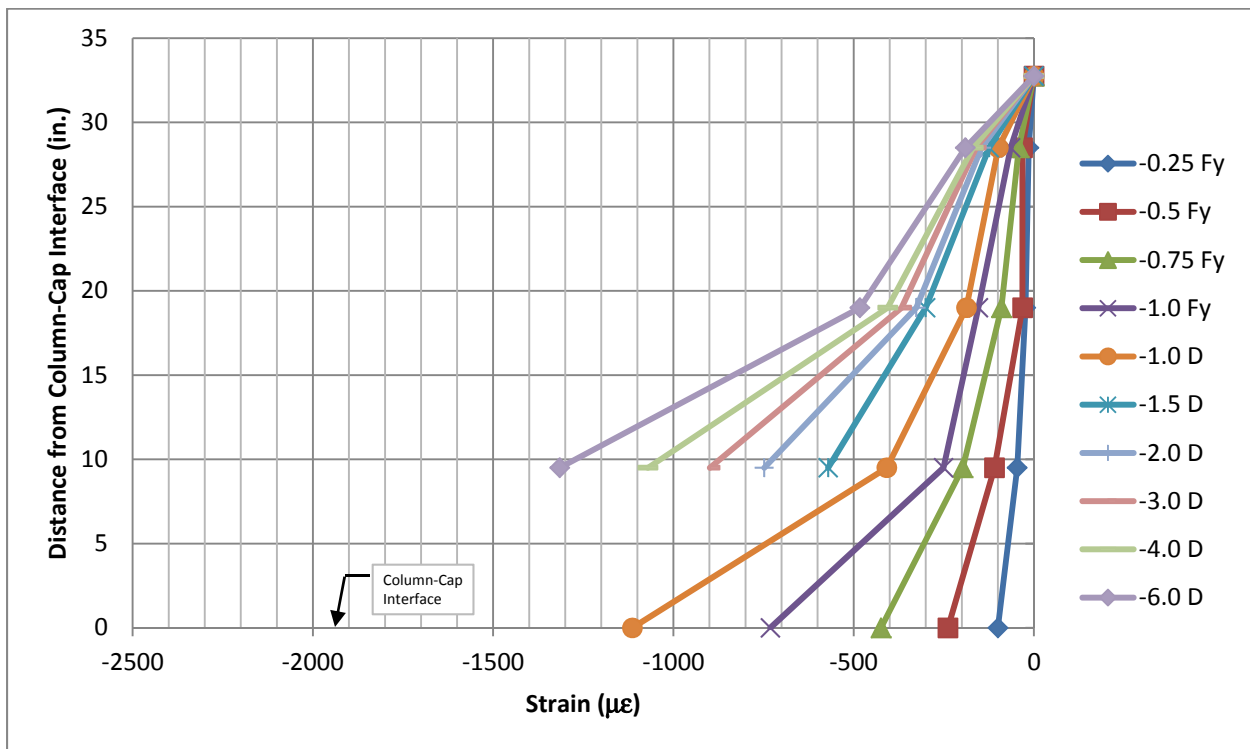


(b) Pull direction loading (tension on as-built connection side)

Figure 6.13: Column Longitudinal Reinforcement Strain Profiles on the As-built Connection Side



(a) Push direction loading (tension on the improved connection side)



(b) Pull direction loading (tension on the as-built connection side)

Figure 6.14: Column Longitudinal Reinforcement Strain Profiles on the Improved Connection Side

### 6.2.3 Connection Response

Another area of interest is the girder rotation responses for both connection details. As shown below in Figure 6.15 for the center girder, when the underside of the girder was rotating away from the cap, thereby opening a gap on the underside of the girder-to-cap connection, for the improved connection detail, the predicted and measured responses matched reasonably well. The initial measured stiffness for the test unit was slightly higher than the predicted, but overall, the measured response indicated that the connection was more flexible than what was initially predicted. Furthermore, the response of the improved connection rotation, when subjected to a negative moment, which also corresponded to the aforementioned gap closing, also indicated that the connection was slightly more flexible than predicted; however, the initial stiffness showed a better correlation, as shown in Figure 6.16. The reasons behind these discrepancies were still somewhat unknown after Phase 1 of testing and, as a result, were further investigated during Phase 2 of testing (Section 6.5).

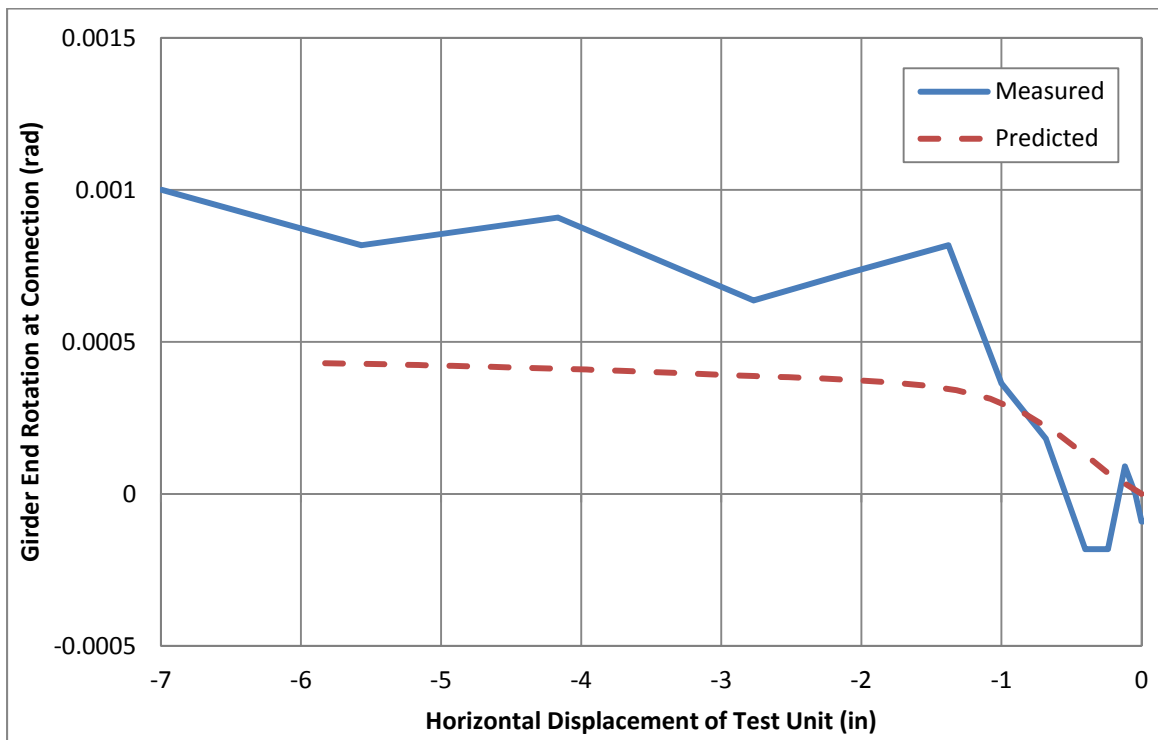


Figure 6.15: Center Girder Improved Connection Girder Rotation/Gap Opening

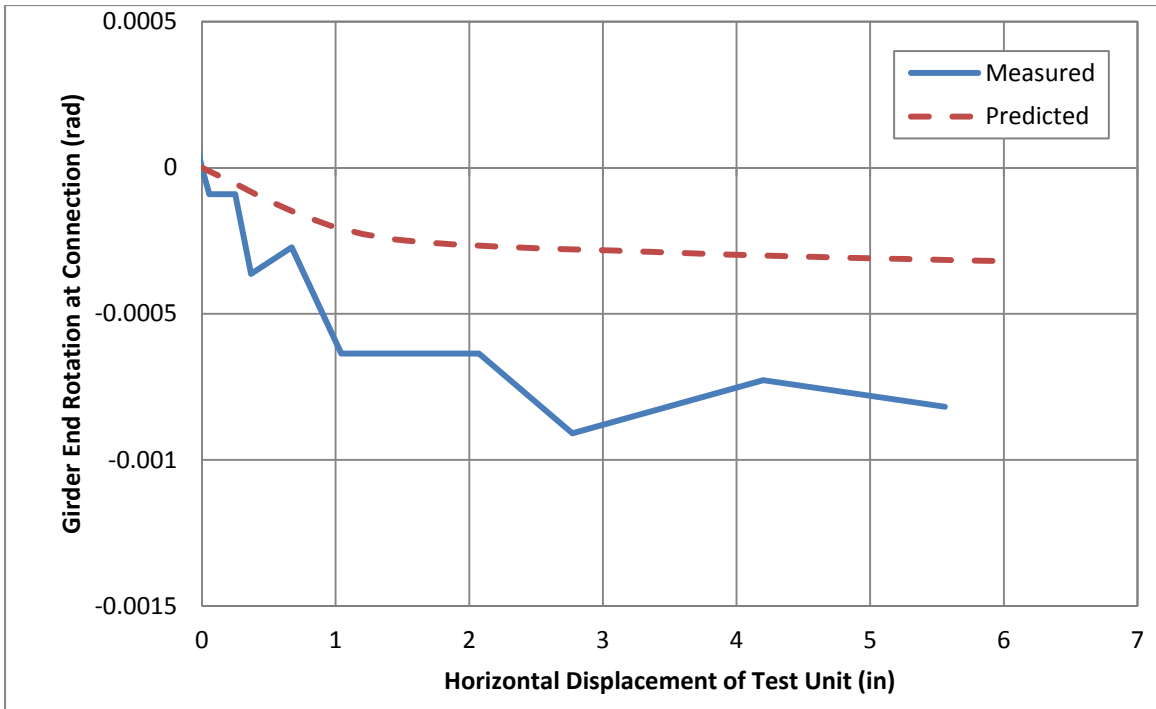
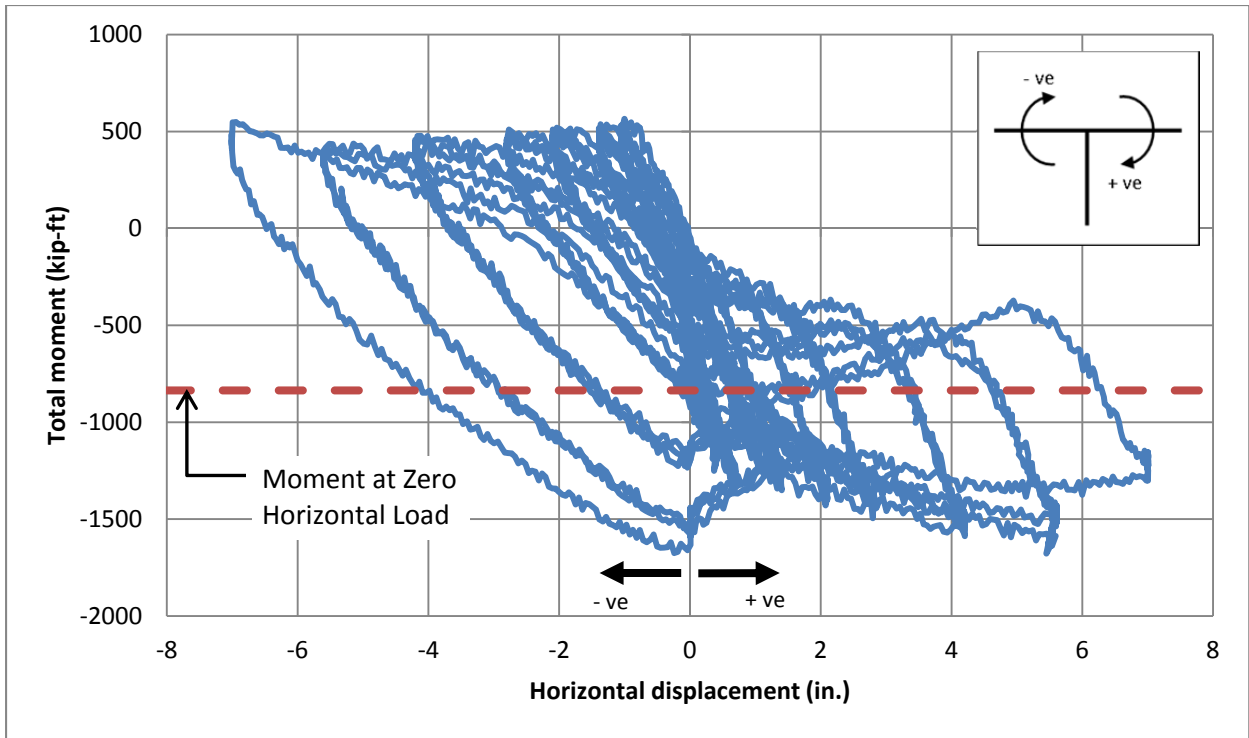
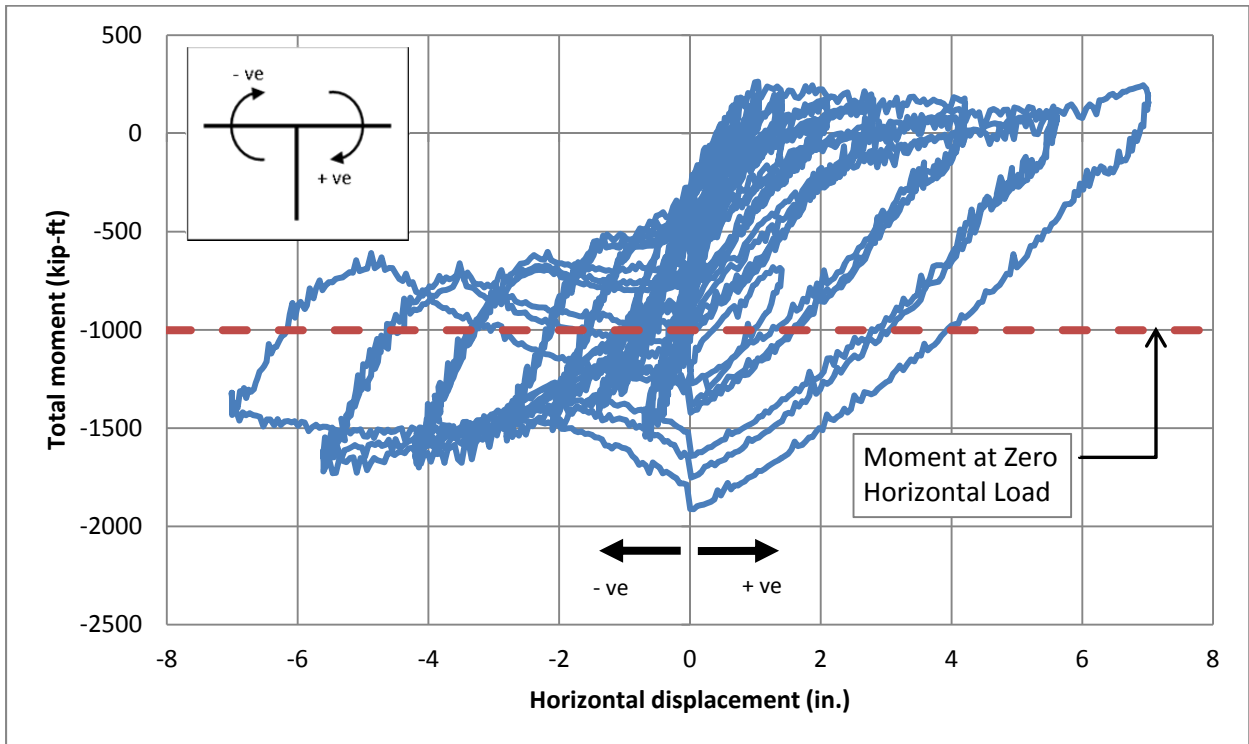


Figure 6.16: Center Girder Improved Connection Girder Rotation/Gap Closing

To consider more closely the behavior of the girder-to-cap connections, an effort was made to distinguish between the behavior of the improved connection on the North side and the as-built connection on the South side. Part of this effort consisted of determining from the data the total moment transfer in the girder-to-cap connections of all five girders. Figure 6.17 provides the total moment on both the improved and as-built sides plotted as a function of the horizontal displacement during the entirety of the Phase 1 horizontal load test. The figures show that both the improved and as-built sides exhibited sizable negative moment capacity. Such behavior was expected since the composite effect of the cap and deck was instrumental in providing the tension resistance that contributed to the negative moment capacity. However, it is interesting to note that the positive moment generated in the improved connection, due to reverse curvature induced by seismic loading, was noticeably higher than the positive moment generated in the as-built connection.



(a) Improved connection



(b) As-built connection

Figure 6.17: Total Moment in all Five Girders at Girder-to-Cap Connection

Figure 6.18 provides a clearer comparison of the total moment in the improved and as-built connections. It should be noted that the negative moment induced in the improved connection at the zero horizontal load condition was slightly lower in magnitude than the negative moment induced in the as-built connection at zero horizontal load, as shown by the dashed lines. The reason for this discrepancy is that the vertical tie-down force on the North improved side that generated the moment in the improved connection was slightly higher than the vertical tie-down force on the South as-built side. Therefore, the best way to compare the moments induced in the improved and as-built connections is to compare the difference between the moment at zero horizontal load and the moment at peak conditions for both connections. The peak condition at ductility levels +6 and -6 were chosen for this comparison as identified on the figure. The comparison reveals that the positive moment difference was 1313 kip-ft for the improved side and 1179 kip-ft for the as-built side, or a demand approximately 11 percent higher in the improved side. Also, the negative moment difference was -743 kip-ft for the improved side and -679 kip-ft for the as-built side, or a demand approximately 9.5 percent higher in the improved side. Thus, despite the influence of the as-built connection deterioration on the improved side demand, the data shows that a higher demand was still generated in the improved side.

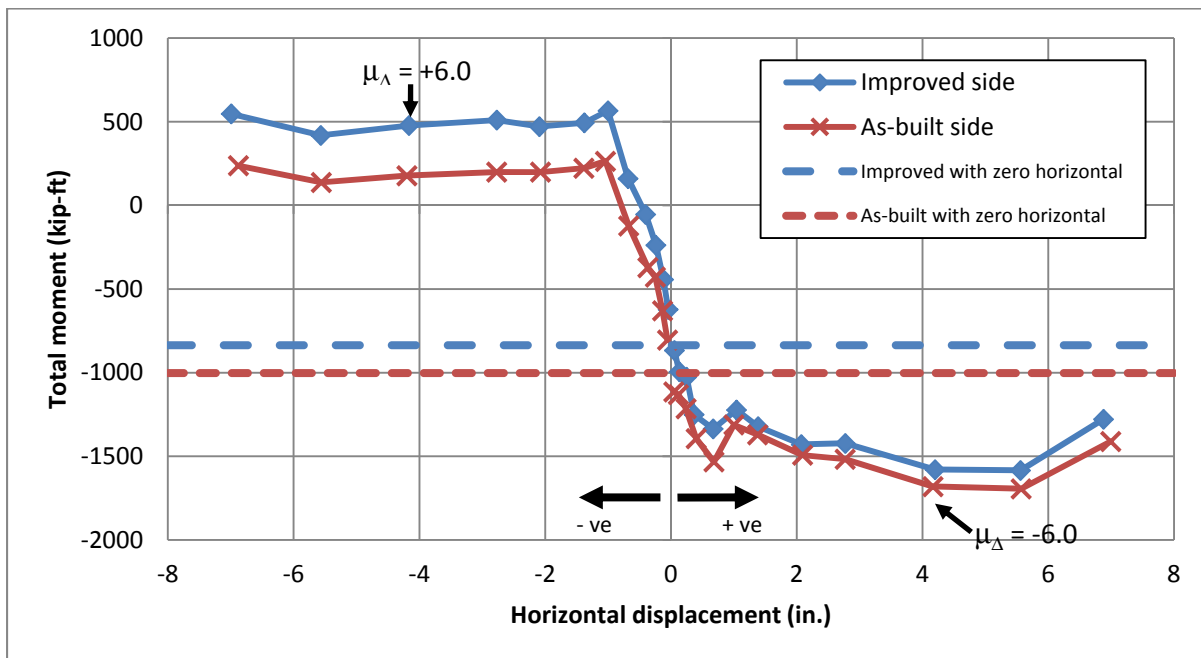
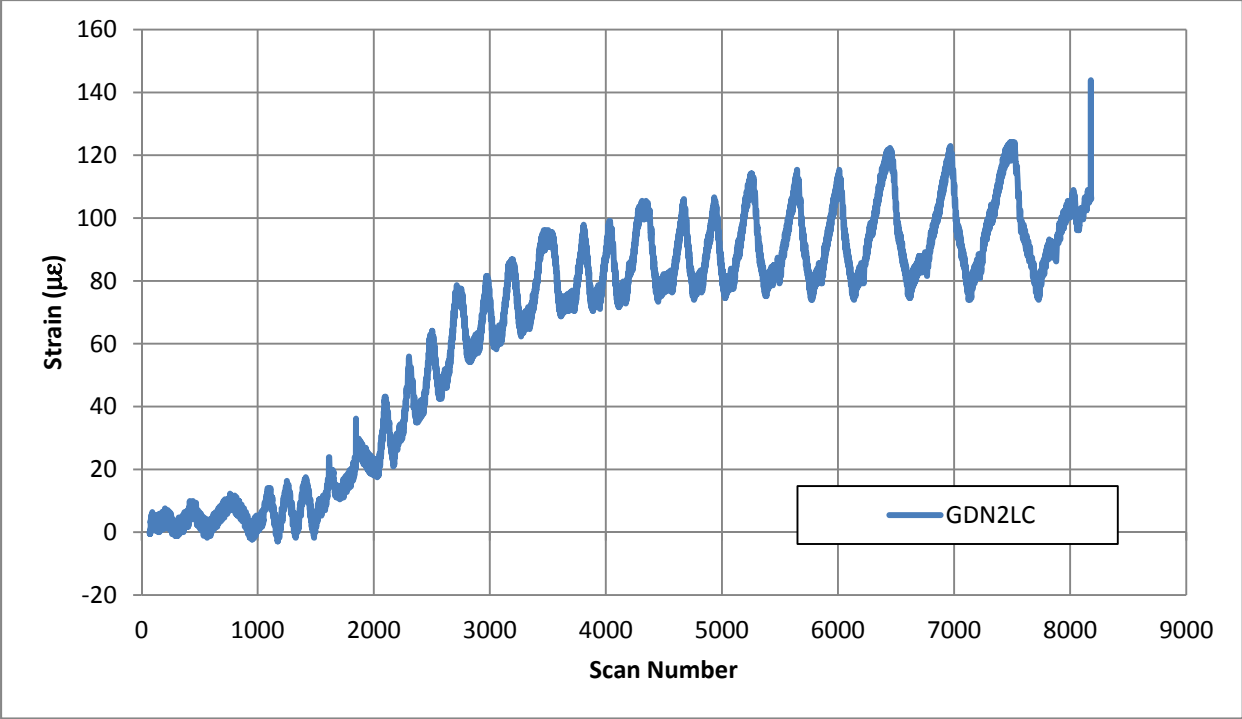
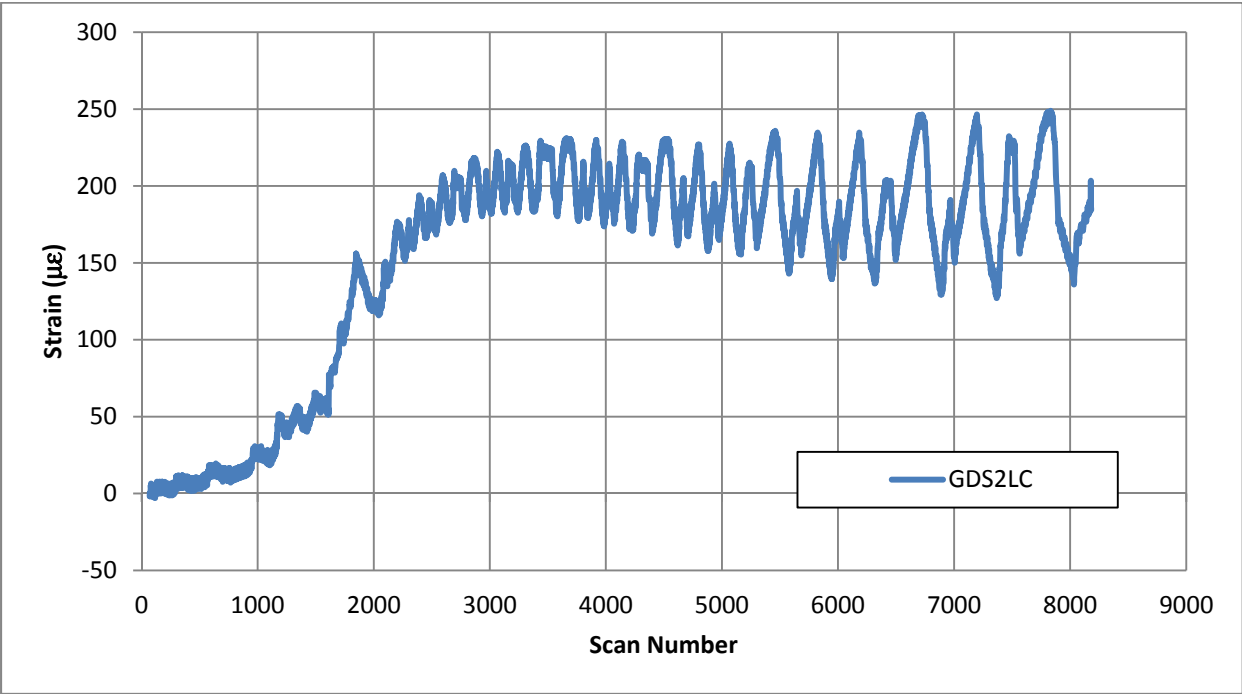


Figure 6.18: Total Moment in all Five Girders at Peak Load Conditions

The girder dowel behavior was also of interest in the connection region. One interesting aspect of the behavior to note is the apparent occurrence of residual strains at certain locations. Figure 6.19 shows strain histories from locations near the end of two different girder dowels, one from the connection of the North intermediate girder to the cap and the other from mirror-image location of the connection of the South intermediate girder to the cap. Ordinarily, strain histories such as these might be assumed to be due to gauge drift and error. However, the remarkable similarity of strain histories from various corresponding similar locations on the girder dowels indicates that this data was valid. The data is indicative of deformation in the girder dowels. As the specimen was loaded in a particular direction, the girder dowel was deformed due to the interaction between the girder and the diaphragm. When the load was reversed, the dowel bar relaxed a bit but did not return all the way to its original relaxed position, thus inducing residual strains that are clearly seen in the variance of the mean strain in the strain histories.



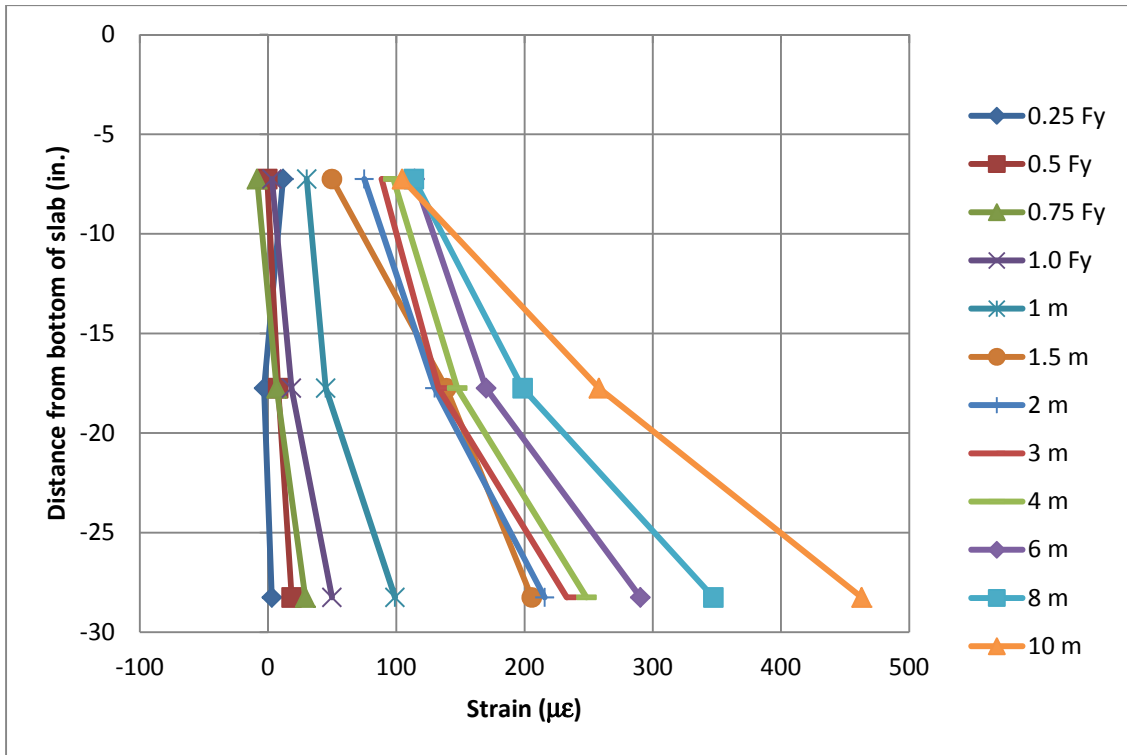
(a) Improved side



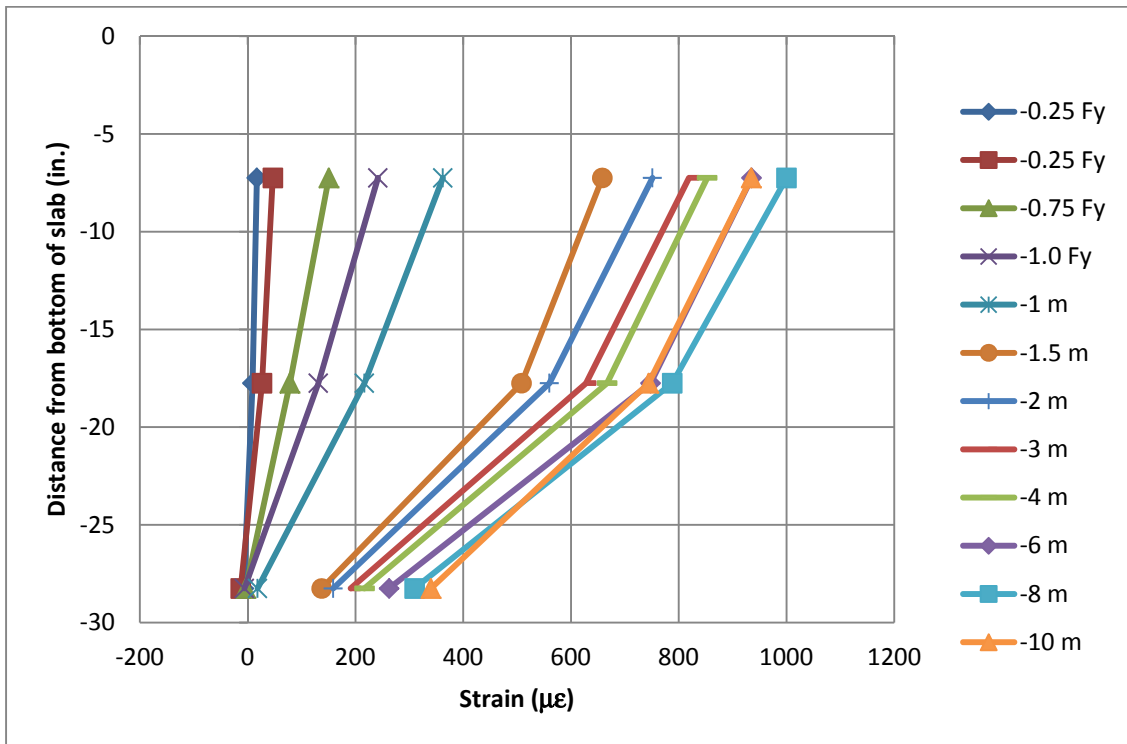
(b) As-built side

Figure 6.19: Girder Dowel Bar Strain Histories

Figure 6.20 provides dowel strain profiles from the upper, middle, and lower dowels for the center girder on the improved side in both the push and pull directions. The plots clearly show that the lower, middle, and upper dowels all behaved proportionally during the test. Also, it is clearly seen that, for the push direction loading, the magnitude of engagement progresses from highest to lowest in the lower, middle, and upper dowels, as expected for that load direction, and for the pull direction loading the magnitude progresses from highest to lowest in the opposite direction (upper, middle, then lower), as expected for that load direction. One final observation that is interesting to note is that for both the push and pull directions there was a larger increase in magnitude between load steps  $1.0 \mu_{\Delta}$  and  $1.5 \mu_{\Delta}$  than there was between any of the other load steps. The loading mechanism that engaged the dowels was more actively engaged at that load level. This transition in engagement also corresponded with the beginning of the increase in mean strain seen in the strain histories that was discussed in Figure 6.19.



(a) Push direction load steps



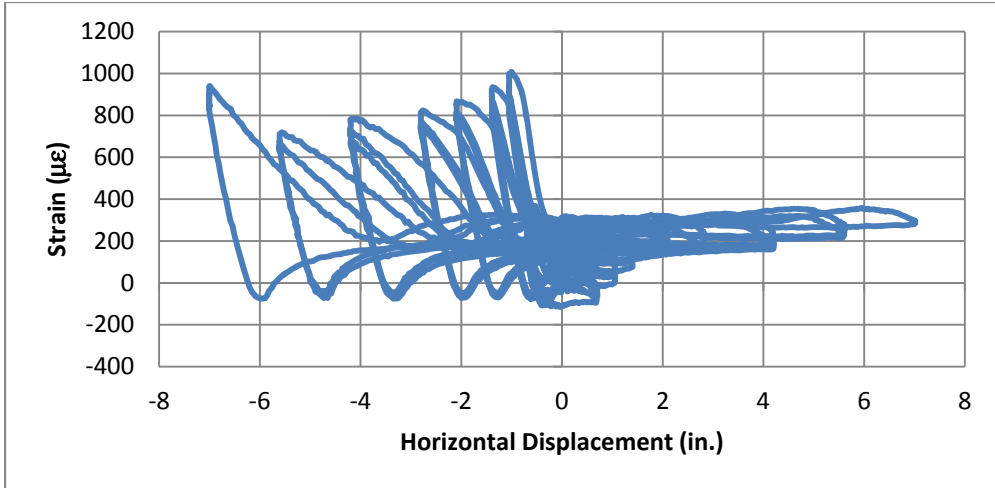
(b) Pull direction load steps

Figure 6.20: Dowel Strain Profiles using Data from Upper, Middle, and Lower Dowels on Center Girder

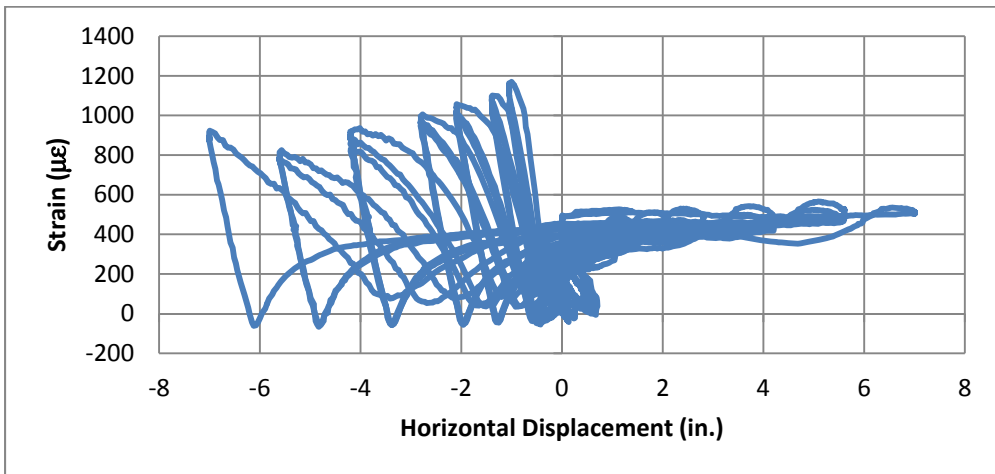
The unstressed strands that were part of the improved girder-to-cap connection on the North side also provided some helpful data related to the connection performance. Strain histories from the strands on one exterior girder and two intermediate girders are shown in Figure 6.21. Each of these gauges was located on its respective strand at the outer edge of the diaphragm. (Note that the strain gauges for the unstressed strand on the center girder were damaged, so no data is available from the center girder strand.)

The strain histories from each girder clearly show engagement in the pull (negative horizontal displacement) direction. This behavior was to be expected given that the pull direction load induced tension at the bottom of the girders, which is where the unstressed strands were located. Similarly, the lack of engagement of the strands in the push direction matches with expectations, since the push direction produces compression in the strand location. The engagement of the unstressed strands for each load step, including successful engagement without failure at the largest lateral displacements, shows that the unstressed strands provided a successful load transfer mechanism and improved the integrity of the connection.

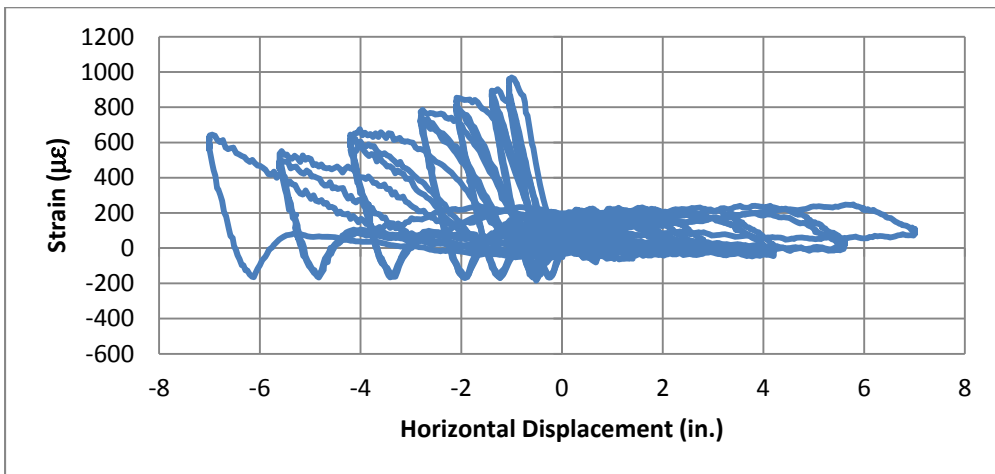
Also of note is the engagement of the unstressed strand in the exterior girder at small displacements. Figure 6.21(c) shows that a strand strain of just less than  $1000 \mu\epsilon$  was measured in the exterior girder strand at a displacement of 1 inch. This strain corresponds to a stress of approximately 29 ksi, or approximately  $0.5 F_y$ , indicating that the exterior girder is engaged in the load transfer even at a relatively small displacement. The unstressed strand data indicates that the intermediate and exterior girders do contribute significantly in the lateral load distribution. To explore this distribution further, strain data from the deck reinforcement was also investigated.



(a) West intermediate girder



(b) East intermediate girder



(c) East exterior girder

Figure 6.21: Unstressed Strand Strain Histories

### 6.2.4 Deck Reinforcement

Figure 6.22 provides the deck reinforcement strain data for the peak loads during the horizontal load test. To provide clear comparison, the strains from push direction loading on the improved side and pull direction loading on the as-built side have been combined on one plot, as these are the load directions that produced tension in the deck reinforcement. These plots reveal a couple of interesting trends. First, the load was seen to be distributed across the center, intermediate, and exterior girders already at 0.25 F<sub>y</sub> and also during the higher load cycles. Second, a noticeable increase in strain magnitude was observed between the 1.0 μ<sub>Δ</sub> and 3.0 μ<sub>Δ</sub> load steps. This more abrupt change matches the behavior that was observed in the girder dowels (see Figure 6.20). Third, it is seen that the strain demand was noticeably higher on the improved side than on the as-built side, another indication that a higher moment demand was generated on the improved connection despite the influence of the deterioration of the as-built connection.

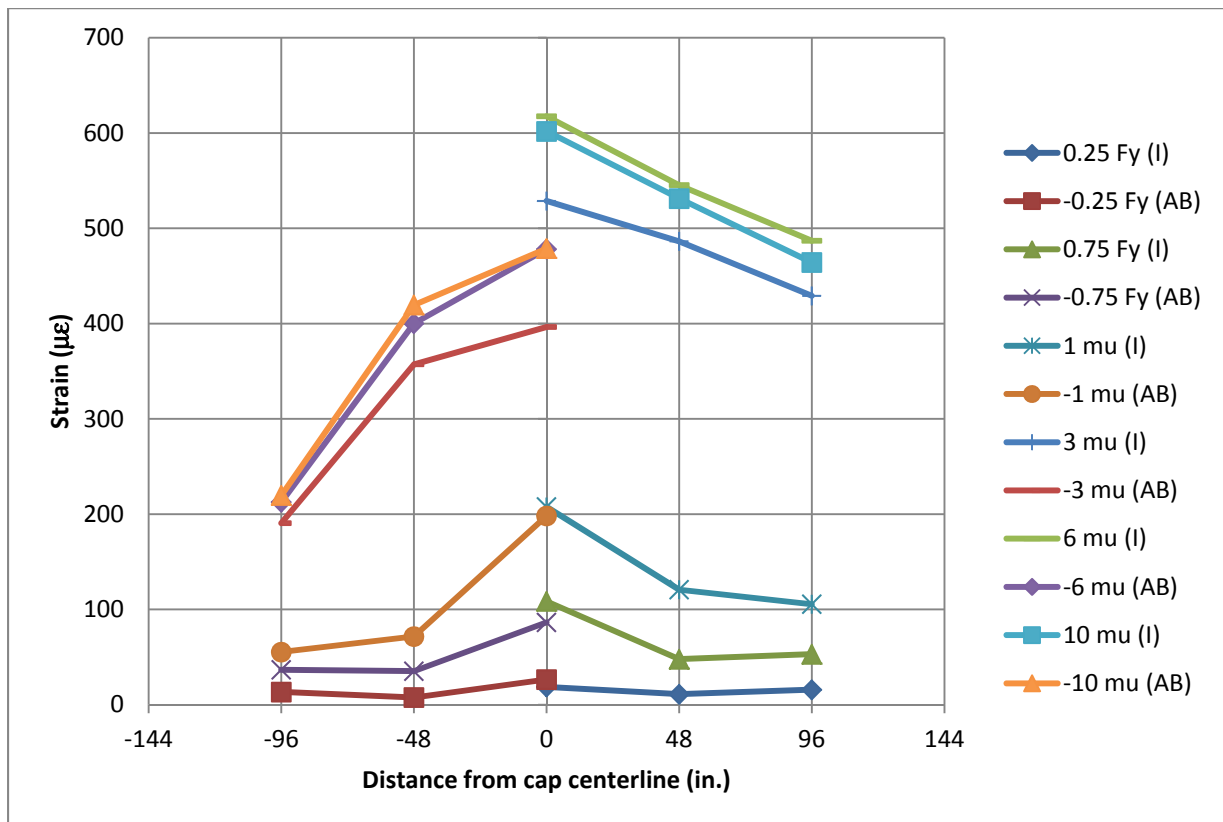


Figure 6.22: Deck Reinforcement Transverse Strain Profiles for Peak Loads for Improved Side Push Direction and As-built Side Pull Direction Peaks

### 6.2.5 Girder Load Distribution

The deck reinforcement was also used for further investigation of the distribution of the seismic moment among the exterior, intermediate, and center girders of the test specimen. In order to eliminate the influence of the vertical tie-down force simulating the gravity load, the strain data from the deck reinforcement was biased based on the zero-horizontal-load condition between each of the horizontal load peaks. This process provided strain data related only to the cyclic horizontal load simulating the seismic behavior. Figure 6.23 shows the resulting strains in the deck reinforcement 1.5 feet away from the diaphragm edge, on the improved connection side, from an exterior girder, the adjacent intermediate girder, and the center girder, plotted versus the horizontal displacement of the deck during the Phase I testing. It should be noted that this deck reinforcement data would be expected to provide the best load distribution data for the positive horizontal displacements, since such displacements produced a negative moment in the improved connection and hence tension in the deck reinforcement. For the positive displacements, this data shows that the intermediate girder exhibited slightly higher strains, followed by the center girder and finally the exterior girder. However, all three girders clearly carried significant portions of the load.

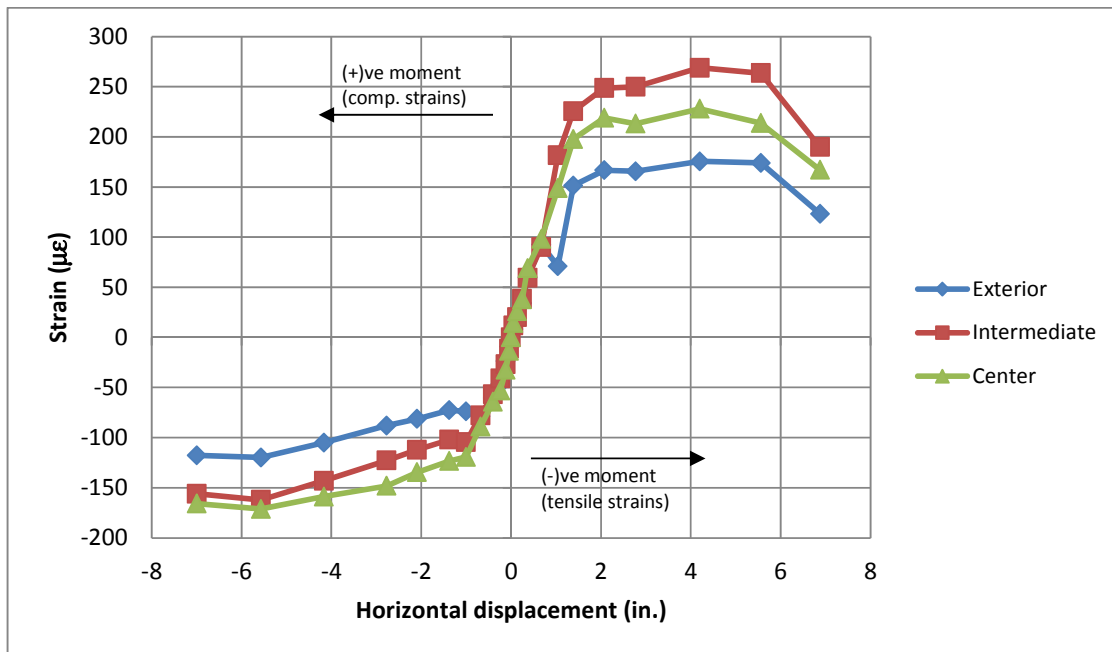


Figure 6.23: Deck Reinforcement Strains on Improved Connection Side 1.5 feet from Diaphragm Edge, above the Exterior, Intermediate, and Center Girders

To further investigate the distribution using this strain data, the fractional portions of strain carried by the exterior, intermediate, and center girders were determined. Since data was only available for one of the exterior and one of the intermediate girders, the data from these two girders was multiplied by two in determining the total summation of strains. However, for the fractional contribution, the single value from these two girders was used; hence, the total fractional distribution reported for the single exterior, single interior, and center girders does not result in a value of 1.0 (or 100%). Figure 6.24 shows these fractional distributions plotted versus the horizontal displacement. As before, the positive displacement values are especially of interest, as they correspond to the superstructure being submitted to negative moment. It can be seen here that for lateral displacements larger than about  $\pm 1$  inch, the distribution remained fairly constant, with the center girder carrying around 20% of the load, the intermediate girder carrying just under 25%, and the exterior girder carrying just over 15%. These numbers compare reasonably well to the grillage analysis, which predicted that the center, intermediate, and exterior girders would carry 22.8%, 21.2%, and 17.4%, respectively.

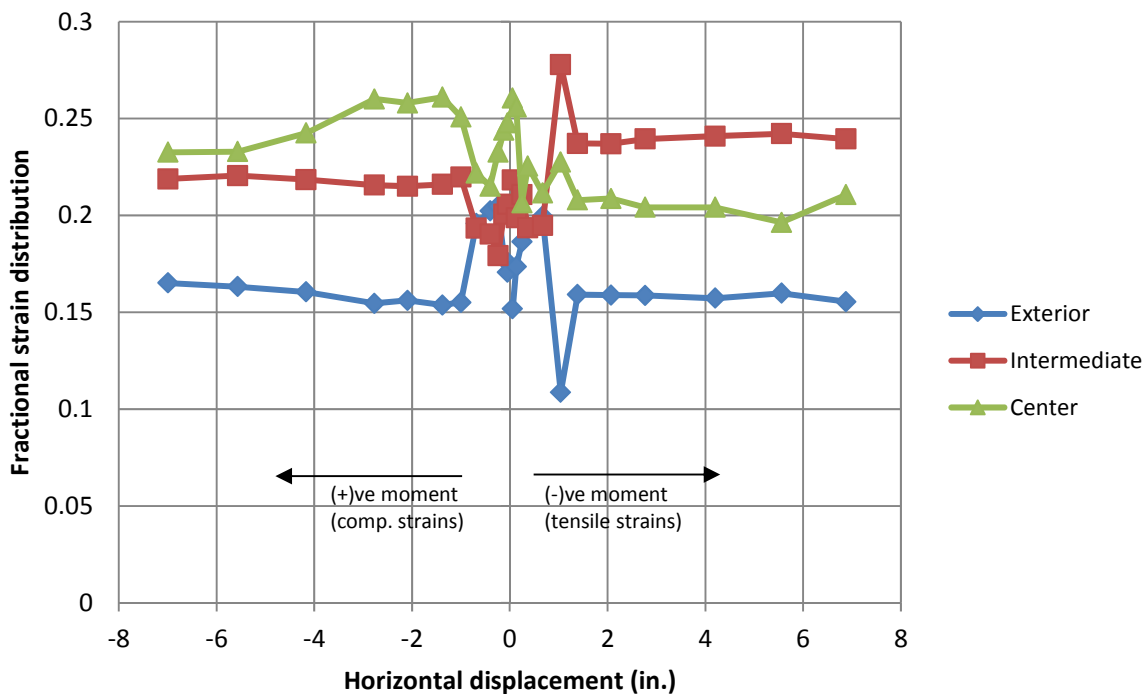


Figure 6.24: Contribution of Moment Resistance by Girders on the Improved Connection Side 1.5 feet from the Diaphragm Edge

Figure 6.25 provides the same data as Figure 6.24, but the range of the horizontal axis has been reduced to focus on the initial load steps. The first positive-horizontal-displacement step shows a strain distribution of 26.0%, 21.8%, and 15.1% to the center, intermediate, and exterior girders, respectively. This distribution indicates that already at very small displacements (this was in fact the load step corresponding to the  $+0.25 F_y$  condition), the load was distributed among all the girders. In subsequent load steps of  $+0.5 F_y$ ,  $+0.75 F_y$ ,  $+1.0 F_y$ , and  $+1.0 \mu_\Delta$ , the distribution gradually shifted away from the center girder, until it steadied at the levels shown in the higher displacements of Figure 6.24 and reported in the preceding paragraph.

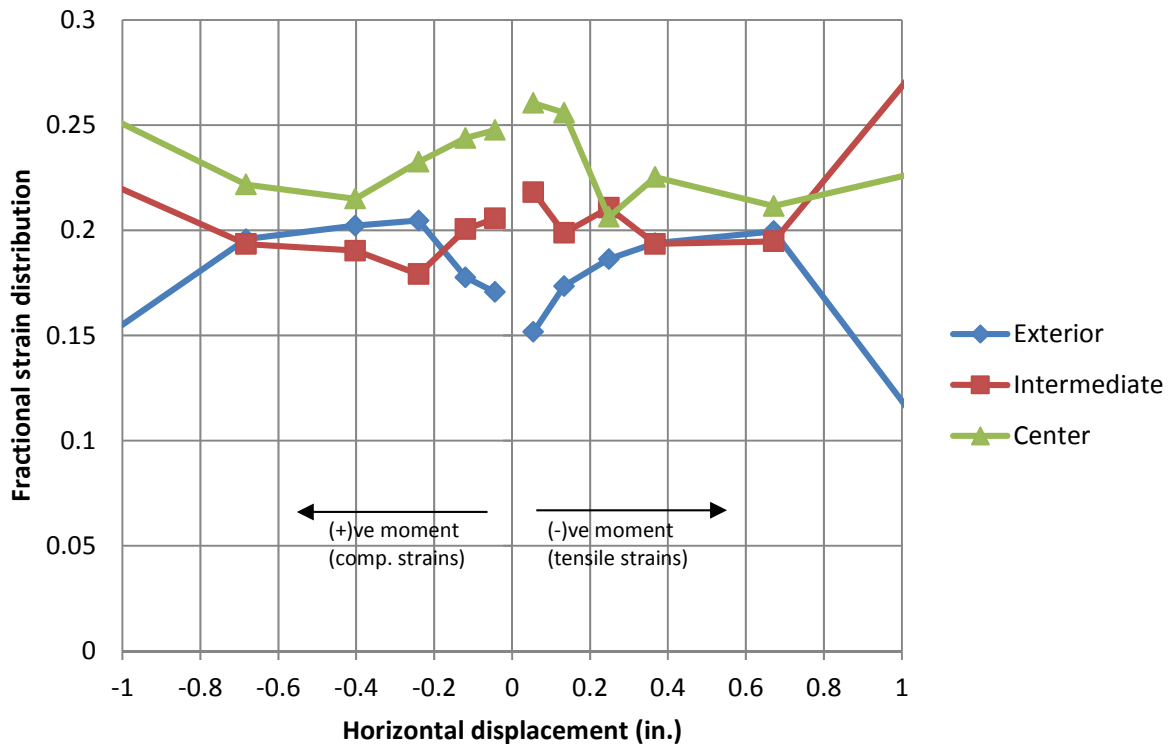


Figure 6.25: Figure 6.24 Repeated, with Horizontal Axis Range Reduced to focus on Small Lateral Displacements

Figure 6.26 provides the strain data from the deck reinforcement above the exterior and intermediate girders on the as-built connection side, 1.5 feet away from the diaphragm edge. No

strain data was available for the center girder at this location, because the gauge was damaged during construction. Therefore, the distribution for the center girder cannot be analyzed at this location; however, the exterior and intermediate girders can still be examined and compared. It should be noted that for the as-built connection, the negative displacements produced negative moment and therefore tension in the deck reinforcement; hence, the negative displacements would likely provide the better indicator of load distribution. This data shows that there were measurable strains in the reinforcement above both the exterior and intermediate girders during the horizontal displacement peaks, with slightly higher magnitudes in the exterior girder. Figure 6.27 provides the fractional distributions, and it can be seen that for the higher negative displacements, the exterior girder experienced 113% of the measured strain for the intermediate girder. An increase in the load distribution to the exterior girder such as exhibited here is possible if the tributary width of the deck for the exterior girder is less than the intermediate girder's deck width, and such was the case with this test specimen. Figure 6.28 provides a closer look at the small displacements, and again it can be seen that although the distribution shifted slightly as the displacements increased, the distribution to the exterior girder was sizeable already in the very first load step of  $-0.25 F_y$ .

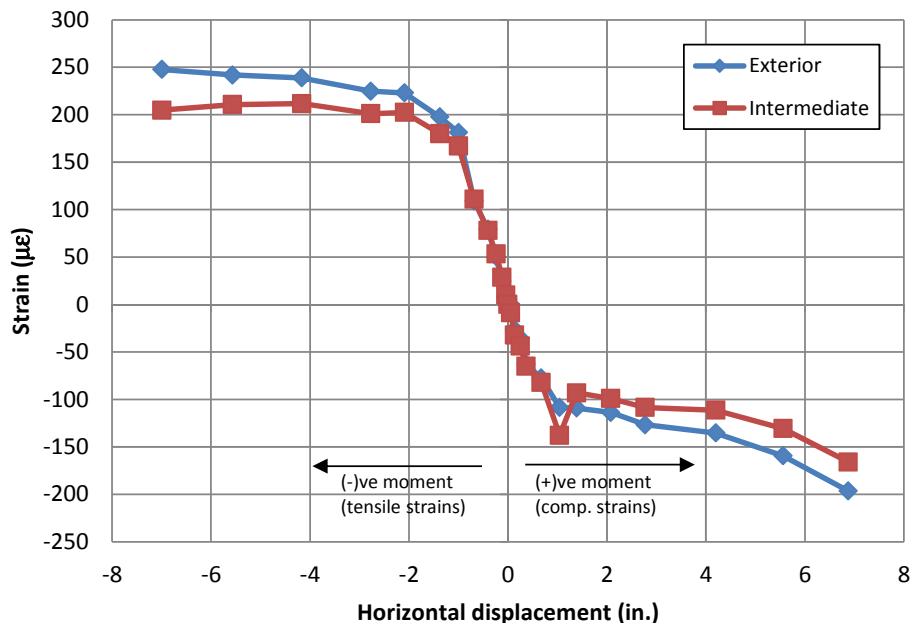


Figure 6.26: Deck Reinforcement Strains on As-built Connection Side, 1.5 feet from Diaphragm Edge, above the Exterior and Intermediate Girders

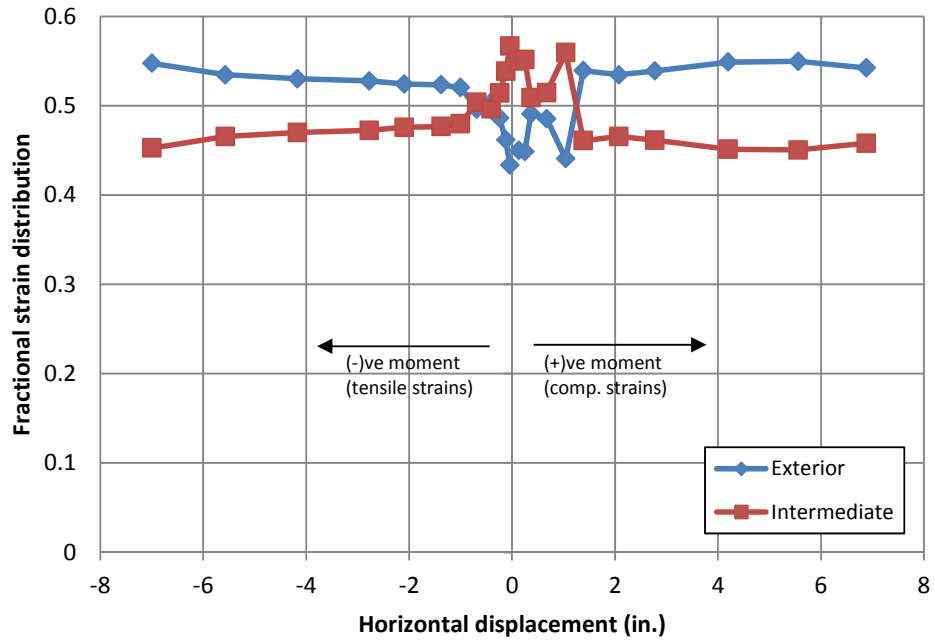


Figure 6.27: Contribution of Moment Resistance by Girders on the As-built Connection Side 1.5 feet from the Diaphragm Edge

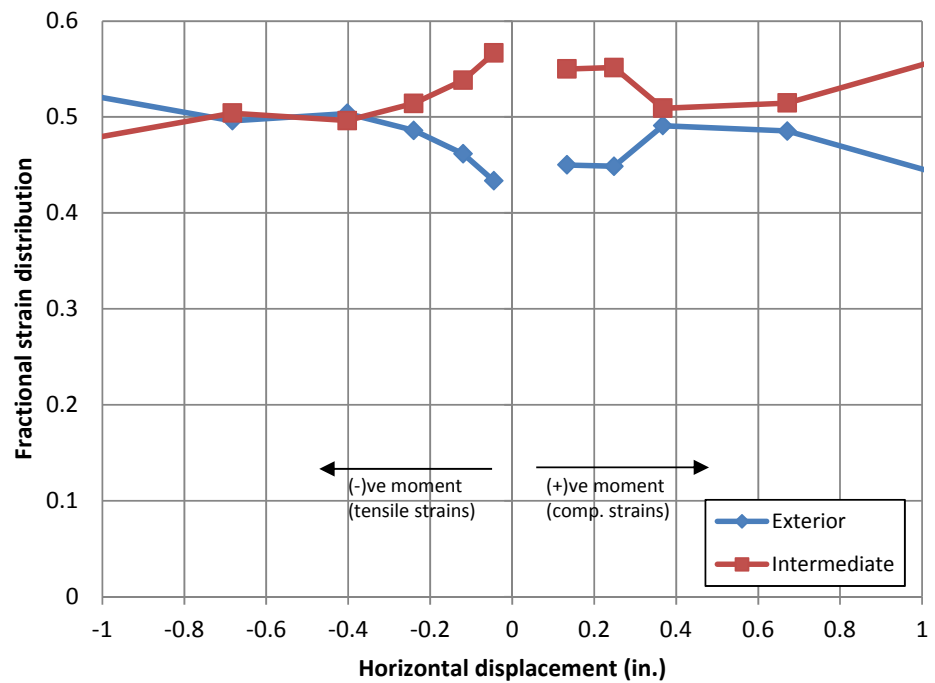


Figure 6.28: Figure 6.27 Repeated, with Horizontal Axis Range Reduced to focus on Small Lateral Displacements

### **6.3 Final Observations of Phase 1 Test**

Overall, the seismic performance of the connections, and the test unit as a whole, was extremely good. The as-built girder-to-cap connections behaved as a fixed connection instead of a pinned connection, contrary to current assumptions presented in the Caltrans' Seismic Design Criteria regarding precast girder connections to an inverted-T bent cap. This observation suggests that minimal as-built measures would be required in order to ensure a satisfactory performance of the inverted-T/I-girder bridges in the field. Furthermore, it was established that a satisfactory agreement was achieved between the predicted response of the grillage model and the measured response of the test unit.

### **6.4 Phase 2 Observations**

During the preliminary, low-level displacement half-cycles, only insignificant damage to the test unit was observed. Under negative displacements, the main observations were extensions of the cracks on the top of the deck that had formed during the horizontal testing phase. By the time the superstructure had been displaced by -0.25 in., it had already subjected the connection, on both sides of the bent cap, to a moment approximately 13% greater than the maximum negative moment that was achieved during the horizontal load-test phase. It wasn't until a displacement of -1 and -1.5 in. that the majority of the reinforcement in the deck had begun to yield, as shown in Figure 6.29, which depicts the strain data for the deck reinforcement that was located at the stem of the inverted-T and above the center, and West intermediate and exterior girders, on the as-built side of the bent cap.

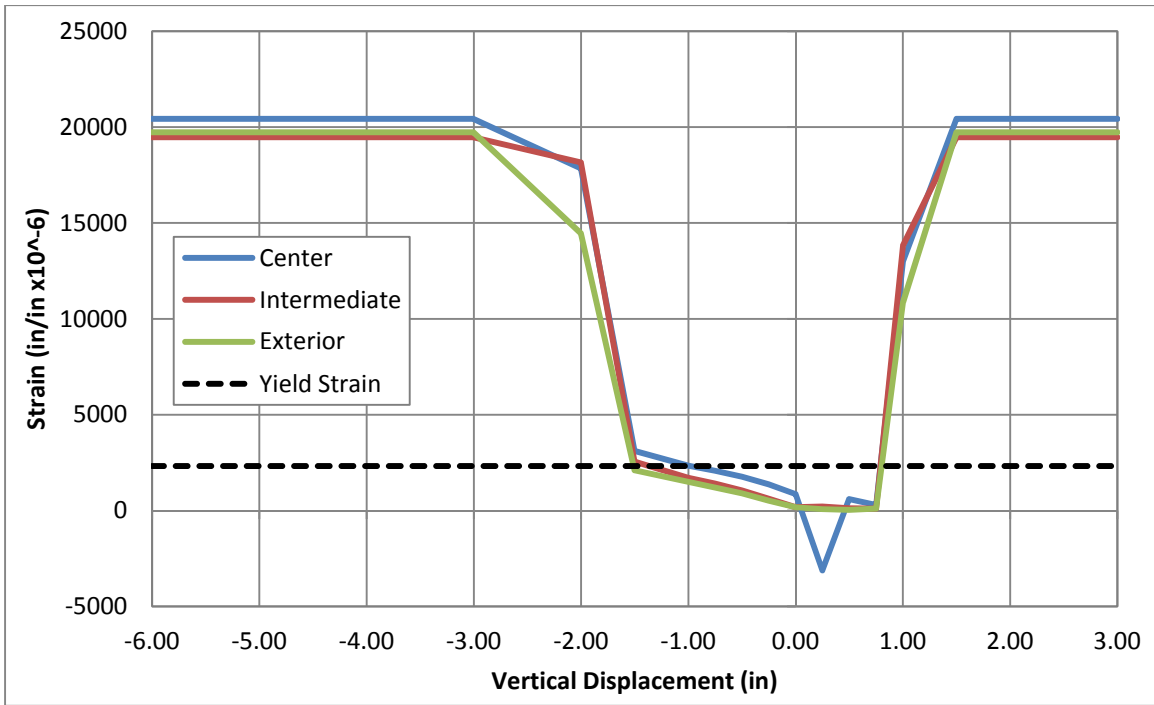


Figure 6.29: Vertical Displacement vs. Deck Reinforcement Strain above the Inverted-T Stem on the As-built Connection Side of the Cap Beam at Each Girder

At -1.5 in., the majority of the new cracks that had formed on the top of the deck were within the cap region, some of which had become irregular, extending longitudinally along the length of the deck, which was believed to be due to debonding between the deck reinforcement and the concrete as a result of the high strain demand as witnessed in Figure 6.30. It was also observed at this stage that a significant number of the cracks in the deck, which had developed under negative moments on both sides of the bent cap, had extended and penetrated the full depth of the deck, cracking the top flanges of the girders closer to the cap beam. Some of these cracks had also begun to extend into the web of the girders as inclined shear cracks, as can be seen in Figure 6.30.

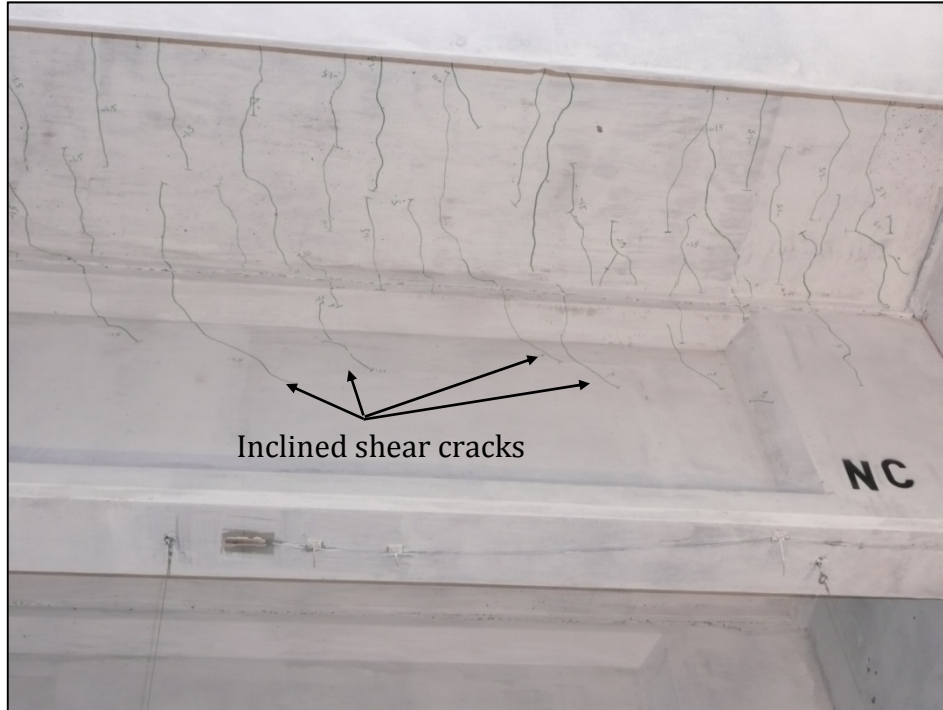


Figure 6.30: Inclined Shear Cracking Observed on the Center Girder on the Improved Connection Side at -1.5 in. Vertical Displacement

Under the positive low-level displacements, the main observation was also the extension of cracks that were formed during the horizontal testing phase. At a displacement of +0.25 in., the minor cracking that was observed during the horizontal load-test, along the bottom surface of the cap-to-diaphragm interface, had extended all the way along the length of the cap beam. Some longitudinal cracks had also formed at the edges of the bottom flanges of the girders within the diaphragm, which indicated that the girders were attempting to pull out of the diaphragm and away from the cap beam. The aforementioned cracking was observed on both the as-built and improved connection sides of the cap. Once the superstructure had been displaced by +0.5 in., the as-built connection was subjected to a moment approximately 27% greater than the maximum positive moment achieved during the horizontal load-test phase. At a displacement of +0.75 in., the improved connection side of the cap remained essentially unchanged and experienced no new damage from what was observed during the previous cycles of loads. However, the as-built side was beginning to experience some significant degradation. The gap between the bottom flanges of both the interior and exterior girders and the cap beam had

widened to a width of 0.2 in. The 1-in. thick grout along the bottom interface between the exterior girders and cap had also begun to separate and fall off the connection, leaving a gap of approximately 1 in., as shown in Figure 6.31. Penetration cracks were also observed on the face of the diaphragm, in a circular manner, around each girder (Figure 6.32, repeated). This was likely due to the girders, together with the dowels, attempting to pull out of the concrete in the diaphragm.

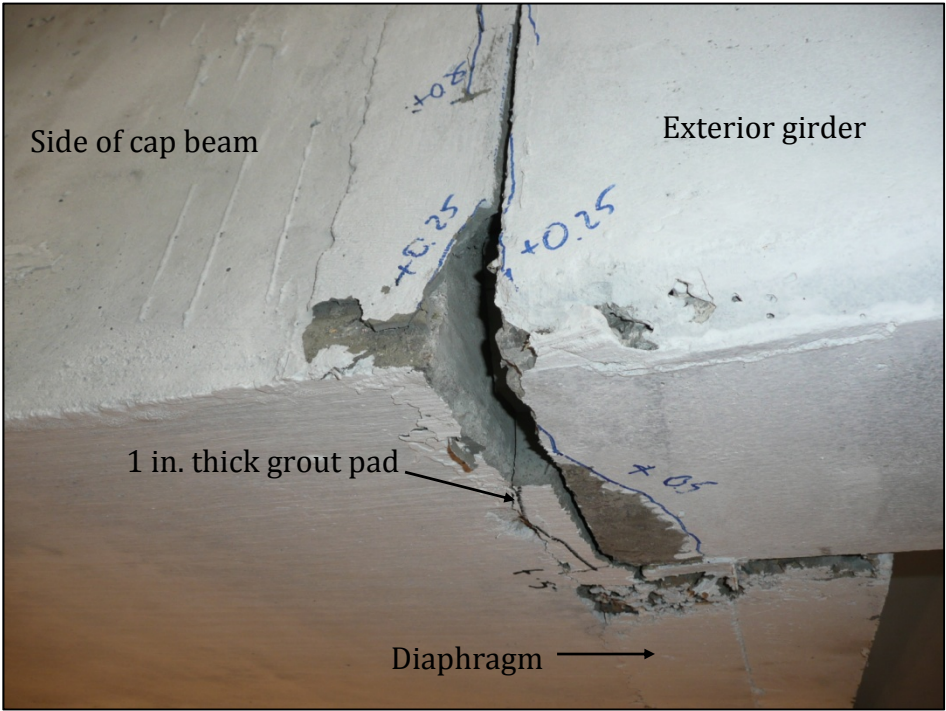


Figure 6.31: Partially Spalled Grout Pad at Girder-to-Cap Interface on the As-built Connection Side at +0.75 in. Displacement

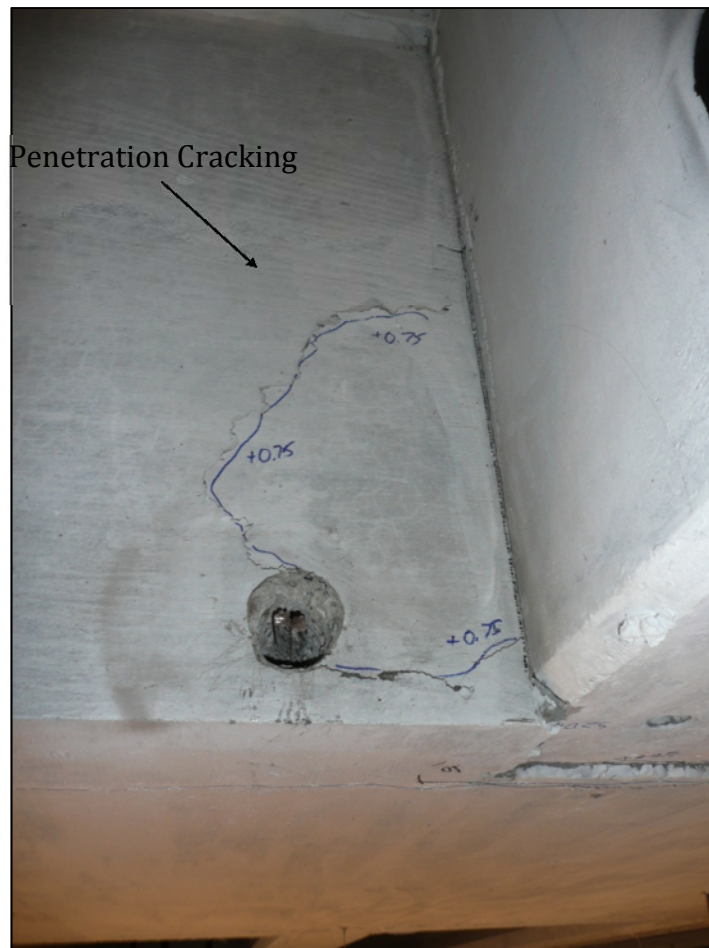


Figure 6.32: Penetration Cracks on the Face of the Diaphragm on the As-built Connection Side at +0.75 in. Displacement (Repeated)

During the first cycle, at a displacement of -2 in., a few new cracks had formed in the deck, while the majority of the existing cracks, on both connection sides, continued to extend and widen across the width of the deck. The most predominant cracks were located at the stem of the inverted-T and at the face of the diaphragm. The cracks at the stem of the inverted-T had a width of approximately 0.075 in., while the crack at the face of the diaphragm had an approximate width of 0.02 in. on the improved side of the connection and 0.025 in. on the as-built side, as

shown in Figure 6.33. The observation of the cracks extending across the entire width of the deck indicated that all of the girders were being engaged in resisting the moment imposed upon the girder-to-cap connection. The gap between the bottom flanges of the girders and the cap, due to the spalling of the grout along the interface, also appeared to have closed at this displacement level.

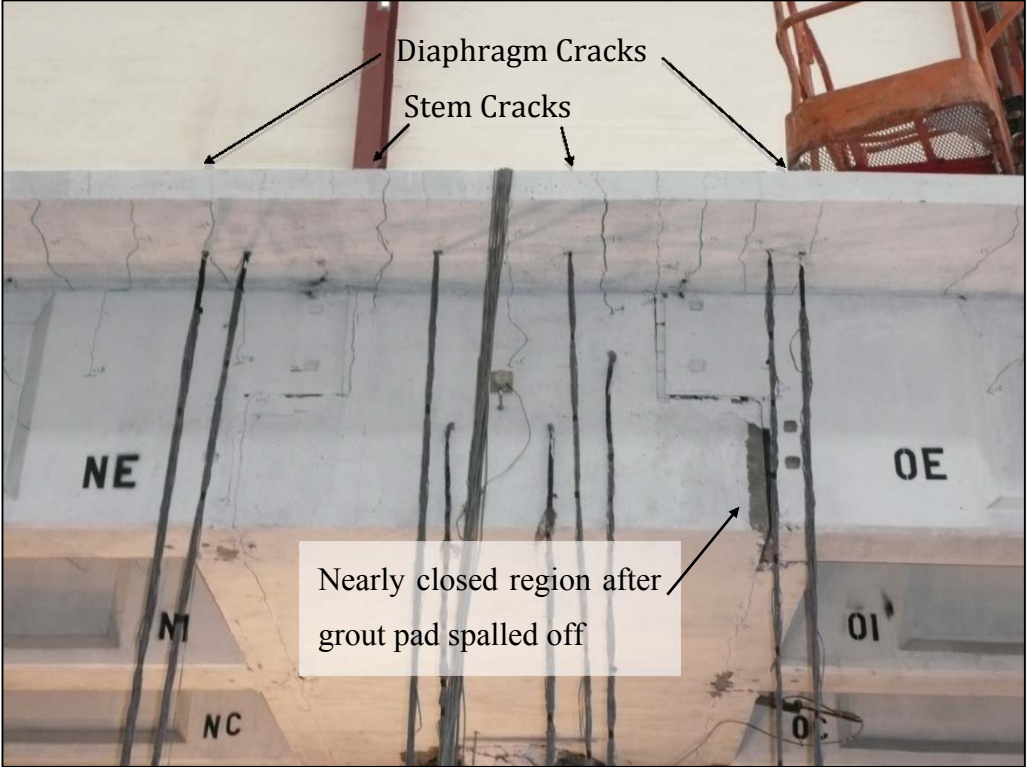


Figure 6.33: Deck Cracking Observed near the Cap Beam at -2 in. Displacement

On the other end of the aforementioned cycle level, at an upward displacement of +1 in., the grout along the bottom of the interface between the girder and the cap continued to spall, likely due partially to crushing as well as a lack of a direct form of attachment to the cap beam, resulting in a significant loss of grout along the girder-to-cap interface on the as-built side. The penetration cracks on the face of the diaphragm were also much more pronounced on the as-built connection side of the cap beam. Significant crack opening and pull out was observed between the bottom flanges of all of the girders and the cap on the as-built connection side as well. The separation between the bottom flange and the cap was measured at approximately 0.4 inches for

each girder. Furthermore, a significant crack, which signaled a separation, between the underside of the deck and the top of the diaphragm was observed in all of the bays on the as-built connection side, which measured 0.075 in. in the exterior bay and 0.035 in. in the intermediate bay (Figure 6.34). The improved connection side remained essentially unchanged as no new cracking or spalling of the grout pad was observed. Finally, no concrete crushing was observed on top of the deck and no cracking was observed in the bottom flanges of the girders on either side of the cap beam.

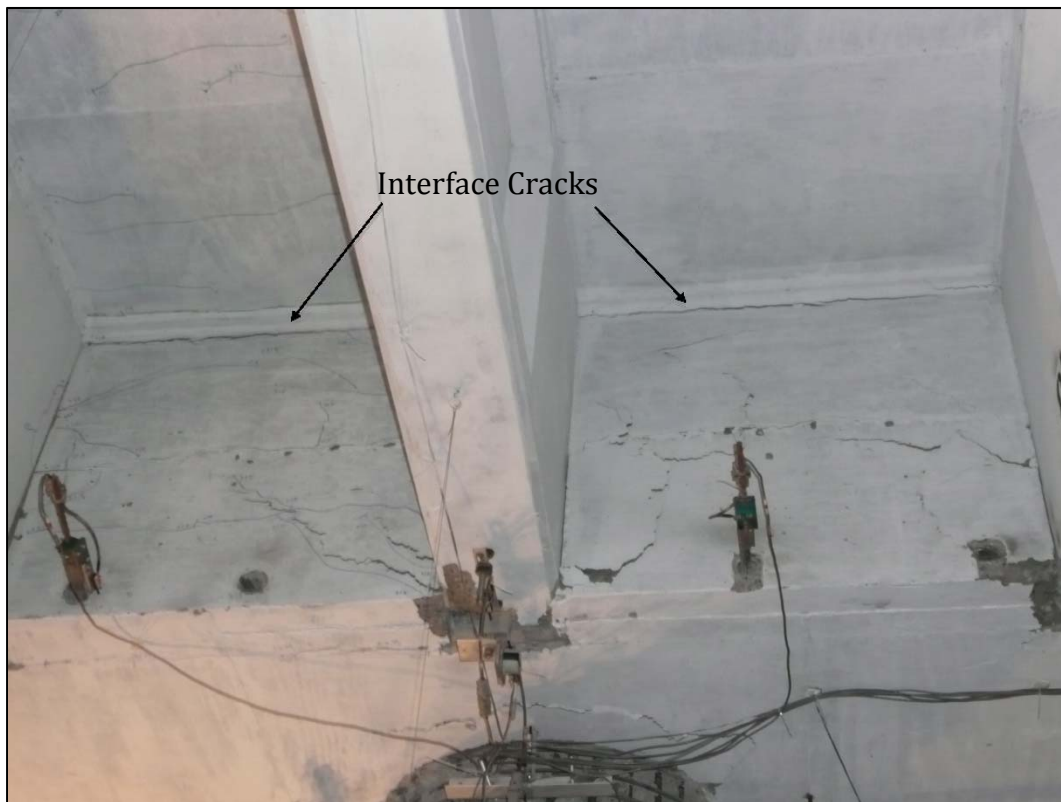


Figure 6.34: Deck-to-Diaphragm Interface Cracking at +1 in. Displacement

At a displacement of -3 in., the gap between the exterior girder and cap beam on the as-built connection side had completely closed. A significant number of crack extensions were observed on top of the deck. The crack along the stem of the inverted-T increased in width to 0.12 in. on the as-built side and 0.1 in. on the improved side, while the crack at the edge of the diaphragm increased to 0.075 in. on the as-built side and 0.04 in. on the improved side. Both of the aforementioned cracks extended all the way through the deck on the as-built connection side.

Some diagonal cracking was also noticed in the Southwest quadrant of the deck, near the location of the actuator.

When the superstructure was displaced to a level of +1.5 in., a significant gap opening was observed between the bottom flanges of the girders and the cap, on the as-built connection side of the cap beam. As the connection on the as-built side opened following the previous negative displacement cycle, concrete spalled off the bottom flanges of the girders. The penetration cracks on the face of the diaphragm opened and increased in length significantly. A few new penetration cracks were also observed within each bay on the as-built side. At this point, the majority of the grout along the bottom of the interface between the girders and the cap had fallen out of the connection. The improved connection side of the cap beam, however, experienced no significant damage. All of the grout along the interface between the girders and the cap was still present, no penetration cracks were observed on the face of the diaphragm, and the deck did not appear to have separated from the top of the diaphragm on this side. For all practical purposes, the improved connection side appeared undamaged.

No significantly new observations were made on either side of the cap beam when the girders were subjected to -4 in. of displacement. As the as-built connection closed, following the previous positive displacement cycle, concrete spalled off the diaphragm, exposing some of the reinforcement between the cap and the diaphragm. Atop the deck, increased diagonal cracking was observed throughout and a fairly considerable amount of new flexural cracking was observed over the cap region.

At a displacement of +2 in., very large gap openings were observed on the as-built connection side, between the bottom flanges of the girders and the cap. Significant damage was observed within the diaphragm, as the penetration cracks increased significantly and the diaphragm itself began to break away from the cap beam, as shown in Figure 6.35. No new damage was observed on the improved connection side of the cap beam. However, based on the force-displacement plots and the fact that the crack in the deck at the top of the stem of the inverted-T and the cap was larger than the crack between the bottom flange of the cap and the girder, it was clear that the cap was rotating about the plastic hinge in the top of the column,

which had formed during the first testing phase, and the hinge that had formed on the as-built connection side of the cap as the connection degraded. As a result, it was not possible to develop the required moment or rotation to exercise the improved girder-to-cap connection to its full capacity, which explained the lack of degradation of this connection region. This was further verified when the protocol was changed so that the South actuators were held at zero displacement, while the North side was displaced by +2 in. The cap beam continued to rotate about the column plastic hinge and the as-built connection, which dictated the response on the improved connection side, by limiting the moments and rotations generated, and again prevented the new connection from being isolated and exercised. However, the improved connection during the test was subjected to a 10% higher maximum positive moment than that applied to the as-built connection at the same displacement level of +1 in.



Figure 6.35: Damage to As-built Connection Exterior Girder at +2 in. Displacement

The final portion of the test was completed using the original load protocol that was developed. Both sides were displaced by -6 in., followed by +3 in., and a final cycle to -6 in,

shown in Figure 6.36 and Figure 6.37. Based on the force-displacement plots for the structure at -6 in. during the test, it appeared as though both connection details still had some additional negative moment capacity, as a significant drop in strength was not noted. However, when the structure was cycled to +3 in., a 42% drop in strength was noticed, which indicated that the as-built connection detail had already reached its ultimate capacity. Therefore, the ultimate displacement for the positive as-built connection was defined as the point at which the strength had decreased by 20% from the maximum force that was applied, which corresponded to a displacement of approximately 1.5 in. This was also apparent by observing the significant amount of damage and pull out of the girders that was observed at a displacement of 1.5 in., as well as the subsequent displacement cycles. Therefore, it was decided that the behavior of the as-built connection had been adequately captured and the test was terminated.



Figure 6.36: Displaced Test Unit at -6 in. of Displacement



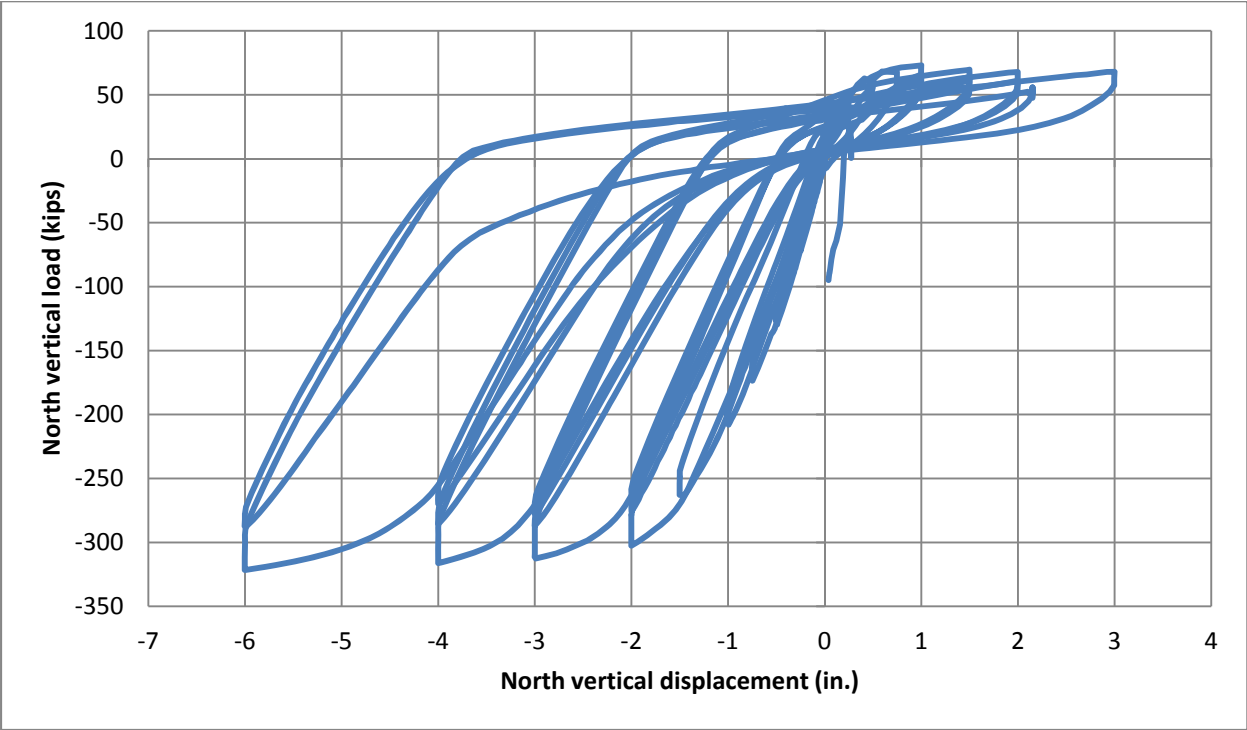
Figure 6.37: Overall Response of Test Unit at +3 in. of Vertical Displacement

## 6.5 Phase 2 Test Results

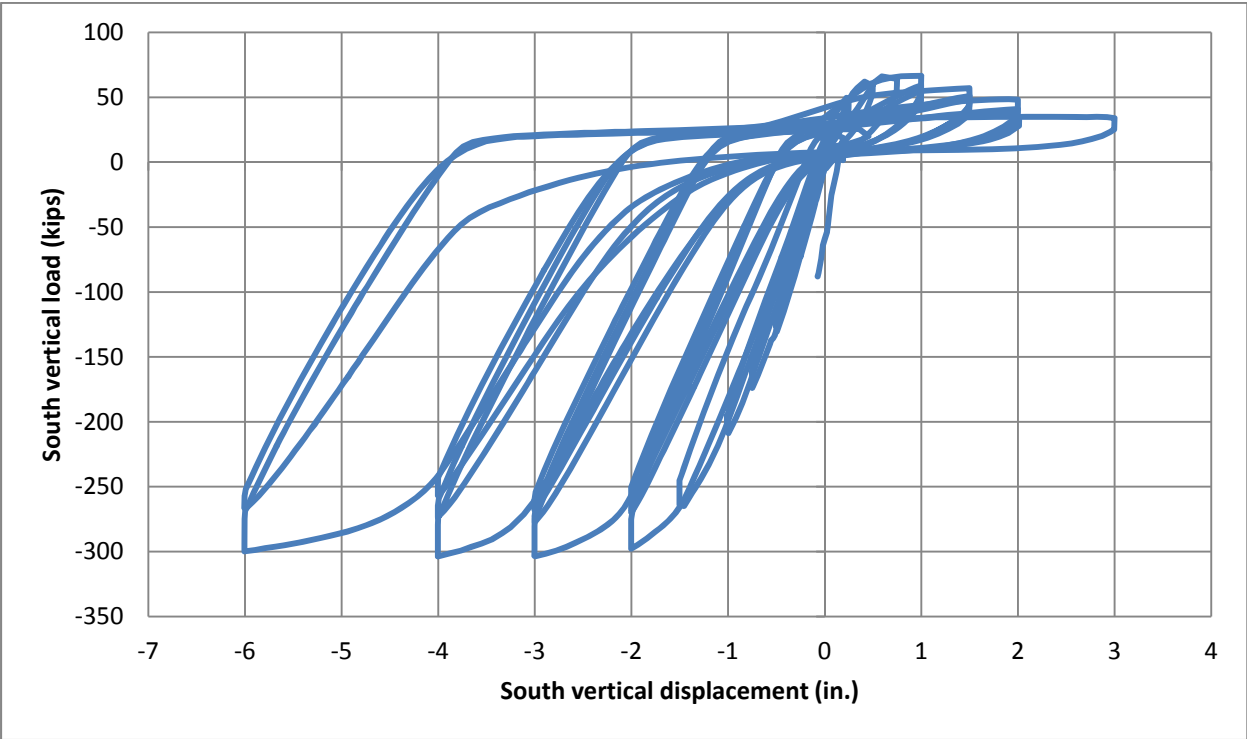
### 6.5.1 Overall Vertical Load Response

The test structure experienced a maximum positive displacement of 3 inches and a maximum negative displacement of 6 inches. Both the positive and negative responses were as good, if not better than expected. In fact, the force vs. displacement plot indicated that the structure still had additional negative moment capacity when the test was terminated, as a significant drop in strength was not noticed. Therefore, it is likely that a displacement greater than negative 6 inches could have been achieved. However, extensive and significant cracking was noticed in the deck at the end of the test, with the largest cracks corresponding to the stem of the inverted-T and the outer edge of the diaphragm. Since the cracks spanned the entire width of the structure, it was demonstrated that all of the girders were still actively engaged in resisting the applied moment. Finally, as noted earlier, the response of each connection detail was not adequately isolated and thus, the new connection detail was not fully tested. As the as-built connection yielded, the entire cap beam began to rotate about the column plastic hinge and the as-built connection, thereby limiting the forces and rotations experienced within the new connection detail.

Figure 6.38 provides a first look at the test data related to the overall specimen response during the Phase 2 testing. This plot of the vertical load versus the vertical displacement for both the improved (North) connection and the as-built (South) connection exhibits a clear hysteresis behavior. While the data initially appears to indicate that both sides experienced plastic deformation, observation during testing indicated that inelastic deformation was exclusively occurring to the as-built connection side while elastic behavior was essentially maintained on the improved connection side throughout the entirety of the test. Thus, the data here is dominated by the inelastic deformation and rotation on the as-built side. To show that behavior more clearly, the cap rotation, cap displacement, and girder displacement data was carefully investigated so these observations could be verified.



(a) Improved connection side



(b) As-built connection side

Figure 6.38: Vertical Load-Displacement Response

As a first step in investigating the difference in behavior between the improved and as-built sides, the vertical girder displacements for both sides at peak loads were compared. These data are provided in Figure 6.39. While subtle, this plot does show a difference in behavior between the improved and as-built sides, as the load on the improved side due to peak vertical displacements holds steady for both positive and negative displacements. However, the load on the as-built side at peak displacements showed strength degradation for both positive and negative displacements at the higher displacement steps outside the range of -3 inches and + 1 inches. The strength degradation that occurred to the positive moment resistance was significant and corresponded to a 15% (at 1.5 in.), 28% (at 2 in.), and 49% (at 3 in.) reduction of the maximum moment resistance recorded at 1 in. vertical displacement. The negative moment degradation was insignificant and experienced a maximum reduction of about 5 percent. This figure also confirms that, for the higher displacement steps, the rotation occurring in the damaged as-built connection prevented a larger load from being imposed on the improved connection, i.e., the displacements applied at the girder ends produced rotation in the as-built connection rather than generating larger moments in the improved connection. Thus, what appears to be inelastic behavior in the improved connection is actually caused by the applied displacement producing inelastic rotation in the as-built girder-to-cap connection rather than being caused by inelastic hysteresis actions within the improved connection.

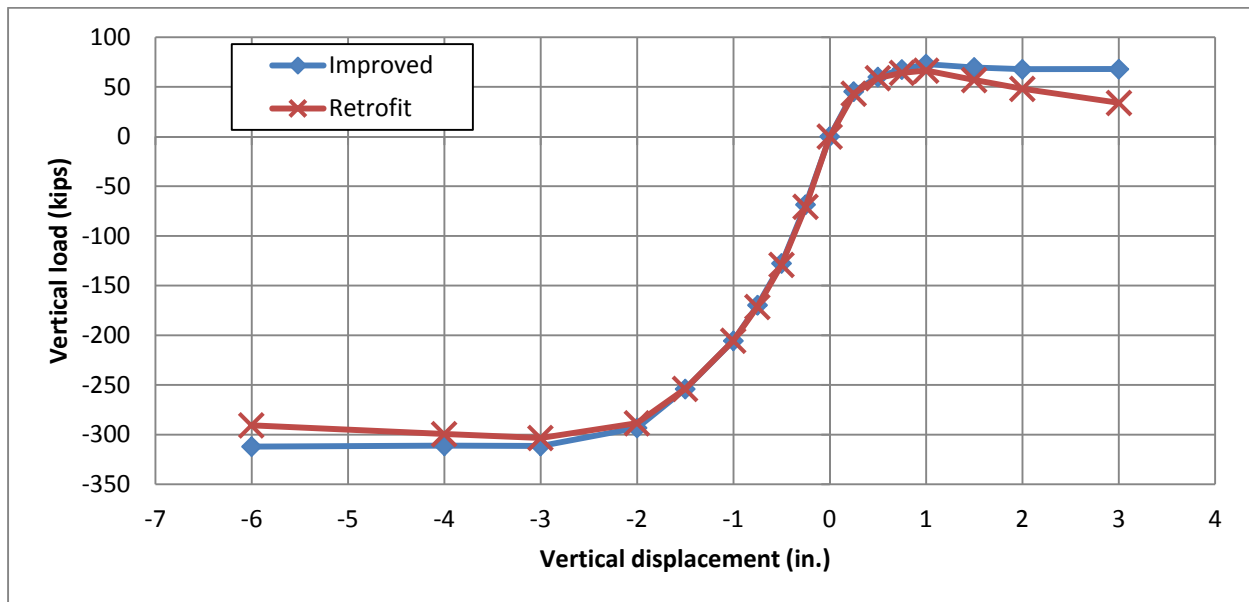


Figure 6.39: Comparison of Peak Load-Displacement Behavior

For the aforementioned reasons, the cap rotation and displacement data was further examined to isolate the girder behaviors on the improved side and on the as-built side. The observed behavior during the higher displacement steps of the Phase 2 test indicated that the girders were rotating relatively freely about the as-built girder-to-cap connection (approximately 1.5 feet south of the cap centerline, as shown in Figure 6.40). Therefore, the rigid body rotation that occurred in the girders due to the hinge behavior needed to be accounted for in establishing the improved connection behavior. Rotation devices were located at the centerline of the cap and recorded data throughout the Phase 2 test. The vertical displacement of the cap centerline was also recorded throughout the duration of the Phase 2 test. Therefore, the combined behavior of the vertical displacement of the cap and the rotation of the cap was investigated to account for the rigid body rotation in the girders due to the hinge behavior.

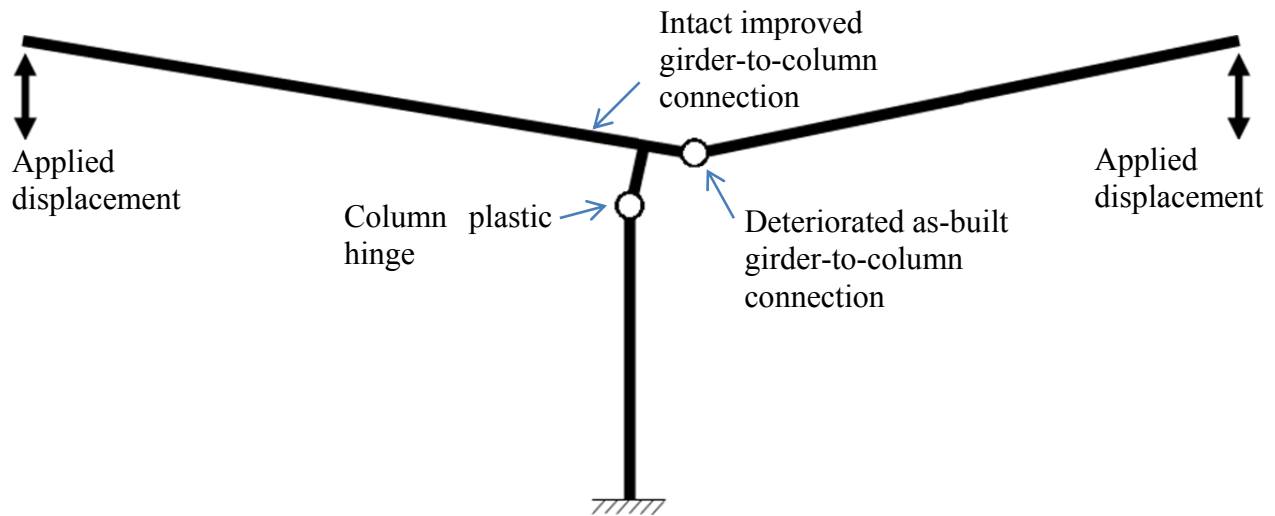
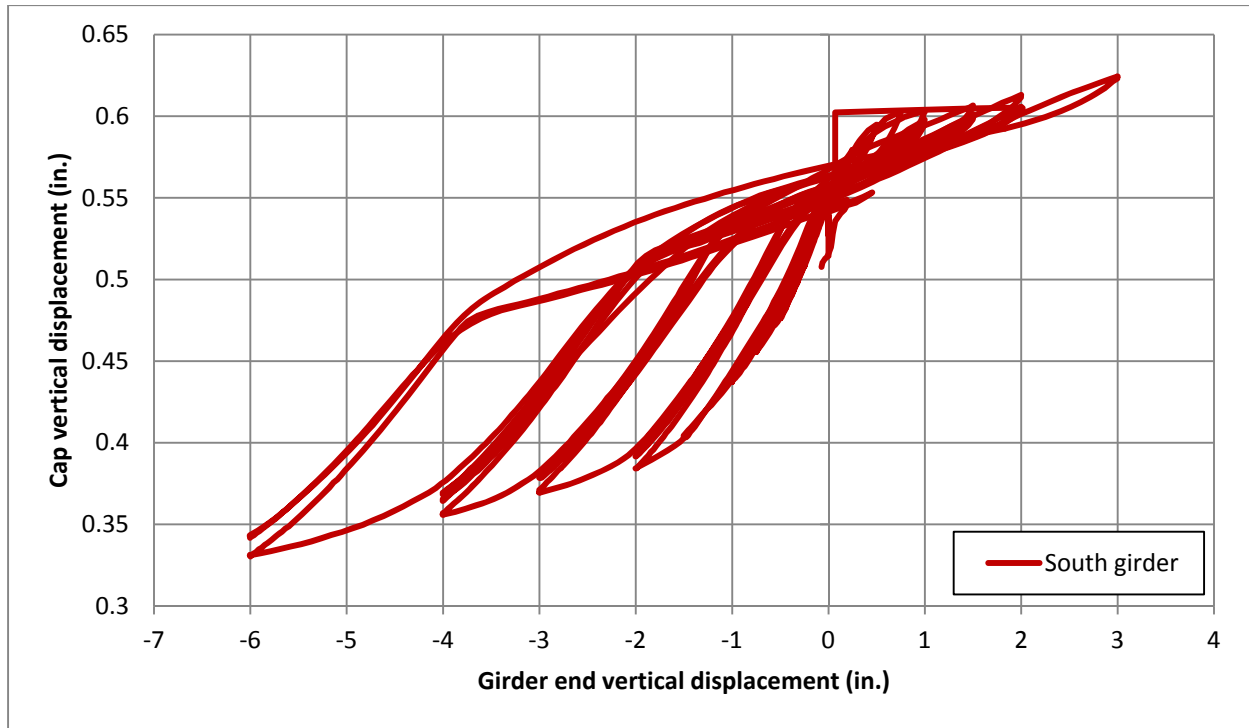
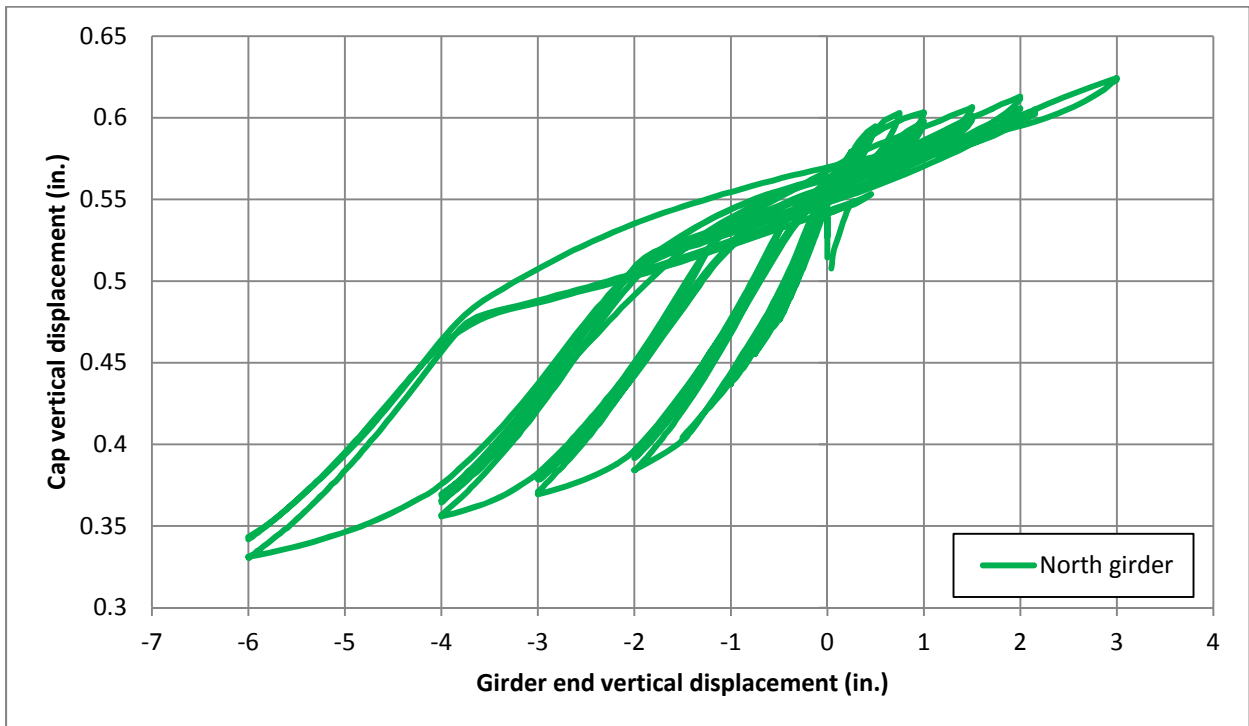


Figure 6.40: Rotation of girders about as-built connection

The cap beam vertical displacement during the Phase 2 test is provided in Figure 6.41, plotted versus the as-built girder end vertical displacement (a) and versus the improved girder end vertical displacement (b). These two plots reveal a very similar hysteresis; however, this similarity in shape does not indicate a similarity in behavior of the girders overall but rather an indication that the displacement data from both the improved and as-built sides is dominated by the performance of the deteriorated as-built connection. It is interesting to note that the behavior is observed to be much more linear for the positive girder end displacements.



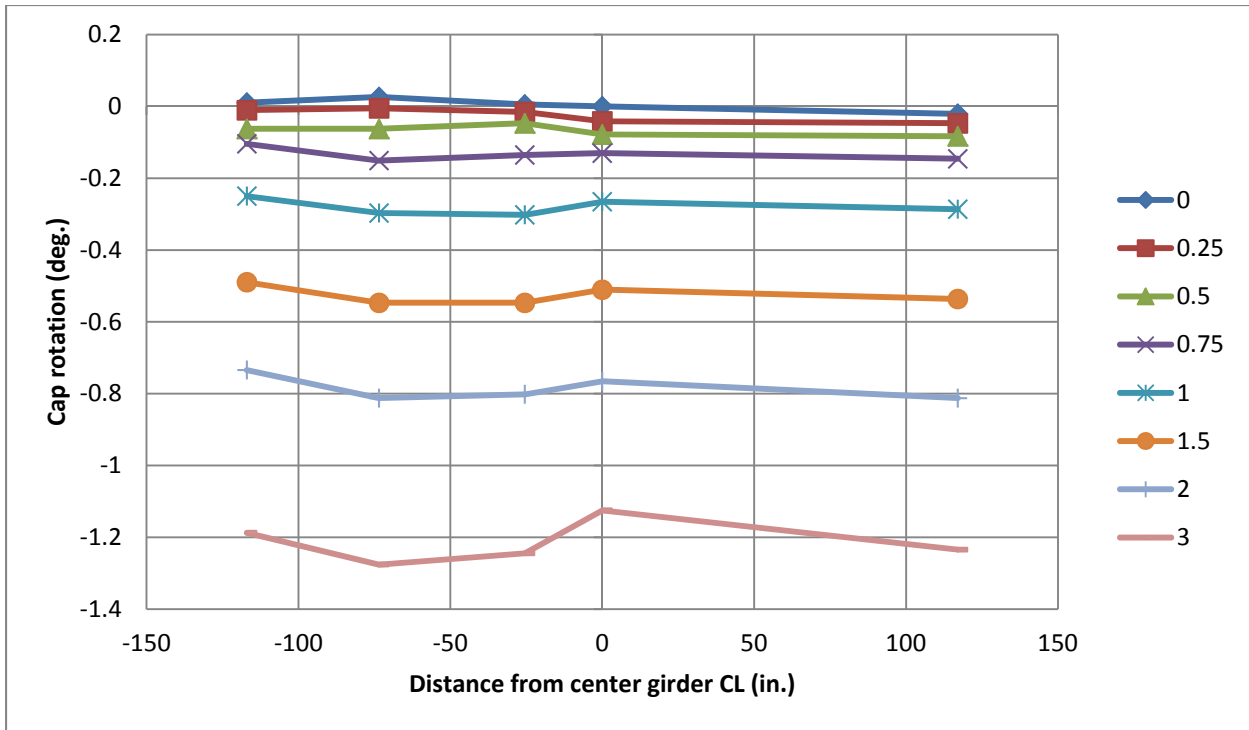
(a) Plotted versus south girder vertical displacement



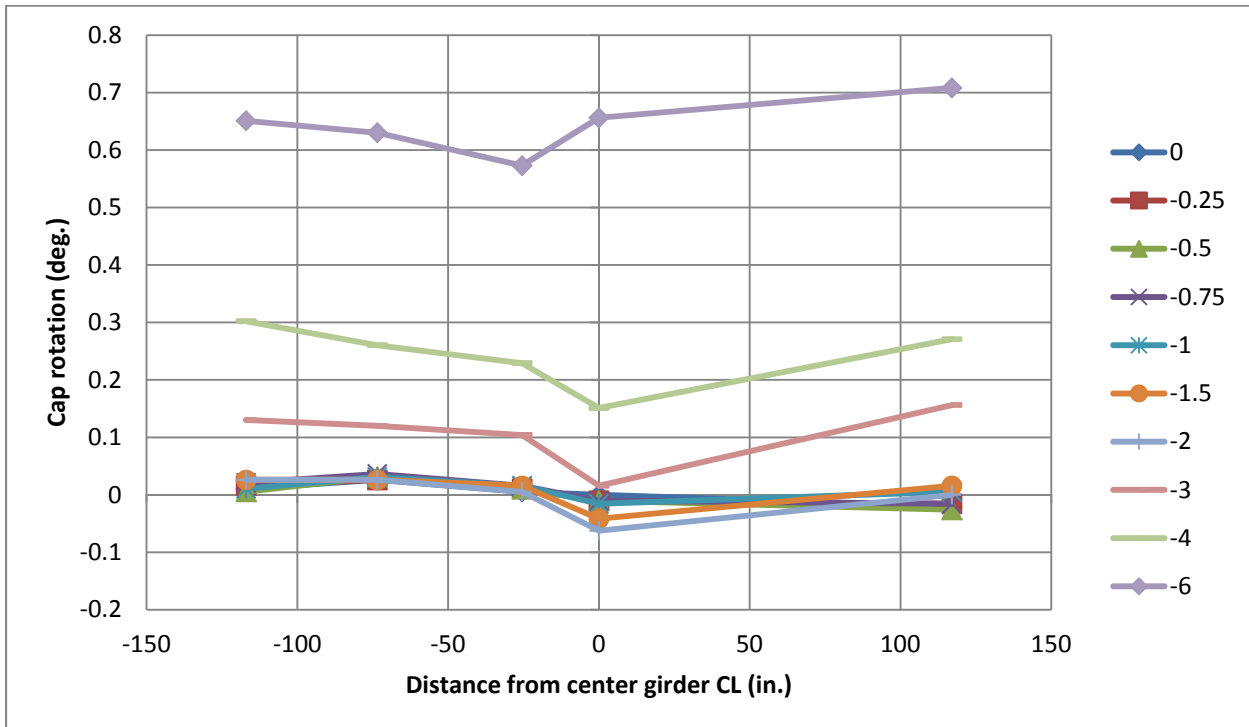
(b) Plotted versus north girder vertical displacement

Figure 6.41: Cap Beam Vertical Displacements during Phase 2 Test

In order to determine whether the rotation data from the cap beam was valid, the data from each of the four rotation devices was combined to produce the rotation profiles at the peak girder end displacements that are provided in Figure 6.42. These profiles reveal that, although there was a small amount of twist in the cap for both the positive and negative girder end displacements, the cap rotation was relatively similar across the length of the cap for the peak displacements. Thus, the average rotation determined from the four rotation devices is valid data to use in determining the girder rotation at the cap location.



(a) Positive girder end displacement



(b) Negative girder end displacements

Figure 6.42: Cap Beam Rotation Profiles

To isolate the behavior of the improved connection on the improved connection side of the test specimen, the cap beam rotation and its vertical displacement were used to determine the rigid body rotation of the girders. Thus, the actual flexural displacement of the girders with improved connection to the cap could be isolated after excluding the rotation of the cap about the deteriorated as-built connection. The cap rotation data was incorporated into the girder deflection data by using the average rotation from the five cap rotation devices, assuming the as-built cap-to-girder connection as the point of rotation, and using trigonometry to determine the vertical displacement due to rotation at each of the girder vertical displacement device locations. In addition, the average column growth, measured by two vertical displacement devices on either side of the column, was also subtracted from the girder vertical displacement data.

In a further attempt to isolate the improved connection behavior, the girder vertical displacements modified as described in the above paragraph were plotted versus the total moment at the improved (North) girder-to-cap connection across all five girders. Further discussion on the total moment was provided earlier in Figure 6.17 and Figure 6.18. Vertical girder displacement histories on the improved side for the center girder are provided in Figure 6.43. The figure provides displacement histories for four different gauges along the length of the girder, and the legend in the figure provides the longitudinal distance from the cap centerline to each gauge location. Only the center girder data is provided because there are no significant differences observed in the data from the intermediate and exterior girders.

Examination of this figure reveals that the attempts to isolate the improved side behavior produced some result, in that the hysteresis behavior in the positive moment (corresponding in this case also to positive vertical girder load and displacement) direction was eliminated. However, displacement drift remains in this data, occurring between each load step. The drift appears to be related to the as-built connection deterioration, as it appears that the as-built connection contribution to the data has not been completely isolated from the improved connection data.

The data is seen to be quite linear for the location 56 inches from the cap centerline. However, at each of the subsequent locations (112 in., 168 in., and 192 in. from the cap centerline), an increasing amount of drift is observed to have occurred during each load step. This drift is especially evident in the four highest negative load steps, as 4 distinguishable loops are noticeable for the 112 in., 168 in., and 192 in. locations.

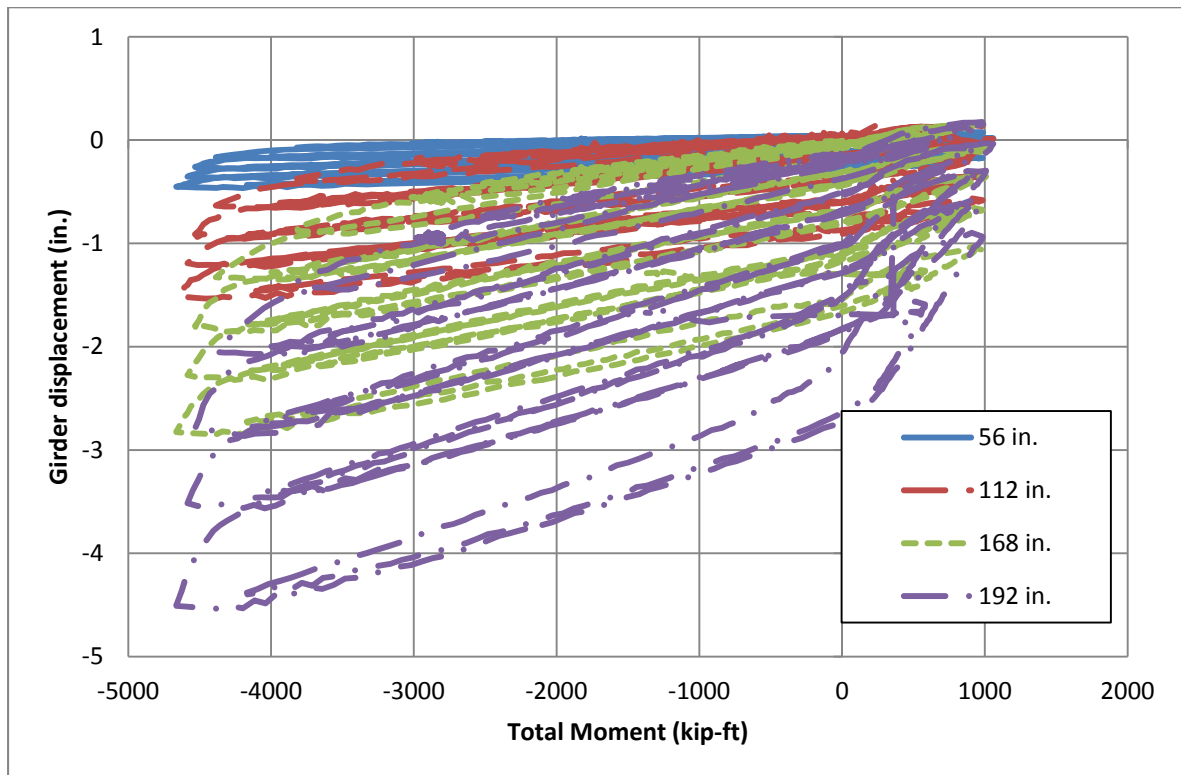


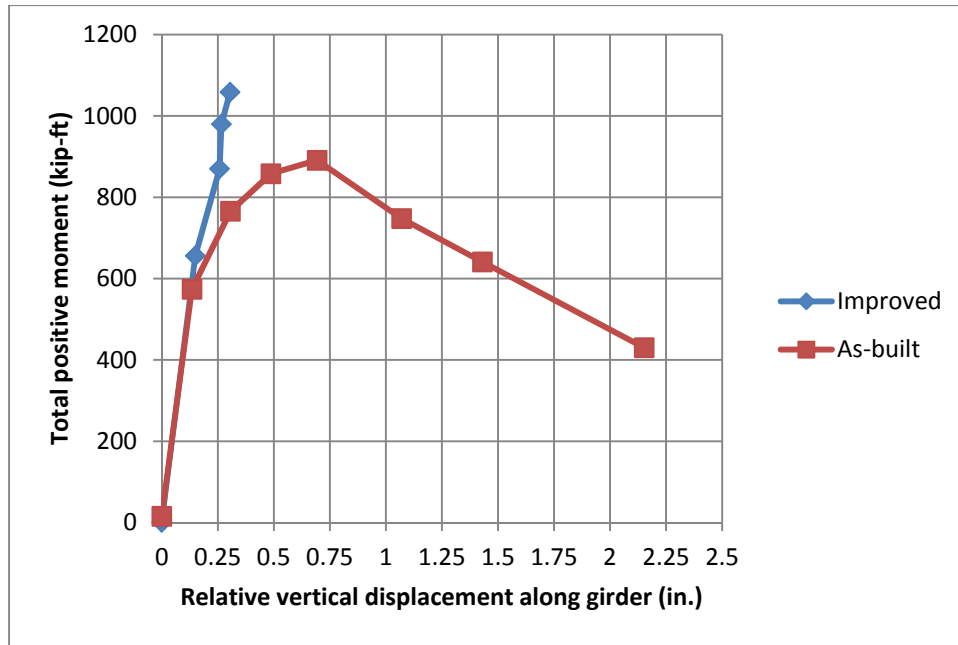
Figure 6.43: Vertical Displacement Histories from Transducers along the Length of the Improved Side Center Girder

To better compare the vertical deflection behavior of the girders on the improved connection side with the girders on the as-built connection side, the relative vertical displacement of the girders with respect to a displacement transducer just outside each of the connection regions was used. This relative displacement data was compiled for the first peak displacement steps for both sides. This exercise was completed for the applied displacements producing both positive and negative moments in the connections, and the absolute values of the moments and

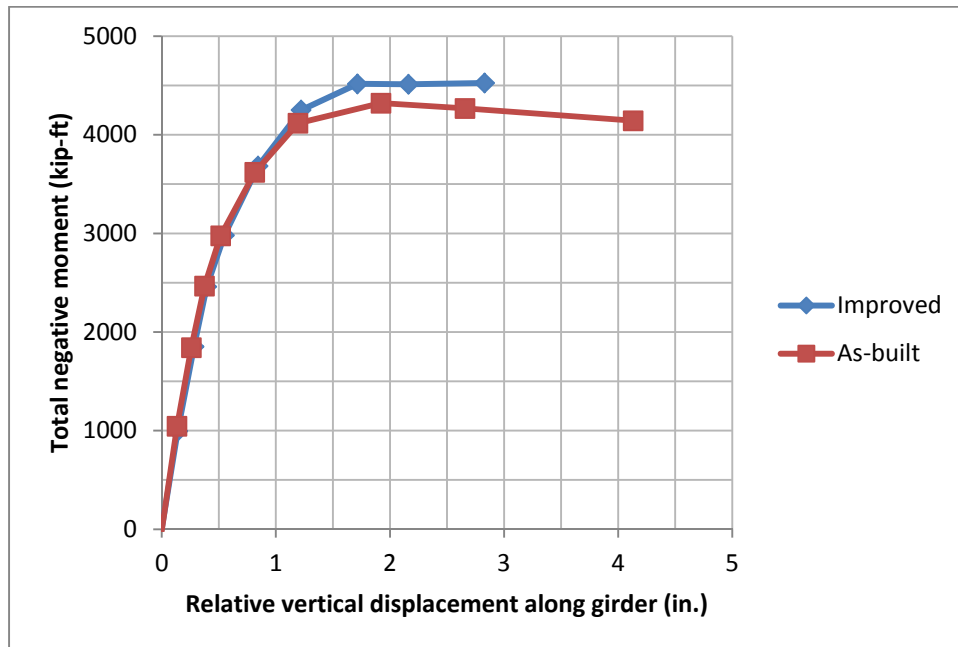
displacements were then used to superimpose the results from both the improved and as-built sides for easy comparison. The results of this data reduction are shown in Figure 6.44.

The comparison of the improved and as-built sides when subjected to positive moment clearly exhibits a difference in behavior between the two connection types. While the improved connection side remained essentially elastic throughout the test and carried a total moment close to 1100 kip-ft, the as-built connection side clearly shows a degrading softening behavior, with a maximum positive total moment close to 900 kip-ft followed by a gradual deterioration in total load. It should be noted that the data from the improved side at higher displacements than the maximum total moment were removed in this plot for clarity, as the data-reduction process incorporating cap rotations and displacements produced some irregular results for those few points. One further observation of the positive moment loading is that the elastic portions of both the improved connection and the as-built connection have almost identical slopes, indicating a very similar stiffness for both connections prior to the inelastic action in the as-built connection. These findings are consistent with the test observations in that the as-built connections gradually failed starting from a positive displacement of about 0.75 inches.

A difference between the improved and as-built connections due to negative moment loading was also observed, although the difference is more subtle than for positive moment loading. While both sides exhibited some inelastic action, the as-built connection showed a slight decrease in strength while the improved connection retained its strength. Also, it appears that the as-built connection experienced larger displacements in comparison to the improved side. Both of these observations are due to the loss of the grout pads at the bottom portion of the girder-to-cap connection on the as-built side (see Figure 6.31). Overall, the comparative responses of the two connections in Figure 6.44 confirm the superiority of the improved connection details over the as-built connections.



(a) Positive moment loading



(b) Negative moment loading

Figure 6.44: Relative Vertical Girder Displacements for Peak Displacement Steps

### **6.5.2 Girder-to-Cap Connection Response**

Given that the Phase 2 test focused on vertical loading of the girder ends, the primary force and deflection data for the girders has already been provided with the overall response in Section 6.5.1. However, further investigation of the girder behavior is provided in the section that follows.

A comparison of the data collected against the predictions based on the SAP2000 grillage model for the total force applied to the superstructure on the as-built connection side of the bent cap versus the relative girder displacement, established by subtracting the displacement of the string potentiometer located closest to the center of the cap beam and the actuator displacement, is shown in Figure 6.45. A relative girder displacement, rather than the displacement of the actuator, was plotted against the force applied to the superstructure in order to remove some of the errors in the measured displacements due to the rotation of the cap beam about the as-built connection and top column plastic hinge, as has been discussed at length in the results presented previously in this report. Although the predicted responses captured the general trend adequately, there were some discrepancies observed. For example, the connection actually achieved a greater moment resistance than what was predicted under positive moments while a lower than predicted resistance was seen under negative moments. The increased positive moment resistance was likely due to the increased concrete strengths that were achieved at the time of testing, thereby increasing the stiffness of the members, but not included in the model. However, it is seen that the effective superstructure stiffness values that were input into the grillage model appeared satisfactory for predicting the stiffness of the system.

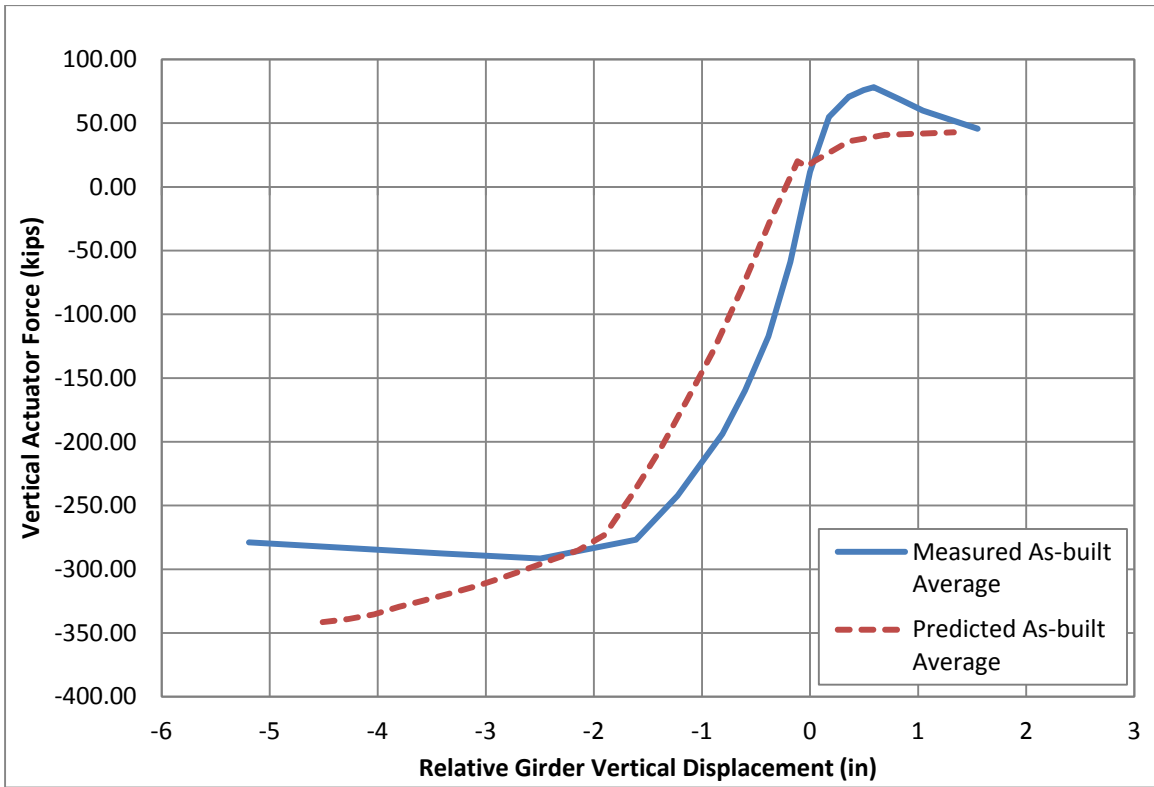


Figure 6.45: Predicted vs. Measured Total Force vs. Relative Displacement for As-built Connection

The connection also achieved larger rotations than were initially predicted, as shown in Figure 6.46 and Figure 6.47. At the end of the testing, it was apparent that the dowel bars within the girders had punched out of the diaphragm, especially at the exterior girders, rather than being fully embedded in the diaphragm and contributing to a fully effective dowel bar action, as shown in Figure 6.48. This was further demonstrated by examining the strains along the bottom, most extreme row of dowels (Figure 6.49), which showed that the strains within the dowels didn't gradually increase and surpass the expected yield strain, as required for a fully effective dowel bar action to develop, until the connection had already reached its ultimate displacement. Additionally, the shear friction mechanism that was expected to take place between the girder and the diaphragm was not as dominant as expected, as the concrete around the girder and within the entire diaphragm, cracked and spalled due to the punching of the dowels. The lack of these primary mechanisms occurring within the connection is the likely explanation for the increased displacement for the girders that was somewhat observed, due to an increase in rotation within the connection. Also, the lower negative moment resistance that was observed within the connection was most likely due to the spalling of the grout pad along the girder-to-cap interface. The loss of this pad increased the rotations experienced within the connection and also effectively decreased the lever arm for the actuator forces about the connection during lower displacement levels, before the girder and the cap came back into full contact with one another.

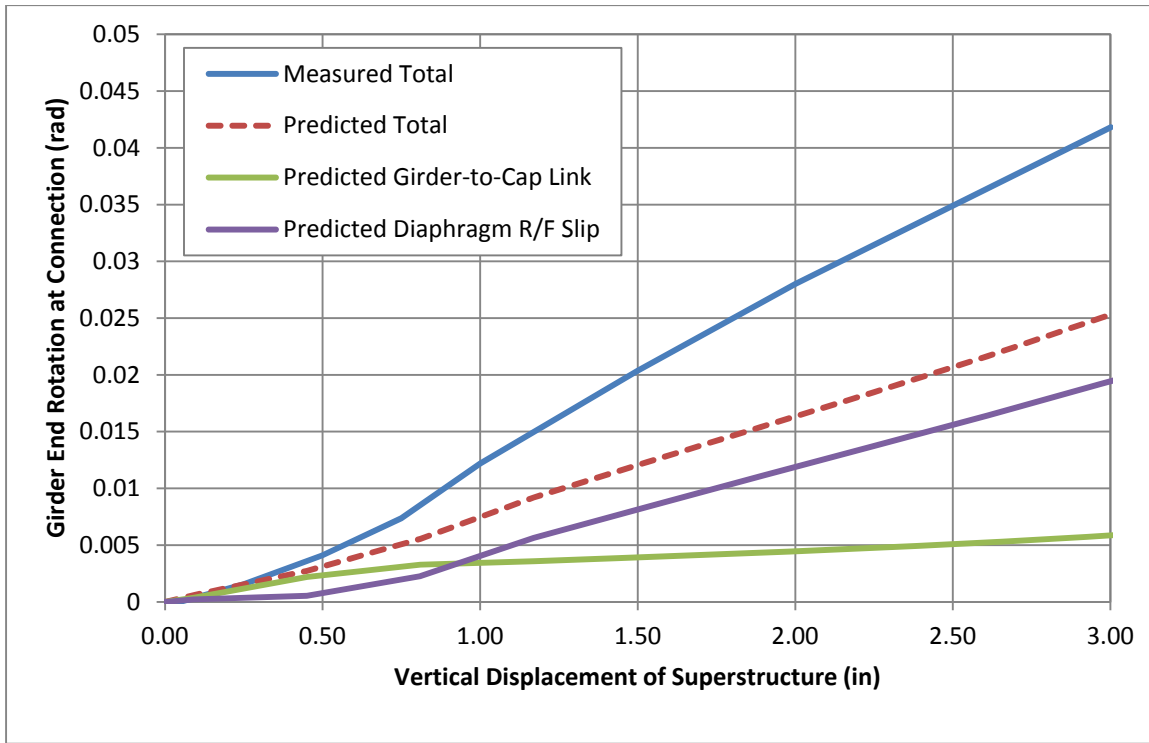


Figure 6.46: Positive Vertical Displacement vs. Center As-built Girder Rotation

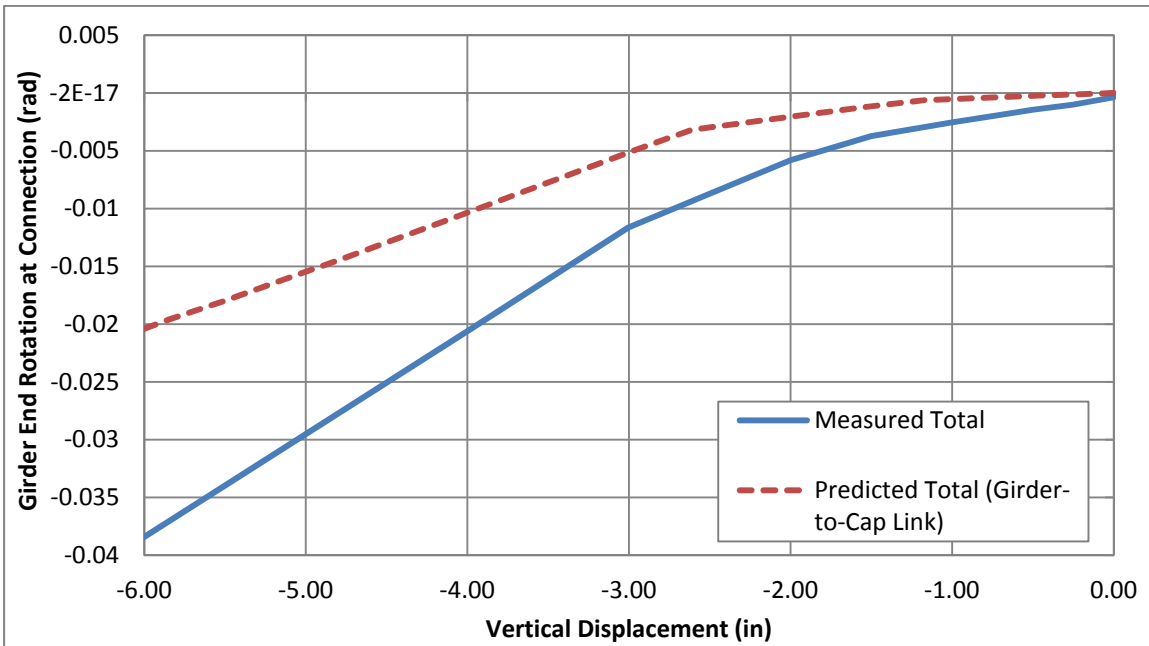


Figure 6.47: Negative Vertical Displacement vs. Center As-built Girder Rotation

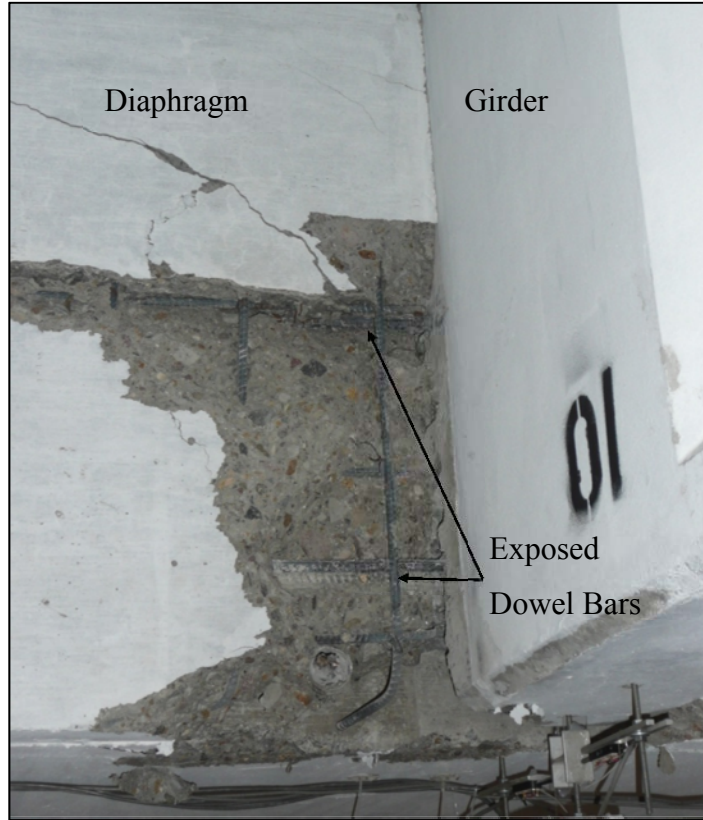


Figure 6.48: Damage Surrounding the Interior Girder in the As-built Connection Region

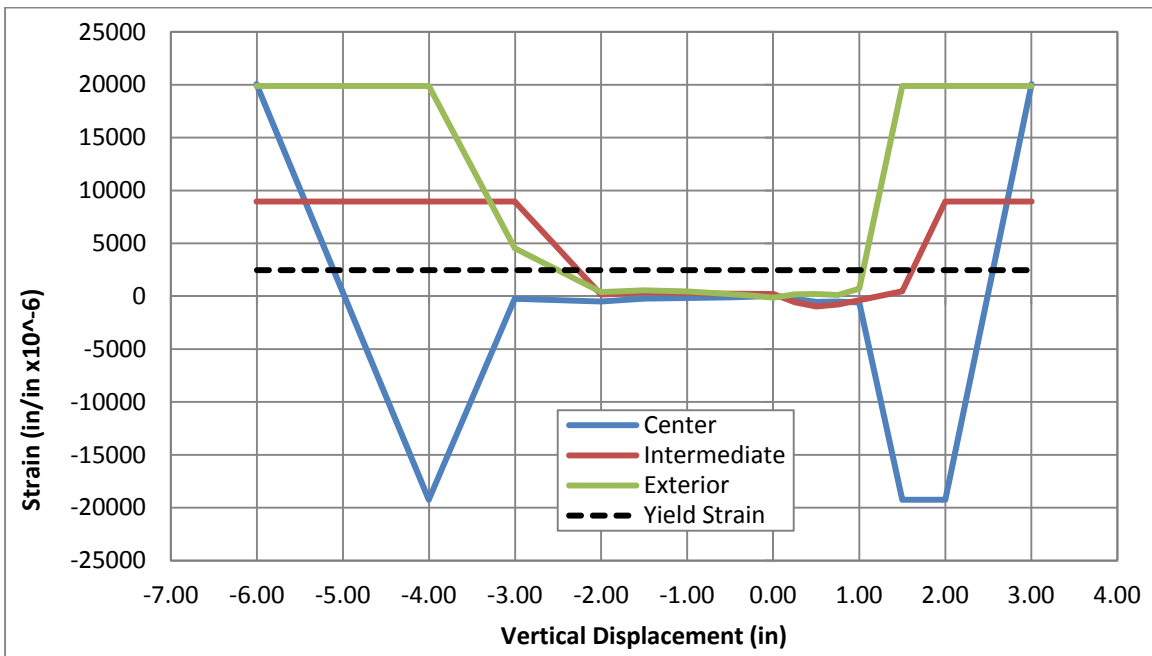


Figure 6.49: Vertical Displacement vs. Bottom Row Dowel Bar Strain on the As-Built Connection Side of the Cap Beam

The participation of these mechanisms was further investigated within the grillage model by breaking the total predicted rotation into its individual link element components. This was done in order to identify which component was the most significant cause of the discrepancies. Both Figure 6.46 and Figure 6.47 indicate that the girder-to-cap link element was the primary source behind the difference between the measured and predicted responses. As shown in the aforementioned figures, the defined properties for the girder-to-cap link element were too stiff and underestimated the rotations experienced within the connection. As discussed, this was due to the lack of a fully developed dowel bar action, shear-friction mechanism, and the loss of the grout pad along the girder-to-cap interface. Unfortunately, the 3-D finite element model that was used to derive the girder-to-cap link element properties did not adequately account for the degradation of the diaphragm, which in turn resulted in an over-prediction in regard to the contribution of each mechanism and the overall strength and stiffness of the connection. In order to improve the accuracy of the grillage model predictions, it is recommended that the 3-D finite element model be revised to more accurately reflect the measured behavior of the test unit, thus improving the derived input response used in the grillage model.

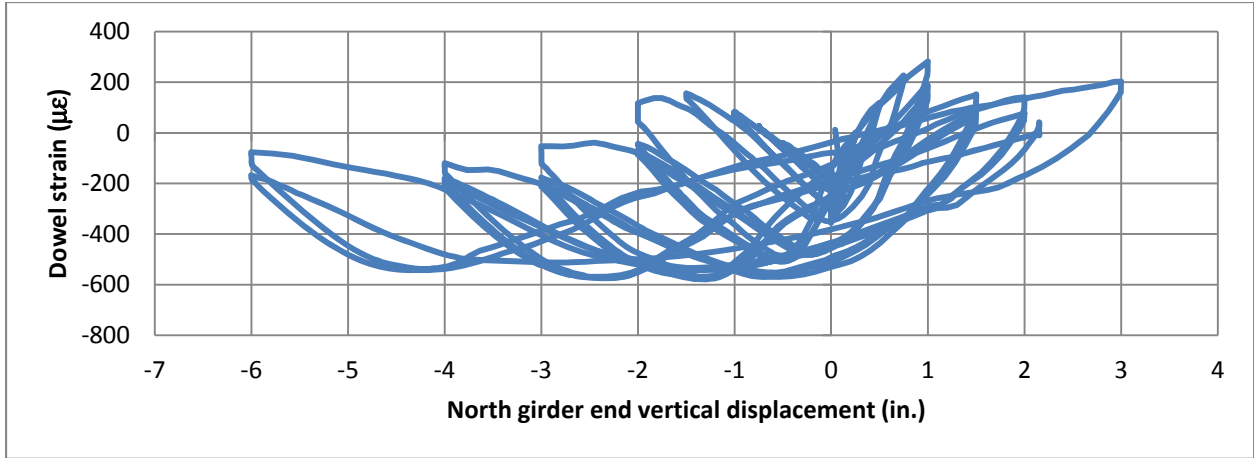
In general, the as-built connection detail performed much better than expected and confirmed that it can actually act as a fixed connection until the column hinge is fully developed under combined gravity and seismic loads. It was clear that the connection had a significant moment resistance beyond what is currently assumed in design practice and did not exhibit significant damage until the superstructure was displaced vertically by -3 and +1 in., at which point the moment in the connection was approximately 4.9 and 1.4 times greater than the maximum moment applied during the horizontal load-test phase, respectively. In contrast, it is suggested in Caltrans' Seismic Design Criteria that these positive moment connections be assumed to act as pinned connections.

The girder-to-diaphragm dowels were instrumented with strain gauges to examine their effectiveness in maintaining the integrity of the girder-to-cap connection. Strain histories from gauges on the improved side center girder, an intermediate girder, and an exterior girder are plotted versus girder end vertical displacement in Figure 6.50. The dowels reported here were

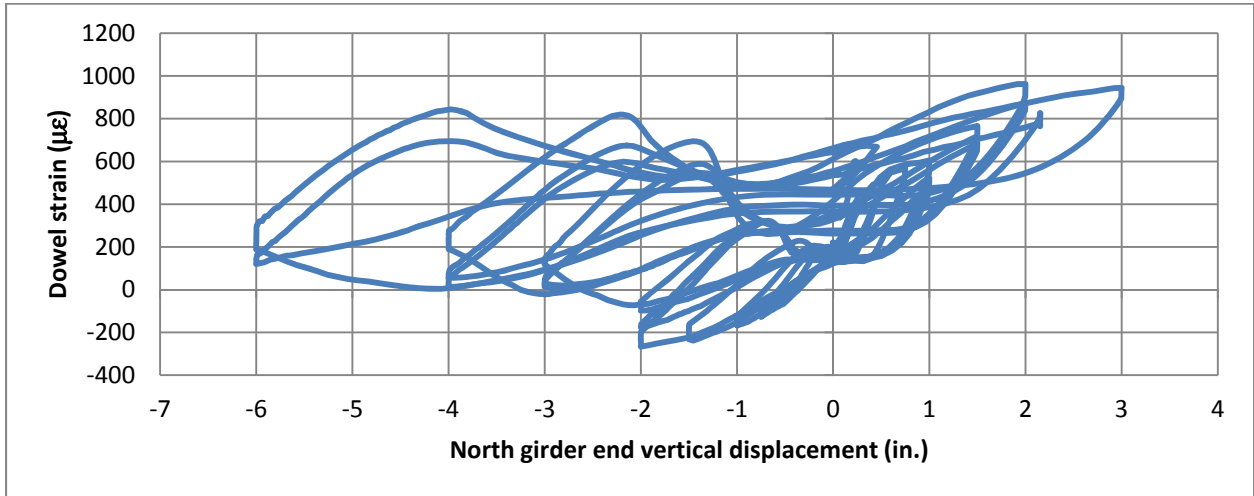
the lower dowels for each of the girder connections, and the strain gauge reported for each of the dowels was located at the interface between the girder and the diaphragm. It can be seen here that the strains on each girder dowel were small but measurable throughout the duration of the vertical load test, indicating that the dowels remained intact and instrumental in transferring load throughout the test. The magnitude of recorded strain for each girder is also of interest, as it is noted that the largest positive strain magnitudes occurred at the largest positive displacement load step. This behavior should be expected, since positive displacements of the girder ends produced tension on the bottom side of the girder in the location of the dowel strains that are provided here.

Although there were girder dowels instrumented with strain gauges on the as-built connection also, the considerable damage that occurred in the girder-to-cap connection during the Phase 1 test rendered little meaningful strain data during the Phase 2 test. This difference in behavior between the improved side and the as-built side was another indicator, beyond visual observation, of the increased performance of the improved connection.

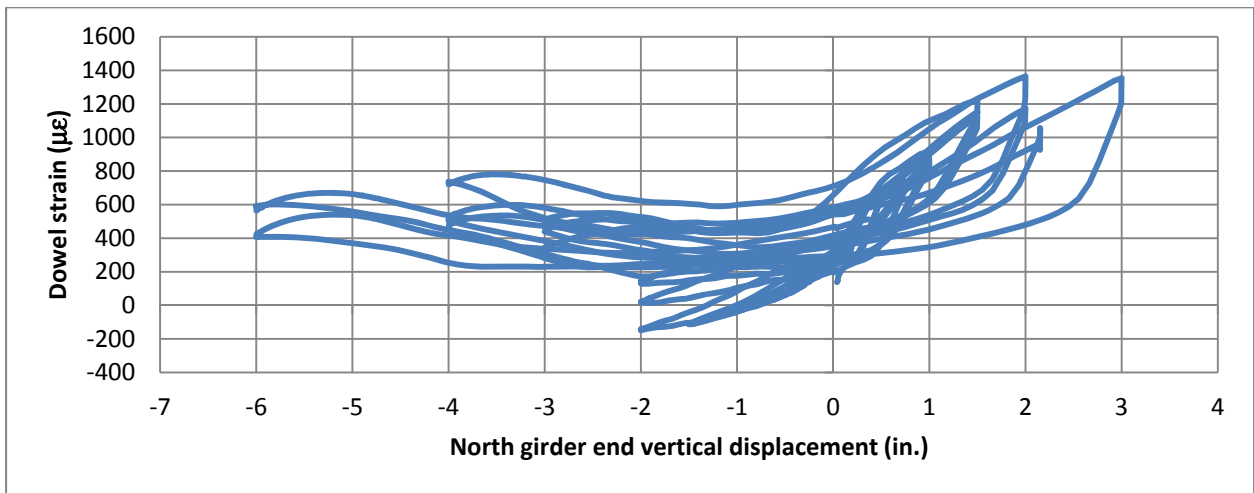
The Phase 2 data from the gauges on the unstressed strands in the improved connection were also investigated. Although many of these gauges experienced damage during the Phase 1 horizontal load testing, several of them provided data throughout the duration of the Phase 2 test. One of the strain histories from a gauge on the west exterior girder is provided in Figure 6.51, plotted versus the girder end vertical deflection. This data shows that this strand was engaged throughout the test. Also of note are the increased strain magnitudes during the positive girder end vertical displacements; this behavior matches what would be expected since positive displacements produce tension in the bottom side of the girder at the location of the unstressed strands.



(a) Exterior girder



(b) Intermediate girder



(c) Center girder

Figure 6.50: Strain Histories from Lower Girder-to-Diaphragm Dowels

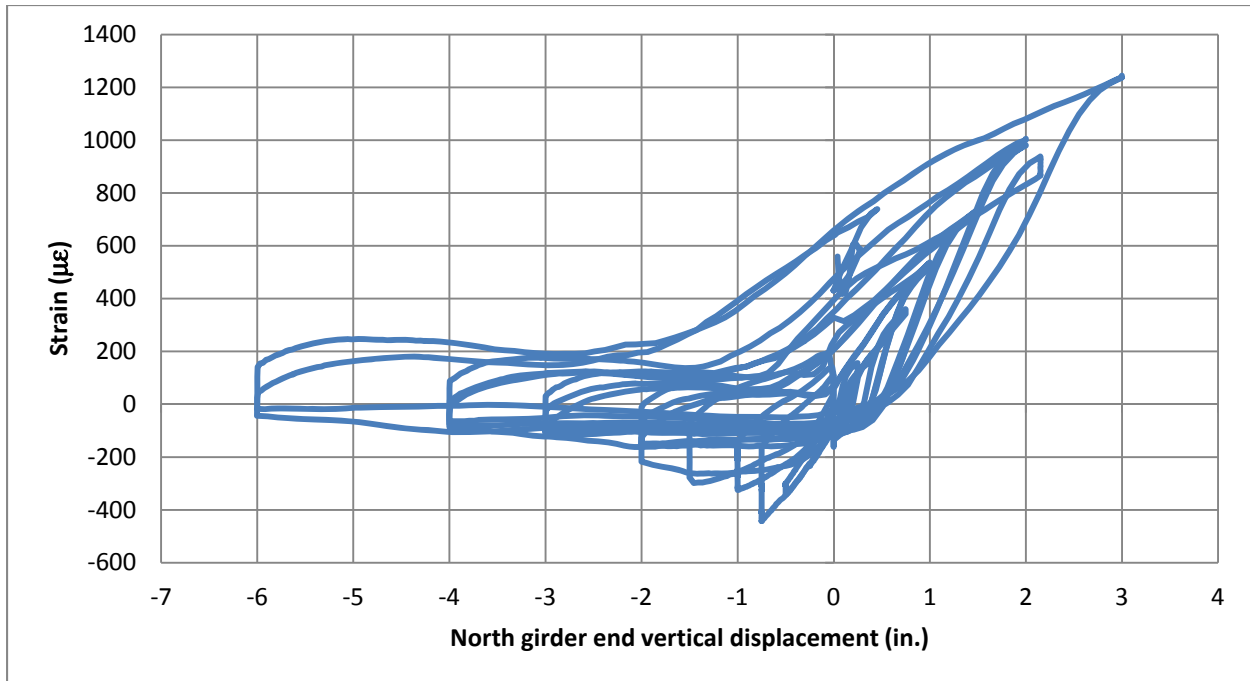


Figure 6.51: Strain History on Unstressed Strand in Exterior Girder-to-Cap Improved Connection

### 6.5.3 Girder Load Distribution

One way in which the girder load distribution was examined was by using the data from the unstressed strands connecting the girders to the cap beam. Figure 6.52 (repeated) shows the gauge locations, and Figure 6.53 provides strain profiles for selected negative displacement steps. The positive displacement step profiles provided very little useful data, likely because of the rigid body rotation that was occurring as a result of the as-built connection deterioration. A limited number of gauges survived the Phase 1 horizontal load testing and provided data to develop partial strain profiles. The gauges on the unstressed strand on the center girder in particular did not survive; therefore, this data is more useful for investigating general trends in girder load distribution rather than specifically quantifying the load distribution behavior. One interesting trend here is that the exterior girder at +96 in. seemed to pick up higher loads under the positive displacement load steps while the exterior girder at -96 in. seemed to increase in load for the negative displacement load steps. Another interesting trend is that, similar to the girder dowel behavior, the unstressed strands in all the girders seemed to carry considerable load, indicating that the load is distributed among all five girders to varying degrees.

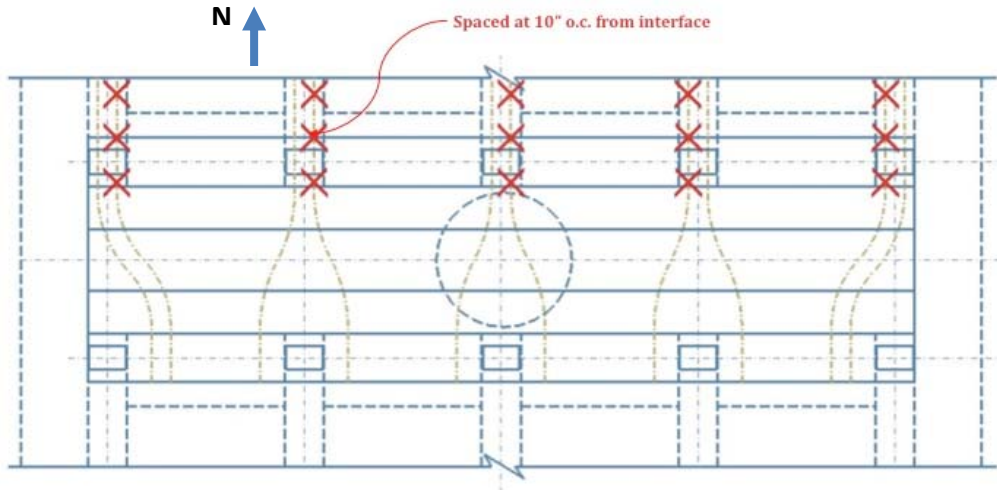


Figure 6.52: Unstressed strand strain gauge locations

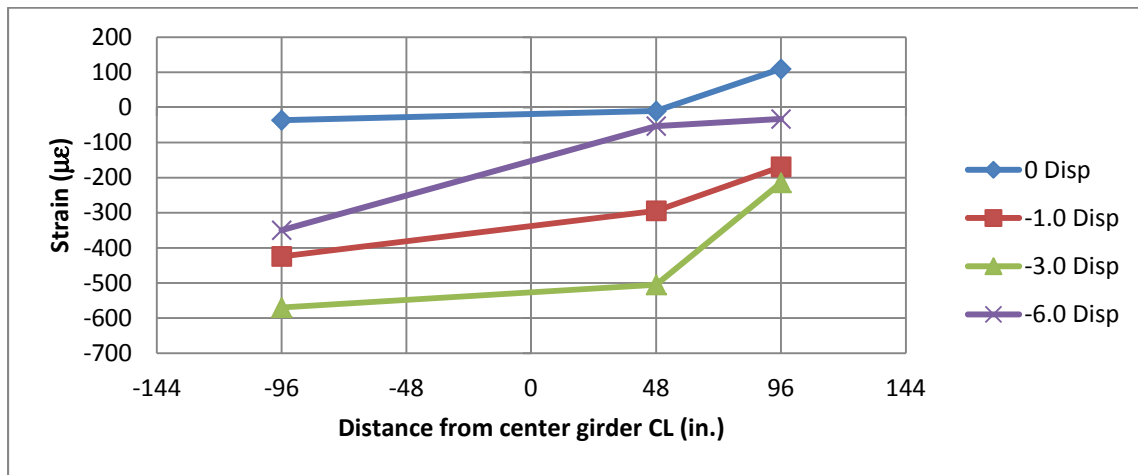


Figure 6.53: Transverse strain profiles from unstressed strands in improved connection (from gauges located 10" north of interface)

The other interesting behavior to note on the unstressed strand data in Figure 6.53 is that all of the gauges recorded compressive strains for the negative displacement steps, as would be expected since negative displacement at the girder ends produces compression in the bottom flange of the girders.

The deck reinforcement behavior was also investigated. Gauge locations are provided in Figure 6.54 (repeated). Figure 6.55 provides strain profiles across the specimen for gauges located on the deck reinforcement directly above the girders and approximately above the outer

edge of the cap flange. Figure 6.56 provides similar data for the gauges that are above the outer edge of the cap stem. Note that only the negative displacement steps are included here, since the negative displacements produce the tensile behavior in the deck reinforcement.

The deck reinforcement data indicates that for the vertical displacement steps, the load distribution across the five girders was surprisingly uniform, even for the low displacements. While the center girder did pick up slightly higher strains, specifically at the gauge locations above the cap stem edge shown in Figure 6.56, the intermediate girders (at +/- 48 in. from the center girder) and the exterior girders (at +/- 96 in. from the center girder) picked up considerable strains at all the displacement steps. This girder load distribution will continue to be investigated in subsequent work after this report.

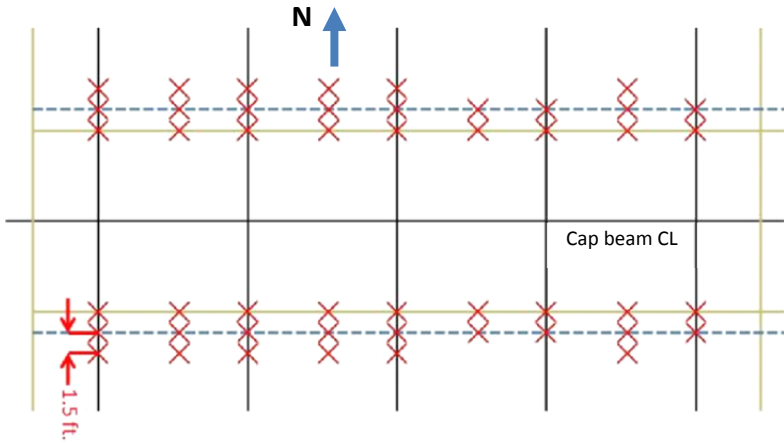
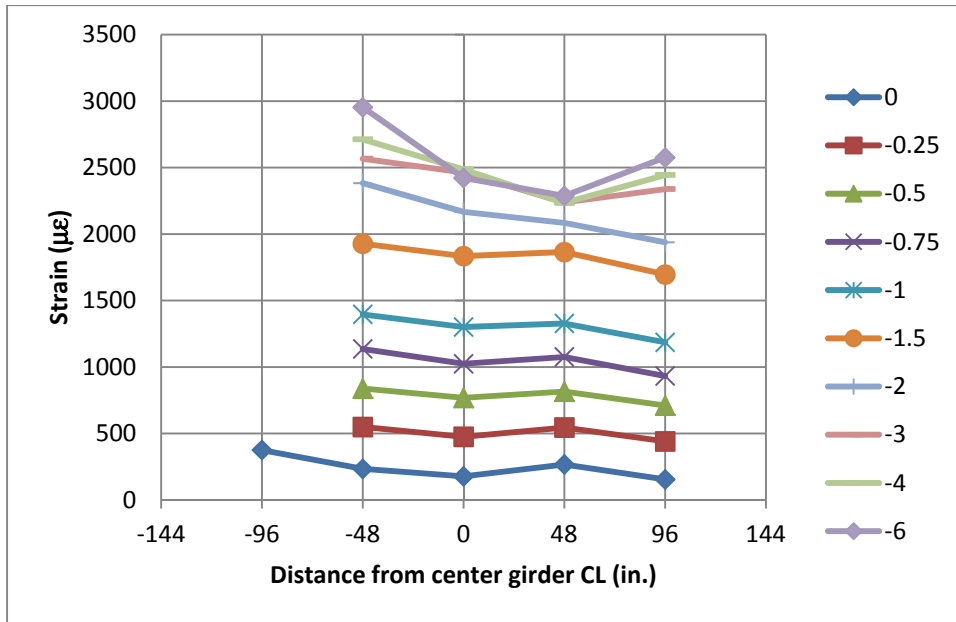
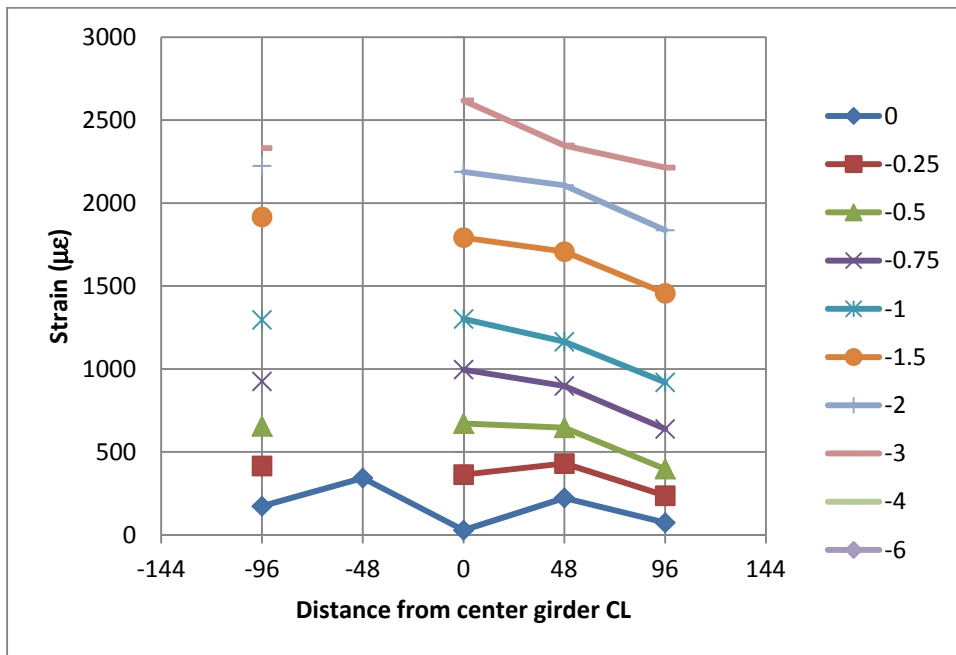


Figure 6.54: Deck Reinforcement Strain Gauges

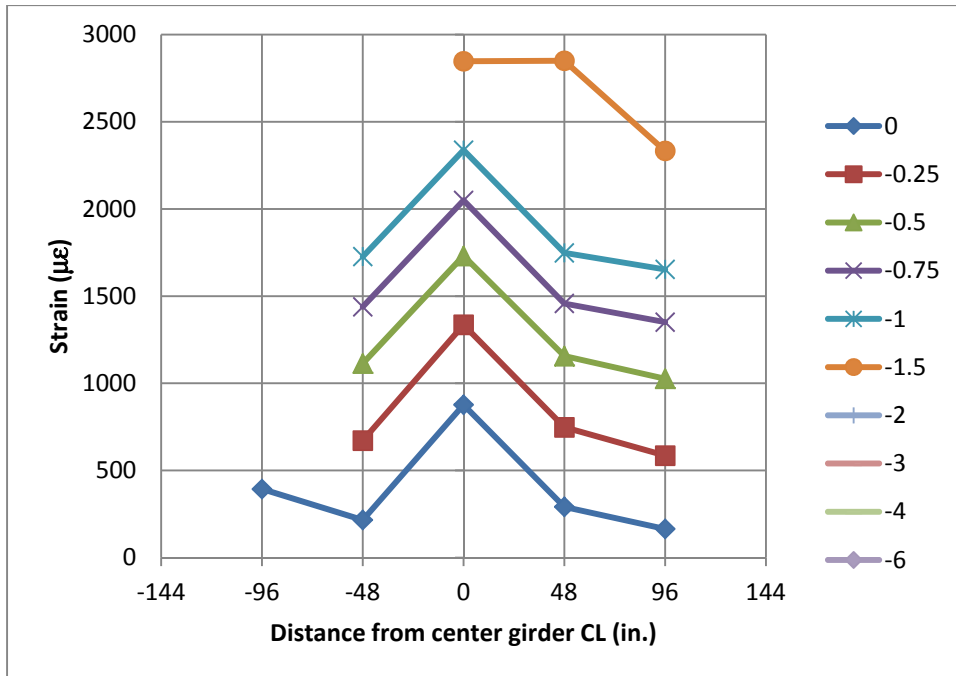


(a) Improved side

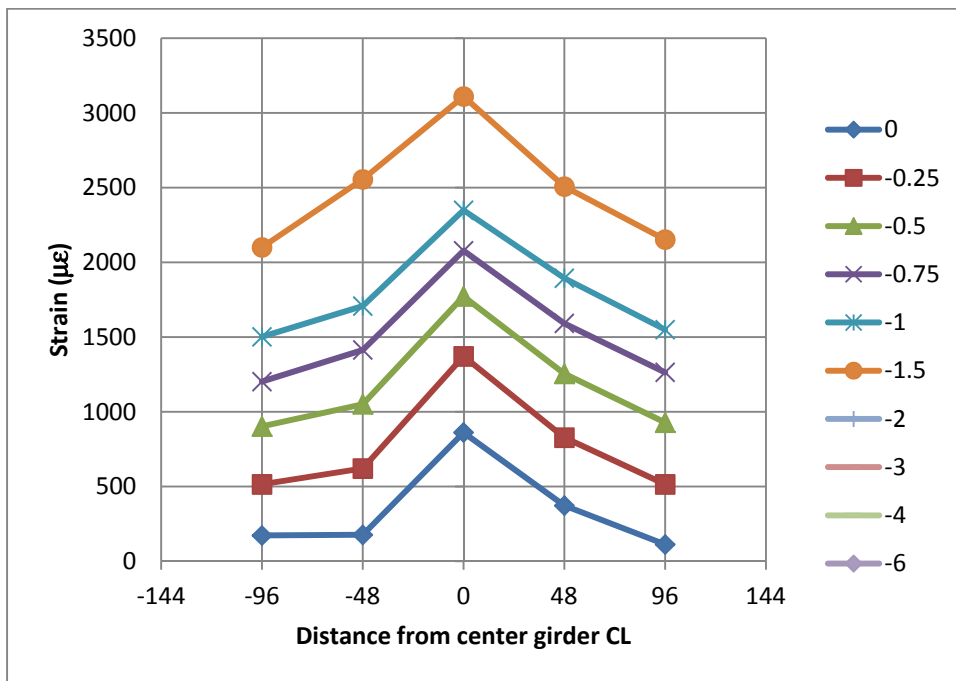


(b) As-built side

Figure 6.55: Deck Reinforcement Strain Profiles from Gauges approximately above Cap Flange Outer Edge for Peak Displacement Steps



(a) Improved side



(b) As-built side

Figure 6.56: Deck Reinforcement Strain Profiles from Gauges approximately above Cap Stem Outer Edge for Peak Displacement Steps

## **Chapter 7. Summary and Conclusions**

### **7.1 Overview**

The goal of the research presented herein was to gain a better understanding of the seismic behavior, as well as the overall moment resistance and shear transfer capability, of a precast I-girder to inverted-T bent cap bridge connection using analytical and experimental investigations. An improved connection detail was also requested by Caltrans in order to ensure the development of a fully continuous moment connection between the superstructure and bent cap.

Currently, Caltrans engineers design bridges that incorporate an inverted-T bent cap and precast girders with no confinement requirement at the top of the column. This is because the current as-built design of the precast girder-to-cap connection region is conservatively assumed to be a pin connection, based on recommendations from Caltrans' Seismic Design Criteria (Caltrans, 2006) regarding the use of precast components, which results in a very inefficient and expensive design for these structures. However, it is very likely that these as-built conditions have considerable positive and negative moment resistances, which have the potential for significant cost savings and improved design efficiency. Furthermore, given the extensive structural damage that occurred to bridges during the Loma Prieta earthquake, Caltrans has made it a priority to investigate and ensure that all bridge structures will perform adequately during a future seismic event (Housner & Thiel, 1990).

Therefore, a prototype I-girder to inverted-T bent cap bridge was designed by PBS&J and used to develop a 50% scale test unit. The test unit was then modeled using finite element and the physical structure was constructed and tested. Using information obtained from previous studies regarding moment continuity between girder-to-cap connections, as outlined in the literature review presented in Chapter 2, an improved connection detail was proposed in order to provide a dependable fully continuous moment connection. As outlined in Section 3.3, the improved connection was established by grouting untensioned prestressing strands along the length of the girders and through the girder-to-cap connection into the inverted-T bent cap.

As discussed in Chapter 4, a finite element grillage model of the test unit was created using SAP2000, a finite element software, and was used to better analyze and predict the behavior of

the test unit during both phases of testing. The properties and definitions used to define specific components of the test unit were first validated against an alternate, 3-D finite element model of the test unit as shown in Section 4.1 as well as preliminary data collected from the test unit. It was then possible to use the grillage model to make predictions, and identify areas of interest, regarding the behavior of the test unit. Finally, comparisons between the measured response of the test unit and the preliminary predictions were performed in order to verify the sufficiency of the model and identify any possible modifications that could have been made in order to achieve more accurate results. A monotonic pushover analysis of the grillage model found that the as-built connection detail would have a significant moment capacity and would adequately allow for the formation of a plastic hinge at both the top and bottom of the column in a seismic event. However, it was expected that the connection would sustain damage as a result. Additionally, it was concluded that the improved connection detail would provide a fully continuous moment connection between the superstructure and inverted-T bent cap.

Based on the conclusions drawn from the grillage model, the test unit was constructed and subjected to two phases of testing at the Powell Laboratory of UCSD in order to validate the results of the finite element grillage model and provide more information regarding the performance of the inverted-T bent cap connection. The test unit consisted of a single, circular column, an inverted-T bent cap, and two half spans consisting of five I-girders on either side of the bent cap. One span incorporated Caltrans' current, or as-built, connection detail between the I-girders and the inverted-T bent cap, whereas the other span incorporated the improved connection detail. During the testing, it was expected that the connections between the I-girders and inverted-T cap, in the test unit, would behave as fully continuous connections and thus the top end of the column was designed with adequate amounts of confinement reinforcement.

The first phase of testing simulated the combined effects of gravity and seismic loading on the inverted-T test unit. The gravity load effects on the test unit were simulated using two sets of vertical tie-downs and four actuators positioned in the vertical direction. In addition, two horizontal actuators placed at each end of the superstructure simulated the horizontal seismic load effects. As part of the horizontal load test, the test unit was subjected to the following positive and negative horizontal force and displacement ductility levels:  $\pm 0.25F'_y$ ,  $\pm 0.5F'_y$ ,

$\pm 0.75F'_y$ ,  $\pm 1.0F'_y$ ,  $\pm \mu_{\Delta}1 \times 3$ ,  $\pm \mu_{\Delta}1.5 \times 3$ ,  $\pm \mu_{\Delta}2 \times 3$ ,  $\pm \mu_{\Delta}3 \times 3$ ,  $\pm \mu_{\Delta}4 \times 3$ ,  $\pm \mu_{\Delta}6 \times 3$ ,  $\pm \mu_{\Delta}8 \times 2$ ,  $\pm \mu_{\Delta}10 \times 1$ , where  $F'_y$  and  $\mu_{\Delta}$  correspond, respectively, to the first yield force and displacement ductility of the test unit. Each of the force-controlled levels, denoted as a multiplication of  $F'_y$ , consisted of one cycle to the corresponding positive and negative force. Similarly, each of the displacement-controlled levels were cycled to the corresponding positive and negative displacement at the given ductility level; however, three cycles were performed at each level, with the exception of  $\mu_{\Delta}8$  and  $\mu_{\Delta}10$ , in order to capture any effects due to degradation of the structure. Since initial predictions did not expect the structure to achieve  $\mu_{\Delta}10$ , and the column needed to be somewhat preserved for the vertical load testing phase, the testing at  $\mu_{\Delta}8$  was limited to two cycles while testing at  $\mu_{\Delta}10$  was terminated after one cycle.

The second phase of testing expanded upon the results and observations made from the horizontal seismic load test, by subjecting the girder-to-cap connections to a larger moment demand and attempting to quantify the ultimate moment capacity of each connection type. This was achieved by mounting two vertical actuators, on both the North and South spans, at what was the location of the hold-down force during the horizontal testing phase. Accordingly, the actuators were mounted at a distance of 16 feet from the center of the cap beam, on both sides. The superstructure was then subjected to the following positive and negative horizontal displacement levels: -0.25 in., -0.5 in., -0.75 in., -1 in., -1.5 in., +0.25 in., +0.5 in., +0.75 in., +1 in./-2 in.  $\times 3$ , +1.5 in./-3 in.  $\times 3$ , +2 in./-4 in.  $\times 3$ , +3 in.  $\times 1$ /-6 in.  $\times 2$ .

## **7.2 Summary of Test Results**

### **7.2.1 Phase 1**

Overall, the performance of the test unit was extremely good in resisting the simulated combined gravity and horizontal seismic load. The as-built girder-to-cap connections behaved as a fully continuous connection instead of a pinned connection. Contrary to what was expected as a result of the aforementioned grillage and 3-D finite element analysis, as well as the current assumptions in Caltrans' Seismic Design Criteria regarding precast connection details, degradation of the positive as-built connection was not observed, which could have been due to limited flexural cracks developing in the girder-to-cap regions. Additionally, the improved girder-to-cap connection detail performed as expected, as a fully continuous connection, and did

not experience any significant damage or degradation throughout the testing. Therefore, as intended, plastic hinges developed at the top and bottom column ends and a maximum horizontal displacement of 7 in., corresponding to a displacement ductility of 10, was achieved. Buckling of several column longitudinal bars, as well as the beginning of a confinement failure, was observed in the plastic hinge region as the test unit neared its ultimate displacement capacity.

### **7.2.2 Phase 2**

The second phase of testing was successful in that it adequately exercised the as-built connections, established the required moment capacities, and ensured a satisfactory shear transfer through the as-built connection. It was clear that the as-built connection detail had a significant capacity for both positive and negative moments. The as-built connection reached its ultimate capacity at a displacement of +1.5 in. and seemed to still have a reserve capacity at -6 in. even though the test was terminated. Unfortunately, due to the progressive failure of the as-built connection during this test, and the damage to the column ends that was sustained during the horizontal seismic load test, the improved connection was not tested to its full capacity. However, the superior performance of the improved connection over the old connection was clearly demonstrated by the test. Since the as-built connection detail degraded before the improved connection, reaching its capacity, it is apparent that the presence of the grouted, untensioned strands improved the performance of the connection detail to the extent that useful design recommendations can be formulated for inverted-T bridge bents used to support precast I-girders.

## **7.3 Conclusions**

### **7.3.1 Experimental Study**

Based on the observations made during both phases of testing, as well as the results of the finite element grillage model, the follow conclusions can be drawn:

- Both the as-built and improved girder-to-cap connection details performed essentially as a fully continuous connection and showed little to no degradation during the horizontal load testing (Phase 1). The positive and negative moment capacities of each connection detail were more than adequate to fully develop a plastic hinge at both the top and bottom of column. Finally, both connection details successfully transferred shear forces from the superstructure into the cap beam.

- The as-built connection detail, though it did experience significant degradation, performed adequately during the vertical load testing (Phase 2). The as-built connection did not experience significant degradation until the positive and negative moment within the connection was approximately 4.9 and 1.4 times greater than that of the maximum moment applied during the horizontal load test. However, the contribution of the dowel action of the embedded dowels between the girder and diaphragm, as well as the shear-friction between the girders and the diaphragm, was not as significant as what was predicted. The improved connection detail seemed to perform better than the as-built detail during the vertical load testing; however, the full moment capacity of the connection was not established, as noted in Chapter 6.
- Based on both Phase 1 and 2 test results and observations, it was concluded that only the top of the column required retrofitting in order to accommodate the formation of a plastic hinge and achieve a satisfactory seismic response. However, it should be noted that doing so will increase the column shear demand, as well as other demands within the system, which should be examined to ensure that the bridge can handle the new force demands. If the top of the column were retrofitted, a maximum horizontal displacement ductility of 10, corresponding to 14 in. of displacement, could be expected for the prototype bridge structure.
- Overall, the grillage model force vs. displacement and girder end rotation at the face of the cap vs. displacement predictions compared very well to the measured response of the test unit for both phases of testing. This proved that the grillage model is an adequate means of predicting the behavior of both current and future inverted-T bridge structures.
- The results of the grillage model could be improved by updating the concrete properties to reflect the compressive strengths recorded at the time of testing, recalculating the column plastic hinge link properties to reflect the increased concrete strengths, and improving the girder-to-cap link element properties by revising the 3-D finite element model that was used in their derivation in order to more accurately reflect the observed behavior of the test unit.
- When using a grillage model to predict the behavior of an I-girder to inverted-T bent cap bridge, subjected to a typical gravity and seismic load combination, it is recommended that Caltrans designers model the connection by simply elastically connecting the

members at their joints, thus coupling their effective stiffnesses and degrees of freedom at common nodes. As shown in Figure 7.1, removing the complicated nonlinear link elements within the connection region of the grillage model that were discussed in Chapter 4, and instead elastically connecting the girder elements directly to the cap beam, produced essentially the same result for the predicted force vs. displacement response during the horizontal load testing.

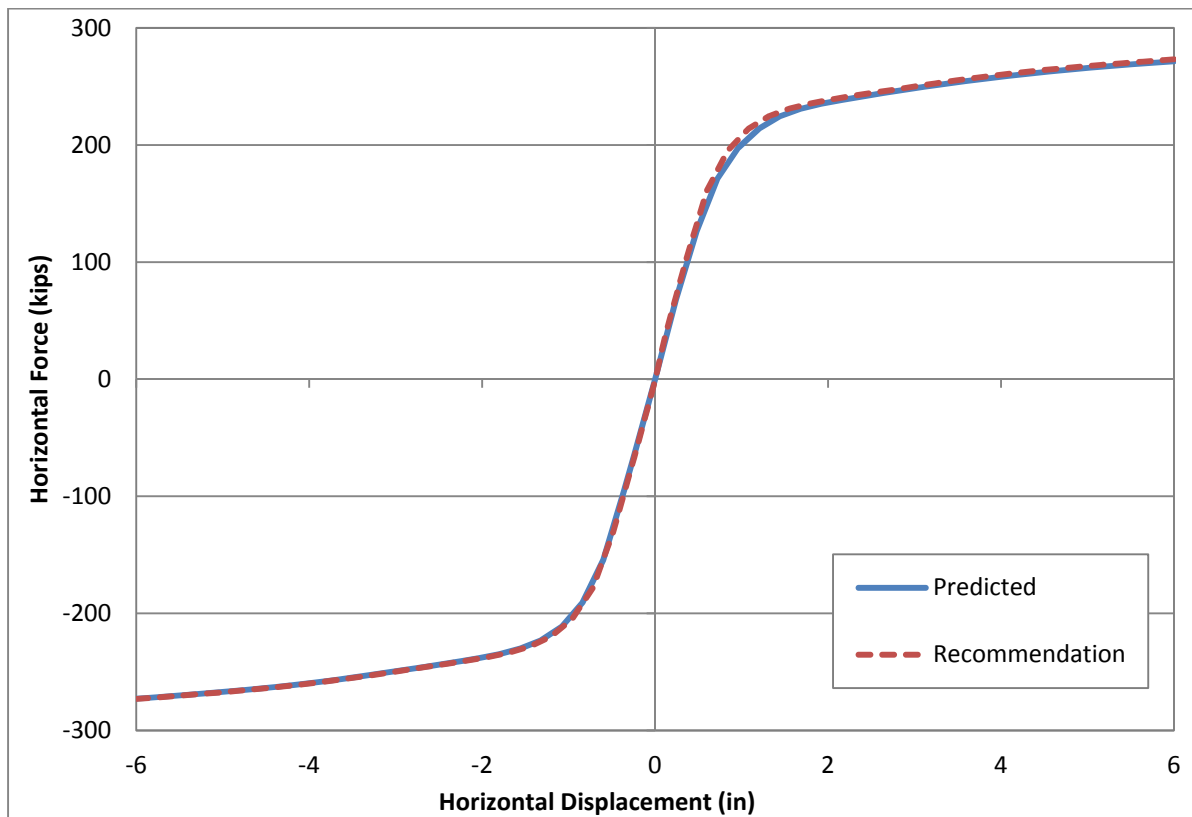


Figure 7.1: Recommended Girder-to-Cap Connection Grillage Modeling Force vs. Displacement Response

### 7.3.2 Analytical Study

The following are the conclusions that were provided from the finite-element analytical investigation:

- The damaged plasticity model in ABAQUS was capable of modeling the effect of confinement on concrete. However, the unconfined material properties had to be modified to allow for the confined results to match closely.

- The concrete material properties were unable to accurately model the tensile behavior of concrete under flexure. The tensile stress could not be reduced to zero stress after cracking; this zero stress was found cause to convergence problems in the analysis.
- The behavior of the current cap-beam-to-girder connection of an inverted-tee cap beam bridge with precast girders was shown to be affected by the capacity of the deck slab in parallel with the cap-beam-to-diaphragm reinforcing bars and the girder-to-diaphragm reinforcing bars acting in series.
- The bridge deck was shown to noticeably affect the behavior and distribution of forces between the girders in the analysis. The middle girder connection was found to resist the most moment, according to the gap displacement between the cap beam and girder. However, the middle girder end reaction was found to be the lowest of the girder reactions. The deck was found to develop a strut which transferred the force from the middle girder out to the exterior girder.
- The end diaphragms on the test unit were found to actively transfer the force from the exterior girder back into the middle girder and intermediate girder.
- The assumed girder stiffness in the grillage model was found to influence the resulting stiffness in the system initially and after yielding.

Many of the above conclusions from the finite element analysis were incorporated into the grillage analysis and subsequently the experimental analysis to further prove their validity. Hence, it is noted that the conclusions of the grillage and experimental work presented in Section 7.3.1 include the lessons learned from the finite element analysis.

#### **7.4 Design Recommendations**

Based on the outcomes of the experimental and analytical investigations of this research project, the following design recommendations are made for bridges consisting of inverted-tee bent cap beams and precast I-girders. As noted above, for existing bridges containing the as-built cap-to-girder connection details as investigated herein:

- Expect the cap beam-diaphragm-girder connection to act as a fixed condition, although it was expected to degrade to a pin connection during seismic loading;

- In consideration of the above expectation, ensure that the top of the column can develop a plastic hinge and has adequate confinement reinforcement; and
- Ensure the column shear resistance is adequate in light of the plastic hinge formation at the column top.

For new bridges to be designed with the cap-to-girder connection details as investigated herein:

- Treat the cap-diaphragm-girder region to be a fixed connection;
- Design the positive cap beam-to-girder moment connection with details of the improved connection adopted in this study including the use of grouted unstressed prestressing strands. As evident from the experimental results, the area of the unstressed strands may be quantified using the positive moment demand with due consideration to the dowel mechanism to be developed in parallel; and
- Design the columns with an anticipation of forming a plastic hinge at top adjacent to the cap beams.

## **7.5 Future Research Directions**

The observations made during both Phase 1 and Phase 2 of the test suggest that minimal retrofit measures are required in order to ensure satisfactory performance of I-girder to inverted-tee bent cap bridges in the field. If it can be shown that vertical accelerations would not cause any significant damage to the as-built positive moment connections, seismic retrofit for the existing inverted-tee bridges, as recommended in Section 7.4, is required only at the column top so that the girder moments can be resisted and a plastic hinge could be developed at this location, resulting in significant cost savings. Though it was observed, at low displacement levels, that the improved connection detail increased the capacity of the connection and prevented the same damage from occurring that was observed within the as-built connection region, the true behavior and ultimate capacity of the improved connection detail was not obtained. Therefore, it is recommended that future research be conducted in order to better investigate the behavior and capacity of the improved connection detail. In order to better understand and provide a higher degree of confidence in the performance of the prototype I-girder to inverted-tee bent cap bridge, it is recommended that the findings and analysis techniques presented in this report be used to create a grillage model of the prototype. Finally, it is noted that the good performance of the test unit not only encourages precast construction but also provides new opportunities for cost-

effective accelerated bridge construction in high seismic regions. As a result, it would be useful to investigate the connection performance for other types of girders as well.

## REFERENCES

- AASHTO. (2003). *LRFD bridge design specifications, 3rd Ed.* Washington, D.C.
- ACI Committee 318. (2005). *ACI 318-05: Building Code Requirements for Structural Concrete and Commentary.* Farmington Hills, MI: ACI.
- Almer, K., & Sanders, D. (2007, November). *23rd US-Japan Bridge Engineering Workshop.* Retrieved January 2009, from Public Works Research Institute:  
<http://www.pwri.go.jp/eng/ujnr/tc/g/pdf/23/23-8-2sanders.pdf>
- Bentley Systems, Inc. (2008). CONSPAN Rating v. 8.0.
- Biggs, R. M., Barton, F., Gomez, J., Massarelli, P., & McKeel, W. J. (2000). *Finite Element Modeling and Analysis of Reinforced-Concrete Bridge Decks.* Charlottesville: Virginia Department of Transportation.
- California Department of Transportation. (2007). *Maintaining California's Bridges.* Retrieved 2009 from California Department of Transportation:  
<http://www.dot.ca.gov/hq/structur/strmaint/>
- Caltrans. (1995). *Bridge Design Aids.* Sacramento.
- Caltrans. (2003). *Bridge Design Specifications.* Sacramento.
- Caltrans. (2006). *Seismic Design Criteria.* California Department of Transportation, Sacramento.
- Caltrans. (2006). *Seismic Design Criteria, v. 1.4.* Sacramento.
- Chen, W.-F., Yamaguchi, E., Kotsovos, M., & Pan, A. (1993). Constitutive Models. *Finite Element Analysis of Reinforced Concrete Structures II*, 36-117.
- Chowdhury, M. R., & Ray, J. C. (1995, September). Further Considerations for Finite-Element Analysis. *Journal of Structural Engineering*, 121(9), 1377-1379.

- Collins, M. P., & Mitchell, D. (1991). *Prestressed Concrete Structures*. New Jersey: Prentice Hall.
- Computers and Structures, Inc. (2008). *CSI Analysis Reference Manual*. Berkeley: Computers and Structures, Inc.
- Dassault Systemes Simulia Corporation. (2008). *ABAQUS v6.8*. Providence, RI.
- Deng, L., Ghosn, M., Znidaric, A., & Casas, J. R. (2001). Nonlinear Flexural Behavior of Prestressed Concrete Girder Bridges. *Journal of Bridge Engineering*, 276-284.
- Dowell, R. K., Seible, F., & Wilson, E. L. (1998). Pivot Hysteresis Model for Reinforced Concrete Members. *ACI Structural Journal*, 607-617.
- FHWA. (2009). Connection Details for Prefabricated Bridge Elements and Systems. *Publication No. FHWA-IF-09-010*.
- Freyermuth. (1969). Design of Continuous Highway Bridges with Precast, Prestressed Concrete Girders. *PCI Journal*, 14-39.
- Gordon, S. R., & May, I. M. (2004). Observations on the Grillage Analysis of Slabs. *The Structural Engineer*, 35-38.
- Hambly, E. (1990). *Bridge Deck Behaviour*. Taylor & Francis.
- Hastak, M., Mirmiran, A., Miller, R., Shah, R., & Castrodale, R. (2003). State of Practice for Positive Moment Connections in Prestressed Concrete Girders Made Continuous. *Journal of Bridge Engineering*, 267-272.
- Hillerborg, A., Modeer, M., & Petersson, P. (1976). Analysis of crack formation and crack growth in concrete by means of fracture mechanics and finite elements. *Division of Building Materials, Lund Institute of Technology, Lund, Sweden*.
- Holombo, J., Priestley, M. N., & Seible, F. (1998). *Longitudinal Seismic Response of Precast Spliced-Girder Bridges*. San Diego: University of California, San Diego.

- Housner, G. W., & Thiel, C. C. (1990). *Competing Against Time: Report of the Governor's Board of Inquiry on the 1989 Loma Prieta Earthquake*. Earthquake Spectra.
- Jaeger, L. G., & Bakht, B. (1982). The Grillage Analogy in Bridge Analysis. *Canadian Journal of Civil Engineering*, 224-235.
- Keogh, D., & O'Brien, E. (1996). Recommendations on the Use of a 3-D Grillage Model for Bridge Deck Analysis. *Structural Engineering Review*, 357-366.
- Kostem, C. N., & Ragazzo, S. C. (1993). Grillage Analogy for Multigirder Bridges. *Computing in Civil and Building Engineering* (pp. 188-192). American Society of Civil Engineers.
- Lee, J., & Fenves, G. (1998, August). Plastic-Damage Model for Cyclic Loading of Concrete Structures. *Journal of Engineering Mechanics*, 124(8), 892-900.
- Levings, J. C. (2009). *Development of a Versatile Section Analysis Tool (VSAT) for use in structural design with a seismic emphasis*. Ames: Iowa State University.
- Lublner, J., Oliver, J., Oller, S., & Onate, E. (1989). A plastic-damage model for concrete. *International Journals of Solids and Structures*, 25(3), 299-326.
- Ma, Z., Chaudhury, S., Millam, J., & Hulsey, J. L. (2007, May-June). Field Tests and 3D FE Modeling of Decked Bulb-Tee Bridges. *Journal of Bridge Engineering*, 12(3), 306-314.
- Miller, R., Castrodale, R., Mirmiran, A., & Hastak, M. (2004). *Connection of Simple-Span Precast Concrete Girders for Continuity*. Washington, D.C.: National Cooperative Highway Research Program.
- Patty, J., Seible, F., & Uang, C. (2002). *Seismic Response of Integral Bridge Connections*. University of California, San Diego, Structural Engineering. San Diego: University of California, San Diego.
- PEER. (2005). *Northridge Earthquake*. (R. o. California, Producer) Retrieved 2009 from Pacific Earthquake Engineering Research Center: <http://nisee.berkeley.edu/northridge/>

- Prabha, P., Seetharaman, S., Arul Jayachandran, S., & Marimuthu, V. (2007). *RUM 2007 Papers*. Retrieved March 2009, from Simulia:  
[http://www.simulia.com/locations/india/rum\\_07\\_papers.html](http://www.simulia.com/locations/india/rum_07_papers.html)
- Priestley, M. N., Seible, F., & Uang, C. (1994). *The Northridge Earthquake of January 17, 1994*. La Jolla: The University of California.
- Priestley, M., Seible, F., & Calvi, G. (1996). *Seismic Design and Retrofit of Bridges*. New York: John Wiley & Sons, Inc.
- Rahal. (2000). *Canadian Journal of Civil Engineering*.
- Rahal, K. N. (2000). Torsional Strength of Reinforced Concrete Beams. *Canadian Journal of Civil Engineering*, 445-453.
- Raynor, D. J., Lehman, D. E., & Stanton, J. F. (2002). Bond-Slip Response of Reinforcing Bars Grouted in Ducts. *ACI Structural Journal*, 568-576.
- Roylance, D. (2001, February). *Mechanics of Materials*. Retrieved March 2009, from Massachusetts Institute of Technology Open Coursework:  
<http://ocw.mit.edu/NR/rdonlyres/Materials-Science-and-Engineering/3-11Mechanics-of-MaterialsFall1999/7F1B1AAF-92A4-48A8-AB55-24CF00601799/0/fea.pdf>
- Salmons, J., & McCrate, T. (1977 йил Jan-Feb). Bond Characteristics of Untensioned Prestressing Strand. *Journal of Prestressed Concrete Institute*, 22(1), 52-65.
- Snyder, R. (2010). *Grillage model analysis of the girder-to-cap beam connection of an inverted-tee cap beam bridge structure designed for seismic loadings*. Iowa State University. Masters degree thesis in progress.
- Srinivas, V., Ramanjaneyulu, K., Sukhesh, K., Sasmal, S., & Gopalakrishnan, S. (2004). Automated Grillage Analysis of Continuous Span I- and T- Girder Bridges. *Journal of Structural Engineering*, 101-110.

- Sritharan, S., Vander Werff, J., Abendroth, R., Wassef, W., & Greimann, L. (2005). Seismic Behavior of a Concrete/Steel Integral Bridge Pier System. *Journal of Structural Engineering*, 1083-1094.
- Staudt, R. H. (2002). *Load Distribution for Steel Girder-Single Concrete Column, Integral-Pier Bridges*. Ames: Iowa State University.
- Tadros, M., Ficence, J., Einea, A., & Holdsworth, S. (1993). A New Technique to Create Continuity in Prestressed Concrete Members. *PCI Journal*, 30-37.
- Takeda, T., Sozen, M. A., & Nielsen, N. N. (1970). Reinforced Concrete Response to Simulated Earthquakes. *Journal of the Structural Division Proceedings of the American Society of Civil Engineers*, 2557-2573.
- Thiemann, Z. (2009). *3-D finite element analysis of the girder-to-cap beam connection of an inverted-tee cap beam designed for seismic loadings*. Iowa State University.
- Tobolski, M. J., Matsumoto, E. E., & Restrepo, J. I. (2006). NCHRP 12-74 Development of Precast Bent Cap Systems for Seismic Regions - Background and Progress. *Fifth National Seismic Conference on Bridges and Highways*.
- TRC/Imbsen Software Systems. (n.d.). WinRECOL, v. 5.0.2.
- TRC/Imbsen Software Systems. (n.d.). XTRACT.
- University of Washington. (2004). *PEER Structural Performance Database*. From University of Washington Civil and Environmental Engineering: [www.ce.washington.edu/~peera1](http://www.ce.washington.edu/~peera1)
- Wight, J. K., & MacGregor, J. G. (2008). *Reinforced Concrete Mechanics and Design*. Prentice Hall.
- Zhao, J., & Sritharan, S. (2007). Modeling of Strain Penetration Effects in Fiber-Based Analysis of Reinforced Concrete Structures. *ACI Structural Journal*, 133-141.

## **Appendix A.      Prototype Drawings**

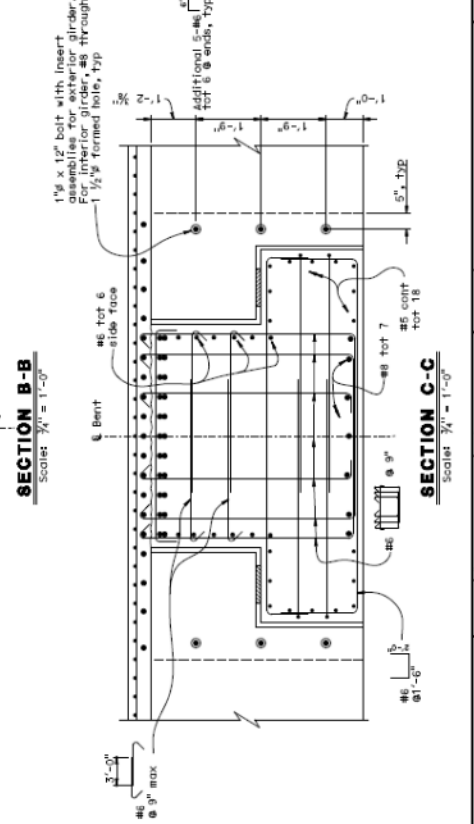
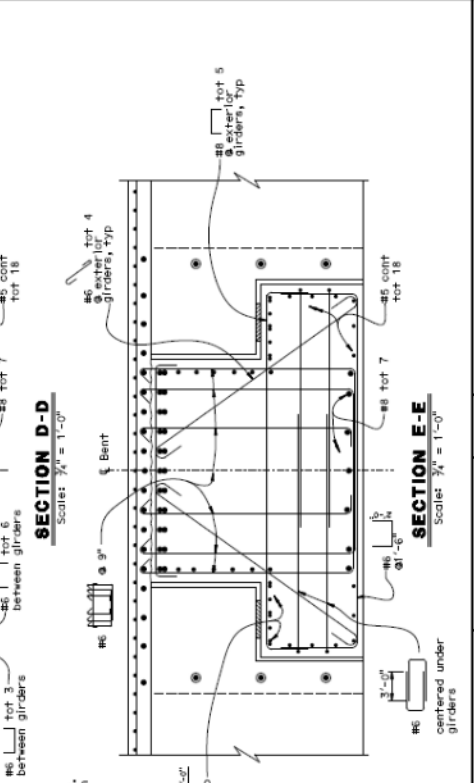
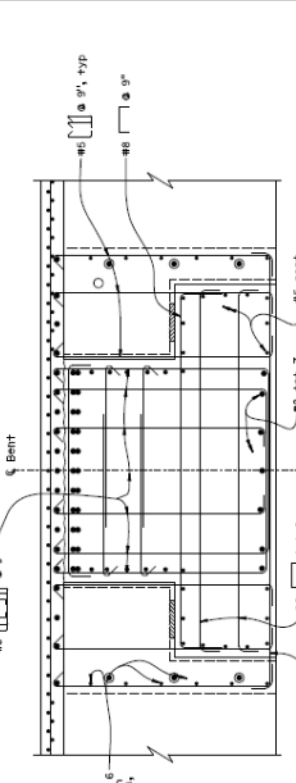
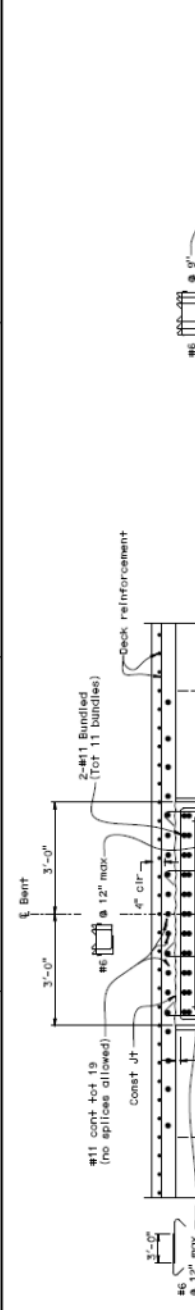




REGISTERED CIVIL ENGINEER STATE OF CALIFORNIA  
 DATE: 10/15/2008  
 PROJECT NO.: 060-00000-01  
 SHEET NO.: 11

PLANS APPROVAL DATE: 10/15/2008  
 The State of California, in the office of the State Engineer, has approved the above plans for the construction of the project herein.

**PROFESSIONAL SEAL**  
 CIVIL ENGINEER  
 STATE OF CALIFORNIA  
 No. 45824



DESIGN OVERSIGHT	DESIGN	DATE	BY	DATE	BY	DATE	BY
DETAILS	REVISION	DATE	BY	DATE	BY	DATE	BY
QUANTITIES	REVISION	DATE	BY	DATE	BY	DATE	BY
DATE: 10/15/2008							

PREPARED FOR THE STATE OF CALIFORNIA DEPARTMENT OF TRANSPORTATION  
 PROJECT ENGINEER: JAY M. HANCOCK  
 SUPERVISOR: CLU X, E.A. X

FILE NO. 060-00000-01 SHEET NO. 11 OF 11







PROJECT NO. \_\_\_\_\_ SHEET NO. \_\_\_\_\_

ROUTE \_\_\_\_\_ TOTAL SHEETS \_\_\_\_\_

REGISTERED CIVIL ENGINEER DATE \_\_\_\_\_

REVISIONS

APPROVAL DATE \_\_\_\_\_

DESIGNED BY \_\_\_\_\_

CHECKED BY \_\_\_\_\_

DATE \_\_\_\_\_

SCALE \_\_\_\_\_

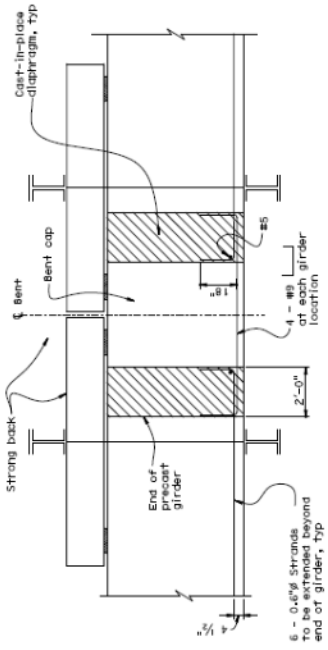
PROJECT TITLE \_\_\_\_\_

PROJECT LOCATION \_\_\_\_\_

PROJECT NO. \_\_\_\_\_

DATE PLOTTED = 7/17/2008

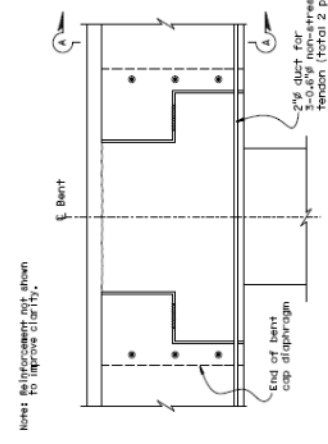
TIME PLOTTED = 11:11:58 AM



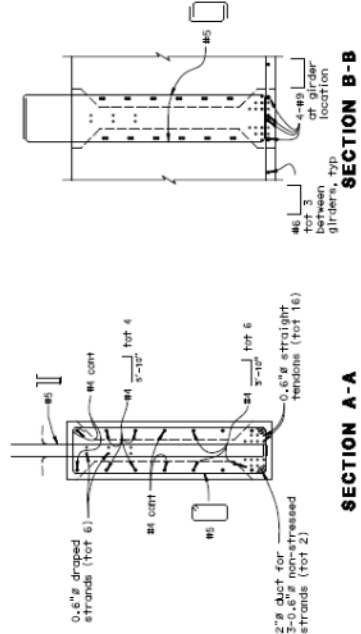
**ELEVATION**  
**ALTERNATIVE "A"**  
Scale: 3/4" = 1'-0"

Legend:

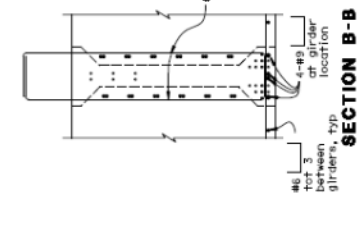
- Reinforcement bars
- 0.6" Strands



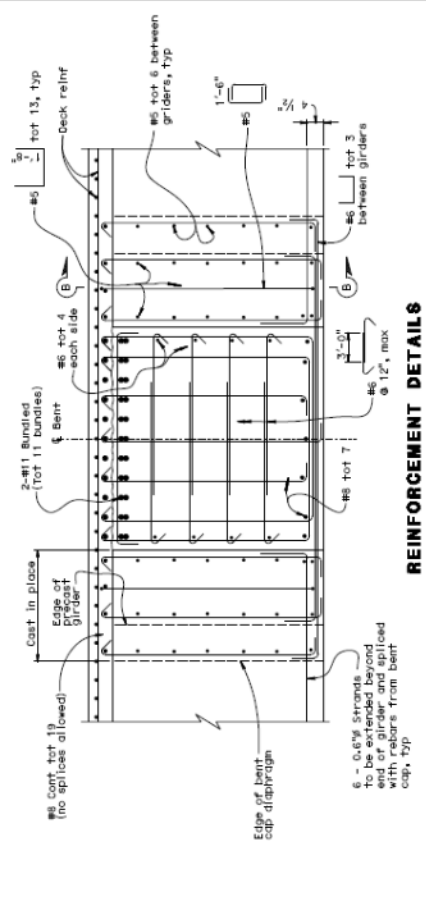
**ELEVATION**  
**ALTERNATIVE "B"**  
Scale: 3/4" = 1'-0"



**SECTION A-A**  
**ALTERNATIVE "A"**  
Scale: 3/4" = 1'-0"



**SECTION B-B**  
**ALTERNATIVE "B"**  
Scale: 3/4" = 1'-0"



**REINFORCEMENT DETAILS**  
**ALTERNATIVE "B"**  
Scale: 3/4" = 1'-0"

DESIGNER	DATE	SCALE	PROJECT NO.	DATE PLOTTED
DRAWN	BY	BY	BY	BY
CHECKED	DATE	DATE	DATE	DATE
APPROVED	DATE	DATE	DATE	DATE
PROJECT TITLE	PROJECT LOCATION	PROJECT NO.	PROJECT SHEET NO.	TOTAL SHEETS
<b>PREPARED FOR THE</b> <b>STATE OF CALIFORNIA</b> <b>DEPARTMENT OF TRANSPORTATION</b>				
<b>FILE NO. H-1028</b>				
<b>PROJECT ENGINEER</b> <b>PROJECT ENGINEER</b> <b>PROJECT ENGINEER</b>				
<b>PREPARED BY</b> <b>PREPARED BY</b> <b>PREPARED BY</b>				
<b>DATE PLOTTED</b> <b>DATE PLOTTED</b> <b>DATE PLOTTED</b>				
<b>TIME PLOTTED</b> <b>TIME PLOTTED</b> <b>TIME PLOTTED</b>				

## Appendix B. Prototype Calculations

### B.1 Prototype Configuration

The general prototype configuration is described in Chapter 3. The elevation, provided earlier in Figure 3.1, is repeated here in Figure B. for convenience.

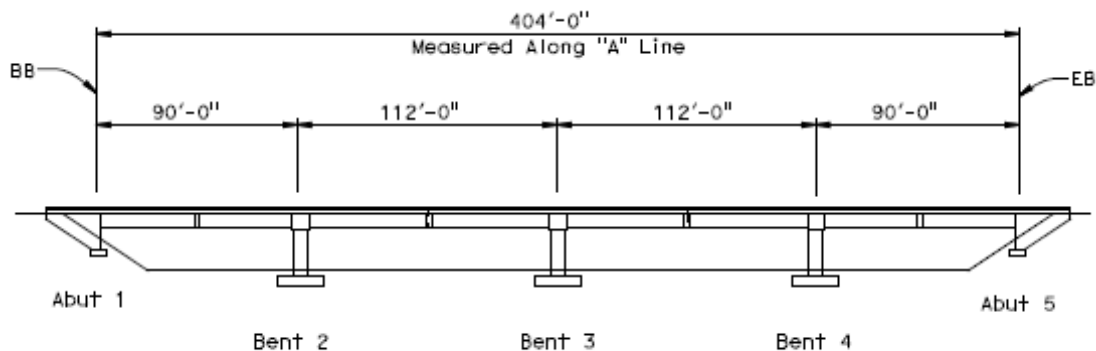


Figure B.1: Prototype Elevation

### B.2 Material Properties

For the design of the prototype, the material properties had to be chosen for the concrete, mild steel and prestressing steel. The properties were chosen to represent standard material properties used in previous designs. Listed below are the specified material properties:

Concrete:

Compressive strength of precast girder at the time of stress transfer:  $f'_{ci} = 5.5 \text{ ksi}$

Compressive strength of precast girder at 28 days:  $f'_c = 7.0 \text{ ksi}$

Compressive strength of deck slab at 28 days:  $f'_c = 4.0$

Compressive strength of bent cap and substructure at 28 days:  $f'_c = 3.6 \text{ ksi}$

Density ( $\gamma$ ) = 0.15 kcf

Reinforcing Steel:

Yield strength ( $f_y$ ) = 60 ksi

Modulus of Elasticity ( $E_s$ ) = 29000 ksi

Prestressing Steel:

Type 0.6-in. Low Relaxation strand

Modulus of Elasticity ( $E_{ps}$ ) = 28500 ksi

Prestressing Steel Ultimate Strength ( $F_{pu}$ ) = 270 ksi

Jacking force of the prestressing strands ( $F_{jack}$ ) =  $0.75F_{pu}$  = 202.5 ksi

### B.3 Column Design

The design of the column was completed using the software WinRECOL after the service loads were calculated for the 20 ft.-7 in. tall column with a diameter of 5.5 ft. The service load was obtained by considering different load combinations considering braking force, wind, superstructure dead load, and two design vehicle loads, HL-93 and P15. The applicable loads were entered into WinRECOL for the design of the column. The required number of reinforcing bars was determined to be 33, #11 bars. From the output, the maximum axial load to be resisted by the column was 2900 kips which corresponded to an axial load ratio of  $0.23f'_cA_g$ . The nominal axial resistance was calculated using the equation from the AASHTO 5.7.4.4-2, present in Eq. (B.1), where  $A_g$  is the gross area of the column,  $A_{st}$  is the total area of longitudinal reinforcement in the column,  $A_{ps}$  is the area of prestressing steel in the column, and  $\epsilon_{cu}$  is the failure strain of concrete in compression.

$$P_n = 0.85 \left( .85f'_c(A_g - A_{st} - A_{ps}) + f_yA_{st} - A_{ps}(f_{pe} - E_p\epsilon_{cu}) \right) \quad (B.1)$$

$$P_n = 0.85 \left( .85(3.6^{ksi})(3407in^2 - 51.48in^2) + (60^{ksi})(51.48in^2) \right) = 11354kips$$

The nominal axial load capacity of the column was 11354 kips, which is much larger than the maximum axial load of 2900 kips; therefore the axial load capacity was satisfactory and the additional capacity was needed, as will be shown below, in the combination ratio. Next, the flexural resistance of the column was checked. From WinRECOL, the maximum flexural load was 7297 kip-ft and the chosen longitudinal reinforcement provided a nominal capacity of 8078 kip-ft, which was satisfactory. Next, the shear design of the column was completed for the design shear force of 1065 kips, the resulting longitudinal design shear force from the maximum

plastic moment of the column divided by the column length. The Bridge Design Aids (BDA) Section 8.16.6.2 Eq. 8-51 (3.2) (Caltrans, Bridge Design Aids, 1995) was used for the shear resistance provided from concrete, where  $b_w$  is the width of the core section of the concrete and  $d$  is the distance from extreme compression fiber to the centroid of the longitudinal reinforcement.

$$\phi V_c = 0.85 * 2\sqrt{f'_c} b_w d \quad (B.2)$$

$$\phi V_c = 0.85 * 2 * \sqrt{3.6^{ksi}} * 62 * 49.6 = 314 \text{ kips}$$

Therefore, the remainder of the shear resistance was to be provided from shear reinforcement. The shear reinforcement needed to be designed for multiple spacings: the plastic hinge region, regions requiring shear reinforcement, and the region of minimum shear reinforcement. The following equations were used for the respective locations. For the confinement region, Eq. 8-62b, presented in Eq. (B.3), from the Bridge Design Specifications (BDS) (Caltrans, Bridge Design Specifications, 2003) was used, where  $\rho_s$  is the ratio of spiral or hoop reinforcement.

$$\rho_s \geq 0.12 \frac{f'_c}{f_y} \left( .5 + 1.25 \frac{P}{f'_c * A_g} \right) \quad (B.3)$$

For the region outside of the plastic hinge where shear reinforcement was required, Eq 8-53 from Section 8.16.6 of the BDS, shown in Eq. (B.4), was used where  $V_s$  is the force to be resisted by steel reinforcement.

$$V_s = \frac{A_v f_y d}{s} \quad (B.4)$$

For the region where the concrete resistance was greater than the design shear force, but one-half the concrete resistance was less than the design shear force, the minimum shear reinforcement was provided according to Eq. 8-63 of the BDS, shown in Eq. (B.5), where  $A_v$  is the area of shear reinforcement.

$$A_v = \frac{50 b_w s}{f_y} \quad (B.5)$$

Next, spacing requirements according to section 8.21.1.1 of the CALTRANS BDS were considered. The maximum spacing of the lateral reinforcement was not to exceed:

- 1/5 of the least dimension of the column =  $1/5 * 62'' = 12.4$  inches
- 6 times the nominal diameter of the longitudinal reinforcement:  
=  $6 * 1.41 \text{ in} = 8.46$  inches
- 8 inches

The maximum spacing allowed would be 8 inches according to the requirements above. Finally, considering the design shear force of 1065 kips and the concrete contribution of 314 kips, the reinforcement was designed. Using Eq. 5.8.3.3-1 from AASHTO, given in Eq. (B.6), the amount of shear resistance needed from the shear reinforcement was found as follows:

$$V_s = \frac{V_n}{\phi} - V_c \quad (\text{B.6})$$

$$V_s = \frac{1065 \text{ kips} - 314 \text{ kips}}{0.85} = 884 \text{ kips}$$

$$\rho_s = .12 \frac{3.6 \text{ ksi}}{60 \text{ ksi}} \left( .5 + 1.25 \frac{1525 \text{ kips}}{3.6 \text{ ksi} * 23.76 \text{ ft}^2 * 144} \right) = 0.00471$$

$$\text{confinement spacing} \leq \frac{4A_{sp}}{D'\rho_s} = \frac{4(0.44)}{62 \text{ in.} * 0.00471} = 6.02 \text{ inches}$$

$$\text{shear reinforcement spacing} \leq \frac{2 * 0.44 \text{ in}^2 * 60 \text{ ksi} * 49.6 \text{ in.}}{884 \text{ kips}} = 2.96 \text{ inches}$$

$$\text{minimum shear reinforcement spacing} \leq \frac{2 * 0.44 \text{ in}^2 * 60 \text{ ksi}}{50 * 62 \text{ in.}} = 17.03 \text{ inches}$$

However, for the maximum spacing of the shear reinforcement, 8 inches was used according to Article 8.21.1.1 of the BDS. Therefore, instead of the value corresponding to the minimum shear reinforcement calculated above, the maximum spacing of 8 inches was used. The confinement spacing provided above ensured that the plastic hinge would form to adequately dissipate energy

while not allowing other inelastic action to occur. In Figure B.2 the layout of the column reinforcement is shown.

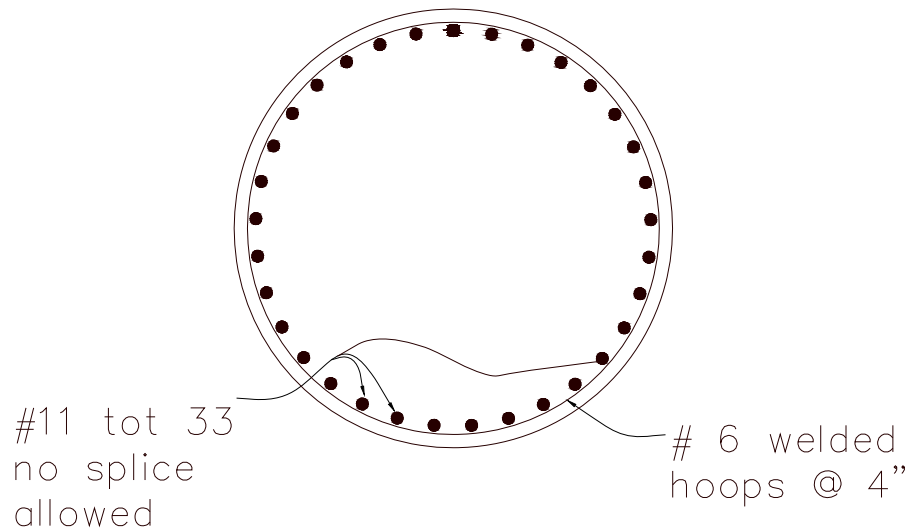


Figure B.2. Column Reinforcement Layout

## B.4 Cap Beam

The design of the cap beam considered two load cases as specified by Article 5.6.1 of AASHTO 2003. The first case involved the live and dead loads during the construction process, while the second case involved the dead and live service loads after the diaphragm was cast in place.

### B.4.1 Construction Loads

First, the loads applied to the inverted-tee section were calculated. During construction the loads on the cap beam were expected to be from the girders, cap beam self-weight, and the weight from the construction equipment. The loads from the interior and exterior girders transmitted to the cap beam were compiled from the self weight, deck and haunch above the girder, intermediate diaphragms and precast components, presented below in Figure B.3 and Table B.1. The point load resulting from the deck loads action on exterior girder,  $P_{Dce}$ , and interior girder,  $P_{DCi}$ , from both spans is given below.

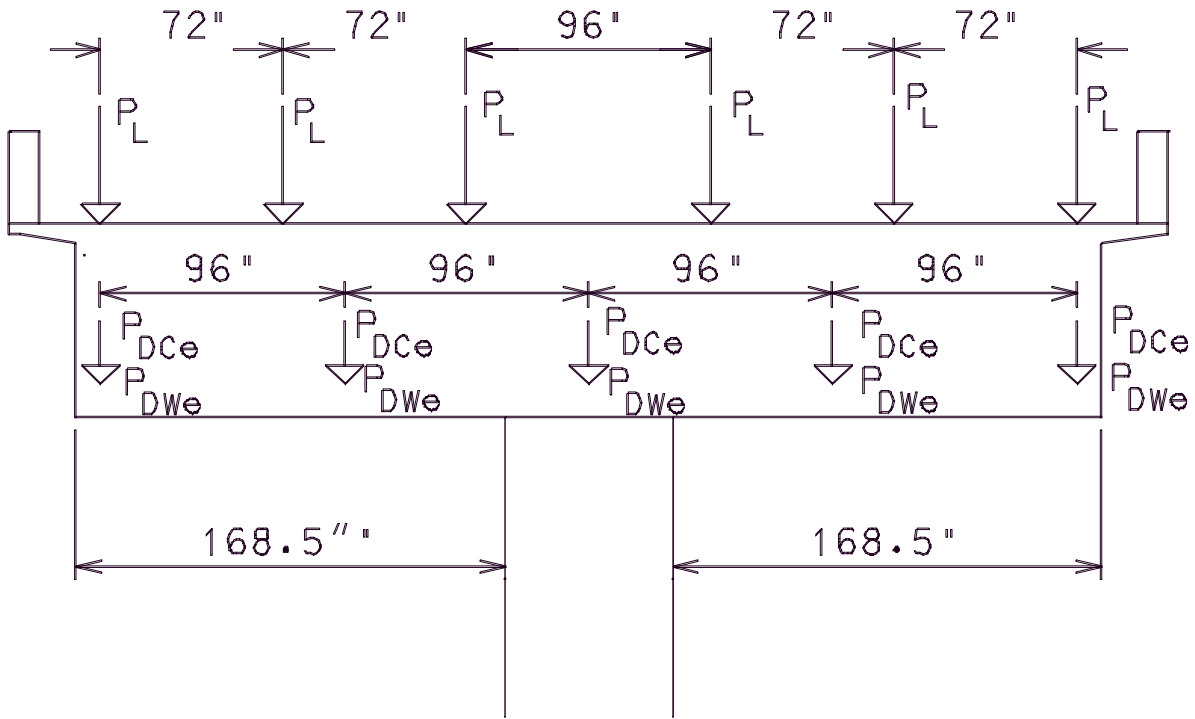


Figure B.3. Load layout on cap beam

Table B.1. Loads from deck components on the girders

	Girder Loads (kip)	
	Interior	Exterior
Self-Weight	34.8	34.8
Deck+Haunch	41.7	39.2
Diaphragm	2.2	1.1
Precast	5.7	3.9

$$P_{Dce} = (34.8 + 39.2 + 1.1 + 3.9)(2) = 158 \text{ kips}$$

$$P_{Dci} = (34.8 + 41.7 + 2.2 + 5.7)(2) = 169 \text{ kips}$$

An additional load needed to be considered from the construction equipment, such as the Bidwell machine. A load of 20 psf was assumed to be exerted on the 20-in. wide overhang in addition to the weight of the machine itself. Therefore, over the 112 ft of the span contributing a load to the cap beam, the construction load,  $P_{const}$ , was taken to be:

$$P_{const} = (0.02) \left( \frac{20 \text{ in.}}{12} \right) (112 \text{ ft.}) + 8 \text{ kips} = 11.7 \text{ kips}$$

Next, the weight of the cap beam,  $w_{cb}$ , including the weight of the diaphragm,  $w_{dia}$ , and deck and haunch above the cap beam,  $w_{d+h}$ , was calculated. The resulting equivalent distributed load ( $w$ ) from the components listed was also calculated.

$$w_{cb} = 44 \text{ ft}^2 * 0.15 \frac{\text{kips}}{\text{ft}^3} = 6.6 \frac{\text{kips}}{\text{ft}}$$

$$w_{dia} = [2.75 \text{ ft.} * 4 \text{ ft.} + 2 \text{ ft.} * 5.5 \text{ ft.}] * 0.15 \frac{\text{kips}}{\text{ft}^3} = 3.3 \frac{\text{kips}}{\text{ft}}$$

$$w_{d+h} = \frac{9.625 \text{ in.}}{12} * 0.15 \frac{\text{kips}}{\text{ft}^3} * (6 \text{ ft.} + 2 \text{ ft.}) = 0.963 \frac{\text{kips}}{\text{ft}}$$

$$w = 6.6 \frac{\text{kips}}{\text{ft}} + 0.963 \frac{\text{kips}}{\text{ft}} + 3.3 \frac{\text{kips}}{\text{ft}} = 10.9 \frac{\text{kips}}{\text{ft}}$$

Finally, with the loads listed above and shown in Table B.1, the AASHTO Eq. 3.4.1-1, presented in Eq. (B.7), was used to find the ultimate shear and moment,

$$Q = \sum n_i \gamma_i Q_i \tag{B.7}$$

where  $Q$  is the load being calculated. Since the structure was designed by conventional design methods,  $n_i$  could be taken as 1.0 for all calculations according to AASHTO Articles 1.3.3, 1.3.4, and 1.3.5. The factors for  $\gamma_i$ , according to AASHTO tables 3.4.1-1 and 3.4.1-2, are 1.25 for dead load and 1.75 for live load, assuming the Strength II limit state. The load from the Bidwell machine was also multiplied by a dynamic load factor that was taken as 1.33. The dynamic load factor is a dynamic load allowance that accounts for the wheel load impact from the moving vehicles.

$$V_u = 1.25 * (158 \text{ kips} + 169 \text{ kips}) + 1.75 * (11.7 \text{ kips})(1.33) + 1.25$$

$$* \left( 10.9 \frac{\text{kips}}{\text{ft.}} \right) (14.042 \text{ ft.}) = 627 \text{ kips}$$

$$M_u = 1.25 * (158 \text{ kips})(13.25 \text{ ft.}) + 1.25 * (169 \text{ kips})(5.25 \text{ ft.}) + 1.25$$

$$* \left( 10.9 \frac{\text{kips}}{\text{ft.}} \right) \frac{(14.042 \text{ ft.})^2}{2} + 1.75 * (11.7 \text{ kips})(1.33)(13.25 \text{ ft.})$$

$$M_u = 5430 \text{ kip} - \text{ft.}$$

Next the capacity of the cap beam needed to be designed to ensure that it would be larger than the ultimate moment calculated above. For the number of reinforcing bars in the cap beam, 22 #11 bundled bars were considered. The depth to the centroid,  $d$ , of the tension reinforcing steel from the extreme compression fiber was found as follows.

$$d = 66 \text{ in.} - 3 \text{ in.} - 1.375 \text{ in.} - 0.75 \text{ in.} = 60.875 \text{ in.}$$

Then the capacity of the section was calculated using Eq. 5.7.3.2.2-1 from the BDS. This equation was simplified due to the absence of prestressing steel, compression steel and flanges in the section. The reduced equation is shown in Eq. (B.8), in which  $A_s$  is the area of longitudinal reinforcing steel and  $a$  is the depth of the compression block, presented in Eq. (B.9),

$$\phi M_n = \phi A_s f_y \left( d - \frac{a}{2} \right) \quad (\text{B.8})$$

$$\text{where, } a = \frac{A_s f_y}{0.85 f'_c b} = \frac{(34.32 \text{ in}^2)(60 \text{ ksi})}{(0.85)(3.6 \text{ ksi})(120 \text{ in})} = 5.61 \text{ in.} \quad (\text{B.9})$$

$$\text{Therefore, } M_n = (0.9)(34.32 \text{ in}^2)(60 \text{ ksi}) \left[ 60.875 \text{ in} - \frac{5.61 \text{ in}}{2} \right] = 107620 \text{ kip} - \text{in} = 8968 \text{ kip} - \text{ft.}$$

As shown above, the capacity significantly exceeded the ultimate moment applied to the section due to the flexural-shear interaction calculated later. Next, the section was checked to ensure the minimum reinforcement required by AASHTO Eq. 5.7.3.3.2, presented in Eq. (B.10), and the check from Article 5.7.3.3.2, shown as Eq. (B.11), were satisfied. The two checks were considered to effectively control the crack width. The amount of tensile reinforcement needed to develop a factored flexural resistance of 8968 kip-ft. above or equal to the lesser of the following values,

$$1.2M_{cr} = 1.2(S_c (f_r)) \quad (\text{B.10})$$

$$1.2M_{cr} = 1.2 * \left( \frac{105.703 \text{ ft}^4}{3.094 \text{ ft}} \right) * 702 \frac{\text{lb}}{\text{in}^2} * \frac{144 \text{ in}^2}{1 \text{ ft}^2} * \frac{1 \text{ kip}}{1000 \text{ lb}} = 4144 \text{ kip} - \text{ft}$$

$$1.33M_u = 1.33 * 5430 \text{ kip} - \text{ft.} = 7221.0 \text{ kip} - \text{ft.} \quad (\text{B.11})$$

In the above equations,  $M_{cr}$  is the cracking moment of the cap beam,  $S_c$  is the section modulus cap beam, and  $f_r$  is the modulus of rupture of concrete. This condition was satisfied with the provided reinforcement. Next, the spacing of steel,  $s$ , was checked to effectively control the crack width. The use of a larger number of closely spaced, smaller bars is more efficient at controlling crack widths than a smaller number of large, widely spaced, bars. The provisions in Article 5.7.3.4 Eq. 5.7.3.4-1 of AASHTO 2003, presented below in Eq. (B.12) account for this and were checked. In this equation,  $\beta_s$  is a ratio of flexural strain at the extreme tension face to the strain at the centroid of the reinforcement layer,  $\gamma_e$  is an exposure factor,  $f_{ss}$  is the tensile stress in steel reinforcement at the service limit state, and  $d_c$  is the cover to the center of the flexural reinforcement closest to the extreme tension fiber. To calculate  $\beta_s$ , Eq. (B.13) was used, and for  $f_{ss}$ , Eq. (B.14) was used; both of these equations were given in Article 5.7.3.4 of AASHTO. For Eq. (14) the  $M$  is the unfactored moment.

$$s \leq \left( \frac{700\gamma_e}{\beta_s f_{ss}} - 2d_c \right) \quad (\text{B.12})$$

$$\beta_s = 1 + \frac{d_c}{.7(h - d_c)} \quad (\text{B.13})$$

$$f_{ss} = \frac{M}{A_s j d} \quad (\text{B.14})$$

Substituting the appropriate values,

$$\beta_s = 1 + \frac{3.75}{.7(66 - 3.75)} = 1.086$$

$$f_{ss} = \frac{4262 * (12)}{34.32 * 0.92 * 60.875} = 26.6 \text{ ksi}$$

$$s_{\text{req'd}} = \frac{700 * .75}{1.086 * 26.6 \text{ ksi}} - 2 * 3.75 \text{ in} = 10.7 \text{ in.}$$

$$s_{\text{provided}} = \frac{72 - 2 * 2.5}{10} = 6.7 \text{ in.}$$

This completed the flexural design of the cap beam, and the reinforcement layout is presented in Figure B.4.

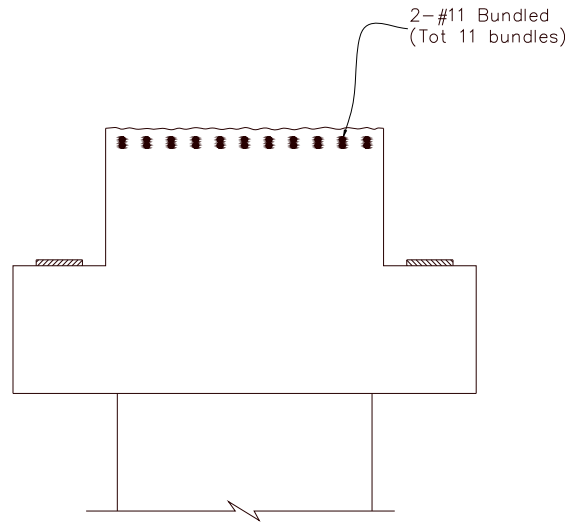


Figure B.4. Cap Beam Top Flexural Reinforcement

The section was then designed for shear. The shear in a concrete member can be resisted in three ways: concrete, shear reinforcement and prestressing. The cap beam had no prestressing, and thus only the shear resistance from the concrete and the shear reinforcement was considered. The shear stress on the section was found by using Article 5.8.2.9 in AASHTO. In that article, Equation 5.8.2.9-1, shown in (B.15), was given for the calculation of the shear stress. Accordingly,

$$v_u = \frac{|V_u - \phi V_p|}{\Phi b_v d_v} \quad (\text{B.15})$$

The AASHTO specification states  $d_v$ , “Need not be taken to be less than the greater of  $0.9d_e$  or  $.72h$ ”, where  $d_e$  is the depth from the extreme compression fiber to the tensile reinforcement and  $\Phi$  is the shear resistance factor taken as 0.9. Consequently, the shear stress in the beam section was calculated as shown below using Eq. (B.15).

$$v_u = \frac{|627|}{0.9 * 72 * 54.79} = 0.177 \text{ ksi}$$

Then, the shear resistance was determined according to AASHTO Article 5.8.3.4, which presents the following three methods for determining the shear resistance:

1. Simplified Procedure for Nonprestressed Sections (Article 5.8.3.4.1);
2. General Procedure (Article 5.8.3.4.2); and
3. Simplified Procedure for Prestressed and Nonprestressed Sections (5.8.3.4.3)

Article 5.8.3.4.2 was chosen for determining the shear resistance of the cap beam. Assuming the section would contain at least the minimum transverse reinforcement as specified in Article 5.8.2.5, Eq. 5.8.3.4.2-1, shown below in Eq. (B.16), was used to determine the strain at the mid-height of the section. The equation was then simplified since no prestressing steel,  $A_p$ , or axial force,  $N_u$ , would be present in the cap beam. The value for  $\theta$ , the angle of inclination of diagonal compressive stresses, was assumed to be  $36.4^\circ$ , by assuming that the shear stress-concrete strength ratio would be very low. This assumption was verified by Table 5.8.3.4.2.1 after  $\epsilon_x$  was calculated.

$$\epsilon_x = \frac{\frac{M_u}{d_v} + 0.5N_u + 0.5|V_u| \cot \theta - A_p f_{po}}{2(E_s A_s + E_p A_p)} \quad (\text{B.16})$$

$$\epsilon_x = \frac{\frac{(5430 * 12)}{54.79} + 0.5 * 627 * \cot 36.4}{2(29000 * 34.32)} = 811 * 10^{-6}$$

With the value of  $\epsilon_x = 811 \times 10^{-6}$  and  $\frac{v_u}{f'_c} = 0.049$ , Table 5.8.3.4.2.1 of AASHTO gives  $\theta = 36.4^\circ$  and  $\beta = 2.23$ , where  $\beta$  is the factor indicating the ability of diagonally cracked concrete to transmit tension and shear. With the investigation of the resistance of the concrete to shear complete, the design of the shear reinforcement could be completed. Since Article 5.8.3.4.2 was used to determine the effectiveness of the cross section to resist shear, Eq. 5.8.3.3-3, shown below in Eq. (B.17), was used to determine the shear resistance of the concrete cross section as follows,

$$V_c = 0.0316\beta\sqrt{f'_c}b_v d_v \quad (\text{B.17})$$

$$V_c = .00316 * 2.23 * \sqrt{3.6} * 72 * 54.79 = 527.4 \text{ kips}$$

With the required nominal shear resistance and the concrete contribution to shear resistance known, the amount of resistance needed from the shear reinforcement was found. Eq. (B.6) was used to solve for  $V_s$  as follows:

$$V_s = \frac{627}{0.9} - 527.4 = 169.3 \text{ kips}$$

The area of steel and spacing needed to be calculated to ensure that the capacity from the steel reinforcement to resist shear was sufficiently provided. This value was obtained by rearranging equation C5.8.3.3-4 of AASHTO (see Eq. (B.18)), to solve for  $\frac{A_v}{s_{req'd}}$  as shown in Eq. (B.19).

$$V_s = \frac{A_v f_y d_v \cot \theta}{s} \quad (\text{B.18})$$

$$\frac{A_v}{s_{req'd}} = \frac{V_s}{f_y d_v \cot \theta} \quad (\text{B.19})$$

$$\frac{A_v}{s_{req'd}} = \frac{V_s}{f_y d_v \cot \theta} = \frac{169 * 12}{60 * 54.79 * \cot(36.4^\circ)} = 0.46 \frac{in^2}{ft}$$

Assuming a #6 shear reinforcement bar at a spacing of .75 ft,

$$\left(\frac{A_v}{s}\right)_{provided} = \frac{6 * 0.44 \text{ in}^2}{0.75 \text{ ft}} = 3.52 \frac{in^2}{ft}$$

The shear reinforcement chosen for the cap beam was greater than the amount required, and the shear resistance of the beam section exceeded the nominal shear force. Over the column, the shear reinforcement spacing is required to be the maximum spacing ( $s_{max}$ ) allowed by AASHTO Article 5.8.2.7, since the shear shear force would be acting into the column. Since the shear stress was calculated from Eq. (B.15) to be less than  $0.125f'_c$ , Eq. 5.8.2.7-2, reproduced in Eq. (B.20), was used to determine the maximum spacing where  $d_v$  is the effective shear depth.

$$s_{max} = 0.4d_v \leq 24.0 \text{ in.} \quad (\text{B.20})$$

$$s_{max} = (0.4 * 54.79 \leq 24.0 \text{ in.}) = 22 \text{ in.}$$

This work completed the design of the cap beam under construction loads, and the corresponding reinforcement layout is shown in Figure B.5.

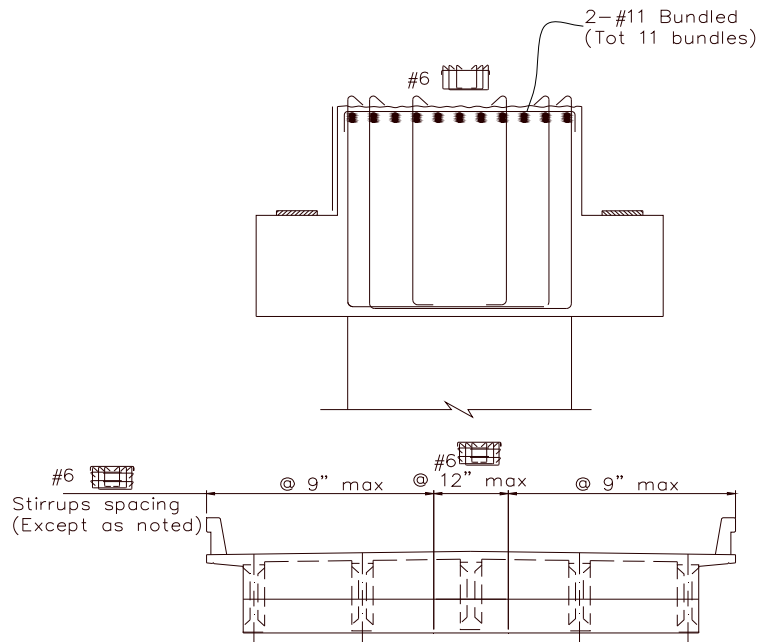


Figure B.5. Cap Beam Reinforcement designed for Construction Loads

#### B.4.2 Service Loads

The cap beam was then designed for the dead and live service loads after the diaphragm was added. In addition to the loads calculated for the construction phase, the composite weight of the superstructure (DC), superimposed dead load (DW), weight of the barriers ( $w_{barr}$ ), weight of formwork ( $w_{form}$ ), and design vehicle load were considered. For the vehicle design loads, the HL-93 and P15 were considered. After a structural analysis, it was concluded that the P15 load governed between the two. All assumed girder loads are presented in Table B.2, and the remaining loads are presented in Table B.3.

The interior girders as shown in this table include the center and intermediate girders while the exterior girder is listed separately. Also worth noting is that the load due to the Bidwell machine is not present because the deck would already be present. Accounting for these changes, the resulting cap beam shear and negative moment demands were determined to be:

Table B.2. Assume Girder Loads for the Service Load Design

	Girder Loads (kips)	
	Interior	Exterior
Self-Weight	34.8	34.8
Deck+Haunch	41.7	39.2
Diaphragm	2.2	1.1
Precast	5.7	3.9
DC	21	21
DW	28.4	28.4

Table B.3. Assumed Additional Loads for the Service Load Design

$w_{barr}$	3.73 kips
$w_{form}$	.28 k/ft
P15	142 kips

$$V_u = 1392 \text{ kips}$$

$$M_u = 10939 \text{ kip} - \text{ft}$$

First, the flexural capacity of the cap beam was calculated and compared against the demand. Unlike previously, two layers of reinforcement were considered in design. The second layer of 19, #11 bars, is the flexural reinforcement to resist the additional loading which is to be located within the depth of the concrete deck cast in place above the cap beam (see Figure B.5). The equivalent depth of the two layers was 65.4 in. and the total area of steel was 63.96 in<sup>2</sup>. The flexural capacity of the section was found using Eq.(3.8).

$$a = \frac{(63.96 \text{ in}^2)(60 \text{ ksi})}{(0.85)(3.6 \text{ ksi})(144 \text{ in})} = 8.71 \text{ in.}$$

$$\phi M_n = (0.9)(63.96 \text{ in}^2)(60 \text{ ksi}) \left[ 65.4 \text{ in.} - \frac{5.61 \text{ in.}}{2} \right] = 210839 \text{ kip} - \text{in} = 17570 \text{ kip} - \text{ft}$$

Since the flexural capacity was found to be greater than the ultimate moment demand, the beam section was assumed to be sufficiently reinforced. Next the beam section was checked to ensure that the minimum reinforcement required by AASHTO 5.7.3.3.2 was provided. The amount of tensile reinforcement needed to develop a factored flexural resistance of 17570 kip-ft above or equal to the lesser of the following values calculated from Eq. (B.10) and (B.11) previously.

$$1.2M_{cr} = 1.2 * \left( \frac{250.3ft^4}{3.15ft} \right) * 702 \frac{lb}{in^2} * \frac{144in^2}{1ft^2} * \frac{1kip}{1000lb} = 9636 \text{ kip} - \text{ft}$$

$$1.33M_u = 1.33 * 10939 \text{ kip} - \text{ft} = 14549 \text{ kip} - \text{ft}$$

This condition was found to be satisfied with the provided reinforcement. Next, the spacing of steel needed to be checked to effectively control the crack width. The provisions in Article 5.7.3.4 of AASHTO needed to be satisfied for this check. Eq. (B.12) from above was used to calculate the following.

$$s \leq \left( \frac{700 * 0.75}{1.0488 * 26.1ksi} - 2 * 2.5 \text{ in.} = 14.2 \text{ in.} \right)$$

The maximum spacing provided was 9 in., which was less than the maximum permitted spacing of 14.2 in. The reinforcement layout is presented in Figure B.6. Next, the shear capacity design was performed as required by Article 5.8.2.9 in AASHTO and Eq. (B.15). The shear stress acting on the section was determined as:

$$v_u = \frac{|1392|}{0.9 * 144 * 58.86} = 0.182 \text{ ksi}$$

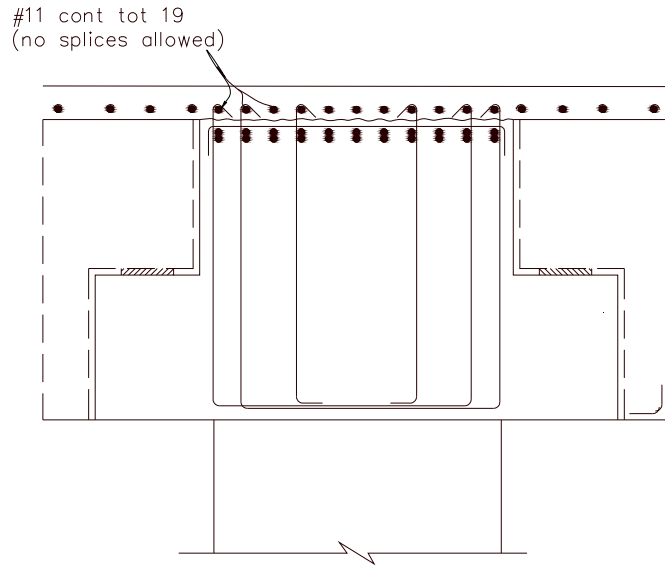


Figure B.6. Cap Beam Flexural Reinforcement under Service Loads

Next, the shear resistance of the section was calculated according to AASHTO article 5.8.3.4.2. Using Eq. (B.16), the strain at mid-height of the section was calculated.

$$\epsilon_x = \frac{\frac{(10939 * 12)}{58.86} + 0.5 * 1392 * \cot 36.4}{2(29000 * 63.96)} = 856 \times 10^{-6}$$

With values of  $\epsilon_x = 856 \times 10^{-6}$  and  $\frac{v_u}{f'_c} = 0.049$ , Table 5.8.3.4.2.1 of AASHTO gives  $\theta = 36.4^\circ$  and  $\beta = 2.23$ . The check of the  $\theta$  value is complete and next the design of shear reinforcement needed to be completed. Since article 5.8.3.4.2 was used to determine the shear resistance, Eq. (B.17) is used to determine the shear resistance of the concrete cross section as follows:

$$V_c = 0.0316\beta\sqrt{f'_c}b_vd_v = .0316 * 2.23 * \sqrt{3.6} * 144 * 58.86 = 1133 \text{ kips}$$

With the required nominal shear resistance and the concrete contribution to shear resistance known, the amount of resistance needed from the shear reinforcement was found. For this calculation, Eq. (B.6) was used as follows:

$$V_s = \frac{1392}{0.9} - 1133 = 414 \text{ kips}$$

The area of shear reinforcement per spacing was then calculated. To find this value, Eq. (B.19) was used and compared to the reinforcement provided.

$$\frac{A_v}{s_{req'd}} = \frac{414 * 12}{60 * 54.79 * \cot(36.4^\circ)} = 0.46 \frac{in^2}{ft}$$

$$\frac{A_v}{s_{provided}} = \frac{6 * 0.44in^2}{.75ft} = 3.52 \frac{in^2}{ft}$$

Therefore, the shear reinforcement provided was greater than the amount required, and the check was satisfied.

Next, the flexure-shear interaction was checked. The longitudinal reinforcement would experience greater force due to shear in the cross section. In general, as the shear crack angle decreases and  $V_c$  increases, the tension force in the longitudinal reinforcement becomes greater for a given shear force. To account for this, Eq. 5.8.3.5-1 of AASHTO Article 5.8.3.5 was used. Eq. 5.8.3.5-1 would determine if the chosen longitudinal reinforcement would be sufficient for the flexural-shear interaction. Since no prestressing or axial force was determined to be present in the cap beam, a simplified form of this equation as shown in Eq. (B.21) was used. Accordingly,

$$A_s f_y \geq \frac{|M_u|}{d_v \phi_f} + \left( \left| \frac{V_u}{\phi_v} \right| - .5V_s \right) \cot \theta \quad (B.21)$$

$$\left( (63.96 * 60) = 3838^{kips} \right) \geq \left( \frac{|10939 * 12|}{58.86 * 0.90} + \left( \left| \frac{1392}{0.9} \right| - .5(1405) \right) \cot 36.4 \right) = 3623 \text{ kips}$$

Since this condition was satisfied and the provided longitudinal reinforcement was only 6% greater than that required for the loading conditions; the reinforcement quantity was not adjusted. This completed the design of the cap beam under service loads. The final reinforcement layout of the cap beam is presented in Figure B.7.

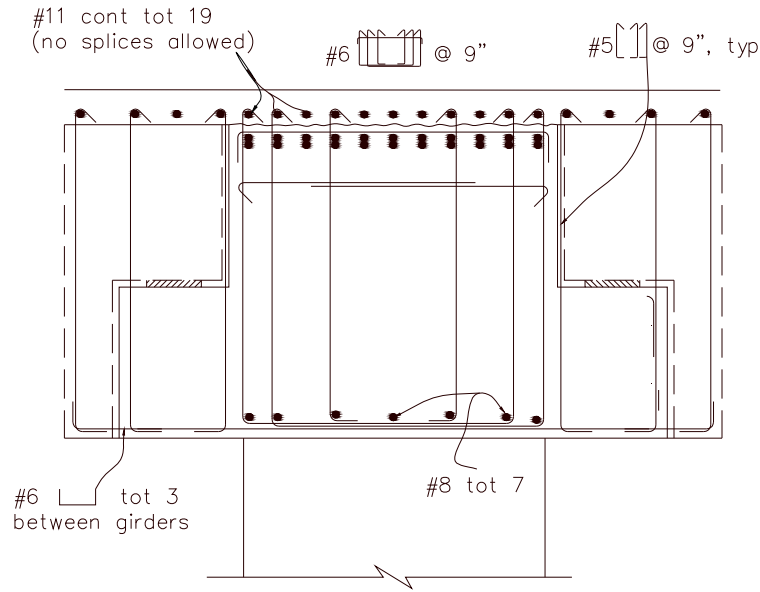


Figure B.7. Cap Beam Reinforcement under Service Load Conditions

### B.4.3 Torsional Demand on the Cap Beam

Finally, the torsional capacity of the cap beam was calculated to ensure that it would be greater than that induced by the column seismic moment. From XTRACT, the overstrength moment of the column ( $\phi M_n$ ) was found to be 17,662 kip-ft when the moment was extrapolated to the centerline of the superstructure. Current design practice considers 40% of the overstrength moment to be applied as a torsional moment on the cap beam. Therefore, the resulting torsional moment on the cap beam was 7,065 kip-ft. Eq. (B.22), from Eq. 5.8.2.1-4 of AASHTO, was used to determine the torsional capacity of the cap beam.

$$T_{cr} = 0.125x\sqrt{f'_c} \frac{A_{cap}^2}{p_c} \quad (B.22)$$

$$T_{cr} = 0.125\sqrt{3600} \frac{(10890in^2)^2}{439.25 in.} = 64033kip - in = 5336 kip - ft$$

According to Article 5.8.2.1, if one-quarter of the capacity is greater than the applied torsional moment, then the shear capacity of the section is affected. Hence,

$$0.25\phi T_{cr} = 0.25 * 0.9 * 5336 \text{ kip} - \text{ft} = 1200.6 \text{ kip} - \text{ft} < T_u = 7065 \text{ kip} - \text{ft}$$

Since one-quarter of the torsional capacity of the cap beam was less than the applied torsion, the torsion needed to be considered as it would reduce the shear capacity of the cap beam. The ultimate shear acting on the cap beam from the dead load was only 538 kips. The equivalent shear force acting on the cap beam from Eq. 5.8.2.1-6, shown in Eq. (B.23) of AASHTO was calculated. The shear resistance from the concrete was 1133 kips, as calculated during the cap beam design under service loads.

$$V_u = \sqrt{V_u^2 + \left(\frac{.9p_h T_u}{2A_o}\right)^2} \quad (\text{B.23})$$

$$V_u = \sqrt{(538 \text{ kips})^2 + \left[\frac{(0.9)(278 \text{ in.})(7065 \text{ in}^2)(12)}{(2)(4104 \text{ in}^2)}\right]^2} = 2640 \text{ kips}$$

During the cap beam shear design, multiple shear reinforcing bars were placed in the section and the capacity was calculated to ensure the equivalent shear force was resisted. Within the cap beam, six-legged #6 bars and six-legged #5 bars were provided at a spacing of 9 in. The resistance provided was calculated with an assumed crack inclination angle of 36.4°.

$$V_s = \frac{[(0.44)(6) + (0.31)(6)](58.86 \text{ in.})(60 \text{ in.})}{(9) \tan(36.4^\circ)} = 2395 \text{ kips}$$

Then the shear resistance provided was calculated using Eq. 5.8.3.3-1, presented in Eq. (B.24), of AASHTO and compared to the ultimate shear force.

$$\phi V_n = \phi(V_c + V_s + V_p) \quad (\text{B.24})$$

$$\phi V_n = (1.0)(1133 \text{ kips} + 2395 \text{ kips}) = 3528 \text{ kips} > V_u = 2640 \text{ kips}$$

This check ensured that the cap torsion would be satisfactorily resisted through the reinforcement provided in the cap beam to resist shear demand.

## B.5 Inverted Tee Ledge Design

To ensure satisfactory performance of the cap beam, the ledges of the inverted-tee were also designed. For the ledge design, the loads transmitted from the girders to the cap beam were considered along with the load transmitted from the diaphragm to the cap beam between the girders. Since the ledge on each side of the cap beam, which supported the girder loads, extended significantly wider than the column, the design needed to ensure that the loads would be satisfactorily transferred to the column. For this purpose, the design steps detailed in the BDA were followed.

First, the loads were calculated at the points where the girders would rest on the cap beam along with the area between the girders where the diaphragm would transmit a load to the cap beam. The loads applied to the ledge from the girders were resulting from design vehicle loads, dead load and the additional dead loads detailed previously in Table B.2 and

Table B.3. For each section, the applied shear load,  $V_u$ , was found as:

Interior Girders:

$$V_u = (1.25)(84.4 \text{ kips}) + (1.25)(49.4 \text{ kips}) \left( \frac{49 \text{ in.}}{96 \text{ in.}} \right) + (1.35)(206.7 \text{ kips}) \left( \frac{49 \text{ in.}}{96 \text{ in.}} \right)$$

$$V_u = 280 \text{ kips}$$

Exterior Girders:

$$V_u = (1.25)(79 \text{ kips}) + (1.25)(49.4 \text{ kips}) \left( \frac{2*31 \text{ in.}}{78 \text{ in.} + 31 \text{ in.}} \right) + (1.35)(206.7 \text{ kips}) \left( \frac{2*31 \text{ in.}}{31 \text{ in.} + 78 \text{ in.}} \right)$$

$$V_u = 280 \text{ kips}$$

Between Girders:

$$V_u = (1.25)(49.4 \text{ kips}) \left( \frac{47 \text{ in.}}{96 \text{ in.}} \right) + (1.35)(206.7 \text{ kips}) \left( \frac{47 \text{ in.}}{96 \text{ in.}} \right) = 167 \text{ kips}$$

Next, the horizontal shear,  $N_{uc}$ , values were calculated according to the BDA. For the same sections, the design values were calculated as per Eq. (B.25):

$$N_{uc} = 0.2 * V_u \tag{B.25}$$

Interior Girders:

$$N_{uc} = 0.2 * (280 \text{ kips}) = 56 \text{ kips}$$

Exterior Girders:

$$N_{uc} = 0.2 * (280 \text{ kips}) = 56 \text{ kips}$$

Between Girders:

$$N_{uc} = 0.2 * (167 \text{ kips}) = 33.4 \text{ kips}$$

Then the capacity of the area below the bearing surfaces was checked to ensure that the demand would not exceed the capacity. First, the flange needed to be checked for the ratio of the bearing point,  $a_v$ , to depth,  $d$ , of the flange, according to BDS 8.16.6.8.1, as follows in Eq. (B.26) and Figure B.8,

$$\frac{a_v}{d} < 1.0 \tag{B.26}$$

$$\left( \frac{12 \text{ in.}}{31 \text{ in.}} = 0.39 \right) < 1.0$$

This check was satisfied, and the flange dimensions were thus adequate. The punching strength of the girders were then calculated. To calculate the effective area for the punching strength, the BDA was used for define the appropriate dimensions. The seat width considered for the interior girders,  $b_{int}$ , was the width of the bearing pad,  $w$ , plus the depth of the corbel,  $d$ . For the exterior girders, the seat width,  $b_{ext}$ , was the width of the bearing pad plus one-half the depth of the corbel plus the edge distance to the end of the cap,  $x$ , which should not exceed one-half the depth according to the BDS. The seat width for the area between the girders,  $b_{between}$ , was the girder spacing minus the bearing pad width minus the depth of the section. Figure B.8 shows the effective widths for the interior and exterior girders; the remaining distance between the girders was used for the width between girders.

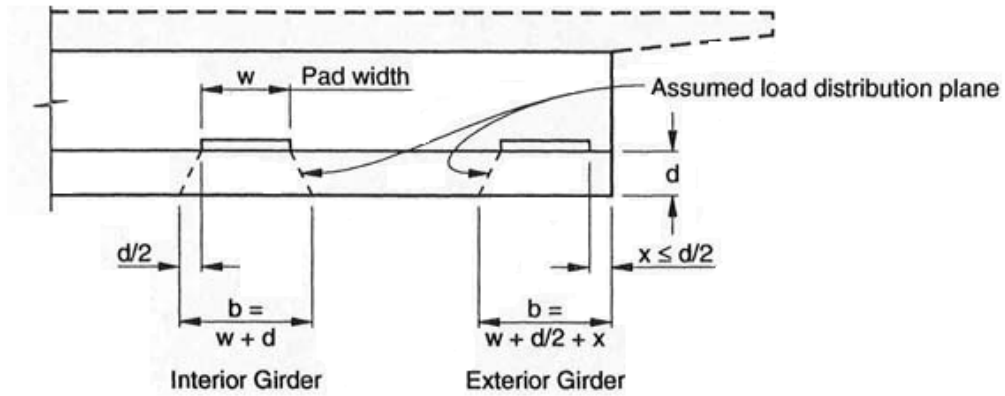


Figure B.8. Distribution Plane Layout (Caltrans, Bridge Design Specifications, 2003)

Accordingly,

$$b_{int} = w_{int} = 18 \text{ in.} + 31 \text{ in.} = 49 \text{ in.}$$

$$b_{ext} = w_{ext} = 18 \text{ in.} + \frac{1}{2}(31 \text{ in.}) = 33.5 \text{ in.}$$

$$b_{between} = w_{between} = 96 \text{ in.} - 18 \text{ in.} - 31 \text{ in.} = 47 \text{ in.}$$

As per BDS 8.16.6.6.2, the shear strength of the concrete shall not be taken greater than the value determined from that presented in Eq. (B.27),

$$\phi V_n = \phi 4 \sqrt{f'_c} b_o d \quad (\text{B.27})$$

$$b_o = 2\left(L + x + \frac{d}{2}\right) + w_{int/ext} \quad (\text{B.28})$$

where  $b_o$  is the length of the perimeter which the load acts on, presented in Eq. (3.28),  $L$  is the bearing pad length, and  $x$  is the edge distance. Therefore, the shear strength under the interior girders was calculated to be:

$$\phi V_n = (0.90)(4)\sqrt{3600}\left(2\left(12 \text{ in.} + 6 \text{ in.} + \frac{31 \text{ in.}}{2}\right) + 49 \text{ in.}\right)(31 \text{ in.}) = 777 \text{ kips} > (V_u \cong 280 \text{ kips})$$

Similarly, for the exterior girders:

$$\phi V_n = (0.90)(4)\sqrt{3600} \left( (12 \text{ in.} + 6 \text{ in.} + \frac{31 \text{ in.}}{2}) + 33.5 \text{ in.} \right) (31 \text{ in.}) = 448 \text{ kips} > (V_u \cong 280 \text{ kips})$$

According to the BDA, the next step in the design was to calculate the primary tension reinforcement needed to resist the loads on the ledge. The tension reinforcement is required to simultaneously resist shear ( $V_u$ ), moment ( $V_u a_v + N_{uc}(h-d)$ ) and tensile forces ( $N_{uc}$ ) acting on the corbel, which are shown in Figure B.9 from the BDA.

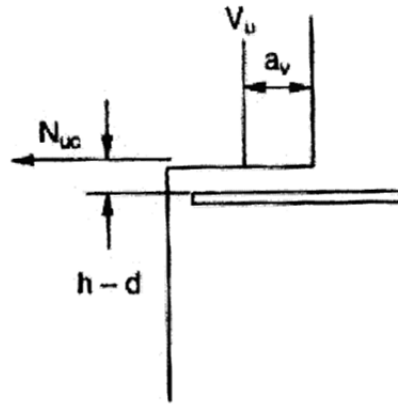


Figure B.9. Forces to be resisted by primary tension reinforcement

The shear design was performed in accordance with Article 8.16.6.4 of the BDA and Eq. (B.29). However, for normal weight concrete, the shear strength shall not be greater than  $0.2f'_c b_w d$  nor  $0.8b_w d$  from BDS 8.16.6.8.3, which are presented below in Eq. (3.30) and (3.31).

$$V_n = \frac{V_u}{\phi} \tag{B.29}$$

$$V_n = \frac{280}{0.9} = 312 \text{ kips}$$

$$V_n \leq 0.2f'_c b_w d \tag{B.30}$$

$$V_n \leq (0.2(31 \text{ in.} * 49 \text{ in.}))(3.6 \text{ ksi}) = 1094 \text{ kips}$$

$$V_n \leq 0.8b_w d \quad (B.31)$$

$$V_n \leq (0.8(31 \text{ in.} * 49 \text{ in.})) = 1215 \text{ kips}$$

Since nominal shear strength was less than the two upper limits suggested in Article 8.16.6.8.3 of the BDS, the equations in Article 8.16.6.4 of the BDS were used to determine the area of needed steel reinforcement in the ledge. The value for coefficient of friction for Eq. 8-56 of the BDS, presented in Eq. (B.32), can be found in Article 8.16.6.4.4c, of the BDS. The required area,  $A_{vf}$ , of steel for the interior girder ledge was determined as:

$$A_{vf} = \frac{V_n}{f_y \mu} \quad (B.32)$$

$$A_{vf} = \frac{312 \text{ kips}}{(60 \text{ ksi})1.4} = 3.71 \text{ in}^2$$

Next, the shear load at the exterior girder was designed. The same articles were used for this design as before, including Eqs. (B.29) to (B.32). Therefore,

$$V_n = \frac{280}{0.9} = 312 \text{ kips}$$

$$V_n \leq (2(31 \text{ in.} * 33.5 \text{ in.}))(3.6 \text{ ksi}) = 747 \text{ kips}$$

$$V_n \leq (.8(31 \text{ in.} * 33.5 \text{ in.})) = 830 \text{ kips}$$

The nominal shear was less than the two calculated values from Article 8.16.6.8.3 of the BDS. Next, the area of steel required for the exterior girder was determined:

$$A_{vf} = \frac{312 \text{ kips}}{(60)1.4} = 3.71 \text{ in.}^2$$

Finally, the area between the girders was found:

$$V_n = \frac{V_u}{\phi} = \frac{167 \text{ kips}}{0.9} = 185.6 \text{ kips}$$

$$A_{vf} = \frac{V_n}{f_y \mu} = \frac{185.6 \text{ kips}}{(60 \text{ ksi})1.4} = 2.21 \text{ in}^2$$

Then the reinforcement to resist the moment was designed. The moment to be resisted was calculated from Article 8.16.6.8.3 of the BDS, presented below in Eq. (B.33). The procedure that was followed for this design is given in BDS section 8.16.3. For each of the three locations, the resulting moment is required to be determined. Then the area of steel required to resist that value was determined from Eq. (B.34).

$$M_u = V_u a_v + N_{uc}(h - d) \quad (\text{B.33})$$

$$M_u \leq \phi A_f f_y \left( d - \frac{A_f f_y}{1.7 f'_c b} \right) \quad (\text{B.34})$$

For the interior girder region,

$$M_u = 280 \text{ kips}(12 \text{ in.}) + 56 \text{ kips}(33 \text{ in.} - 31 \text{ in.}) = 3472 \text{ kip} - \text{in.} = 289.3 \text{ kip} - \text{ft.}$$

$$3472 \text{ kip} - \text{in.} = (0.9)A_f(60 \text{ ksi}) \left( 31 \text{ in.} - \frac{A_f(60 \text{ ksi})}{1.7(3.6 \text{ kips})(49 \text{ in.})} \right)$$

$$\Rightarrow A_f = 2.102 \text{ in.}^2$$

For the exterior girder region,

$$M_u = 280 \text{ kips}(12 \text{ in.}) + 56 \text{ kips}(33 \text{ in.} - 31 \text{ in.}) = 3472 \text{ kip} - \text{in.} = 289.3 \text{ kip} - \text{ft.}$$

$$3472 \text{ kip} - \text{in.} = (0.9)A_f(60 \text{ ksi}) \left( 31 \text{ in.} - \frac{A_f(60 \text{ ksi})}{1.7(3.6 \text{ ksi})(33.5 \text{ in.})} \right)$$

$$\Rightarrow A_f = 2.116 \text{ in.}^2$$

For the region between the girders,

$$M_u = 167 \text{ kips}(12 \text{ in.}) = 2004 \text{ kip} - \text{in.} = 167 \text{ kip} - \text{ft.}$$

$$2004 \text{kip} - \text{in.} = (0.9)A_f(60 \text{ ksi}) \left( 31 \text{ in.} - \frac{A_f(60 \text{ ksi})}{1.7(3.6 \text{ ksi})(47 \text{ in.})} \right)$$

$$\Rightarrow A_f = 2.102 \text{in.}^2$$

The third primary tension reinforcement that was considered was the reinforcement resisting the tensile forces. The force,  $N_{uc}$ , shown above in Figure B.9 was also considered in this design calculation. The area of steel required,  $A_n$ , to resist the force  $N_{uc}$  was determined using Article 8.16.6.8.3d, presented in Eq. (B.35), as follows:

$$N_{uc} \leq \phi A_n f_y$$

$$A_n = \frac{N_{uc}}{0.9 f_y} \tag{B.35}$$

Therefore, using the values for  $N_{uc}$  listed previously, the area of steel required for each of the three design sections were determined to be:

Interior Girder,

$$A_n = \frac{56 \text{ kips}}{(0.9)(60 \text{ ksi})} = 1.037 \text{ in.}^2$$

Exterior Girder,

$$A_n = \frac{56 \text{ kips}}{(0.9)(60 \text{ ksi})} = 1.037 \text{ in.}^2$$

Between Girders,

$$A_n = \frac{0 \text{ kips}}{(0.9)(60 \text{ ksi})} = 0 \text{ in.}^2$$

After the values of tension steel required to resist shear ( $V_u$ ), moment ( $V_u a_v + N_{uc}(h-d)$ ) and tensile forces ( $N_{uc}$ ) acting on the corbel separately were designed, the amount of steel required to resist the forces simultaneously was determined. According to Articles 8.16.6.8.3e and 8.16.6.8.5 of

the BDS, the area of steel provided,  $A_s$ , is required to be greater than the three values presented in Eq. (B.36),

$$A_s \geq \begin{cases} \frac{2}{3}A_{vf} + A_n \\ A_f + A_n \\ 0.04 \left( \frac{f'_c}{f_y} \right) bd \end{cases} \quad (\text{B.36})$$

Therefore, using Eq. (B.36), for each design section the area of steel required was:

Interior Girder,

$$A_s \geq \begin{cases} \frac{2}{3}(3.704 \text{ in.}^2) + 1.037 \text{ in.}^2 = 3.51 \text{ in.}^2 \\ 2.102 \text{ in.}^2 + 1.037 \text{ in.}^2 = 3.14 \text{ in.}^2 \\ .04 \left( \frac{3.6 \text{ ksi}}{60 \text{ ksi}} \right) (49 \text{ in.})(31 \text{ in.}) = 3.65 \text{ in.}^2 \end{cases}$$

$$A_s \geq 3.65 \text{ in.}^2 \Rightarrow 4 - \#8 @ 9 \text{ in.} \Rightarrow A_s = 4(0.79 \text{ in.}^2) \left( \frac{12 \text{ in.}}{9 \text{ in.}} \right) = 4.21 \text{ in.}^2$$

Exterior Girder,

$$A_s \geq \begin{cases} \frac{2}{3}(3.704 \text{ in.}^2) + 1.037 \text{ in.}^2 = 3.51 \text{ in.}^2 \\ 2.116 \text{ in.}^2 + 1.037 \text{ in.}^2 = 3.153 \text{ in.}^2 \\ .04 \left( \frac{3.6 \text{ ksi}}{60 \text{ ksi}} \right) (33.5 \text{ in.})(31 \text{ in.}) = 2.5 \text{ in.}^2 \end{cases}$$

$$A_s \geq 3.51 \text{ in.}^2 \Rightarrow 5 - \#8 @ 12 \text{ in.} \Rightarrow A_s = 5(0.79 \text{ in.}^2) = 3.95 \text{ in.}^2$$

Between Girders,

$$A_s \geq \begin{cases} \frac{2}{3}(2.21 \text{ in.}^2) + 0 \text{ in.}^2 = 1.473 \text{ in.}^2 \\ 1.207 \text{ in.}^2 + 0 \text{ in.}^2 = 1.207 \text{ in.}^2 \\ 0.04 \left( \frac{3.6 \text{ ksi}}{60 \text{ ksi}} \right) (47 \text{ in.})(31 \text{ in.}) = 3.5 \text{ in.}^2 \end{cases}$$

$$A_s \geq 3.5 \text{ in.}^2 \Rightarrow 4 - \#8 @ 9 \text{ in.} \Rightarrow A_s = 4(0.79 \text{ in.}^2) \left( \frac{12 \text{ in.}}{9 \text{ in.}} \right) = 4.21 \text{ in.}^2$$

Figure B.10 shows the primary tension reinforcement for the interior girder only; the other two sections will change size and spacing accordingly. Next, the secondary tension reinforcement

required was designed. The steel required was obtained from the equation described in Article 8.16.6.8.4 of the BDS and presented in Eq. (B.37). The steel was to be placed parallel to  $A_s$  with the total area greater than  $.5(A_s - A_n)$ . According to the BDS, the steel “shall be distributed uniformly within two-thirds of the effective depth adjacent to  $A_s$ .” Therefore, for the three sections, the required steel is,

$$A_h \geq 0.5(A_s - A_n) \quad (\text{B.37})$$

The areas were determined to be:

Interior Girder,

$$A_h \geq .5(4.21 \text{ in.}^2 - 1.037 \text{ in.}^2) = 1.59 \text{ in.}^2$$

$$\Rightarrow \text{use 2 - double legged \#6} = A_h = 1.76 \text{ in.}^2$$

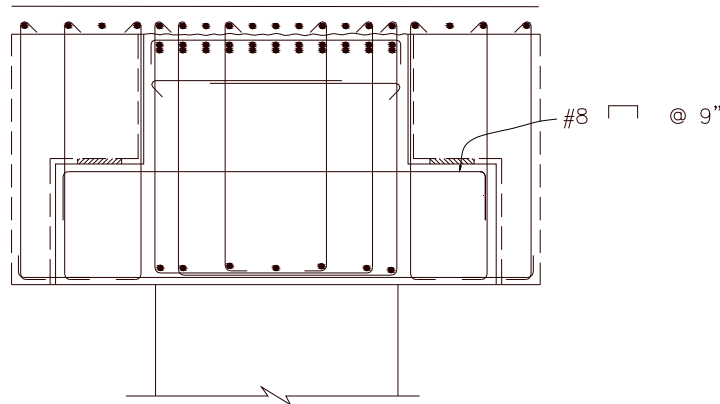


Figure B.10. Primary tension reinforcement for the interior girders

Exterior Girder,

$$A_h \geq 0.5(3.95 \text{ in.}^2 - 1.037 \text{ in.}^2) = 1.46 \text{ in.}^2$$

$$\Rightarrow \text{use 2 - double legged \#6} = A_h = 1.76 \text{ in.}^2$$

Between Girders,

$$A_h \geq .5(4.21 \text{ in.}^2) = 2.11 \text{ in.}^2 \Rightarrow \text{use } 6 - \#6 = A_h = 2.64 \text{ in.}^2$$

Figure B.11 shows the secondary tension reinforcement for the interior girders, with the sizing and spacing of the other two sections to be adjusted accordingly. Next, according to the BDA, the longitudinal corbel distribution reinforcement ( $A'_s$ ) was designed. The bars should be centered under the exterior bearing pads. The minimum area should be one-half of the primary tension reinforcement, as presented in Eq. (B.38). The steel should be uniformly spaced and extend a distance “d” beyond the seat width. For the exterior girders, the steel required was determined as:

$$(A'_s)_{min} = 0.5A_s \tag{B.38}$$

$$(A'_s)_{min} = 0.5(3.95 \text{ in.}^2) = 1.98 \text{ in.}^2 \Rightarrow 5 - \#6 = 2.2 \text{ in.}^2$$

For the other locations, a minimum of 3-#5 reinforcing bars were specified.

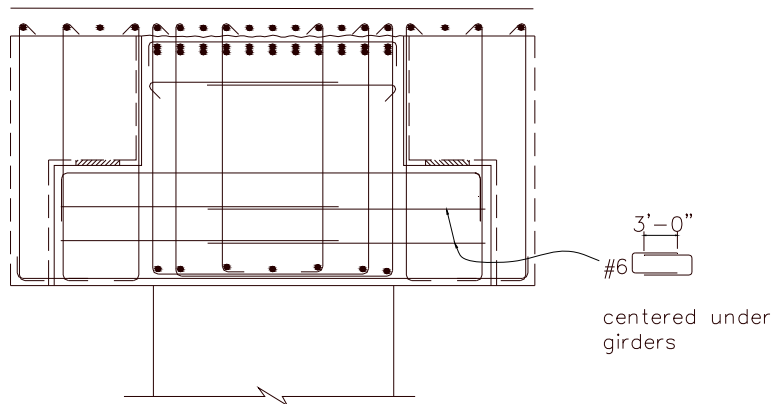


Figure B.11. Secondary tension reinforcement for the interior girders

The longitudinal corbel distribution reinforcement at the exterior girder is shown in Figure B.12 with the additional side reinforcement required. Next, the cap beam was designed for the diagonal tension reinforcement,  $(A_v)_{req'd}$ , presented in Eq. (3.39). The girders would apply loads onto the ledge that could have caused diagonal cracks from the location where the ledge

and stem meet. The diagonal reinforcement spanned the crack opening, and the shear could be carried through these reinforcing bars, as shown below in Figure B.13.

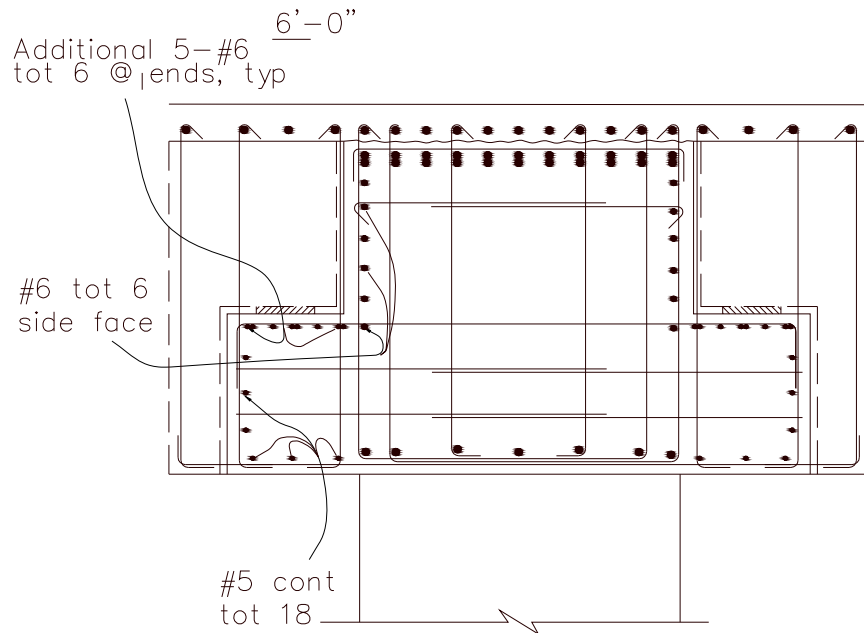


Figure B.12. Longitudinal corbel reinforcement at the exterior girder

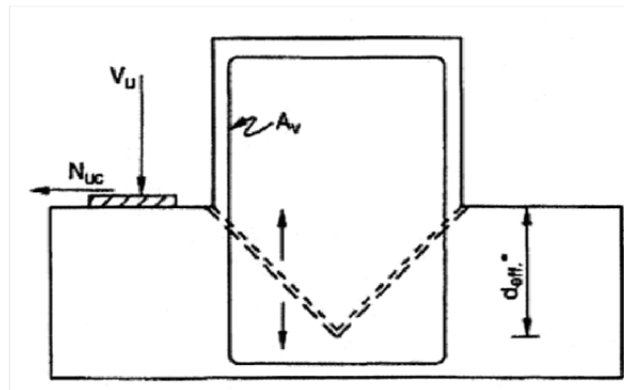


Figure B.13. Corbel diagonal cracking and tension reinforcement (Caltrans, Bridge Design Aids, 1995)

Article 8.16.6.2.3 of the BDS was used to design the required reinforcing. Eq. 8-52 from the BDS, presented below in Eq. (B.40), was used to calculate the force resisted by the concrete, where  $b_w$  are the seat widths calculated previously.

$$(A_v)_{reqd} = \frac{V_s}{f_y} \quad (B.39)$$

$$V_c = 2 \left( 1 + \frac{N_u}{500A_g} \right) \sqrt{f'_c} b_w d_{eff} \quad (B.40)$$

The remainder of the shear force was resisted by the steel being designed. The cracking was assumed to be at a forty-five degree angle, so the value of  $d_{eff}$  could not be greater than one-half the width of the stem of the cap beam. The value for  $N_u$  was taken as the shear from the girder, negative when in tension. Once the force needing to be resisted by reinforcing steel was determined, the contributing resistance from the cap beam reinforcement was checked to determine if it was adequate to be used for the diagonal cracking reinforcement. Therefore, for the three sections, the steel check was completed as presented below.

Interior Girder,

$$V_c = 2 \left( 1 + \frac{280 \text{ kips}}{0.5(49 \text{ in.} \cdot 31 \text{ in.})} \right) \frac{\sqrt{3600 \text{ ksi}}(49 \text{ in.})(31 \text{ in.})}{1000} = 115 \text{ kips}$$

$$V_{s,reqd} = \frac{V_u}{\phi} - V_c = \frac{280 \text{ kips}}{0.9} - 115 \text{ kips} = 196 \text{ kips}$$

To check the contribution of the cap beam shear reinforcement provided from previous design steps, it was assumed only two legs of the reinforcement are effective. Within the distance  $b_{int}$  there were already five sets of #6 bars. The area of steel required was calculated and the area of steel provided from previous design was calculated and compared to check if additional reinforcement was required.

$$(A_v)_{req,d} = \frac{V_{s,reqd}}{f_y} = \frac{196 \text{ kips}}{60 \text{ ksi}} = 3.27 \text{ in.}^2$$

$$(A_v)_{provided} = 5 \text{ sets of 2 legged } - \#6 = 4.4 \text{ in.}^2$$

The provided reinforcement was sufficient to act as the diagonal cracking reinforcement.

Exterior Girder,

$$V_c = 2 \left( 1 + \frac{280 \text{ kips}}{0.5(33.5 \text{ in.} \cdot 31 \text{ in.})} \right) \frac{\sqrt{3600 \text{ ksi}}(33.5 \text{ in.})(31 \text{ in.})}{1000} = 57.4 \text{ kips}$$

$$V_{s,req'd} = \frac{V_u}{\phi} - V_c = \frac{280 \text{ kips}}{0.9} - 57.4 \text{ kips} = 254 \text{ kips}$$

Similar to the interior girder region, the provided cap beam shear reinforcement provided from previous design steps was checked to see if that satisfied the area of steel required. It was assumed only two legs of the reinforcement were effective. Within the distance  $b_{int}$  there were four sets of #6 bars.

$$(A_v)_{req'd} = \frac{V_{s,req'd}}{f_y} = \frac{254 \text{ kips}}{60 \text{ ksi}} = 4.23 \text{ in.}^2$$

$$(A_v)_{provided} = 4 \text{ sets of 2 legged } - \#6 = 3.52 \text{ in.}^2$$

Since the provided reinforcement was not sufficient to act as the tension reinforcement, additional steel was designed to satisfy the requirement. According to the BDA, when using diagonal bars, the effective area is determined by adjusting according to the angle of the bar. Additional bars were placed at a 45 degree angle from vertical, so the additional steel required was:

$$(V_s)_{req'd} = 254 \text{ kips} - (3.52 \text{ in.}^2)(60 \text{ ksi}) = 42.8 \text{ kips}$$

$$(A_v)_{req'd} = \frac{V_{s,req'd}}{f_y} = \frac{42.8 \text{ kips}}{60 \text{ ksi}} = 0.72 \text{ in.}^2 \Rightarrow 4 - \#6@45^\circ = 4(0.44) \cos(45^\circ) = 1.25 \text{ in.}^2$$

For the exterior girder region, an additional 4-#6 reinforcing bars placed at a 45 degree angle was required for the diagonal cracking design as shown in Figure B.14.

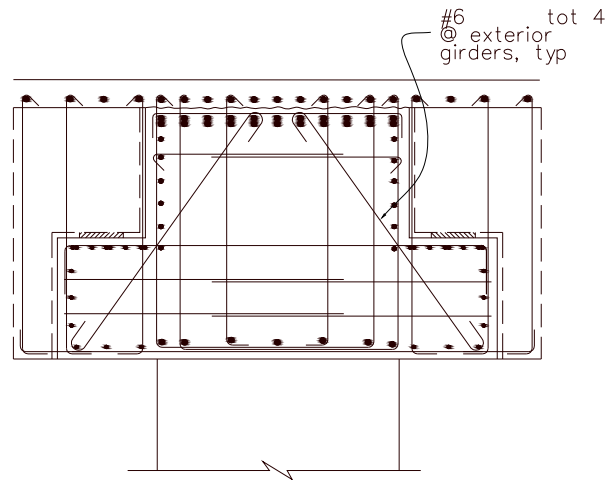


Figure B.14. Corbel diagonal cracking reinforcement

Between Girders:

$$V_c = 2 \left( 1 + \frac{-167 \text{ kips}}{0.5(47 \text{ in.} * 31 \text{ in.})} \right) \frac{\sqrt{3600 \text{ ksi}}(47 \text{ in.})(31 \text{ in.})}{1000} = 135 \text{ kips}$$

$$V_{s,req'd} = \frac{V_u}{\phi} - V_c = \frac{167 \text{ kips}}{0.9} - 135 \text{ kips} = 51 \text{ kips}$$

Similar to the previous two regions, the assumption of only 2 legs effective was used. Within the distance  $b_{\text{between}}$  there were five sets of #6 bars.

$$(A_v)_{req'd} = \frac{V_{s,req'd}}{f_y} = \frac{51 \text{ kips}}{60 \text{ ksi}} = 0.85 \text{ in.}^2$$

$$(A_v)_{provided} = 5 \text{ sets of 2 legged } - \#6 = 4.4 \text{ in.}^2$$

From the described calculations, only the region under the exterior girder required any additional diagonal steel. The rest of the sections satisfied the check by the contribution of the existing shear reinforcement present. The existing shear reinforcement was utilized in this design step because the loads being considered in the design were accounted for in the previous shear design of the cap beam and were not additional loads on the cap beam.

The final step in the cap beam ledge design was the calculation of the development length ( $l_{hb}$ ) for the #8 ledge bars. From Article 8.29.2 of the BDS, the basic development length for a hooked bar with the yield strength equal to 60,000 psi is to be taken as:

$$l_{hb} = \frac{38d_b}{\sqrt{f'_c(ksi)}} = \frac{1200d_b}{\sqrt{f'_c(psi)}} \quad (B.41)$$

where  $d_b$  is the bar diameter. However, since the side cover was greater than 2½ inches, the development length could be multiplied by 0.7 according to Article 8.29.3.2 of the BDS. Therefore, the development required was:

$$l_{dh} = \frac{38(1 \text{ in.})}{\sqrt{3.6(ksi)}} = 20.03 \text{ in.} \cdot (0.7) = 14 \text{ in.}$$

Based on the above estimate, the #8 bar was provided with 16 in. of development length, which completed the cap beam ledge design and the cap beam design.

## B.6 Dapped End Beam

The shear resistance of the concrete section was required to be checked; the same procedures used previously in designing the cap beam were used. From Article 5.8.3.4.2 of AASHTO, the strain can be determined. Then, by checking Table 5.8.3.4.2-1 of AASHTO, the appropriate angle of inclination and shear stress ratio can be determined with iteration. First, the actual shear stress ratio was determined. The shear stress ratio is given below and the values for  $d_v$ , the effective shear depth, and  $b_v$ , the effective web width, were determined from Article 5.8.2.9 of AASHTO.

$$d_v = 0.9(66 \text{ in.} - 5 \text{ in.}) = 54.9 \text{ in.} \approx 55 \text{ in.}$$

$$b_v = 19 \text{ in.} \Rightarrow \text{width of the block end of the girder}$$

$$V_u = 1.25DL = 1.25 * 84.4 \text{ kips} = 106 \text{ kips}$$

$$v_u = \frac{|V_u - \phi V_p|}{\Phi b_v d_v} = \frac{106 \text{ kips}}{55" \times 19"} = 0.101 \text{ ksi}$$

$$\frac{v_u}{f'_c} = \frac{0.101 \text{ ksi}}{5.5 \text{ ksi}} = 0.0184$$

Given the value for the actual shear stress ratio, the midsection strain was calculated by assuming an angle of inclination for the cracks. Once the midsection strain was calculated, the strain value and the shear stress ratio was used to check if the assumed angle of inclination was correct. The previously presented Eqs. (3.15) and (3.16) were used. However, the girder prestressing in the section did provide a force,  $V_p$ , to resist the shear force present. The moment used for the strain calculation was taken between the  $V_u$  and center of gravity of the vertical ties. For the angle of inclination,  $33.7^\circ$  was assumed.

$$V_p = (0.6 * 270 \text{ ksi})(6 * 0.217 \text{ in}^2) \left( \frac{24 \text{ in.}}{30 \text{ in.}} \right) \sin(5.836^\circ) = 17 \text{ kips}$$

$$N_u = 0.2 * V_u = 0.2 * 84.4 \text{ kips} = 21 \text{ kips}$$

$$M_u = 106 \text{ kips} * 18.5 \text{ in.} = 1961 \text{ kip} - \text{in.}$$

$$d_v = 66 \text{ in.} - 2 \text{ in.} - 3.5 \text{ in.} = 60.5 \text{ in.}$$

$$\epsilon_x = \frac{\frac{1961 \text{ kip} - \text{in.}}{60.5 \text{ in.}} + .5(21 \text{ kips}) + .5|106 \text{ kips} - 17 \text{ kips}| \cot(33.7^\circ)}{2((29000 \text{ ksi})(3.472 \text{ in.}^2))}$$

$$\epsilon_x = 554 * 10^{-6}$$

Next, by consulting Table 5.8.3.4.2-1 in AASHTO, the angle of inclination listed for a shear stress ratio of 0.0184 and a midsection strain of  $554 \times 10^{-6}$  was  $33.7^\circ$ , which was assumed. Therefore, the section was adequate to be used in designing the shear resistance.

## B.7 Dapped End Reinforcement

A strut-and-tie design was completed to efficiently design the dapped end reinforcement. For the strut-and-tie analysis the nodes were placed at the location of the bearing pad support, locations of point loads, and other suitable locations where struts and/or ties cross. The layout of the model chosen for analysis is shown below in Figure B.15. The point loads applied at nodes B and E were equivalent to the sum of the distributed force within the contributory area of the node. The distributed force was equal to the reaction at node A, which was  $V_u$ , distributed evenly over half the length of the cap beam.

Table B.4 presents the resultant values for the struts and ties for the model shown. In addition to the loads considered above, the additional dead load and live load acting on the span was checked to ensure proper transfer of these loads from the girders to the diaphragm with appropriate engagement of the dapped end.

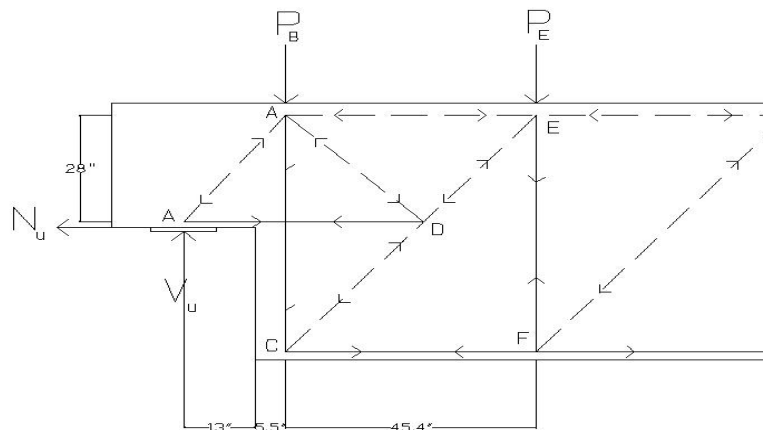


Figure B.15. Diagram showing the Strut and Tie model used for detailing the Dapped End of girders

Table B.4. Forces in Struts and Ties in the model shown

Strut/Tie	Force (kips)
C <sub>AB</sub>	127
T <sub>AD</sub>	91
C <sub>BD</sub>	74.4
T <sub>BC</sub>	158
C <sub>BE</sub>	21.1
C <sub>CD</sub>	197.6
T <sub>CF</sub>	118.6
C <sub>DE</sub>	127.4
T <sub>EF</sub>	97.9

First, the amount of force required to be transferred was calculated, and then the value of force transferred through shear friction from girder to diaphragm was calculated. The remainder of the force not able to be transferred by shear friction was assumed to transfer through the dapped end.

$$V_u = (1.25)(49.4 \text{ kips}) + (1.35)(206.7 \text{ kips}) = 341 \text{ kips}$$

Next the shear transfer through shear friction was required to be calculated. The steel acting in the shear transfer included the three 1-in. dowel bars connecting each side of the girder to the diaphragm along with four #11 bars placed transversely in the deck. The shear force provided from the steel was:

$$\phi V_{sf} = (0.9)[(1.0)(4 * 1.56 \text{ in.}^2)(60 \text{ ksi}) + 3(9.6 \text{ kips})] = 363 \text{ kips}$$

The shear resistance provided from the steel was greater than the shear demand estimated on the section, and therefore, the dapped end was considered to not be required to provide any additional shear transfer.

With the forces estimated from the strut and tie analysis, adequate reinforcement was designed to resist all forces. Steel reinforcement was needed to resist the tension forces from

nodes A-D, B-C and C-F. Using 60 grade steel, the area of reinforcement required for each of these ties is given below.

Tie AD,

$$A_s = \frac{T_u}{\phi f_y} = \frac{91 \text{ kips}}{(0.9)(60 \text{ ksi})} = 1.69 \text{ in.}^2$$

Tie CF,

$$A_s = \frac{T_u}{\phi f_y} = \frac{118.6 \text{ kips}}{(0.9)(60 \text{ ksi})} = 2.20 \text{ in.}^2$$

Tie AD,

$$A_s = \frac{T_u}{\phi f_y} = \frac{158 \text{ kips}}{(0.9)(60 \text{ ksi})} = 2.93 \text{ in.}^2$$

For Tie AD, in addition to the steel provided by the dapped end reinforcement, an additional steel amount was provided to resist the bursting stresses expected in this region from the prestressing strands. From the CONSPAN analysis, the amount of reinforcement needed to control bursting stresses was  $1.93 \text{ in}^2$ . Therefore, the area of steel required in the dapped end region at tie AD was estimated as follows,

Tie AD,

$$A_s = 2.93 \text{ in}^2 + 1.93 \text{ in}^2 = 4.86 \text{ in}^2$$

To provide adequate reinforcement to resist the tie forces, four #7 bars were used and detailed as shown in Figure B.16. In addition to the #7 bars, four #5 hoops were provided at the anchorage region of the prestressing strands to aid in resisting the bursting stresses.

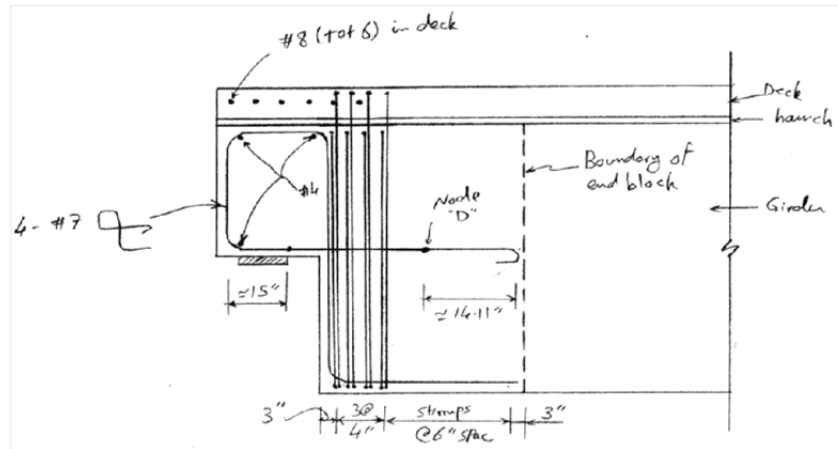


Figure B.16. Dapped End Region Reinforcement Layout

## B.8 Top Deck Reinforcement

Additional bars were provided over the cap beam for each girder to resist the negative moment acting at that location. From the CONSPAN output, the negative moment over the exterior and interior girders was 3661 kip-ft and 3516 kip-ft, respectively. Adequate negative moment reinforcement was then designed to resist the greater value, 3661 kip-ft. The process for the design was similar to that which was used for designing the flexural reinforcement of the cap beam, and Eqs. (B.8) and (B.9) were used for this purpose. The girders were spaced at 8-foot intervals and the compressive strength of the concrete was assumed to be 3.6 ksi. To determine the required deck steel, Eq. (B.8) was solved for  $A_s$ . Hence,

$$3661 \text{ kip} - \text{ft.} \left( \frac{12 \text{ in.}}{1 \text{ ft.}} \right) = 0.9A_s(60 \text{ ksi}) \left( 71.7 \text{ in.} - \frac{0.85(3.6 \text{ ksi})(96 \text{ in.})}{2} \right)$$

$$\Rightarrow A_s = 11.53 \text{ in.}^2$$

To provide the required amount of steel, ten #10 reinforcing bars were provided per girder location. The development length of the reinforcing bars was then calculated. From Section 8.25.1 of the BDS, the development length required for the negative moment reinforcement was determined from the following equation:

$$l_d = \frac{0.04A_b f_y}{\sqrt{f'_c}} = \frac{0.04 * 1.27 \text{ in.}^2 * 60000 \text{ psi}}{\sqrt{3600 \text{ psi}}} = 50.8 \text{ in.} = 4.23 \text{ ft.}$$

The above designed reinforcement was terminated in two separate locations: point of 50% of the moment capacity and point of zero negative moment. According to the CONSPAN output, the location of moment equal to 50% of the resisting moment capacity was at 13.5 feet from the centerline of the cap beam. By adding the development length of the bars to that distance, a length of 17.73 feet was obtained, and thus a length of 18 feet was used. A further calculation was then performed to ensure that proper capacity was provided. Therefore, at the location the reinforcing bars were fully developed, 13.77 feet from the cap beam centerline, the moment demand due to the applied loading was found to be 1884 k-ft, from CONSPAN. The provided moment capacity, assuming five #10 bars were effective, was:

$$\phi M_n = (0.9)(5 * 1.27 \text{ in}^2)(60 \text{ ksi}) \left( 71.7 \text{ in.} - \frac{(5 * 1.27 \text{ in.}^2)(60 \text{ ksi})}{0.85(3.6 \text{ ksi})(96 \text{ in.})} \right) \frac{1 \text{ ft.}}{12 \text{ in.}}$$

$$= 2030 \text{ kip} - \text{ft.} > 1884 \text{ kip} - \text{ft.}$$

Finally, the location to terminate the remainder of the bars was determined. An assumption that the bars would continue a distance equal to twice the length of the terminated bars was made. Therefore, the bars would extend 36 feet from the centerline of the cap beam before terminating them. The development length for these bars was the same as above, so the moment at a distance 31.77 feet from the centerline was checked to ensure that the negative moment at this location was zero. From the CONSPAN output, there was zero negative moment at that location, and thus the reinforcement was terminated as shown in Figure B.17.

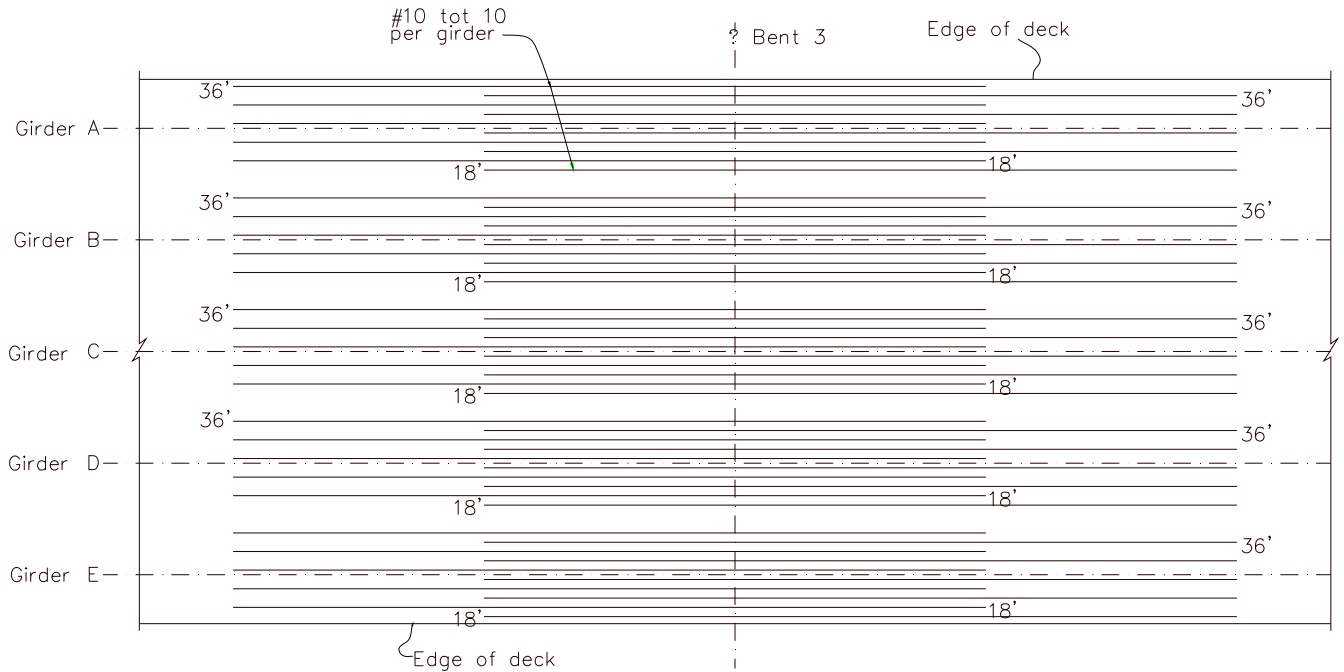


Figure B.17. Additional Deck Reinforcement

### B.9 Column-Bent Cap Joint Shear

The joint was detailed adequately to resist all possible shear forces from the superstructure and column for the column overstrength flexural capacity. This process ensured the force could be transferred effectively between the two components. The SDC details the steps required to ensure proper design of the joint. The first step was to check the principal stresses in the joint to ensure they are less than the allowable, according to Article 7.4.2 of the SDC, and they are listed below in Eqs. (B.42) and (B.43) where  $p_c$  is principal compression and  $p_t$  is principal tension.

$$p_c \leq 0.25 * f'_c \tag{B.42}$$

$$p_t \leq 12 * f'_t \tag{B.43}$$

To find the principal stresses for the joint shear stress, the vertical normal joint stress and horizontal normal joint stress were required before proceeding on to the principal stress calculation. The values for the stresses were obtained by using Eq. 7.10 in Article 7.4.2.1 and Eq. 7.13 to 7.17 in Article 7.4.4.1 of the SDC presented below in Eqs. (B.44) to (B.49).

$$B_{cap} = D_c + 2 (ft) \quad (B.44)$$

$$v_{jv} = \frac{T_c}{A_{jv}} \quad (B.45)$$

$$A_{jv} = l_{ac} * B_{cap} \quad (B.46)$$

$$f_v = \frac{P_c}{A_{jh}} \quad (B.47)$$

$$A_{jh} = (D_c + D_s) * B_{cap} \quad (B.48)$$

$$f_h = \frac{P_b}{B_{cap} * D_s} \quad (B.49)$$

where  $v_{jv}$  is the vertical joint shear stress,  $T_c$  is column tensile force at the overstrength moment,  $A_{jv}$  is the effective vertical joint area,  $l_{ac}$  is the length the column longitudinal reinforcement is embedded into the cap,  $B_{cap}$  is the bent cap width,  $f_v$  is the vertical stress acting on the joint,  $P_c$  is the column axial force,  $A_{jh}$  is the effective horizontal joint area,  $D_c$  is the cross-sectional dimension of the column in the direction of bending, and  $D_s$  is the depth of the superstructure at the bent cap. With the equations available, the joint stresses were calculated.

$$B_{cap} = 5.5 \text{ ft.} + 2 \text{ ft.} = 7.5 \text{ ft.} = 90 \text{ in.}$$

$$A_{jv} = 59 \text{ in.} * 90 \text{ in.} = 5310 \text{ in}^2$$

$$v_{jv} = \frac{3032 \text{ kips}}{5310 \text{ in.}^2} = 0.571 \text{ ksi} = 571 \text{ psi}$$

$$A_{jh} = (5.5 \text{ ft.} + 6.3 \text{ ft.}) * 7.5 \text{ ft.} = 88.5 \text{ ft.}^2 = 12746.3 \text{ in.}^2$$

$$f_v = \frac{1547 \text{ kips}}{12746.3 \text{ in.}^2} = -0.121 \text{ ksi} = -121 \text{ psi}$$

In the above calculations, positive stress is a tensile stress and negative stress is a compressive stress. Next the principal stresses were calculated from Eq. 7.12 of the SDC, given below in Eq. (B.50), as follows,

$$p = \frac{f_h + f_v}{2} \pm \sqrt{\left(\frac{f_h - f_v}{2}\right)^2 + v_{jv}^2} \quad (\text{B.50})$$

$$p_c = \frac{-121}{2} - \sqrt{\left(\frac{121}{2}\right)^2 + 571^2} = |-635 \text{ psi}| < 0.25(3600 \text{ psi}) = 900 \text{ psi}$$

$$p_t = \frac{-121}{2} + \sqrt{\left(\frac{121}{2}\right)^2 + 571^2} = 514 \text{ psi} < 12\sqrt{(3600 \text{ psi})} = 720 \text{ psi}$$

The stresses in the section were determined to be less than the allowable limits. The section was then checked for required reinforcement. First, a check was performed to see if the minimum reinforcement could be provided or if a more detailed reinforcement design based on a force transfer model was required. In Article 7.4.4.2 of the SDC, if the principal tensile stress does not exceed  $3.5\sqrt{f'_c}$  then only the minimum joint shear reinforcement is required. The corresponding stress limit was found to be 210 psi, which was less than the principal tensile stress. Therefore, section 7.4.4.3 was to be considered in the reinforcement design. The joint was then designed for vertical stirrups, horizontal stirrups, horizontal side reinforcement and j-dowel bars. For the vertical stirrups ( $A_s^{jv}$ ), Eq. 7.19 was to be used as presented in Eq. (B.51), where  $A_{st}$  is the total area of longitudinal bars being anchored from the column.

$$A_s^{jv} = 0.2 * A_{st} \quad (\text{B.51})$$

$$A_s^{jv} = 0.2 * (33 * 1.56 \text{ in.}^2) = 10.296 \text{ in.}^2$$

According to the SDC, existing stirrups in the cap beam can be considered for the vertical stirrups. Within the column six 4-legged #6 bars and eight 6-legged #9 bars were provided from previous design. The total area of steel provided was  $31.68 \text{ in.}^2$ , and thus no additional vertical stirrups were needed. Next, the area of horizontal stirrups ( $A_s^{jh}$ ) were detailed. From Eq. 7.20 of the SDC, shown below in Eq. (B.52), the required area of steel was calculated.

$$A_s^{jh} = 0.1 * A_{st} \quad (B.52)$$

$$A_s^{jh} = 0.1 * (33 * 1.56 \text{ in}^2) = 5.15 \text{ in}^2$$

Within the joint region, from the previous cap beam design, there were 14 sets of double legged #6 bars in the horizontal direction. The area provided was 12.32 in.<sup>2</sup>, and therefore, no additional reinforcement was provided. Third, area of horizontal side reinforcement ( $A_s^{sf}$ ) was detailed. From Eq. 7.21 of the SDC, presented in Eq. (B.53), the area of steel required is the greater of the two values that are proportional to the area of cap beam flexural steel ( $A_{cap}$ ) as given below.

$$A_s^{sf} \geq \begin{cases} 0.1 * A_{cap}^{top} \\ 0.1 * A_{cap}^{bot} \end{cases} \quad (B.53)$$

$$A_s^{sf} \geq \begin{cases} 0.1 * (41 * 1.56 \text{ in}^2) = 6.4 \text{ in}^2 \\ 0.1 * (0) = 0 \end{cases}$$

The area of top flexural reinforcement controlled for the calculation, and the required amount of steel was determined to be 6.4 in.<sup>2</sup>. In the cross section, there already existed two #8 and twelve #6 bars. The total area of steel provided was 6.86 in.<sup>2</sup>, which was greater than the area required. According to the SDC, the bars must be spaced less than 12 in. along the side of the cap beam. The existing steel already had been placed at spacing less than 12 in. Therefore, the reinforcement spacing was satisfactory. The next reinforcement designed was J-dowels according to Article 7.4.4.3d of the SDC. The required amount of steel ( $A_s^{j-bar}$ ) was found from Eq. 7.22, provided below in Eq. (B.54), and was based on the area of column longitudinal reinforcement,  $A_{st}$ ,

$$A_s^{j-bar} = 0.08 * A_{st} \quad (B.54)$$

$$A_s^{j-bar} = 0.08 * 51.48 \text{ in}^2 = 4.12 \text{ in}^2$$

However, since a large amount of additional vertical stirrups were provided, some of the vertical legs could be considered as J-dowels. Therefore, the amount of required vertical stirrups,  $A_s^{jv}$ , and the amount of J-dowel reinforcement,  $A_s^{j-bar}$ , was to be less than the provided steel in the

section. The amount of steel provided was 31.68 in.<sup>2</sup> and the combined amount of steel required was 14.41 in.<sup>2</sup>, requiring no additional steel for J-dowels. Finally, the transverse reinforcement ratio in the joint was to exceed the value calculated in Eq. 7.23 of the SDC, reproduced in Eq. (B.55). The transverse reinforcement in the column is allowed to be extended into the cap beam to meet the requirement. The following ratio was obtained for the joint region:

$$\rho_s = 0.4 * \frac{A_{st}}{l_{ac}^2} \quad (B.55)$$

$$\rho_s = 0.4 * \frac{51.48 \text{ in.}^2}{(59 \text{ in.})^2} = 0.00592$$

The longitudinal bars were extended as close as possible to the top flexural reinforcement of the cap beam. The provided confinement reinforcement was #6 hoops at 4 in. spacing with a 2 in. clear cover. Eq. (B.56) provides the equation used to calculate ratio of the reinforcement provided,  $\rho_s$ , where  $A_b$  is the reinforcement bar area,  $D'$  is the diameter of the confined concrete core and  $s$  is the spacing of the reinforcement.

$$\rho_s = \frac{4A_b}{D's} \quad (B.56)$$

$$\rho_s = \frac{4(0.44 \text{ in.}^2)}{(61.25 \text{ in.})(4 \text{ in.})} = 0.00718$$

The provided reinforcement ratio was greater than the required and that completed the detailing for the column-bent cap joint shear.

The prototype structure designed in this chapter was similar to many bridges designed in the recent times in the state of California. The structure was detailed for flexure and shear of the cap beam and column, and adequate force transfer through the joints and connections.

## Appendix C.      Prototype Material Properties

Table C.1. Concrete material properties

4.5 ksi Concrete	
Dilation Angle	32
Eccentricity	0.1
fbo/fco	1.16
K	0.666
viscosity Paramter	0
E	3605000 psi
Compressive Stress (psi)	Inelastic Strain
1600	0
2450	0.0005
3000	0.0011
4500	0.0035
4400	0.0059
3900	0.0089
3300	0.0145
2800	0.0195
2400	0.0245
2000	0.0295
400	0.0495
Tensile Stress (psi)	Cracking Strain
100	0
200	2.77E-05
300	5.55E-05
400	8.32E-05
497	0.000110125
300	0.04

a) 4.5 ksi concrete

7 ksi Concrete	
Dilation Angle	32
Eccentricity	0.1
fbo/fco	1.16
K	0.666
viscosity Paramter	0
E	4768962
Compressive Stress (psi)	Inelastic Strain
2400	0
4800	0.0005
7153	0.001
7000	0.0035
6500	0.0059
6000	0.0089
5000	0.0145
4200	0.0195
3400	0.0245
2500	0.0295
400	0.0495
Tensile Stress (psi)	Cracking Strain
132	0
264	2.77E-05
396	5.54E-05
528	8.30E-05
627	0.000103796
400	0.04

b) 7 ksi concrete

Table C.2. Steel material properties

Prestressing Steel	
E	28500000
Yield Stress	Plastic Strain
200000	0
240000	0.002982
270000	0.042982

a) Prestressing Steel

Reinforcing Bar Steel	
E	29000000
Yield Stress	Plastic Strain
60000	0
68000	0.02
90000	0.08
80000	0.25
1000	0.3

b) Reinforcing Bar Steel

